Mass-spectrometric in-situ measurements of atmospheric volatile organic compounds onboard passenger and research aircraft

Zur Erlangung des akademischen Grades eines

DOKTORS DER NATURWISSENSCHAFTEN

von der Fakultät für Physik des

Karlsruher Instituts für Technologie (KIT)

genehmigte

DISSERTATION

von

Dipl.-Phys. Garlich Fischbeck

Datum der mündlichen Prüfung:	20. Oktober 2017
Referent:	Prof. Dr. Johannes Orphal
Korreferent:	PD Dr. Michael Höpfner

Abstract

Despite being present in the atmosphere at very low levels, volatile organic compounds (VOCs) have profound effects on the atmosphere, it's self-cleansing capacity as well as on climate change and human health. Nevertheless, many unknowns and uncertainties remain concerning their emissions, atmospheric fate and impact, as reliable atmospheric measurements of these compounds are challenging and thus, not routinely conducted.

This work contributes to rectifying this deficiency by providing a new proton transfer reaction mass spectrometer (PTR-MS), fully customized for airborne measurements of VOCs and about two times more sensitive and light-weight than previously used PTR-MS. Such instrumental developments are of crucial importance, as instruments suited for VOC measurements onboard aircraft are not commercially available.

This thesis reports on the final set-up and first successful airborne deployment of the new device as well as well as on the steps, which were necessary to achieve them. The outstanding instrumental performance in terms of precision, sensitivities, detection limits and the range of detectable species is demonstrated based on the data of first airborne measurements and a thorough laboratory characterization. With the new instrument considerably more species of interest can be measured now in the upper troposphere and lowermost stratosphere (UTLS). This is also of great value for future measurements onboard the CARIBIC passenger aircraft, on which an adapted version of the new device will be regularly deployed starting in October 2017.

Another focus of this study is the assessment of emissions of acetone and acetonitrile by analyzing data collected during 214 flights of the CARIBIC passenger aircraft between 2006 and 2015. New top-down estimates for North American and Southeast Asian acetone sources are provided and compared to bottom-up estimates. The strong discrepancy found between two biomass burning emission inventories of acetonitrile, one of which generated in this work, is evaluated by comparing model simulations with the CARIBIC in-situ observations in the UTLS.

Contents

1. Volatile Organic Compounds (VOCs) in the atmosphere

The air we breathe comprises 78 % nitrogen and 21 % oxygen in terms of volume. The remaining 1 % is composed of a variety of trace gases including volatile organic compounds (VOCs) (e.g. Möller, 2014). These are carbon containing substances with a high vapor pressure that easily evaporate at room temperature and, as a result, are predominantly found in the gas phase. Although several definitions are in use, most of them have in common that "volatile" means a vapor pressure above 10 Pa at 20–25°C (e.g. Spengler et al., 2011).

Carbon monoxide (CO), carbon dioxide (CO_2) are commonly excluded from the group of VOCs, as they are considered to be inorganic compounds. Also methane (CH_4) is usually considered apart from other VOCs due to its role as direct greenhouse gas. To emphasize this, the more accurate term non-methane volatile organic compounds (NMVOCs) is sometimes used synonymously.

Besides the above-mentioned exceptions, the number of VOCs is large and not conclusively known. The number of organic compounds that has been identified in the atmosphere so far is assumed to be in the range of 10^4 to 10^5 (Goldstein and Galbally, 2007). However, a much larger number of atmospheric VOCs may exist (National Research Council, 1991; Goldstein and Galbally, 2007).

Despite being present at extremely low concentration, many VOCs have profound impacts on atmospheric chemistry affecting air quality and climate. The objective of this chapter and the two following sections is to reflect the current knowledge about the sources and sinks of VOCs and their role in atmospheric chemistry. The third section reviews different measurement techniques and platforms to detect VOCs in the atmosphere. In the last part of this chapter, the framework of atmospheric modeling to evaluate the current knowledge about VOCs and to assess the impact of individual compounds and sources is introduced.

1.1. Sources

About 1300 Tg of non-methane VOCs are on average released into the atmosphere each year (see Table 1.1). With regard to other oxidizable compounds in the atmosphere, this amount is above the direct emissions of CO ($\sim$1100 Tg a^{-1}) and more than twice as large as the global CH_4 emissions ($\sim$550 Tg Tg a^{-1}). Biogenic emissions (85 %) constitute the by far largest source of VOCs on the Earth's surface, followed by anthropogenic emissions (10 %) and release from biomass burning (5 %) (see Table 1.1). Nevertheless, the source allocation for specific VOCs (see Table 1.2) as well as the composition of emission on regional scales can be quite different.

Source Type	Annual Emissions [Tg a^{-1}]	Proportion [%]	References
Anthropogenic	129 ± 19	10 ± 2	*1 – 12*
Biogenic	1107 ± 150	85 ± 12	*13 – 16*
Biomass burning	61 ± 32	5 ± 3	*1 – 3, 17 – 20*
Total	1297 ± 201	100	*1 – 20*

Table 1.1.: Estimates of global annual VOC emissions from different sources (mean and standard deviation of literature values including emission inventories). [1] Lamarque et al., 2013; [2] EDGARv4.2 (Janssens-Maenhout et al., 2011); [3] EDGARv3.2FT200 (Olivier et al., 2005); [4] Piccot et al., 1992; [5] Müller, 1992; [6] ACCMIP (Lamarque et al., 2010); [7] ECLIPSE Gains 4a (Höglund-Isaksson, 2012; Klimont et al., 2013) ; [8] HYDE1.3 (van Aardenne et al., 2001); [9] Middleton, 1995; [10] Seinfeld and Pandis, 2016; [11] Peeters and Fantechi, 2009; [12] Seinfeld and Pandis, 1998; [13] Guenther et al., 1995; [14] Guenther, 2002; [15] Guenther et al., 2012; [16] Sindelarova et al., 2014; [17] Andreae and Merlet, 2001; [18] MACCity (van der Werf et al., 2006; Lamarque et al., 2010; Granier et al., 2011; Diehl et al., 2012; Heil et al., 2012); [19] GFASv1.0 (Kaiser et al., 2012); [20] GFED3 (van der Werf et al., 2010).

Biogenic emissions

Isoprene accounts for almost half of the total biogenic source in terms of mass (see Table 1.2) and is almost exclusively emitted by vegetation (Guenther et al., 2012; Wagner and Kuttler, 2014). The same is true for the group of terpenes including mono- and sesquiterpenes. However, many other VOCs emitted by plants are also released by human activities and biomass burning (e.g. ethanol, methanol and acetone).

The reasons why plants emit VOCs and the factors regulating it (e.g. temperature, humidity, light) have been object of intensive research (Kesselmeier and Staudt, 1999; Peñuelas and Llusià, 2001; Kegge and Pierik, 2010; Possell and Loreto, 2013; Vivaldo et al., 2017) and are well described in the reviews of Laothawornkitkul et al. (2009) and Loreto et al. (2014).

Group or Compound	Example Compound	Annual Emissions [Tg a^{-1}] BIO†)	ANT‡)	BB⋆)	Total
Isoprene	–	535			535
Monoterpenes	α-Pinene	162			162
Ethanol	–	21	6 *)	1 *)	28
Methanol	–	100	2	8	110
Acetone	–	44	1	2	47
Alkenes	Ethene	51	16	8	75
Alkanes	Ethane		40	5	45
Aromatics	Toluene	8 ◇)	30	3	41
Acids	Acetic acid	7	10	20	37
Aldehydes	Formaldehyde	26	5	9	40
Nitriles	Acetonitrile			2	2
Other		153	19	3	175
All		1107	129	61	1297

Table 1.2.: Estimated primary emissions of VOCs according to their sources: Biosphere (BIO), anthropogenic activities (ANT) and biomass burning (BB). The total emissions in the last row are taken from Table 1.1. The estimates for other VOCs are the difference between the total emissions and the sum for the specified groups and individual VOCs.
†) Guenther et al. (2012); ‡) MACCity (van der Werf et al., 2006; Lamarque et al., 2010; Granier et al., 2011; Diehl et al., 2012; Heil et al., 2012); ⋆) GFED3 (van der Werf et al., 2010); ∗) Kirstine and Galbally (2012); ◇) Guenther et al. (2012) and Misztal et al. (2015).

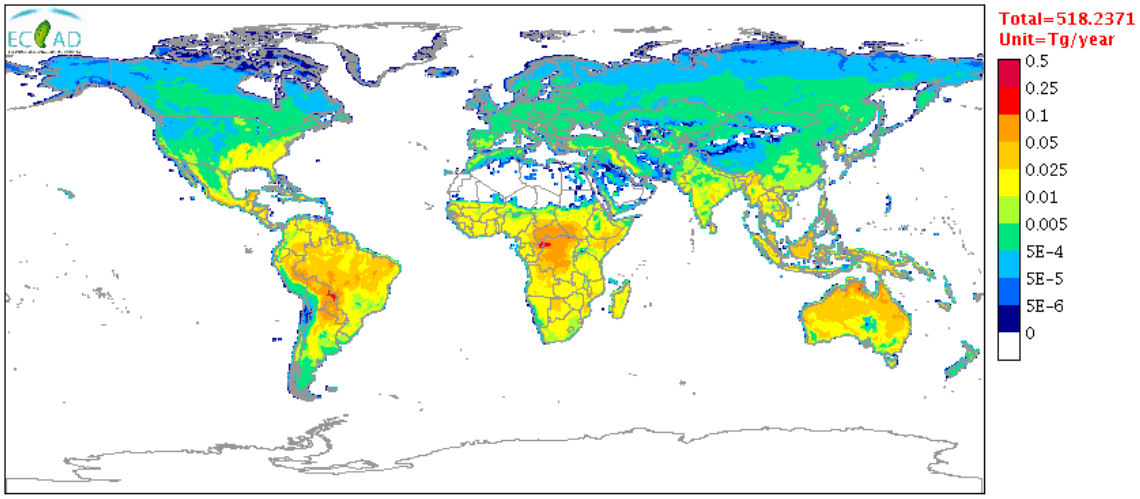

Figure 1.1.: Spatial distribution of biogenic VOC emissions, exemplarily shown for isoprene and the year 2008 (last available year in the database). For each pixel, the total annual emissions are displayed in terms of mass as specified in the MEGAN-MACC inventory (Sindelarova et al., 2014). Map created with the data visualization tool of the ECCAD database (ECCAD, 2013).

In Figure 1.1, the geographical distribution of biogenic emissions is shown for the case of isoprene. Throughout the year, emissions dominate in the tropics due to the

generally higher temperatures and solar radiation fluxes there (e.g. Guenther et al., 1999). The tropical rainforests and the (sub-)tropical savannas are particularly large sources of biogenic emissions. However, due to the decline of rainforests in response to climate change, the Northern Hemisphere is expected to become a more significant source of biogenic emissions in future (Lathière et al., 2005).

Anthropogenic emissions

Although biogenic emissions dominate globally, the anthropogenic contribution to local or regional VOC emissions can be substantial, in particular in urban and industrialized regions (e.g. Baker et al., 2008; Borbon et al., 2013). Anthropogenic VOC emissions originate from a wide variety of sources including the production, storage and usage of fossil fuels and solvent use in paints, consumer products and industrial processes. With a proportion of about 70 %, the exploitation of fossil fuels constitutes by far the largest source on a global scale (Lamarque et al., 2010). As natural gas, crude oil and refined products thereof contain large amounts of VOCs, a considerable fraction already evaporates during production and storage (e.g. Harley and Kean, 2004; Tamaddoni et al., 2014).

During combustion, hydrogen and carbon atoms of the fuel compounds are oxidized to water and carbon dioxide (CO_2), respectively. However, in practice, incomplete

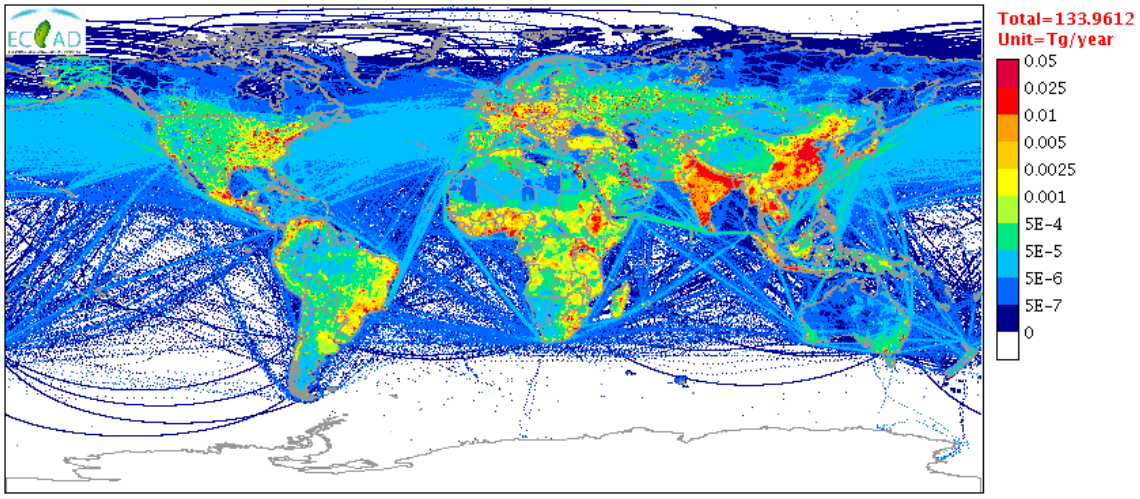

Figure 1.2.: Spatial distribution of anthropogenic (non-methane) VOC emissions, exemplarily shown for 2008. For each pixel, the total annual emissions are shown in terms of mass as specified in the EDGARv4.2 inventory (Janssens-Maenhout et al., 2011). Map created with the data visualization tool of the ECCAD database (ECCAD, 2013).

combustion leads to the formation of CO and a variety of VOCs as by-products (e.g. Wallington et al., 2006; Russell, 2013; Mellouki et al., 2015). Further VOC emissions result from unburned fuel that is carried over to the exhaust (Wyatt, 2013). Consequently, the actually emitted VOCs and their relative abundances strongly depend on the chemical composition of the fuel and the combustion conditions (Harley and Kean, 2004).

Typical VOCs, which are predominately emitted by anthropogenic sources, include the group of alkanes (e.g. ethane, propane and butane) and aromatic compounds such as benzene and toluene (see Table 1.2; for airborne measurements of benzene see Section 3.4.2).

At least in industrialized nations, a large share of emissions from internal combustion engines is nowadays avoided due to the reformulation of fuels and the deployment of emission control systems (e.g. von Schneidemesser et al., 2010; Borbon et al., 2013; Huang et al., 2017). In Germany, the VOC emissions from motor vehicles have been reduced by a factor of 12 in the last 15 years (Umweltbundesamt, 2017).

However, on a global scale, such achievements are compensated due to the fact that major sources of anthropogenic VOCs have moved from industrialized nations to developing countries (Grubler et al., 2012; Crippa et al., 2016; Huang et al., 2017). In Figure 1.2, the global distribution of anthropogenic VOC emissions is shown. Particularly large quantities of anthropogenic VOCs are emitted in Southeast Asia and China.

Biomass Burning

Another strong source of VOCs attributable to the combustion of carbonaceous "fuels" is the burning of biomass. Although biomass burning occurs naturally in the form of wild fires ignited by lightning strikes, human-induced fires, including open and domestic biomass burning (e.g. for heating and cooking), dominate globally (e.g. Innes, 2000).

In Figure 1.3, the global distribution of emissions from biomass burning is shown. Similar to the biogenic source of VOCs (cf. Figure 1.1), biomass burning emissions dominate in the tropics (e.g. Seiler and Crutzen, 1980; Crutzen and Andreae, 1990). In this part of the world, fire is widely used e.g. for deforestation, cultivation of fields (slash-and-burn agriculture), burning of agricultural residues and domestic cooking

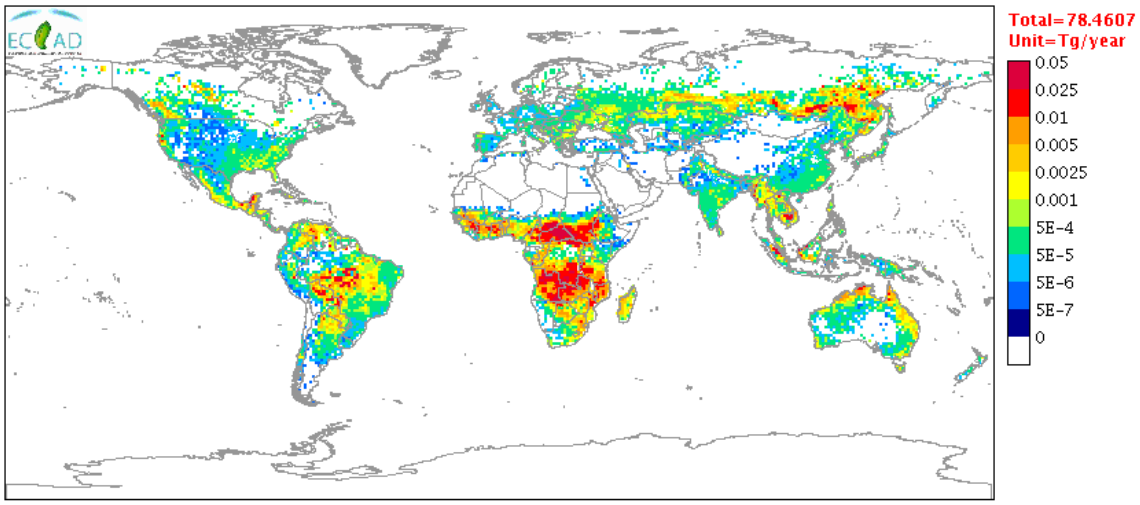

Figure 1.3.: Spatial distribution of (non-methane) VOC emissions from biomass burning, exemplarily shown for 2008. For each pixel, the total annual emissions are displayed in terms of mass as specified in the MACCity inventory (van der Werf et al., 2006; Lamarque et al., 2010; Granier et al., 2011; Diehl et al., 2012). Map created with the data visualization tool of the ECCAD database (ECCAD, 2013).

(Hao and Lio, 1994). Besides in the tropics, larger emissions from biomass burning also occur at high latitudes in the Northern Hemisphere due to boreal forest fires (e.g. Harden et al., 2000; Turetsky et al., 2011).

In general, VOCs are emitted from the burning of biomass and biofuels as a result of incomplete combustion. The chemical composition varies widely and depends strongly on the fuel type, moisture content and the form of combustion (e.g. smoldering or flaming) (Lobert et al., 1990; Simoneit, 2002; Williams, 2004). Impressive compilations of species known to be emitted by biomass burning have been provided by Andreae and Merlet (2001) and Akagi et al. (2011). A compound that has been given special attention to in many studies is acetonitrile. Although not being emitted in particularly large quantities, acetonitrile belongs to the very few VOCs, which are almost exclusively emitted by biomass burning (Lobert et al., 1990; Holzinger et al., 1999) and thus, constitutes an ideal tracer (Akagi et al., 2011).

Uncertainties

Although the characterization of emissions has significantly improved during the last decades, estimates of compound-specific global emissions are still subject to considerable uncertainty due to the poor data coverage in many regions and the lack

of continuous measurements (e.g. Michel et al., 2005; Harley et al., 2007; Guenther et al., 2012; Messina et al., 2016; Li et al., 2017).

While the ranges given in Table 1.1 only reflect the variation among different studies, the uncertainty of emission estimates for specific sources and VOCs commonly lies between a factor of 1.5 and 4 (Lamb et al., 1987; Olivier et al., 2003; Streets et al., 2003; Guenther et al., 2012).

Constraining these estimates is of upmost importance to better assess the impact of VOCs on climate and air quality, addressed in the next section. It is also important to note that so far only sources on the Earth's surface have been considered. In the next section, a further substantial source of atmospheric VOCs will be introduced.

1.2. Atmospheric fate and impact

Following emission, atmospheric transport and dispersion processes distribute the VOCs in the atmosphere, where they are involved in a series of chemical reactions and physical processes leading to their eventual removal. Consequently, the extent to which individual VOCs are distributed in the atmosphere strongly depends on their reactivity and atmospheric sinks. Short-lived VOCs like e.g. isoprene (∼1-2 h lifetime according to Atkinson, 2000) can only be found in the vicinity of their sources in the lowest part of the atmosphere, the planetary boundary layer with an altitude range of approximately 0–2 km*. Other VOCs have sufficiently large atmospheric lifetimes (days to weeks) to cross the boundary layer temperature inversion and enter the free troposphere (2–12 km)* above it. Very long-lived species with tropospheric lifetimes exceeding several months (e.g. acetonitrile, see Chapter 6) even penetrate into the stratosphere (12-50 km)* although convective transport across the tropopause, which constitutes the boundary between the troposphere and stratosphere, is significantly impeded (e.g. Vardavas and Taylor, 2007). In general, the atmospheric lifetime of a species and thus, its distribution depends on its physical properties, its reactivity and the presence of reaction partners.

Physical processes such as dry and wet deposition onto the Earth's surface lead to an instantaneous and complete removal from the atmosphere, but due to the low polarity and water solubility of many primary emitted species, these processes only

*The given altitudes are only approximate values, as the boundaries of the different atmospheric layers vary substantially depending on time and location.

constitute a minor sink for them (e.g. Mullaugh et al., 2015). Instead, the by far dominating loss mechanism of atmospheric VOCs is (photo-)chemical degradation. The gas phase oxidation by hydroxyl radicals (OH) is the most important sink in this respect, but also photolysis and reactions with O_3, NO_3 and halogen radicals play a role (e.g. Williams and Koppmann, 2007).

In general, the atmosphere acts as a giant photochemical reactor, in which VOCs are gradually broken down to carbon dioxide and water. However, this overall process involves many reactions and inevitable leads to the (secondary) formation of oxygenated VOCs (for an overview, see Jenkin et al., 1997; Atkinson and Arey, 2003; Atkinson et al., 2006).

For some of these compounds (e.g. formaldehyde, formic and acetic acid), the secondary produced amounts exceed the primary emissions (Koppmann and Wildt, 2007; Paulot et al., 2011), e.g. it is believed that each year ∼1600 Tg of formaldehyde are produced in-situ due to the oxidation of methane, isoprene and other VOCs (Stavrakou et al., 2009).

Subsequent products of the photochemical degradation of individual VOCs generally decrease in volatility, resulting in an increased probability of these compounds to condense onto pre-existing particles or create new particles through nucleation (e.g. Budisulistiorini et al., 2015). Furthermore, the presence of VOCs, or rather deviations in their concentrations, may shift entire photochemical equilibria and thus, influence the concentrations of key species in atmospheric chemistry (e.g. radicals, ozone and other greenhouse gases).

It is primarily this impact on other atmospheric constituents that makes VOCs so important for atmospheric research. Several trace gases formed by chemical reactions involving VOCs or being influenced by them are known to have profound effects on air quality and climate (e.g. Koppmann, 2010). The most familiar ones are ozone and organic aerosol (e.g. Ebi and McGregor, 2008).

VOCs as precursors of ozone and organic aerosol

Ozone is formed in the troposphere when atomic oxygen ($O(^3P)$) resulting from the photolysis of nitrogen dioxide (NO_2) combines with molecular oxygen (O_2). The reverse reaction, which converts ozone and nitrogen oxide (NO) to O_2 and NO_2, also takes place. However, in the presence of VOCs, there are further reactions that

convert NO to NO_2 and thus, the overall equilibrium between ozone and nitrogen oxides (NO_x = NO + NO_2) is shifted towards an enhanced ozone production (e.g. Thornton et al., 2002). As a greenhouse gas, ozone has a direct radiative forcing effect leading to global warming when tropospheric ozone concentrations increase (e.g. Shindell et al., 2006). Due to its role as primary source of OH, the most important oxidizing agent of the atmosphere, ozone, more specifically changes in the ozone concentrations, may also influence the lifetimes of other greenhouse gases (e.g. Fiore, 2014). Near the surface, it is a key constituent of photochemical smog and known to have adverse effects on human health and ecosystems if present at high concentration (Haagen-Smit, 1952; Mellouki et al., 2015).

The impact of organic aerosol on public health is believed to be even greater (e.g. Alves et al., 2017). It has been estimated that air pollution due to particulate matter, to which organic aerosol is a major contributor (e.g. Cabada et al., 2004), leads to 3.3 million premature deaths per year (Lelieveld et al., 2015). In addition, organic aerosols have a direct radiative effect on climate by reflecting or absorbing incoming light and an indirect one by influencing cloud formation and properties as cloud condensation and ice nuclei (e.g. Haywood and Boucher, 2000). Overall, the interaction of aerosols with radiation and clouds leads to a slightly negative radiative forcing, but the uncertainty associated with it is large (Myhre et al., 2013).

Besides the production of ozone and organic aerosol, the degradation of VOCs has profound effects on the atmosphere's self-cleansing capacity, which is largely determined by the hydroxyl radical (e.g. Prinn, 2003; Lelieveld et al., 2016). Reaction with OH is the main loss mechanism of organic trace gases from the atmosphere (e.g. Williams, 2004). While the initial reaction consumes OH radicals, subsequent (photo-)oxidation steps may lead to either a regeneration of OH (e.g. Lelieveld et al., 2008) or a net production of HO_x (= OH and HO_2). The contribution of this secondary source to the overall HO_x budget can be significant, especially in the dry upper troposphere, where the primary source of OH – the photolysis of ozone followed by the reaction of $O(^1D)$ with water vapor – is rather ineffective (Singh et al., 1995; Jaeglé et al., 1998; Regelin et al., 2013; Neumaier et al., 2014).

Upper Troposphere and Lowermost Stratosphere (UTLS)

The upper troposphere (UT) is also of interest in another respect: Together with the lowermost stratosphere (LS), it forms the UTLS, an atmospheric region particularly

sensitive to climate change (e.g. Lackner et al., 2009). Conversely, changes in the structure and trace gas composition of the UTLS may have a strong feedback on climate (e.g. Riese et al., 2012). As the processes controlling it, including the role of VOCs, are not yet fully understood, frequent and comprehensive measurements of the composition of the UTLS (i.e. comprising as many relevant atmospheric constituents as possible and covering the full spatial extent of the UTLS) are of vital importance.

Concurrent measurements of secondary air pollutants and their precursors will help to better understand the underlying formation mechanism. The platforms suitable to perform such measurements and the techniques used to measure VOCs in the atmosphere are presented in detail in the next section.

1.3. Measurement techniques and platforms

The composition of the atmosphere can be monitored using two different approaches: (i) in-situ measurements and (ii) remote sensing observations. In situ (Latin expression for "on site") refers to measurements conducted directly at the point of interest. This requires the instrumentation to be transported to the atmospheric region under investigation and to be in direct contact with the air masses.

In contrast, remote sensors acquire information about air masses far away (remote) from the sensor without being in physical contact with them. Instead the technique uses the fact that the natural electromagnetic radiation traveling through the atmosphere interacts with the atmospheric constituents, e.g. each type of molecule absorbs and emits radiation at characteristic wavelengths. Therefore, the electromagnetic radiation propagated by an atmospheric region allows direct conclusions about its molecular composition.

Optical spectrometers (e.g. Fourier transform or differential optical absorption spectrometers) are used on the Earth's surface, onboard aircraft, balloons and satellites (e.g. Friedl-Vallon et al., 2004; Bernath et al., 2005; Fischer et al., 2008; Wunch et al., 2011; Friedl-Vallon et al., 2014). In order to identify the presence of a species with these instruments, its spectral signature needs to be well known (e.g. documented in the high-resolution transmission molecular absorption database HITRAN; Rothman et al., 2012), strong enough and relatively free of interferences from other gases, which limits the number of detectable species.

Satellite observations have the great advantage that a quasi-global coverage is obtained with a single instrument – a fact ensuring a uniform quality of the data set. To achieve a similar data product with ground-based observations, a large number of spectrometers have to be globally distributed and regularly calibrated against each other. Despite this unique advantage of satellite platforms, the spatial and temporal resolution of atmospheric trace gas profiles derived from satellite data is rather coarse ($>$ 3 km vertical resolution: $\sim$300 km horizontal resolution for limb sounder and $\sim$10 km for nadir sounders; Bernath, 2017) and does not allow to investigate local dynamics over short timescales.

Here, in-situ measurements provide a more detailed insight in the atmospheric composition and its variability on smaller time and spatial scales. The latter is particularly important as the variability in the spatial and temporal distribution of atmospheric trace gases in the UTLS can be quite large (Fischer et al., 2008). Aside from reasons related to the atmosphere (e.g. mixing timescales, atmospheric transport barriers such as the tropopause), the high variability in atmospheric VMRs is also due to the fact that most VOC emissions on the Earth's surface are highly variable in time and space (cf. Figures 1.1–1.3). To better assess these emissions and small-scaled atmospheric processes (e.g. stratospheric-tropospheric exchange), in-situ measurements are indispensable.

Another advantage of in-situ measurements is the large range of available measurement techniques (for an overview see Heard, 2008, and Nozière et al., 2015), allowing for the detection of far more species than it is possible with remote sensing. Nevertheless, measurements of VOCs are still less common than measurements of other atmospheric constituents (e.g. NO, NO_2, CO, CO_2, O_3), because their accurate quantification is more difficult (e.g. Apel et al., 2008). Besides being present at very low concentrations (volume mixing ratios in the UTLS typically range from several ppb[†] to less than 1 ppt[†]) and thus, requiring highly sensitive instruments, there are VOCs that tend to stick to surfaces of the sampling system, whereas others are erratically formed in the measurement system (e.g. Apel et al., 2003).

The most established and widespread technique for in-situ measurements of VOCs is gas chromatography (GC). Compounds are separated in columns coated with a fine film of a stationary phase according to their interaction strength with the phase. The longer a compound interacts with the stationary phase, the more time it takes to migrate through the column. Coupled to some form of detector, it is a

[†]1 ppb = 1000 ppt = 10^{-9} mol mol^{-1}, i.e. 1 VOC molecule in 10^9 air molecules, cf. Section 2.1.

highly specific method to identify a variety of hydrocarbons and oxygenated VOCs in complex gas mixtures. However, for the detection of low concentrations, a complex pre-concentration of the sample is necessary.

When deployed onboard aircraft, the long retention times of compounds in conventional GC columns become a major obstacle. Even for the newly-developed Fast-GC systems (Apel et al., 2003; Wenk et al., 2010; Jäger et al., 2014; Wenk, 2016; Bourtsoukidis et al., 2017), the chromatographic runtimes (∼3–5 min) are still above the desired time resolution, which is necessary to investigate small scale variabilities using aircraft.

Meanwhile, another analytical method overcoming this problem has been widely used to detect VOCs in atmospheric research: Proton transfer reaction mass spectrometry (PTR-MS) (Lindinger et al., 1998) allows real time monitoring of most VOCs, as it requires no sample pre-treatment and offers a much better time response than GC (in the order of a few seconds), while being sufficiently sensitive for atmospheric measurements of many VOCs. This combination of a high time resolution and a high sensitivity makes PTR-MS an ideal candidate for airborne in-situ measurements in the remote atmosphere, where concentrations are low, but highly variable.

The measurement technique of PTR-MS relies on soft chemical ionization of VOCs by proton transfer from hydronium ions (H_3O^+). Although this limits the range of detectable species to those having proton affinities greater than that of water, most VOCs of atmospheric interest can be detected by PTR-MS (for details, see review by de Gouw and Warneke, 2007).

For more than a decade after its introduction, PTR-MS instruments have been commonly equipped with quadrupole mass filters, which have a good sensitivity, but need to scan through the mass spectrum and cannot resolve isobaric compounds, i.e. two VOCs of the same nominal mass but different accurate mass. The application of time-of-flight (TOF) mass analyzers overcomes this problem, as the entire mass spectrum is simultaneously acquired with high resolution. However, without further modifications, current PTR-TOF-MS are still about one order of magnitude less sensitive compared to quadrupole-based systems (Warneke et al., 2015). Advanced PTR-TOF instruments, which compensate this deficiency by making use of additional ion guides in front of the mass spectrometer (e.g. Sulzer et al., 2014; Yuan et al., 2016; Breitenlechner et al., 2017), have just begun to find their way into the market (TofWerk, 2017).

Aircraft platforms

Both techniques, GC and PTR-MS have been successfully deployed onboard aircraft, which are a key platform for measurements in the upper troposphere and lower stratosphere (UTLS). As aircraft can move freely in the lower atmosphere, they are particularly well suited to investigate the dynamics of the UTLS and bridge the gap between ground-based and space-borne observations.

Both, research and passenger aircraft may be considered as platforms. Research aircraft are ideally suited for case and process studies, as they allow for targeted measurements at controllable times and places (Schumann et al., 2013). The instrumental payload as well as the time and region, in which flights are performed, are adapted to the scientific objectives. Flight routes can be chosen according to forecasts and observations during flight. It is thus possible to chase atmospheric phenomena (Schumann et al., 2013) or to repeatedly sample the same air masses to investigate their temporal evolution (Stohl et al., 2004). However, flight hours are expensive and measurements are usually restricted to dedicated short term campaigns over defined regions. Due to this fact and changing payloads, research aircraft observations hardly complement each other and are not suited for long term analysis.

In contrast, deployment onboard passenger aircraft is less expensive and enables regular observations with the same instrumentation over several years. Due to the various flight routes of commercial aircraft, a good geographical coverage can even be obtained with a single aircraft. In this respect, passenger aircraft observations combine several advantages of satellite platforms (good coverage in terms of space and time and comparability of data) with the high resolution and precision of airborne in-situ measurements.

Moreover, commercial aircraft provide an ideal platform to investigate the UTLS, as their cruising altitude coincides with this important region at midlatitudes. Due to the variable height of the tropopause, commercial airliner frequently cross the tropopause, which ensures sampling of both tropospheric and stratospheric air.

The use of commercial aircraft for atmospheric research goes back to the late 1960s: Seiler and Junge (1969) measured atmospheric carbon monoxide onboard a Lufthansa Boeing 707 in 1968. Several projects followed measuring either ozone, carbon monoxide, water vapor, nitrogen oxides or a combination of these onboard passenger aircraft (Fabian and Pruchniewicz, 1977; Holdeman et al., 1977; Brunner et al., 1998, Marenco et al., 1998).

A more comprehensive set of instruments for simultaneous measurements of a larger number of species was first deployed onboard commercial aircraft in the framework of the CARIBIC project (Civil Aircraft for the Regular Investigation of the atmosphere Based on an Instrument Container; e.g. Brenninkmeijer et al., 1999).

As the data used in this study mainly originates from CARIBIC measurements and a new mass spectrometer for VOC measurements has been developed for deployment within this project (see Section 3.5), the project will be described in more detail in the following section. The subsequent section is dedicated to the new German research aircraft HALO, on which the new mass spectrometer has been successfully deployed for the first time (see Section 3.4).

1.3.1. CARIBIC project

In former projects using commercial aircraft as platform for atmospheric measurements, only a few selected species were measured. This is due to the fact that only relatively small sensors, which are capable of autonomous operation over longer time periods, but limited to the detection of single species, can be permanently installed in the aircraft fuselage. However, to learn more about the origin of observed variations, e.g. contributions of different pollution sources or complex coupling of atmospheric processes and chemistry, it is of decisive importance to simultaneous measure a larger number of species and aerosol properties, which complement and supplement each other. The CARIBIC project aims to measure such a large set of species and properties using passenger aircraft.

For this purpose, more sophisticated instruments and sample collecting systems, which cannot be permanently installed in the fuselage due to their overall size, weight and need for regular maintenance, are required. The CARIBIC project overcomes this problem by accommodating a comprehensive suite of such instruments – provided by different research institutes across Europe – in a modified airfreight container (see Figure 1.5), which can be flexibly deployed on selected flights in the cargo bay of a passenger aircraft. Only the dedicated air inlet system, which supplies the instruments with ambient air during measurements flights, is permanently installed in the aircraft's fuselage.

The operation of the CARIBIC container started in 1997 using a Boeing 767 of LTU Airlines as platform (Brenninkmeijer et al., 1999). Measurements were conducted once or twice per months on two consecutive long-haul flights, i.e. on a flight from Germany

to the Caribbean, South Africa, Sri Lanka or the Maldives and the subsequent return flight. However, this first phase, also referred to as CARIBIC I, ended in 2002 due to the decommissioning of the aircraft.

The second phase (CARIBIC II) started in December 2004 with a larger and more advanced version of the container (3.2 × 1.5 × 1.6 m, current weight: 1.6 t) being deployed for the first time onboard the Lufthansa Airbus A340-600 "Leverkusen" (Brenninkmeijer et al., 2005 and 2007). This aircraft exclusively serves long-range routes from Germany to North and South America, South Africa and Asia, which enables to sample a variety of different source regions with the CARIBIC container. Since May 2005, the enhanced CARIBIC container is regularly deployed onboard this aircraft on 4–6 consecutive flights per month.

Meanwhile, it accommodates 15 instruments for in-situ measurements and a differential optical absorption spectrometer (DOAS) for remote sensing of atmospheric trace gases (Dix et al., 2009). In total, about 100 trace species and aerosol parameters can be simultaneously monitored with the container, including O_3, total and gaseous H_2O, NO, NO_y, CO, CO_2, CH_4, mercury and e.g. the number size distribution of aerosol particles. VOCs such as acetone and acetonitrile are measured with a strongly modified commercial PTR-MS (Ionicon, Innsbruck, Austria; see Sprung and Zahn, 2003, 2005 and 2010). In addition, air and aerosol samples are collected for post-flight analysis (Schuck et al., 2009; Baker et al., 2010; Martinsson et al., 2014).

Until April 2014, flights started in Frankfurt, but since then the aircraft is stationed in Munich and measurements are done on flights from and to Munich. Figure 1.4 shows the routes of all flights, on which the CARIBIC container was deployed until February 2016. As the aircraft only performs flights in- and outbound of its home base, the flight pattern is naturally centered around Germany and there are regions, which were sampled less frequently (mainly in the Southern Hemisphere) or not at all (e.g. the Pacific Ocean). Despite this limitation, large parts of the Northern Hemisphere midlatitudes have been frequently sampled during all seasons.

In March 2016, a larger modification of the container was started entailing the temporary suspension of measurement flights. The modification includes the installation of several new instruments and e.g. the exchange of the above-mentioned PTR-MS by a completely new version, based on this work (see Section 3.5). A recently made picture of the container including the new PTRMS-CARIBIC is shown in Figure 1.5. First measurement flights with the new payload are expected to take place in October 2017.

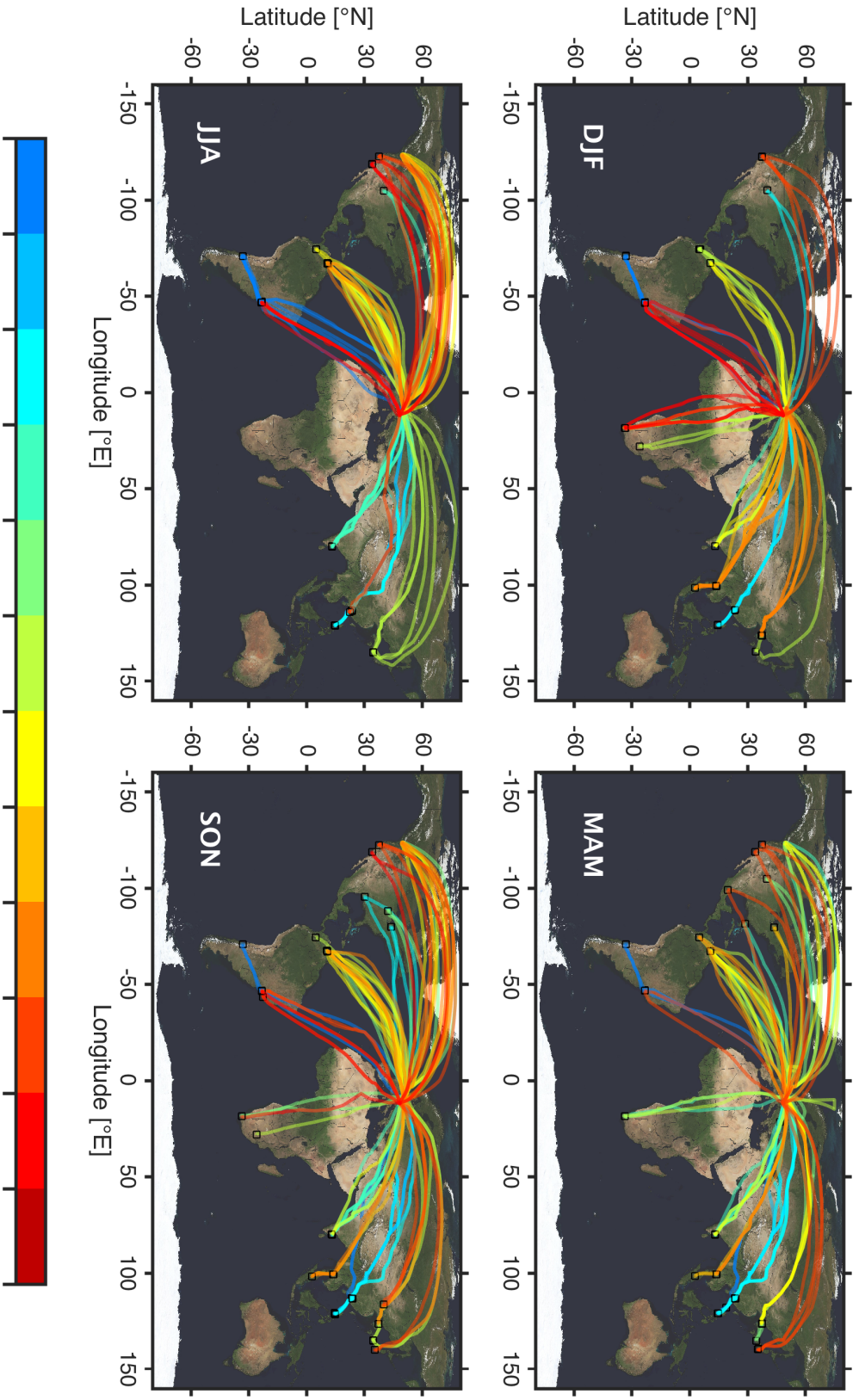

Figure 1.4.: Measurement flights of the CARIBIC passenger aircraft since May 2005. Flight paths are grouped according to season and color-coded by year. Satellite image courtesy of NASA's Earth Observing System (EOS).

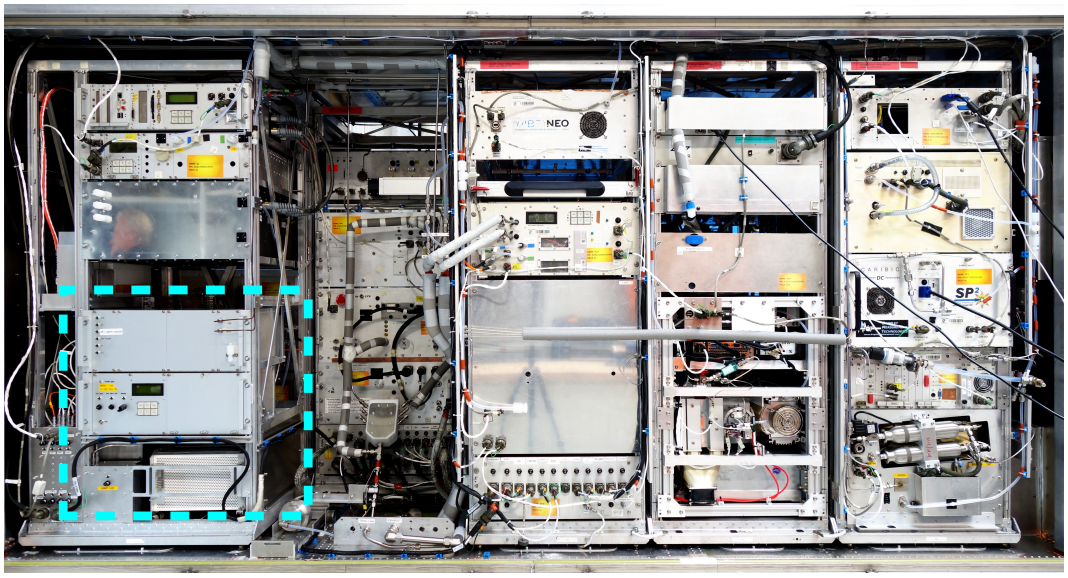

Figure 1.5.: Front side view of the CARIBIC container interior as of 11 September 2017. The new PTRMS-CARIBIC is installed in the lower left corner (cyan dash-lined box). The connections to the air inlet system permanently installed in the aircraft's fuselage are positioned on the right-hand side next to the PTRMS in the bottom plate. Image courtesy of Simon Heger (KIT).

1.3.2. HALO aircraft

The high altitude and long range research aircraft (HALO) is the current flagship of German research aircraft (Krautstrunk and Giez, 2012). It is a Gulfstream G550 business jet, which has been strongly modified to accommodate various instruments in the cabin and under the fuselage and wings. With a maximum payload of ∼3 tons, it can carry much more scientific instrumentation than most other research aircraft, thus enabling a more comprehensive investigation of complex atmospheric processes (e.g. Schumann, 2007; Mech et al., 2014).

Moreover, the high range of up to 12500 km (depending on the scientific payload) allows measurements over continental scales and in remote regions, which are not accessible with smaller aircraft. With a maximum ceiling altitude of 15-16 km, it belongs to the few available research aircraft suited for sampling the lower stratosphere (e.g. Schumann, 2007). It is in service since 2010 and operated by the Flight Facility of the German Aerospace Center (DLR) in Oberpfaffenhofen. Meanwhile, several scientific campaigns have been performed with HALO (e.g. Wendisch et al., 2016; Stevens et al., 2016; Voigt et al., 2017; Gottschaldt et al., 2017).

1.4. Modeling tools and emission inventories

In the past, much has been learnt about the atmosphere from in-situ and remote sensing observations. These observations motivated further laboratory studies, investigating single atmospheric reactions under controlled conditions and initiated the development of numerical models to simulate the behavior of the atmosphere. As controlled experiments to test a certain hypothesis are not possible in the large-scale atmosphere, atmospheric models provide a powerful tool to study the atmosphere.

Moreover, models offer the possibility to test the current understanding of atmospheric processes and chemistry by comparing the simulations with observations. If the model reproduces major features of the atmosphere, it can be used to predict its future state. As simulations can be easily done for different scenarios, models also allow to assess the impact of specific changes in the atmospheric system.

However, the capability of a model to reproduce the behavior of trace gases in the atmosphere strongly depends on the range of processes included in the model and the model input, such as the parametrization of chemical reactions, physical processes and trace gas emissions. The latter is commonly based on the data of emission inventories, providing geographically and temporally allocated (gridded) emission estimates for a specific category of sources. In Figures 1.1–1.3, such emission data is shown for the three major sources (biogenic, anthropogenic and biomass burning emissions).

As it is not possible to monitor each individual emission source on Earth, inventories extrapolate the emissions found at a few sources at a specific date to many other sources and time periods by making various assumptions. It is for this reason, that emission inventories have large uncertainties (Guenther et al., 2006; Frey, 2007; Guenther et al., 2012; Messina et al., 2016).

Comparison of model results with in-situ measurements or inverse model studies are therefore crucial to constrain the emissions and help to find errors in the inventories (e.g. Hein et al., 1997; Jacob et al., 2002; Palmer et al., 2003; de Foy et al., 2007; Song et al., 2015). In this work, CARIBIC in-situ measurements of acetone (Section 5.8f.) and acetonitrile (Section 6.5) are compared to a variety of emission inventories (see Sections 5.3.1 and 6.2.2).

1.5. Focus of this work

The first focal point of this study lies in the completion of a new, innovative PTR-MS for the measurement of atmospheric VOCs onboard aircraft. As instruments meeting the technical and scientific requirements for operation onboard aircraft are commercially not yet available, the development of such an instrument is an essential necessity to continue research in the field of atmospheric sciences and fill the gaps in the current knowledge and understanding of atmospheric VOCs. The budgets of many organic compounds are not yet closed. The new instrument contributes to this task by exploring the distribution of VOCs in specific regions of interest (research aircraft campaigns) and by monitoring it on much larger spatial and temporal scales during its future deployment onboard the CARIBIC passenger aircraft.

The underlying measurement principle is introduced in Chapter 2. A detailed description of the instrumental development and the final set-up is given in Chapter 3. The focus here lies on the unique custom-made developments and the many adaptions made upon mechanical completion to pass the aeronautical certification and enable an autonomous and successful operation onboard aircraft. First results of its deployment onboard the research aircraft HALO are shown and discussed. The topic is completed by an intensive laboratory characterization of the instrument and a detailed outlook on future measurements in Chapter 4.

The second part of this work deals with the evaluation of data from a total of 214 CARIBIC flights conducted between 2006 and 2015. In Chapter 5, the frequently observed correlation between acetone and CO is systematically investigated in terms of its spatial and temporal variation in the UT and with regard to its temporal evolution inside plumes. The results are utilized to derive acetone emission fluxes for two important source regions, North America and Southeast Asia, and these top-down estimates are compared with bottom-up inventories.

Another focus lies on constraining the emissions from biomass burning to better assess their impact on climate change (Chapter 6). For this purpose, acetonitrile as a trace gas almost exclusively emitted by biomass burning is implemented into the chemistry climate model ICON-ART, which is subsequently utilized to model its atmospheric distribution. Multi-annual simulations based on different emission scenarios (inventories) are performed and compared among each other as well as with the extensive data set of CARIBIC in-situ observations.

2. Proton Transfer Reaction Mass Spectrometry (PTR-MS)

Proton transfer reaction mass spectrometry (PTR-MS) is a well-developed analytical technique for detecting and identifying small quantities of organic compounds in air. The measurement principle and the wide-ranging applications of PTR-MS have been extensively described in the literature, e.g. in the reviews of Lindinger and Jordan (1998), de Gouw and Warneke (2007), Blake et al. (2009) and more recently in a book by Ellis and Mayhew (2014). In this chapter, the basic principle and its technical realization are explained.

2.1. Basic principle

All types of mass spectrometers have in common that the compounds of interest must be ionized. In PTR-MS, this ionization process is based on a proton transfer

$$XH^+ + M \longrightarrow MH^+ + X, \tag{2.1}$$

where XH^+ is the proton donor, also referred to as reagent ion, and M is some neutral molecule, which shall be detected (e.g. Hansel et al., 1995). The reaction is exothermic and thus takes place spontaneously, if the proton affinity of M is higher than that of X. In PTR-MS, this fact is used by choosing a reagent ion (namely protonated water, H_3O^+) that selectively ionizes most compounds of interest, but not the main constituents of air such as N_2, O_2, Ar and CO_2 (e.g. Lindinger et al., 1997).

In Table 2.1, the proton affinities of selected gases, including the main constituents of air, are compared to the one of water, which is the base of the reagent ion H_3O^+. In principle, all compounds listed below water can be detected by PTR-MS. This

	Compound	Chemical formula	Proton affinity [kJ mol^{-1}]
	Helium	He	178
	Neon	Ne	201
	Argon	Ar	369
	Krypton	Kr	427
	Oxygen	O_2	421
	Hydrogen	H_2	422
	Nitrogen	N_2	494
	Nitric oxide	NO	531
	Carbon dioxide	CO_2	541
*	Methane	$\mathbf{C}H_4$	544
	Nitrous oxide	N_2O	540
	Carbon monoxide	CO	594
*	Ethane	$\mathbf{C}_2H_6$	596
*	Propane	$\mathbf{C}_3H_8$	626
	Ozone	O_3	626
*	Acetylene	$\mathbf{C}_2H_2$	641
*	Isobutane	$\mathbf{C}_4H_{10}$	678
*	Ethene	$\mathbf{C}_2H_4$	681
	Water	H_2O	**691**
*	Hydrogen cyanide	HCN	713
*	Formaldehyde	CH_2O	713
*	Formic acid	CH_2O_2	742
*	Benzene	C_6H_6	750
*	Propene	C_3H_6	752
*	Methanol	CH_4O	754
*	Acetaldehyde	C_2H_4O	769
*	Toluene	C_7H_8	784
*	Acetic acid	$C_2H_4O_2$	784
*	Propanal	C_3H_6O	786
*	Ethanol	C_2H_6O	776
*	1-Propanol	C_3H_8O	787
*	Acetonitrile	CH_3CN	788
*	p-Xylene	C_8H_{10}	794
*	Acetone	C_3H_6O	823
*	Isoprene	C_5H_8	826
*	Dimethyl sulfide	C_2H_6S	831
	Ammonia	NH_3	854
*	Limonene	$C_{10}H_{16}$	875
*	α-Pinene	$C_{10}H_{16}$	878

Table 2.1.: Proton affinities of the main constituents of air and selected trace gas species. Organic compounds are marked with an asterisk. Table adopted from Ellis and Mayhew (2014) with values taken from Hunter and Lias (1998).

includes the majority of volatile organic compounds present in the atmosphere except for some low-molecular hydrocarbons (e.g. ethane, propane and isobutane).

After their ionization by proton transfer, different VOCs can be separated according to their mass-to-charge ratio and registered by an ion detector. As will be shown below, in PTR-MS, the frequency of detected MH^+ ions, the count rate $i(MH^+)$, is directly proportional to the concentration of M in the sample air.

As the proton transfer reaction (2.1) is first-order in both reactants (Lindinger et al., 1998), it will satisfy the rate equation

$$\frac{\mathrm{d}[\mathrm{M}]}{\mathrm{d}t} = -k_\mathrm{M}\ [\mathrm{M}]\ [\mathrm{H_3O^+}], \tag{2.2}$$

where k_M is the compound-specific reaction rate constant. For exothermic proton transfers, the reaction rate constant is at or close to the collisional rate constant ($\sim 10^{-9}$ cm^3 s^{-1}) (Lindinger and Jordan, 1998). When assuming that the conditions of the reaction are chosen such that the concentration of H_3O^+ ions does not significantly change with time, Equation 2.2 becomes a first-order differential equation. Subsequent integration leads to

$$[\mathrm{M}](t_r) = [\mathrm{M}]_{t=0}\ e^{-k_\mathrm{M}[\mathrm{H_3O^+}]t_r}, \tag{2.3}$$

where $[\mathrm{M}](t_r)$ is the concentration of the compound M after the reaction time t_r and $[\mathrm{M}]_{t=0}$ is the (initial) concentration of M in the sample air. In turn, the concentration of MH^+ ions produced within the time t_r can be expressed as

$$[\mathrm{MH^+}](t_r) = [\mathrm{M}]_{t=0} - [\mathrm{M}](t_r). \tag{2.4}$$

Inserting Equation 2.3 into 2.4 leads to

$$[\mathrm{MH^+}](t_r) = [\mathrm{M}]_{t=0} - [\mathrm{M}]_{t=0}\ e^{-k_\mathrm{M}[\mathrm{H_3O^+}]t_r} = [\mathrm{M}]_{t=0}\ \left(1 - e^{-k_\mathrm{M}[\mathrm{H_3O^+}]t_r}\right), \tag{2.5}$$

whereby the term in brackets can be further simplified by approximating the exponential function with a first-order Taylor polynomial around $t = 0$:

$$[\mathrm{MH^+}] = [\mathrm{M}]_{t=0}\left(1 - 1 + k_\mathrm{M}\ [\mathrm{H_3O^+}]\ t_r\right) = k_\mathrm{M}\ t_r\ [\mathrm{M}]_{t=0}\ [\mathrm{H_3O^+}]. \tag{2.6}$$

Rearranging the terms leads to the equation

$$[\mathrm{M}]_{t=0} = \frac{1}{k_\mathrm{M}\ t_r}\frac{[\mathrm{MH^+}]}{[\mathrm{H_3O^+}]}, \tag{2.7}$$

which is frequently shown in the literature. The measured count rates $i(MH^+)$ and $i(H_3O^+)$ are proportional to the concentrations of MH^+ and H_3O^+, respectively. However, due to the mass-dependent transmission behavior of the mass spectrometer (for details see Section 4.5), the proportional factor Γ is not the same (Steinbacher et al., 2004). Taking this into account, Equation 2.7 changes to

$$[M]_{t=0} = \frac{1}{k_M \; t_r} \frac{\Gamma(H_3O^+)}{\Gamma(MH^+)} \cdot \frac{i(MH^+)}{i(H_3O^+)}. \tag{2.8}$$

This simple relationship between the concentration of a trace gas M and the count rates of MH^+ and H_3O^+ ions is used within PTR-MS to determine the concentrations of organic compounds in the sampled air. The ratio

$$\frac{i(MH^+)}{[M]_{t=0}} = k_M \; t_r \;\; i(H_3O^+) \; \frac{\Gamma(MH^+)}{\Gamma(H_3O^+)}, \tag{2.9}$$

being the ion yield associated with a specific concentration of M, is also referred to as sensitivity α_M.

Volume mixing ratios

As the reaction rate is pressure- and temperature-dependent, the rate constant k_M is conventionally expressed in mol cm^{-3} s^{-1}. Consequently, the concentration $[M]_{t=0}$ in Equations 2.8 and 2.9 is a number density, which also depends on the pressure and temperature. In particular, this means that the concentrations derived with these equations are only valid for the pressure and temperature inside the instrument, where the reactions take place, and not equal to the concentrations in the sample outside of the instrument, where pressure and temperature are different.

To solve this issue, it has become common practice in the PTR-MS community (as well as in atmospheric sciences) to express concentrations in volume mixing ratios (VMR) and sensitivities as the quotient of count rate and VMR (e.g. Vlasenko et al., 2009)

The VMR of a gas is defined as the ratio of the number density of the gas and the number density of the surrounding air. The ratio has the advantage that it remains constant if the temperature or pressure changes (e.g. Schwartz and Warneck, 1995; Ellis and Mayhew, 2014, Seinfeld and Pandis, 2016). The VMR of M can be

calculated as follows, using the ideal gas law and Equation 2.8:

$$\mathrm{VMR(M)} = \frac{[\mathrm{M}]_{t=0}}{[\mathrm{air}]} = \frac{[\mathrm{M}]_{t=0} R\ T}{p N_A} = \frac{R\ T}{k_\mathrm{M}\ t_r\ p N_A} \frac{\Gamma(\mathrm{H_3O^+})}{\Gamma(\mathrm{MH^+})} \cdot \frac{i(\mathrm{MH^+})}{i(\mathrm{H_3O^+})} \tag{2.10}$$

where [air] is the number density of air inside the instrument, p and T are the pressure and temperature during the reaction, N_A is the Avogadro constant and R is the gas constant. The VMR is dimensionless and equals the mole fraction. However, in trace gas analysis the following size units are common

$$\begin{aligned} 1 \quad \mathrm{ppm} &= 10^{-6} \quad \mathrm{mol\ mol^{-1}} \\ 1 \quad \mathrm{ppb} &= 10^{-9} \quad \mathrm{mol\ mol^{-1}} \\ 1 \quad \mathrm{ppt} &= 10^{-12} \quad \mathrm{mol\ mol^{-1}} \\ 1 \quad \mathrm{ppq} &= 10^{-15} \quad \mathrm{mol\ mol^{-1}} \end{aligned}$$

with ppm, ppb, ppt and ppq being the abbreviations of parts per million, billion, trillion and quadrillion. Due to the pressure reduction in the sample air within the instrument, the sensitivity α_M is commonly expressed as counts per second (cps) per ppb:

$$\alpha_\mathrm{M} = \frac{i(\mathrm{MH^+})}{\mathrm{VMR(M)}} = \frac{k_\mathrm{M}\ t_r\ p\ N_A}{R\ T}\ \frac{\Gamma(\mathrm{MH^+})}{\Gamma(\mathrm{H_3O^+})}\ i(\mathrm{H_3O^+}). \tag{2.11}$$

When the sensitivity is known, the VMR of a compound in the sample can be easily determined by dividing the measured count rate by the sensitivity. Nevertheless, the equation also shows that the overall outcome of the proton transfer reactions strongly depends on the following controllable parameters:

- the abundance of $\mathrm{H_3O^+}$ ions
- the pressure and temperature during the reaction
- the transmission of protonated VOCs relative to $\mathrm{H_3O^+}$ ions
- the reaction time.

All these parameters need to be held constant during measurements to ensure the validity of the previously made assumptions and derived equations (e.g. the simple relationship between count rates and VMRs). Furthermore, a high yield of $\mathrm{H_3O^+}$ ions needs to be generated. The next chapter deals with the question how this is technically realized.

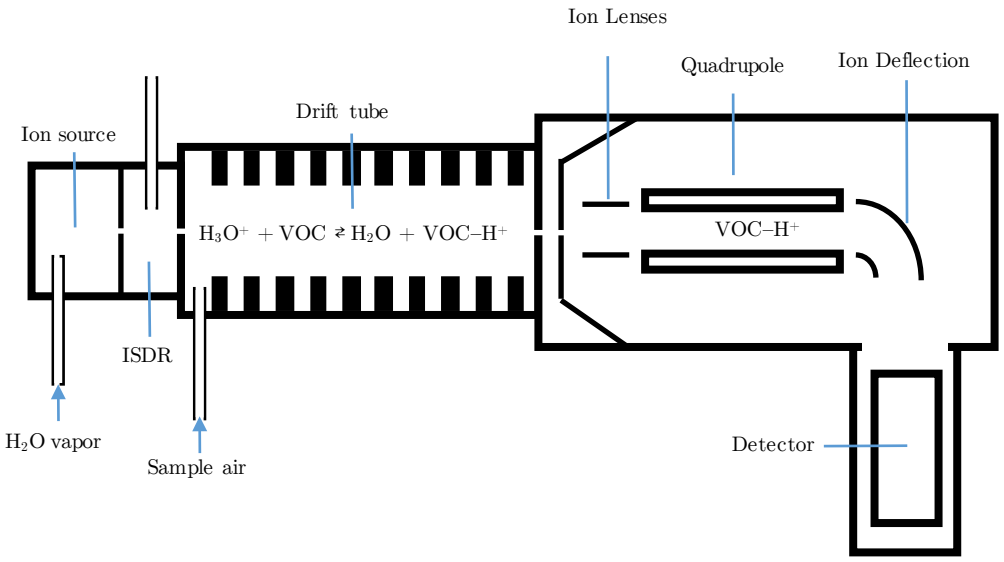

Figure 2.1.: Simplified structure of a quadrupole-based PTRMS. The drawing was mainly adopted from de Gouw and Warneke (2007).

2.2. Basic structure of a PTR-MS

To perform proton transfer reactions and detect the ionized VOCs, PTR-MS instruments consist of the following parts:

- An **ion source**, which generates the H_3O^+ reagent ions in high yield.
- A **drift tube**, which serves as a reaction chamber and enables proton transfer reactions under controlled conditions.
- A **mass analyzer**, which separates the generated ions according to their mass-to-charge ratio.
- A **detector**, which converts the impacting ions into an electrical signal with an amplitude proportional to the number of ions per time.

In Figure 2.1, the schematic structure of a PTR-MS instrument is illustrated. In the following, the major components of a PTR-MS are presented.

2.2.1. Ion source

The standard ion source in PTR-MS is a hollow cathode, which is continuously flushed with water vapor at typical flow rates of 5–10 sml min^{-1} (e.g. de Gouw and Warneke, 2007). The application of a sufficiently high voltage (typically 400–600 V) across the electrodes leads to electron impact ionization of the traversing H_2O molecules yielding a plasma of H^+, H_2^+, O^+, OH^+ and H_2O^+ ions (e.g. Cappellin et al., 2013; Ellis and Mayhew, 2014). The ions created this way are not stable and rapidly react with further H_2O molecules to H_2O^+ and H_3O^+ ions via the following pathways (e.g. Hansel et al., 1995):

$$H^+ + H_2O \longrightarrow \boxed{H_2O^+} + H \tag{2.12}$$

$$H_2^+ + H_2O \longrightarrow \boxed{H_3O^+} + H \tag{2.13}$$

$$\hookrightarrow \longrightarrow \boxed{H_2O^+} + H_2 \tag{2.14}$$

$$O^+ + H_2O \longrightarrow \boxed{H_2O^+} + O \tag{2.15}$$

$$OH^+ + H_2O \longrightarrow \boxed{H_3O^+} + O \tag{2.16}$$

$$\hookrightarrow \longrightarrow \boxed{H_2O^+} + OH \tag{2.17}$$

$$\boxed{H_2O^+} + H_2O \longrightarrow \boxed{H_3O^+} + OH \tag{2.18}$$

Reaction 2.18 also consumes the H_2O^+ ions generated in Reactions 2.12, 2.14, 2.15 and 2.17, which means that all above reactions ultimately lead to the formation of H_3O^+ ions.

The resulting production rate of H_3O^+ is in the order of $\sim 10^{10}$ Hz (Brito, 2011). However, not all reactions fully take place before the ions emerge from the hollow cathode source through an orifice in the bottom electrode. Consequently, some unwanted ions and neutral molecules remain in the ion beam. Moreover, some fraction of the water vapor is not ionized in the source.

To remove parts of the excessive water vapor and to minimize the number of unwanted ions (e.g. Hansel et al., 1995), a further chamber, named ion source drift region (ISDR), is positioned between the hollow cathode source and drift tube (see Figure 2.1). While the water vapor is removed via a lateral connection to a pump, the ions are guided by an electrical field to the exit orifice. The short residence time of ions in the ISDR ($\sim$1-2 µs) allows for further Reactions 2.12–2.18, enhancing the purity of the H_3O^+ ion beam to levels of about 99.5 % or better (Hansel et al., 1995).

2.2.2. Drift tube

The drift tube (DT) is the core of the PTR-MS instrument, where the proton transfer reactions, as introduced in Section 2.1, take place. It consists of typically 10 stacked cylindrical stainless steel electrodes, which are separated by insulating spacers and connected to a resistor chain (e.g. de Gouw and Warneke, 2007; House, 2008). In the present PTR-MS instruments used at KIT the inner diameter and length of the DT are 1.2 cm and about 8.8 cm, resulting in a volume of $\sim$10 cm^3.

At the top of the DT, reagent ions and sample air are fed into the DT via an orifice and a capillary, respectively. At the downstream end of the drift tube, ions and neutral molecules exit the DT via a small critical orifice into the high vacuum system. Due to pumping below the DT, a pressure of $\sim$2 hPa and a constant flow of sample air (depending on the size of the exit orifice; typically 15–30 sml min^{-1}) through the DT is obtained (de Gouw and Warneke, 2007; Ellis and Mayhew, 2014). This ensures that the air in the DT is refreshed in less than 100 ms and results in short instrumental response times.

A pressure of $\sim$2 hPa results in a mean free path of about 0.04 mm, enabling sufficient collisions and thus, proton transfers. A voltage of about 400–600 V is applied across the DT. The resulting potential gradient ($\sim$60 V cm^{-1}) guides the ions towards the end of the DT and enables the fragmentation of unwanted $H_3O^+(H_2O)_n$ cluster ions that might otherwise form and compete with H_3O^+ as proton donor. On the other hand, a too high energy may lead to fragmentation of protonated VOCs, which then challenges compound identification and quantification (Ellis and Mayhew, 2014).

The critical parameter in this respect is the ratio E/N, where E is the electric field strength and N the number density of neutral molecules. It is also referred to as reduced electric field and commonly expressed in the alternative unit Townsend, where 1 Td = 10^{-17} V cm^{-2}. The choice of the E/N ratio is always a compromise between minimizing the presence of cluster ions and fragmentation (e.g. Hansel et al., 1995). Typically, E/N values in the range of 100–140 Td are used (Kajos et al., 2015).

The electric field and pressure ($p \propto N$) also influence the kinetics of the proton transfer reactions. Due to the frequent collisions with neutral molecules and acceleration in between, the ions "drift" on average with a mean drift velocity (Revercomb and Mason, 1975)

$$v_d = \mu \times E = \mu_0 N_0 \times (E/N), \tag{2.19}$$

where μ is the ion mobility in the DT, μ_0 the ion mobility at standard conditions (p_0 = 1013.25 hPa, T_0 = 273.15 K) and N_0 the gas number density at standard conditions. The mean drift velocity v_d and the length l of the DT determine the travel time of H_3O^+ ions through the DT, and thus, the reaction time

$$t_r = \frac{l}{v_d} = \frac{l}{\mu_0 N_0} \cdot \left(\frac{E}{N}\right)^{-1} = \frac{l^2}{\mu_0 U_d} \cdot \left(\frac{T_0}{T}\right)\left(\frac{p}{p_0}\right), \tag{2.20}$$

in which proton transfers can take place. The term on the right side is the result of the following substitutions: $E = U_d/l$, $N = RT/p$ and $N_0 = RT_0/p_0$.

Being proportional to the instrumental sensitivity (see Equation 2.9), the reaction time t_r needs to be hold constant during measurements. This is achieved by actively controlling temperature and pressure in the DT, using a PID-controlled heating and a pressure controller. The heating also prevents wall losses of sticky compounds. Typical reaction times are in the range of 90–120 µs (e.g. Hewitt et al., 2003; Taipale et al., 2008; Sarkar et al., 2016).

At the end of the drift tube, a fraction of the product and remaining reagent ions is extracted via a series of apertures into the mass spectrometer, the major components thereof being described in the following two sections.

2.2.3. Mass analyzer

As an ion detector cannot distinguish between different ions, it is necessary to separate the ions prior detection in order to deduce the count rates $i(MH^+)$ for different compounds M and the one for H_3O^+ ions (see Equation 2.10). This is done by a mass analyzer, which separates the ions according to their mass-to-charge ratio m/z. As only simply charged ($z = 1$) cations occur in PTR-MS (e.g. Steeghs et al., 2004), the m/z ratio directly reflects the ion mass.

Since its advent in 1995 (Hansel et al., 1995), PTR-MS instruments have been equipped with quadrupole mass analyzers (QMA) and for more than a decade, the QMA was the only available mass analyzer in commercial PTR-MS. This changed in 2008, when the first instrument with a time-of-flight (TOF) analyzer became commercially available (Jordan et al., 2009a). Although PTR-TOF-MS are becoming increasingly popular, the QMA is still widely used and often preferred due to its compact size, robustness and simpler handling.

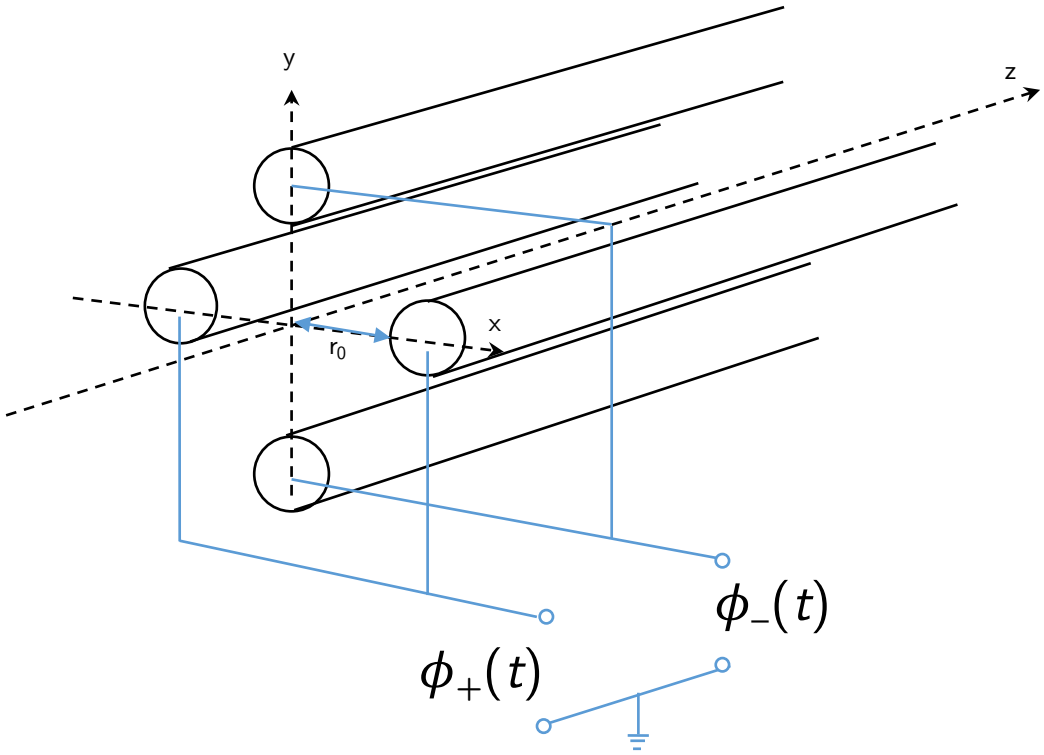

Figure 2.2.: Schematic drawing of the quadrupole rod system and its internal electrical connections. Adopted from Gross (2013).

Also the PTR-MS instruments presented in this work use a QMA. As the technique is well established and a commercial QMA (Pfeiffer Vacuum, Asslar, Germany) is used, only a short phenomenological description will be provided. For details, please refer to the comprehensive literature (e.g. Dawson, 1976; Douglas, 2009).

In general, a QMA consists of four parallel rods, which are equidistantly spaced around a virtual center axis (see Figure 2.2). In the installed version, the rods have a diameter of 8 mm and a length of 200 mm, whereas the distance r_0 between the rods and the center axis is about 9 mm.

For mass analysis, the potentials applied to the rods have a static and an oscillating component that can be expressed as (e.g. Campana, 1980; de Hoffmann and Stroobant, 2007)

$$\phi_{\pm}(t) = \pm \left(U + V \cos(\omega t)\right), \tag{2.21}$$

where U is a direct current (DC) voltage and V the amplitude of the oscillating

part, which alternates with a radio frequency ω (here: 2.25 MHz). Opposite rods are maintained at the same potential, that is ϕ_+ for the rods in x-direction and ϕ_- for the rods in y-direction. This way, an oscillating quadrupolar field is generated in the x-y-plane, which causes ions to oscillate in these directions as they pass through the quadrupole along the z-axis (Ellis and Mayhew, 2014). As has been shown elsewhere, the temporal evolution of the amplitude of this 2-dimensional oscillation can be described based on the terms (e.g. Dawson, 1976; de Hoffmann and Stroobant, 2007)

$$a = \frac{8e}{r_0^2}\,\frac{U}{\omega^2}\left(\frac{m}{z}\right)^{-1} \text{ and } \; b = \frac{4e}{r_0^2}\,\frac{V}{\omega^2}\left(\frac{m}{z}\right)^{-1}, \tag{2.22}$$

where e is the elementary charge. Depending on the values of a and b, the amplitude of the ion oscillation either remains small or increases exponentially with time while the ion traverses through the quadrupole (Douglas, 2009). In the former case, ions can pass the quadrupole, whereas in the latter case, the ions diverge and strike one of the rods, i.e. they lose their charge and get lost for detection. The stability of the ion trajectories thus depends on the m/z ratio of the ions, the amplitudes U and V and the frequency ω – a fact, which is used in QMA to distinguish between different ions.

The radio frequency ω is typically kept constant while the amplitudes U and V are subsequently varied so that only ions within a specific m/z window can pass the quadrupole and reach the detector at a time (Douglas, 2009).

2.2.4. Ion detector

If ions pass the quadrupole, they are subsequently deflected towards the ion detector, which is positioned off-axis to avoid counting of ultraviolet photons from the ion source discharge (see Figure 2.1). Due to its ability to detect even low ion currents at high speed, a secondary electron multiplier (SEM) (e.g. Allen, 1939; Geno, 1992) is commonly used in quadrupole-based PTR-MS instruments (e.g. Beauchamp and Zardin, 2017). The SEM used here (SEV 217; Pfeiffer Vacuum, Asslar, Germany) consists of a series of 18 successively arranged cylindrically shaped dynodes, made of copper beryllium and connected to a network of 18 MΩ resistors (see Figure 2.3). Whereas the last dynode is grounded, a high negative voltage (2.0–3.5 kV) is applied to the first dynode (called conversion dynode), so that the positively charged ions exiting the quadrupole are accelerated towards it (e.g. de Hoffmann and Stroobant, 2007).

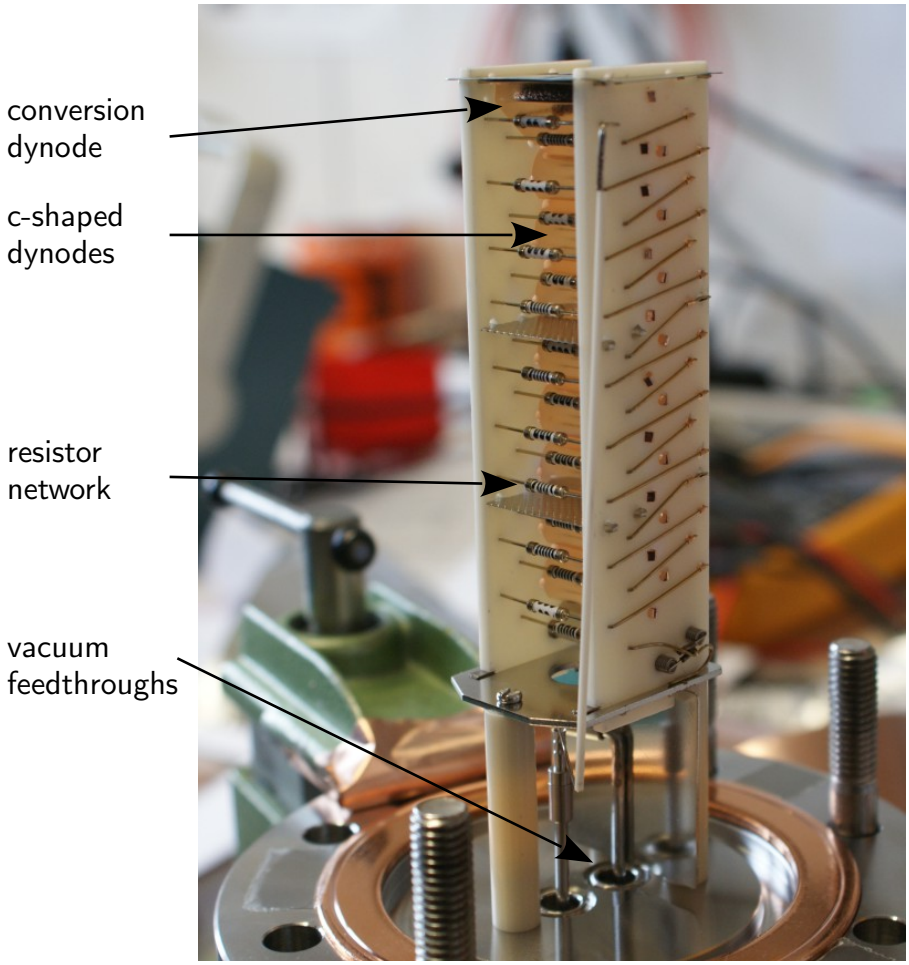

Figure 2.3.: Secondary electron multiplier SEV 217.

Whenever an ion hits the conversion dynode, several secondary electrons are released from atoms in the surface layer. As the subsequent dynode lies on a potential about 100-200 V below the conversion dynode, these electrons are then accelerated to the next dynode, where they release further secondary electrons. In this way, each ion generates an avalanche of secondary electrons and the low incoming ion current is amplified by several orders of magnitudes (the manufacturer specifies a gain rate greater than 10^8 for new detectors operated at 3.5 kV). Due to the voltage drop at a resistor, the amplified current generates an output pulse (of typically 0.5 V over a time period of $\sim$3 ns), which, if the amplitude exceeds a certain threshold, is counted by the internal electric circuit board to calculate the ion count rate.

Counting statistics

As shown elsewhere (e.g. Hayward et al., 2002; de Gouw and Warneke, 2007), the measured count rates follow a Poisson distribution

$$P_\mu(X = n) = \frac{\mu^n}{n!} e^{-\mu}, \tag{2.23}$$

where $P_\mu(X = n)$ is the probability of detecting n ions in a certain time interval if, on average, μ ions are observed within this period. As the standard deviation of a Poisson distribution is given by

$$\sigma_\mu = \sqrt{\mu}, \tag{2.24}$$

the statistical noise of an ion count rate

$$i(\mathrm{MH^+}) = \frac{\mu}{t_{\mathrm{dwell}}}, \tag{2.25}$$

where μ is the number of $\mathrm{MH^+}$ ions observed within the measurement time t_{dwell}, is given by

$$\sigma_{i(\mathrm{MH^+})} = \frac{\sigma_\mu}{t_{\mathrm{dwell}}} = \frac{\sqrt{\mu}}{t_{\mathrm{dwell}}}. \tag{2.26}$$

Rearranging Equation 2.25 and substituting it into Equation 2.26 leads to the important relationship

$$\sigma_{i(\mathrm{MH^+})} = \frac{\sqrt{i(\mathrm{MH^+}) \cdot t_{\mathrm{dwell}}}}{t_{\mathrm{dwell}}} = \sqrt{\frac{i(\mathrm{MH^+})}{t_{\mathrm{dwell}}}}, \tag{2.27}$$

from which follows that the relative uncertainty in a measured count rate

$$\frac{\sigma_{i(\mathrm{MH^+})}}{i(\mathrm{MH^+})} = \frac{1}{\sqrt{i(\mathrm{MH^+}) \cdot t_{\mathrm{dwell}}}}, \tag{2.28}$$

decreases when the count rates and/or measurement time are increased. The reciprocal of the relative uncertainty is known as the signal-to-noise-ratio

$$\frac{S}{N} = \frac{i(\mathrm{MH^+})}{\sigma_{i(\mathrm{MH^+})}} \propto \sqrt{i(\mathrm{MH^+}) \cdot t_{\mathrm{dwell}}}, \tag{2.29}$$

which increases with the square root of the count rate and measurement time.

Detection limit

The smallest quantity of a compound that can be reliably measured, i.e. distinguished from the background signal within a stated confidence interval, is commonly referred to as limit of detection (LOD) (e.g. Armbruster and Pry, 2008; Amann et al., 2010). It becomes crucial when measuring very low concentrations as it is the case for VOCs in the upper troposphere and lower stratosphere. Although several definitions of the LOD exist (Currie, 1997), here the LOD is derived from the smallest measure x_{LOD} as defined by the International Union of Pure and Applied Chemistry (IUPAC, Goldbook, 2014):

$$x_{\mathrm{LOD}} = \bar{x}_{\mathrm{blank}} + k\ \sigma_{\mathrm{blank}} \tag{2.30}$$

where $\bar{x}_{blank}$ and σ_{blank} are the mean and standard deviation of the background (blank) detector signal and k is a factor chosen according to the desired confidence interval. However, when converting x_{LOD} into a VMR using the compound-specific sensitivity α (in ppb cps^{-1}), the background signal needs to be subtracted (Long and Winefordner, 1983) and one obtains

$$\mathrm{VMR}(x_{\mathrm{LOD}}) = \frac{(\bar{x}_{\mathrm{LOD}} - \bar{x}_{\mathrm{blank}})}{\alpha} = k\ \frac{\sigma_{\mathrm{blank}}}{\alpha} = k\ \mathrm{VMR}(\sigma_{\mathrm{blank}}), \tag{2.31}$$

i.e. the LOD equals k-times the noise of the background measurement expressed as VMR. Hence, the factor k specifies the signal-to-noise-ratio (S/N). The observed noise is usually dominated by statistical fluctuations in the ion count rate (Poisson noise), but further contributions from instabilities in the DT pressure or electrode voltages may exist (Ellis and Mayhew, 2014).

In Chapter 4, these findings are used to quantify the performance of the new airborne PTR-MS instrument, presented in this work, including an assessment of atmospheric trace gases that can be reliable measured with it in the UTLS. The development of the instrument and its most distinctive features compared to other PTR-MS are subject of the next chapter.

3. Development of PTR-MS for airborne measurements

The use of PTR-MS at the Institute of Meteorology and Climate Research (IMK) started in the early 2000s, when a commercial instrument (IONICON, Innsbruck, Austria) was modified for the use onboard the CARIBIC passenger aircraft (Sprung and Zahn, 2003; Sprung and Zahn, 2005). In 2007, the development of more lightweight and more sensitive instruments was initiated, the first to be deployed onboard the new research aircraft HALO (Zahn et al., 2009; Brito et al., 2009).

A higher sensitivity potentially enlarges the number of detectable species and the temporal resolution of measurements, which is essential for a better understanding of the chemical processes and budgets of these compounds in the atmosphere. Also a lightweight construction is advantageous in many regards. Less weight is not only associated with lower deployment costs, but can also decide on the deployment itself, namely when the payload of the aircraft is close to its full capacity.

As a matter to save weight and to become more flexible for future modifications, it was soon decided to replace the individual commercial control and supply units by a new integrated control system, named after its V25 microcontroller[†]. Developed at the Max Planck Institute for Chemistry (MPI-C) in Mainz, the V25 is a compact and robust modular system comprising an embedded computer and a large number of slots for different input/output (I/O) modules. However, the modules necessary for control of PTR-MS still had to be developed by the MPI-C.

The first airborne operation of the new instrument, here named PTRMS-HALO, was originally scheduled for summer 2009 as part of the scientific HALO mission OMO (Oxidation Mechanisms Observations), which will be described in more detail in Section 3.4. However, in 2009 the integrated V25 system was far not yet sufficiently advanced to take over any of the envisaged functions. The main functions, such as the

[†]built-in microcontroller by NEC (Nippon Electric Company), sold between 1985 and 2003

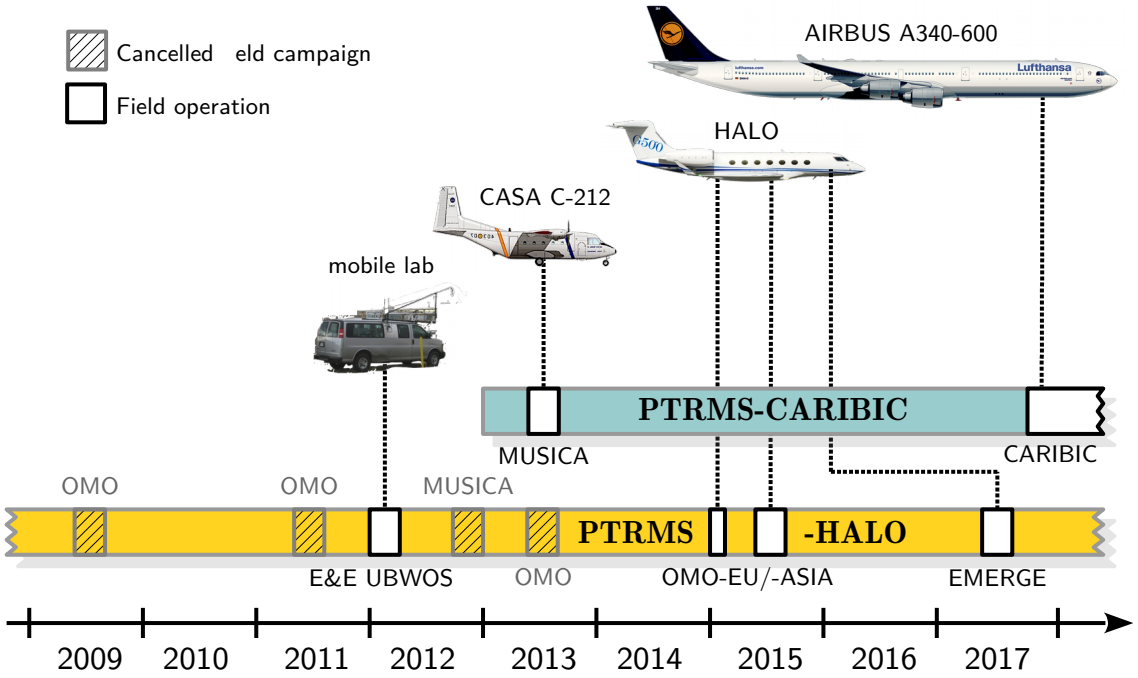

Figure 3.1.: Chronological sequence of postponed and completed field campaigns involving the largely identical instruments PTRMS-CARIBIC (green timeline) and PTRMS-HALO (yellow timeline) and four different platforms (mobile lab, CASA C-212 turboprop aircraft, HALO jet aircraft and CARIBIC passenger aircraft).

control of the mass spectrometer, the turbo-molecular pumps, the drift tube and the ion source as well as the acquisition of the mass spectra were still not implemented. Fortunately, due to numerous problems with the certification of HALO, the OMO campaign was postponed, initially to summer 2011 and thereafter in further steps to the actual date in summer 2015.

In Figure 3.1, a timeline of the campaign planning and the several postponements of OMO are shown. The considerable delay eventually allowed to finalize the development of PTRMS-HALO with the last steps being taken at the end of 2014.

In Figure 3.2, the different development stages are chronologically illustrated. The instrumental development until mid of 2013 and its first test/field deployment on ground during the E&E UBWOS (Energy & Environment - Uintah Basin Winter Ozone Study) campaign in 2012 were part of previous PhD projects (Brito, 2011; Geiger, 2015) and will be briefly summarized in the following section. The debugging of the new hardware, the finalization and optimization of the control software and

Figure 3.2.: Milestones in the development of the lightweight PTRMS-HALO. The contributions of the involved PhD projects are marked in different colors.

the implementation of all changes requested by the certification company were done within the present PhD project.

Also due to the considerable work spent over the last almost 10 years within three PhD projects, it is worth to list the two most important achievements and unique features of the new instrument at first:

- It is by far the most compact and lightweight PTR-MS in airborne research at the moment. As will be shown later, its sensitivity and low detection limits can easily keep up with larger PTRMS instruments and outdo most values reported in the literature.
- It is the first PTR-MS worldwide having a custom-made control unit, which is capable of mass spectra acquisition. This unique feature allowed to fully automatize the measurement process and thus, to develop the first PTR-MS, which can be deployed onboard research aircraft without being actively controlled by an operator. Due to its modular design and open software, it can also be easily extended and adapted to future missions and instrumental developments, some of which are currently in planning. This is a further decisive advantage compared to instruments using the commercial hard- and software.

After the successful deployment onboard HALO during OMO-Asia in summer 2015 (see Figure 3.1), the instrument was thoroughly characterized in the laboratory (see Chapter 4) to demonstrate its excellent performance and to point out further areas for improvement.

Besides PTRMS-HALO, the build-up of a largely identical instrument, here named as PTRMS-CARIBIC, started in 2012 to replace the somewhat aged and partially commercial PTRMS deployed in the CARIBIC laboratory since 2005. In a not fully working status, the PTRMS-CARIBIC was deployed for the first time in summer 2013 (see Figure 3.1) during the airborne field campaign MUSICA (MUlti-platform remote Sensing of Isotopologues for investigating the Cycle of Atmospheric water), which will be described in Section 3.2. The technical experiences gathered during the campaign led to a partial redesign of the instrument, which is presented in Section 3.5. The resulting modified device will go into operation onboard the CARIBIC passenger aircraft in October 2017 (see Figure 3.1).

3.1. Previous projects

In 2011, Brito presented a first prototype of the PTRMS-HALO, which is subject of the first subsection. Later in 2011, the OMO campaign was again cancelled and it became clear that the campaign would not take place before 2013. Therefore, alternative ways of deployment were considered, leading to the participation in the E&E UBWOS campaign, described in the second subsection. The third part is dedicated to instrumental changes until mid of 2013 and the instrument's status when it was taken over by the author.

3.1.1. The PTR-IF-MS (2007 – 2011)

The PTR-IF-MS was the first prototype of the PTRMS-HALO for deployment onboard the research aircraft HALO (Brito, 2011) and was finished in spring 2011 (see Figure 3.2). It was already ∼35 kg lighter than the instrument used onboard the CARIBIC aircraft and included several promising new in-house developments:

- A **lightweight vacuum chamber system**. The used commercial quadrupole mass spectrometer (Pfeiffer Vacuum, Asslar, Germany) is by default installed in a heavy stainless steel vacuum chamber system. Being an absolute novelty in PTR-MS, this chamber system was replaced by a much lighter custom-made version, entirely made out of aluminum and extensively processed (e.g. honed) to obtain a comparably smooth inner surface. At the time of writing, the PTR-MS of IMK are still the only ones worldwide equipped with such a lightweight vacuum chamber.

- An **unheated permeation device for in-flight calibration** (Brito and Zahn, 2011). While increasing the overall data accuracy, calibration-induced measurement gaps could be completely avoided by using isotopically labelled compounds. Another benefit of this technique is the possibility to calibrate compounds, which are not stable in gas cylinders.

- An **ion funnel (IF) enhanced drift tube**, which led to the title PTR-IF-MS. The idea of an ion funnel is to refocus the ion beam towards the end of the drift tube to enhance the number of ions reaching the mass spectrometer. This ion focusing is realized by applying a RF potential to the funnel's electrodes, being a set of cylindrical plates arranged in distances of 1–2 mm. The generated electric field creates an effective electric potential, which radially focuses the

ions towards the critical orifice at the end of the drift tube and thus, leads to a higher proportion of ions entering the mass spectrometer (Shaffer et al., 1997; Kelly et al., 2009; Barber et al., 2012). A laboratory version of the funnel increased the instrument's sensitivity by 30 % (Brito, 2011). Only recently, this technique found its way in commercially available PTR-MS (Jordan et al., 2017).

- A **chemically inert proportional valve** in the sample inlet line. The purpose of the valve was to obtain a constant pressure in the inlet system for different ambient pressures, which vary strongly during airborne operation. Compared to the conventional solution – a flow restriction followed by a branch-off to the spectrometer and a pressure controller – a proportional valve does not only save weight, but also significantly reduces the load of the backing pump. In order to avoid wall losses of VOCs, the standard body of the commercially available valve (Parker Hannifin, Cleveland, Ohio) was replaced by an in-house manufactured version made of PEEK (polyether ether ketone).

Despite all these promising new features, the PTR-IF-MS was still far away from being ready for deployment onboard aircraft. Measurements were only possible in the laboratory using additional hardware. The ion funnel was operated using an external sine wave generator (Agilent Technologies, US) and a broad range RF power amplifier (17 kg; 28 × 16 × 41 cm; BEKO Elektronik, Germany) (see Figure 5.11 in Brito, 2011). At that time, no commercial RF supply was suited for the intended field usage (i.e. small-sized, light-weight, power-saving and optimized with respect to electromagnetic interferences) and the development of a customized solution was still at the beginning.

But even in the absence of the funnel, reliable measurements were only possible when connecting the mass spectrometer to its commercial control unit QMS 700 (10 kg; 48 × 38 × 13 cm; Pfeiffer Vacuum, Germany) and a Windows-PC running the commercial control software (Inficon AG, Liechtenstein). Major parts of the newly developed V25 control unit, which was supposed to take over this task, were still at an early prototype stage in 2011 (Brito, personal communication).

3.1.2. E&E UBWOS (2011–2012)

The E&E UBWOS (Energy & Environment – Uintah Basin Winter Ozone Study) campaign took place between January and March 2012 in the Uintah Basin, a region

in the northeast corner of Utah, where high surface concentrations of ozone had been observed during wintertime (Edwards et al., 2014). Containing large deposits of unconventional hydrocarbon resources, the basin has experienced a renaissance in oil and gas drilling since the advances in horizontal drilling made hydraulic fracturing increasingly popular in the early 2000s.

However, hydraulic fracturing is a highly controversial technique and suspected to threaten the environment in various ways, including air pollution (e.g. Howarth et al., 2011; Goldstein et al., 2014; Jackson et al., 2014). VOCs released by these activities can react with sunlight and nitrogen oxides, emitted from the diesel-powered compressor stations, to form ozone. However, the strongest ozone events occurred during cold periods and snow cover, when solar radiation was at a minimum. Therefore, understanding the chemistry causing the high wintertime ozone levels was the main objective of the E&E UBWOS study. To achieve this objective, it was essential to characterize the emission sources of ozone precursors in the basin.

The PTR-MS contributed to this task by monitoring eight specific VOCs, eight isomeric groups and nine masses indicative of (cyclo-)alkanes (see Table 4.2 in Geiger, 2015). Measurements were conducted onboard a van, modified to a mobile laboratory (see Figure 3.1). Enabling flexible measurements in the proximity of different point sources, the latter was well suited to characterize the spatial variability of VOC concentrations in the basin and to quantify individual emission source footprints. Sometimes extremely high mixing ratios of methanol (up to 1 ppm), aromatics and cycloalkanes were observed downwind of oil and condensate tanks (see details in Warneke et al., 2014 and Geiger, 2015).

For acetone, Geiger reported a detection limit of 168 ppt at 1 s integration time and a sensitivity of 172 cps ppb^{-1}. For all other compounds, the detection limit was not stated and the sensitivity somewhat lower (38–158 cps ppb^{-1}).

Prior to the campaign, the prototype PTR-IF-MS was strongly modified. The ion funnel and the calibration unit were removed, as they were both not yet mature enough for field operation. The commercial control unit of the mass spectrometer was provisionally integrated into the rack and measurements had to be done manually using a laptop and the commercial software. In the inlet system, the proportional valve was replaced by the more common solution of a flow-restricting capillary and a pressure controller, which is easier to handle and less prone to contamination compared to the proportional valve.

3.1.3. The ULW-PTR-MS (2013–2014)

The set-up used during E&E UBWOS was only provisional and not suited for airborne usage. Therefore, the instrument was literally rebuilt from scratch after the campaign to meet the stringent requirements for operation onboard HALO. To point out the particular low weight of the instrument, the instrument was renamed to "ultra-light-weight PTRMS (ULW-PTRMS)".

The commercial control unit QMS 700 was again abandoned in favor of the much smaller and lighter V25 system. The internal structure of the sub-rack accommodating the V25 system was strongly modified to enable front-site access to all analog input and outputs, which is particularly useful in the adjustment phase and during troubleshooting.

The inlet system, formerly mounted onto an open panel, was redesigned and integrated into a sub-rack to simplify its certification. Between the internal branch-off to the spectrometer and the exhaust line, a bypass was added to enable a higher (ram pressure driven) flow in the inlet line and to reduce the overall reaction time of the spectrometer. A venting line including a capillary was introduced for automatic venting of the vacuum system after power switch-off, e.g. before landing. To cope with the varying inlet pressures during flight (between 1000 hPa and 150 hPa), a set-up of two critical orifices was integrated by the author. The second orifice is opened at higher altitudes or lower ambient pressures, respectively, to maintain the required sample flow. In addition, all connections between the sub-racks and other parts were made separable so that the two sub-racks can be easily removed for maintenance.

In June 2013, after 6 years of continuous development and shortly before the envisaged start of the HALO campaign OMO, a decisive breakthrough could be achieved. For the first time, the new V25 system was able to control the commercial quadrupole system and acquire mass spectra (see Figure 3.2).

Although being almost ready for field operation, the ULW-PTR-MS could not be deployed within this previous PhD project (by F. Geiger), as the HALO campaign OMO was once again postponed at short notice for another two years. Instead, the new V25 system was tested for the first time – under the supervision of the author – during the forthcoming field campaign MUSICA, which is described in detail in the next section.

3.2. MUSICA

Main objective of the MUSICA (MUlti-platform remote Sensing of Isotopologues for investigating the Cycle of Atmospheric water) field campaign was the validation of satellite- and ground-based remote-sensing measurements of water vapor isotopologues on Tenerife by in-situ measurements onboard aircraft (Schneider et al., 2015; Dyroff et al., 2015; Christner, 2015; Schneider et al., 2016). Although initially planned for winter 2012, the campaign finally took place in July and August 2013 involving the remote-sensing instruments:

- Infrared Atmospheric Sounding Interferometer (IASI) onboard the Meteorological Operational Satellites (MetOp) A and B (Clerbaux et al., 2009; Herbin et al., 2009; Schneider and Hase, 2011; Wiegele et al., 2014) and
- Fourier Transform Infrared Spectrometer (FTIR)* stationed at the Izaña meteorological observatory on Tenerife (Schneider et al., 2005; Schneider et al., 2010)

and the following in-situ instruments:

- two commercial Cavity Ring-Down Spectrometer (CRDS)† for the measurement of the isotopic composition of water vapor, one located in Izaña and the other one at the top of Mount Teide (Schneider et al. 2015; González et al., 2016),
- the airborne tunable diode laser absorption spectrometer ISOWAT II, which likewise measures the isotopic composition of water vapor (Dyroff, 2009; Dyroff et al., 2010; Dyroff et al., 2015),
- the airborne Fast and Accurate In-situ Ozone instrument (FAIRO) (Zahn et al., 2012),
- the airborne Passive Cavity Aerosol SPectrometer (PCASP)‡ for the measurement of aerosol size distributions,
- the airborne PTRMS-CARIBIC for VOC measurements.

*IFS 120/5 HR (Bruker Corporation, Billerica, Massachusetts, US)
†L2120-i (Picarro Incorporated, Sunnyvale, California, US)
‡PCASP-100X (Droplet Measurement Technologies Incorporated, Longmont, Colorado, US)

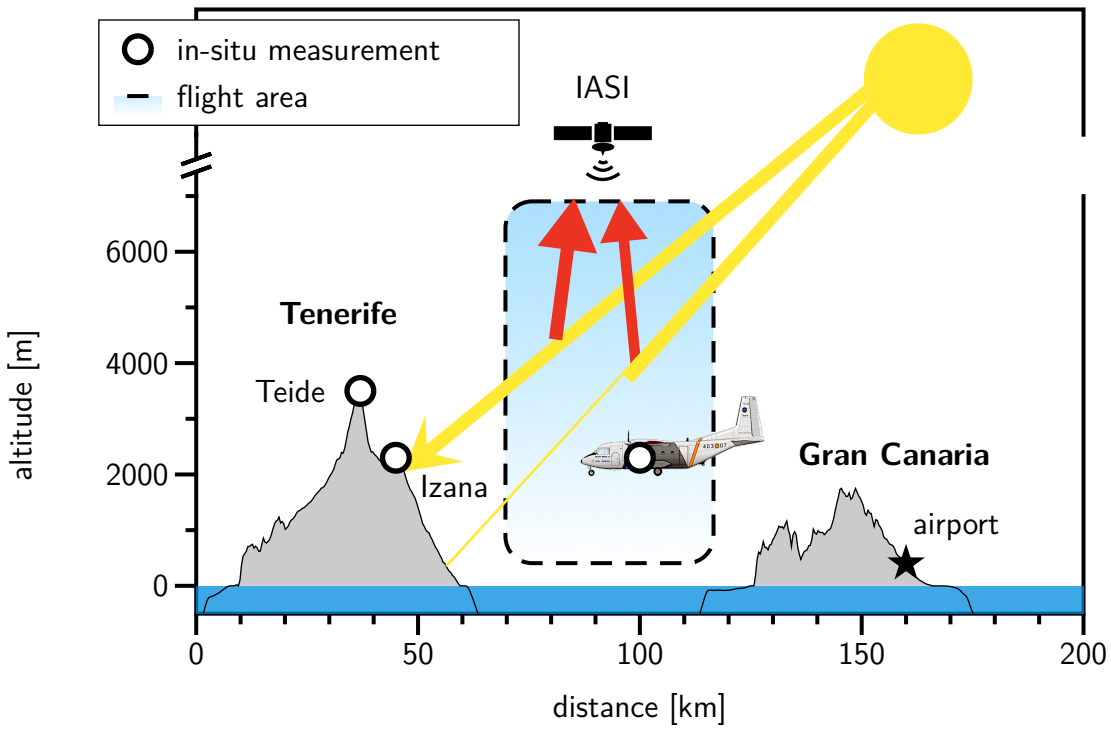

Figure 3.3.: Measurement set-up and sites during the airborne MUSICA campaign. Picture adopted from Schneider (2015).

The 4 airborne instruments were deployed onboard a medium-sized turboprop aircraft (CASA C-212-200) operated by the Instituto National de Technica Aeroespacial (INTA). For the PTRMS-CARIBIC, the deployment offered the unique chance to identify and eliminate potential deficiencies well before its intended use onboard the CARIBIC passenger aircraft.

The installation of all in-situ instruments and three test flights were done at the aircraft's home base in Torrejón de Ardoz near Madrid, Spain. In July 2013, the aircraft was transferred to the airport of Gran Canaria for the campaign MUSICA. In total, seven measurement flights were conducted from Gran Canaria into the viewing field of the ground-based FTIR, i.e. off the southeast coast of Tenerife (see Figure 3.3). All flights were scheduled to coincide with the morning overpasses of the IASI satellites and consisted of race track patterns at different altitudes (0–7 km) to derive vertical trace gas and aerosol profiles.

3.2.1. The PTRMS-CARIBIC as used during MUSICA

In autumn 2012, the MUSICA campaign had to be postponed to summer 2013, which at that time meant that the campaign would coincide with the HALO mission OMO (see Figure 3.1). This two-fold obligation led to the ambitious goal to already start the construction of the (largely identical) PTRMS-CARIBIC, which was mostly assembled by the author himself.

The assembly was finished in time, but due to severe problems with the I/O-modules of the PTRMS-HALO, which had priority, manufacturing of a second set of modules for the MUSICA instrument was delayed. As a coincidence, the OMO campaign was postponed for another two years, so that the control unit of the PTRMS-HALO could be used in the PTRMS-CARIBIC instrument during MUSICA. Figure 3.4 shows the PTRMS-CARIBIC with the control unit of the PTRMS-HALO installed in the cabin of the CASA C-212-200. All parts of the instrument were integrated into an aircraft certified rack, mounted on shock-absorbing rails.

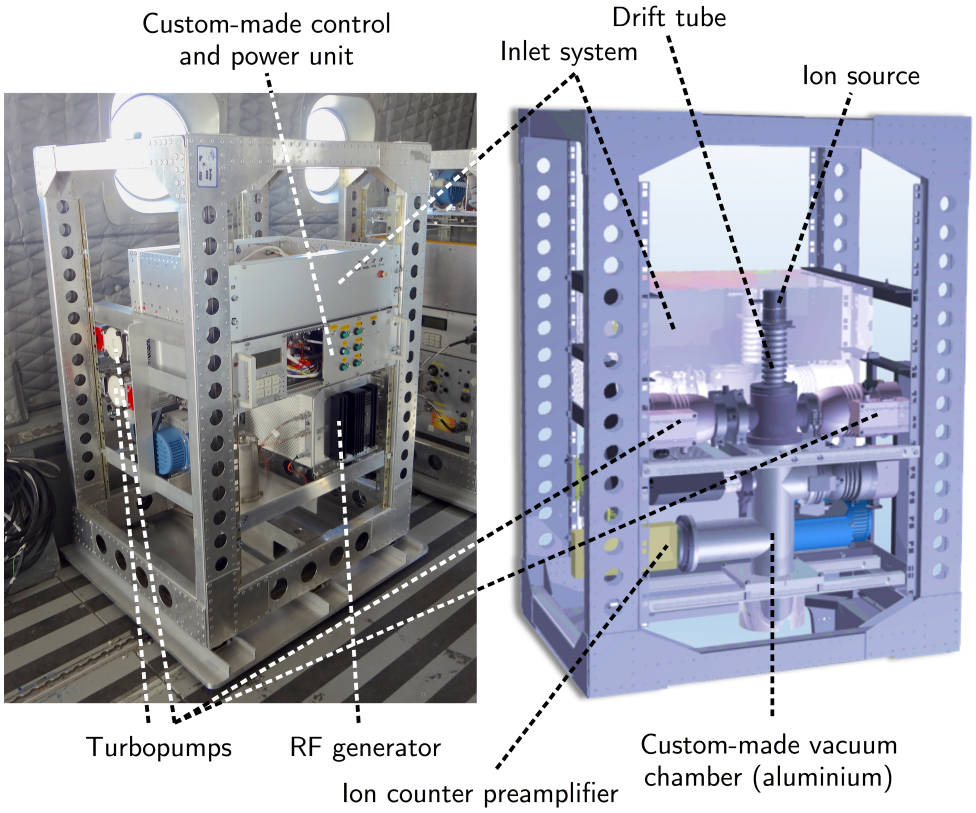

Figure 3.4.: PTRMS-CARIBIC installed in the cabin of the CASA C-212 aircraft (left side) and CAD view of its rear side (right side)

From the very beginning, the campaign's output of the PTRMS-CARIBIC in terms of data quality was uncertain, as the short-term merger of the control unit and mass spectrometer basically did not allow any characterization and functional tests in the laboratory. Also, the new modules in the control unit had never been tested for a longer time period and under field conditions. Indeed, during the campaign, electrical ground problems and electrical malfunctions turned out to be a major issue. The problems mainly affected the accuracy of mass flow and pressure signals needed for instrument control and monitoring, but also drifts and jumps in the signals of the mass spectrometer occurred from time to time. Therefore and because of the missing reliability of further house-keeping (sensor) data, other malfunctions (e.g. leakages) remained unnoticed for a longer time.

Another problem was insufficient cooling of heat-generating components during this early status. As the campaign took place in Spain in summer, temperatures inside the aircraft cabin were considerably higher compared to the laboratory. The high temperatures of sometimes above 40° C led to failures of the I/O modules in the control unit (in particular, the module controlling the mass flow controllers turned out to be sensitive to temperature) and of the turbopumps. This problem could be provisionally solved by adding three fans to the affected components.

Also some other electrical problems could be solved during the integration phase in Madrid, where the instruments were installed into the aircraft, but it took ∼10 days before the instrument could be switched into measurement mode for the first time.

In the absence of a chemical laboratory, the condition of the mass spectrometer was provisionally checked by analyzing ambient air and the head-space of a diluted liquid ethanol sample. In Figure 3.5, the corresponding mass spectra are shown.

In general, the distinctive allocation of two peaks to certain compounds allows an initial assessment of the mass-to-charge assignment. In the head-space spectrum (panel a), the peaks of protonated ethanol (m/z =47) and its fragment ions at $m/z = 45$ (loss of H_2) and $m/z = 29$ (loss of H_2O) (Brown, 2012) are significantly higher than in ambient air (panel b). The omnipresent peaks of the water dimers (m/z= 37) and the ion source impurities NO^+ ($m/z = 30$) and O_2^+ ($m/z = 32$) (e.g. de Gouw and Warneke, 2007) are also visible in the usual pattern, indicating that the ion detection and mass assignment worked.

However, the spectrum reveals that the operation parameters of the ion source and drift tube were not well adjusted. The peaks of the oxygen ions and dimers, which

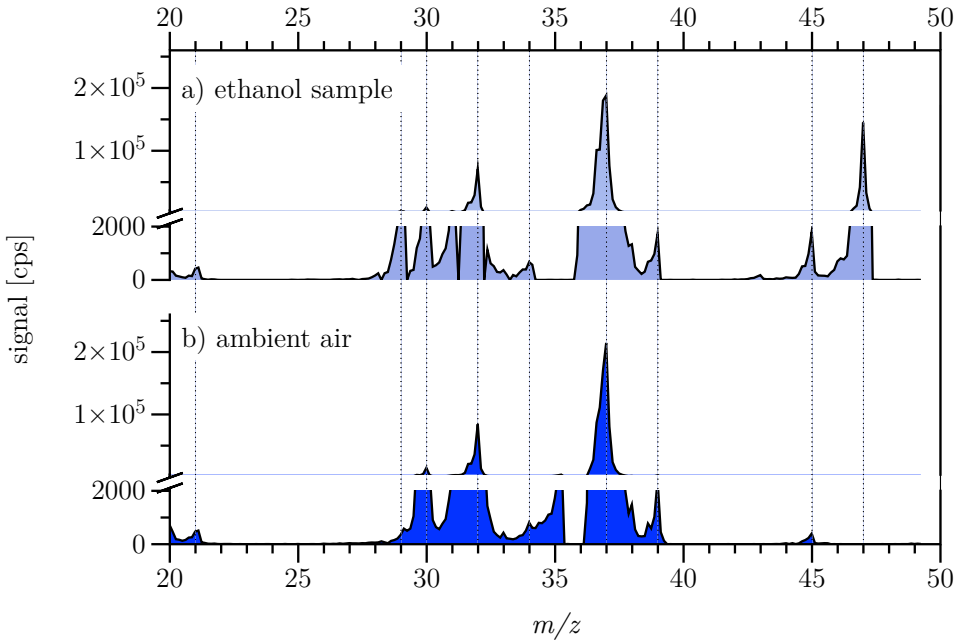

Figure 3.5.: Profile spectrum of a) the ethanol head-space and b) ambient air.

undergo their own reactions with VOCs, are too high compared to the primary ion signal, which is measured via the isotopologue $H_3{}^{18}O^+$ ($m/z = 21$). This could be improved during the campaign by adjusting the electrical fields between the ion source and quadrupole.

Although many problems could be solved during the campaign, reliable measurements allowing a scientific analysis were not obtained. Figure 3.6 shows the acetone data of a typical flight during MUSICA. The aircraft flew racetracks over the sea between Tenerife and Gran Canaria (see Figure 3.3) while frequently changing its altitude to gain vertically resolved data.

The PTRMS-CARIBIC conducted background measurements every 33 minutes for 3 minutes by diverting the sample air through a zero air generator (Pt catalyst). It is worth noting that the background-corrected acetone signal does not show much variability and the expected altitudinal gradient did not show up. The temporal course of the background signal can be caused by one of the following circumstances: (a) After switch-on, the air flow "flushes" impurities from the walls of the newly assembled inlet system. (b) The zero air generator is inefficient, i.e. only a part of acetone is destructed. (c) There is a leakage between the zero air generator and the quadrupole's entrance.

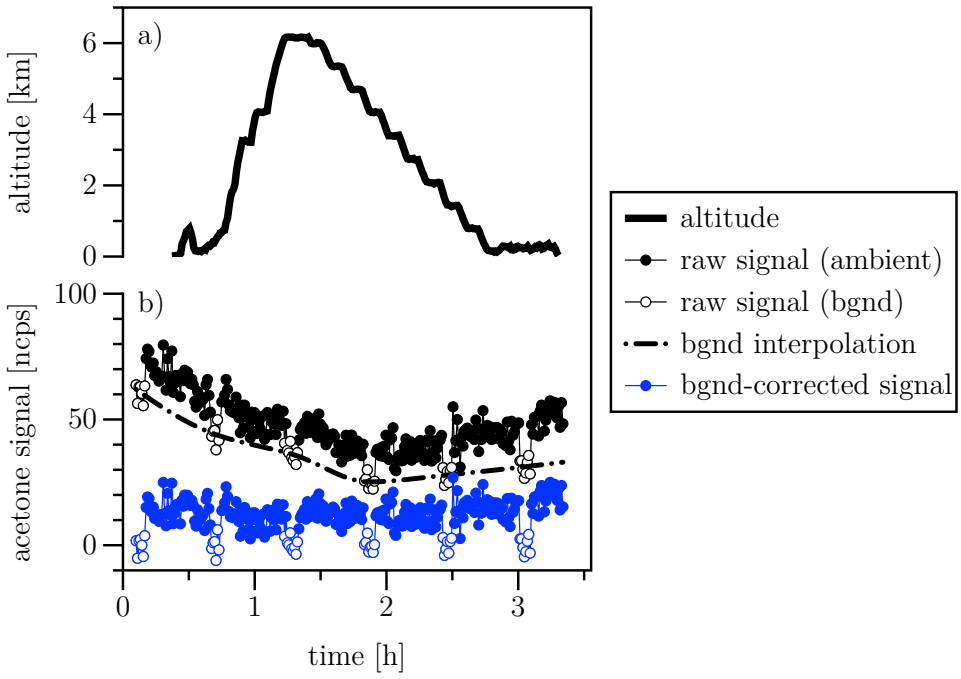

Figure 3.6.: (a) Altitude profile and (b) time series of acetone signal for the flight on 31st of July 2013. The data is normalized to 10^6 cps of primary ions (ncps, cf. Section 4.2.2).

The first case for itself cannot explain the slight simultaneous increase of the background signal and ambient signal. The latter two cases are hard to distinguish. However, the almost uniform spacing between ambient and background signal makes case (c) more likely, as the suspected leakage adds on to both signals. A superposition of all three effects also remains possible. Consequently, the PTR-MS data of the MUSICA campaign had to be rejected for further scientific evaluation. However, the experience gained during the campaign benefitted the further development and operation of all other instruments.

3.3. The PTRMS-HALO

Although the instrument was almost completely assembled in the previous PhD project (Geiger, 2015; see Section 3.1.3), a lot of work was still ahead to bring the instrument into an operational state. The individual and newly developed components had neither been extensively tested nor attuned or harmonized with each other. During the test phase, the high-voltage supply and control of the mass flow controllers and pressure sensors turned out to be prone to error and required time-

consuming troubleshooting and repairs. Also, the control software was far away from being complete. Still, a variety of processes had to be integrated and automatized to enable a safe and reliable deployment onboard aircraft.

Furthermore, the instrument still had to be certified to obtain the permission for operation onboard the HALO aircraft – a process that was not necessary for the MUSICA aircraft campaign. The certification required a multitude of partially time-consuming modifications, which did not improve the instrumental performance, but were solely done to fulfill the requirements of airworthiness and safety.

Also for this reason, it is renounced here to give a complete list of changes (implemented by the author). Instead, this section focuses on the outcome, i.e. on the final instrumental set-up as it has been certified and used onboard the HALO aircraft since then (e.g. during the scientific campaigns OMO and EMERGE). Special emphasis is placed on those custom-made components, which have not yet been described in detail elsewhere. This includes the sophisticated inlet system (Section 3.3.1) and the control software (Section 3.3.3), running on the central control unit (Section 3.3.2). The last part of this section (Section 3.3.4) deals with an integral part of the aeronautical certification, which turned out to be particularly challenging to comply with – the electromagnetic compatibility of the instrument.

3.3.1. Gas inlet system

Main purpose of the gas inlet system is to transfer analyte air from the gas inlet, where it has atmospheric pressure, into the drift tube (DT), where the pressure is ∼2–3 hPa. Besides reducing the pressure in the sample flow, the complex inlet system of PTRMS-HALO also takes over the following functions:

- control of the pressure in the DT
- supply of the ion source with a constant flow of water vapor
- generation of zero air used to determine the system's chemical background
- venting the vacuum system with clean air after shut-down of the pumps

The set-up developed for these purposes is fully custom-made and has been fitted into a 19" subrack called "flow box" (48.3 cm × 35.5 cm × 13.3 cm; 10.4 kg). Figure 3.7 shows a schematic drawing of its main components and flow paths.

When installed in the aircraft, ambient air enters the flow box through the trace gas inlet (Enviscope, Frankfurt, Germany) and the subsequent inlet line (1/4" PFA). As the length of the inlet line is at least 1.5 m (the actual length depends on the installation configuration of the cabin), the inlet system must allow for a high flow of air through the sampling line in order to keep the instrument's response time short.

In PTRMS-HALO, this was realized by implementing a bypass between the sampling and exhaust line. In this case, the flow is simply driven by the pressure difference between inlet and exhaust (ram pressure) and requires no weight- and power-consuming additional pump. However, to avoid an altitude-dependence, the bypass flow is limited and controlled to ∼1 sl min^{-1} using an off-branch mass flow controller (MFC; Bronkhorst, Ruurlo, Netherlands).

In previous versions of the control software, the mass flow controller was always left open. This has been changed so that the bypass line is only active during flight, i.e. when the airspeed is greater than 20 m s^{-1} and the ram pressure is greater than 10 hPa, and closes when the conditions are not fulfilled. With this step, a back-flow of contaminated air from the exhaust line through the bypass into the instrument due to the higher cross section of the exhaust line (3/8" PFA) compared to the inlet line is avoided.

Upstream of the bypass mass flow controller, a fraction of the incoming sample flow (∼55–190 sml min^{-1}, the actual flow rate depends on the inlet pressure) is branched-off to the instrument (red line in Figure 3.7). From here on, only 1/8" PFA tubing are used and the flow path is determined by the position of the five solenoid valves (NResearch, West Caldwell, New Jersey, US).

Status	I	II	III	IV	V
Measurement of ambient air	●	○	◍	●	○
Measurement of zero air	○	●	◍	●	○
Purging of the inlet system	○	●	○	●	○
Venting of the vacuum system	○	○	○	○	●

●: open

○: closed

◍: open if $p_{amb} < 400$ hPa, otherwise closed

Table 3.1.: Position of the valves I-V installed in the inlet system at different operation modes.

In Table 3.1, the valve positions corresponding to the different operation modes are summarized. In previous versions, the valves were continuously operated at their rated voltage of 24 V, whereby much of the power was converted into heat. To prevent this, the control software was modified so that the holding voltage is reduced to 12 V after switching the valve.

Directly after the branch-off from the inlet line, the sample air is either diverted through a custom-made catalytic converter (cyan branch in Figure 3.7) or directed past it (violet branch). Filled with a Pt catalyst (Shimadzu Corp., Japan) kept at 350 °C, the converter oxidizes all VOCs into H_2O and CO_2 and thus, produces zero air, which can be used to determine the chemical background of the system (downstream of the converter) or to vent the vacuum system with VOC-free air.

The diverted sample air or produced zero air is then injected through orifice I into the intermediate pressure stage (IPS, green lines in Figure 3.7), which is controlled to about 50 hPa. From here, a small fraction ($\sim$25 sml min^{-1}) of the sample flow is diverted into the DT via capillary I. The pressure in the DT can be regulated by the pressure in the IPS, which is controlled by an off-branch pressure controller (PC; Bronkhorst, Ruulo, Netherlands). A software PID-controller continuously adjusts the set-point of the PC so that the pressure in the DT (measured by a pressure gauge installed in the flow box) is kept constant.

The critical point in this system is the flow into the IPS, which varies with ambient pressure. Due to the high ceiling altitude of HALO, the ambient pressure can vary by almost one order of magnitude (120–1050 hPa). However, the flow into the intermediate stage must be kept between 50 and 160 sml min^{-1} for the following reasons: If the flow is higher, the pump load of the diaphragm pump (MD1; Vacuubrand, Wertheim, Germany) increases to such an extent that the high vacuum in the mass spectrometer collapses and the mass spectrometer is switched off to avoid damages. If the flow is lower, the PC in the intermediate stage is not supplied with enough air to work properly and control of the DT pressure fails.

Installing a mass flow controller would be the obvious solution of this problem, but due to expected interactions between the VOCs and the surfaces of the MFC, this was not an option. Instead, a sophisticated set-up of two custom-made orifices made of inert PEEK, which has been developed and tested within this work, was implemented in the sampling line.

Orifice I is dimensioned to reduce the flow into the intermediate stage to $\sim$160 sml min^{-1}

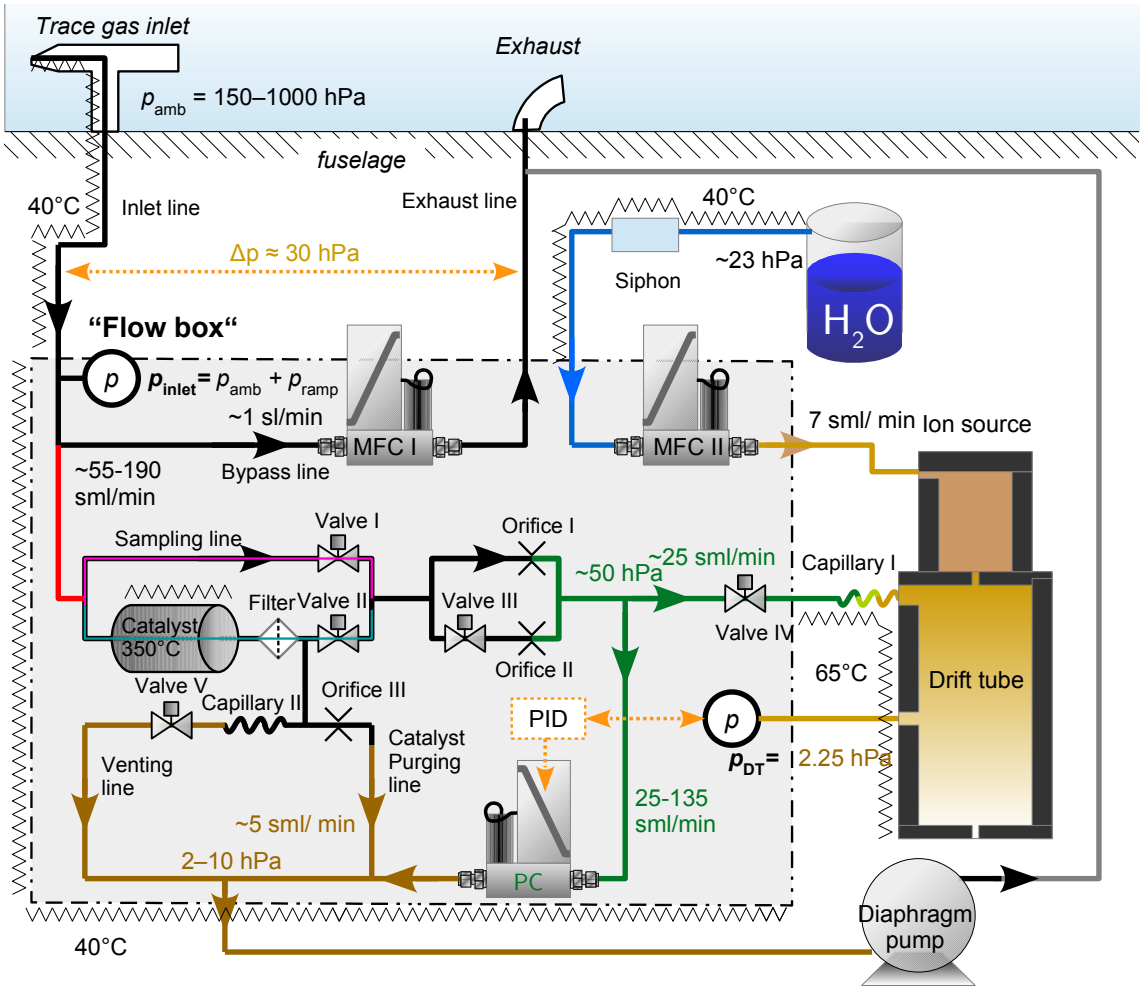

Figure 3.7.: Final set-up of the PTRMS-HALO gas inlet system (also called "flow box" due to its enclose in a subrack). Ambient air enters the "flow box" through the trace gas inlet (top left) in the aircraft's fuselage and the subsequent inlet line, whereby a bypass to the exhaust line ensures a high flow. In front of the bypass, a small proportion of the air is branched off into an arborescent tube system, from which a capillary leads into the drift tube (right). The system has the following purposes: (a) generation of zero air by diverting ambient air through a catalyst, (b) maintaining a constant pressure in the drift tube of ~2.25 hPa, (c) reducing the pressure of incoming ambient air (150–1000 hPa) to the drift tube pressure and (d) venting the mass spectrometer in a controlled manner after shut-down.

at 1050 hPa. However, at maximum flight altitude of HALO (p_{amb} = 120 hPa), the flow through the orifice will decrease by almost one magnitude to ~17 sml min^{-1}. Therefore, a second orifice (orifice II) is needed, which supplies the intermediate stage with an additional flow of at least 35 sml min^{-1} at 120 hPa. The optimal diameters of orifice I and II were calculated to be 130 µm and 190 µm. Tests of

the custom-made laser-drilled orifices (Fraunhofer Institute for Laser Technology, Aachen, Germany) revealed that the best performance is achieved when using drilling diameters of 120 µm and 180µm, respectively.

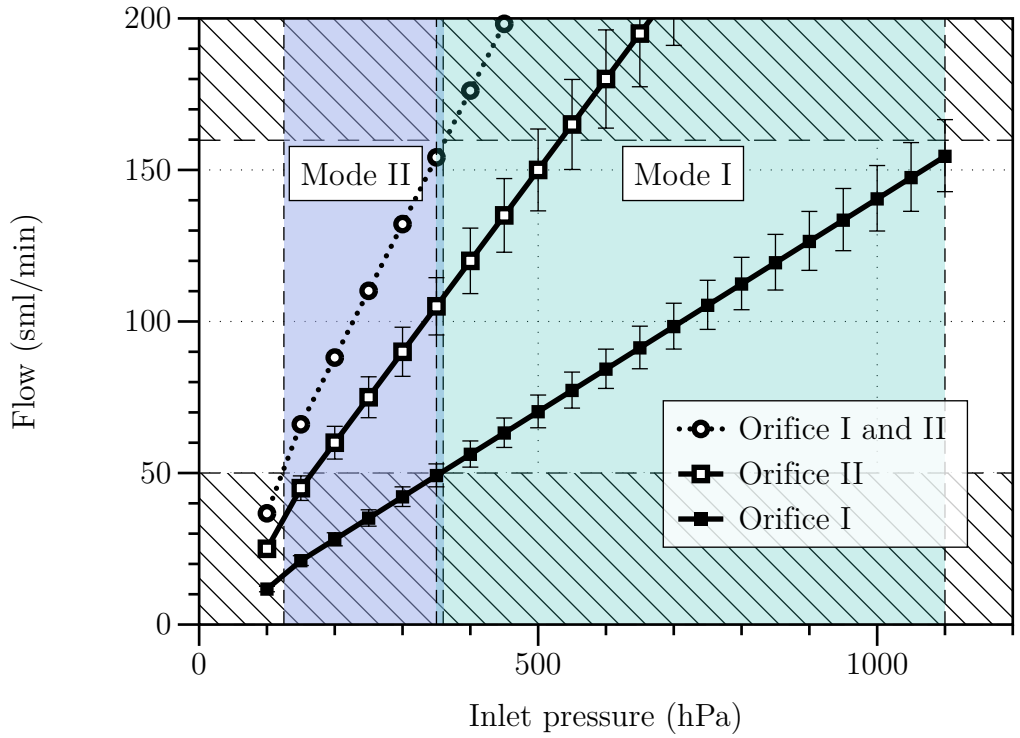

Figure 3.8.: Flow into the intermediate pressure stage for different inlet pressures. The error bars indicate the flow range if the diameter of the orifice deviates by less than ±5 µm. Areas, where the flow into the intermediate stage is out of its range (50–160 sml min^{-1}) are shaded.

In Figure 3.8, the calculated flows through each orifice and the resulting net flow through both orifices are plotted against the inlet pressure. Between 350 and 1100 hPa, the flow through orifice I (Mode I) is in the correct range (50–160 sml min^{-1}) and between 125 and 375 hPa, the same is true for the net flow through orifice I and orifice II (Mode II). Therefore, the valve in front of orifice II needs to be opened (ascent) or closed (descend) at ∼350–375 hPa. Besides the necessary calculations, also the pressure-dependent valve control was implemented within this study. Separate thresholds for opening and closure of the valve were chosen to avoid permanent opening and closing when the inlet pressure (within the noise of the sensor) coincides with the threshold value.

Modification of the zero air generation

Compared to previous versions, also the accuracy of background measurements could be improved. The catalytic converter was replaced by an improved version with a greater internal volume and a better thermal insulation. The former enhances the efficiency of the VOC removal process (larger surface of the catalyst and longer retention time), whereas the latter reduces heat dissipation and thus, power consumption and the warm-up time.

Furthermore, the position of the converter was changed. In previous versions, it was located downstream of orifice I and II in the intermediate pressure stage. The new position of the converter directly after the branch-off from the inlet line (see Figure3.7) has two advantages: 1. As impurities upstream of the converter are not captured, it is reasonable to position it at the beginning of the gas inlet system, which is now the case. 2. At the beginning of the gas inlet system, the pressure is higher compared to the former position behind the orifices I and II ($\sim$50 hPa). The higher pressure results in a higher collision rate of molecules with the catalyst's surface and thus, in a better efficiency.

To avoid a contamination of the converter when the sample air is diverted past it, the converter is continuously flushed with a small flow of sample air ($\sim$5 sml min^{-1}), induced by the pressure gradient at orifice III.

Venting of the vacuum system

As mentioned earlier, another purpose of the gas inlet system is to vent the vacuum chamber with clean air to avoid undesired contamination during periods, in which the chamber is not pumped. In the previous version, the venting line branch-off was positioned upstream of the bypass MFC. In this configuration, the air used for venting could not be fed through the catalytic converter used for zero air generation and an additional charcoal filter had to be installed in the venting line to remove contaminants. Besides the additional space and weight of the filter, the charcoal had to be frequently regenerated to maintain the efficiency of the filter.

In the modified version, presented here, usage of the charcoal filter could be completely avoided by placing the venting line downstream of the catalytic converter (see Figure 3.7). The venting is started by the shutdown-command, which opens valve V and closes all other valves (see Table 3.1). The capillary in front of valve V restricts

the flow through the venting line, as the turbomolecular pumps can be damaged by a too fast pressure increase (15 hPa s^{-1}) in the vacuum chamber. Furthermore, the catalytic converter becomes inefficient at too high flow rates. However, the venting time should be also kept as short as possible, as the catalytic converter is no longer powered after switch-off and loses its operation temperature after some time.

Therefore, the optimum dimension of the capillary has been determined as follows: In a first step, it was measured how fast the normal operation temperature of the converter (350°C) drops to its minimum operation temperature (300°C) after power switch-off (∼10 minutes).

In the next step, the venting times for different capillaries were estimated using a numerical model. At first, the volume flow through each capillary was calculated for a maximum pressure gradient $\Delta p = 1013.25$ hPa using the law of Hagen-Poiseuille. This volume flow was then integrated over a sufficiently short time step $\Delta t = 1$s to determine the amount of moles added to the vacuum chamber. Using the ideal gas law, the total amount of moles in the vacuum chamber were converted to a pressure, which was then taken to calculate the flow through the capillary within the next time step. These calculations were repeated until the pressure gradient fell below 1 %.

Optimal conditions were found for a diameter of 230 µm and a length of 9 mm. The corresponding venting time is 8.4 minutes and the maximum flow through the converter is 1.3 sl min^{-1}. The pressure change rate is ∼5 hPa s^{-1} at the beginning, which is three times below the permissible rate for the turbomolecular pumps (HiPace 80; Pfeiffer Vacuum, Asslar, Germany).

Heatings

The entire tubing from the trace gas inlet to the drift tube must be heated to minimize memory effects as well as the tubing of the ion source water supply (blue line in Figure 3.7) to prevent the formation of water droplets (which would disturb the flow regulation of MFC II).

When the instrument was taken over, only the heating inside the flowbox was already realized. Therefore, all other heatings (inlet line, ion source water supply, drift tube) including temperature sensors have been subsequently added and integrated into the control software within this study. Due to the requirements of airborne operation, the

power supply of the heatings had to be equipped with irreversible temperature fuses to prevent uncontrolled heating in case control fails. As there were no temperature fuses available for temperature above 200°C, the fuse for the catalytic converter was positioned in some distance to the heating element in the converter's isolation shield.

The correct position of the fuse and the relationship between the temperature of the heating element and the one of at the fuse's positions were experimentally determined.

3.3.2. The control unit

A unique selling point of PTRMS-HALO is its new custom-made control unit, which is fully integrated into a compact 19" subrack (48.3 cm × 29.5 cm × 13.3 cm) weighing only 11 kg. At the moment, no other PTRMS worldwide is equipped with such a compact and light-weight control unit, capable of powering and controlling all instrumental components, including the quadrupole mass spectrometer. These unique characteristics could be achieved thanks to the modular V25 system, developed at the MPI-C.

In general, the V25 system consists of the following components:

- a **main unit**, which comprises the embedded NEC V25 controller (microcomputer), a memory card slot for data storage and connections for remote control and network connectivity
- a **control panel**, equipped with a display (4 lines x 20 characters) and keyboard (6 control buttons) for interaction with the operator
- user-specific **I/O-modules**, providing the interface between the V25 system and the instrumental components
- a **backplane**, which connects the modules with the main unit and supplies all V25 components with power.

In PTRMS-HALO, the V25 system is equipped with 11 I/O-modules. Figure 3.9 shows a schematic drawing of the installed components. The control panel is integrated into the front plate of the subrack, whereas the main unit and the I/O modules are installed inside the subrack. All connection sockets of the I/O modules are internally connected with sockets (LEMO, Ecublens, Switzerland) on the rear panel

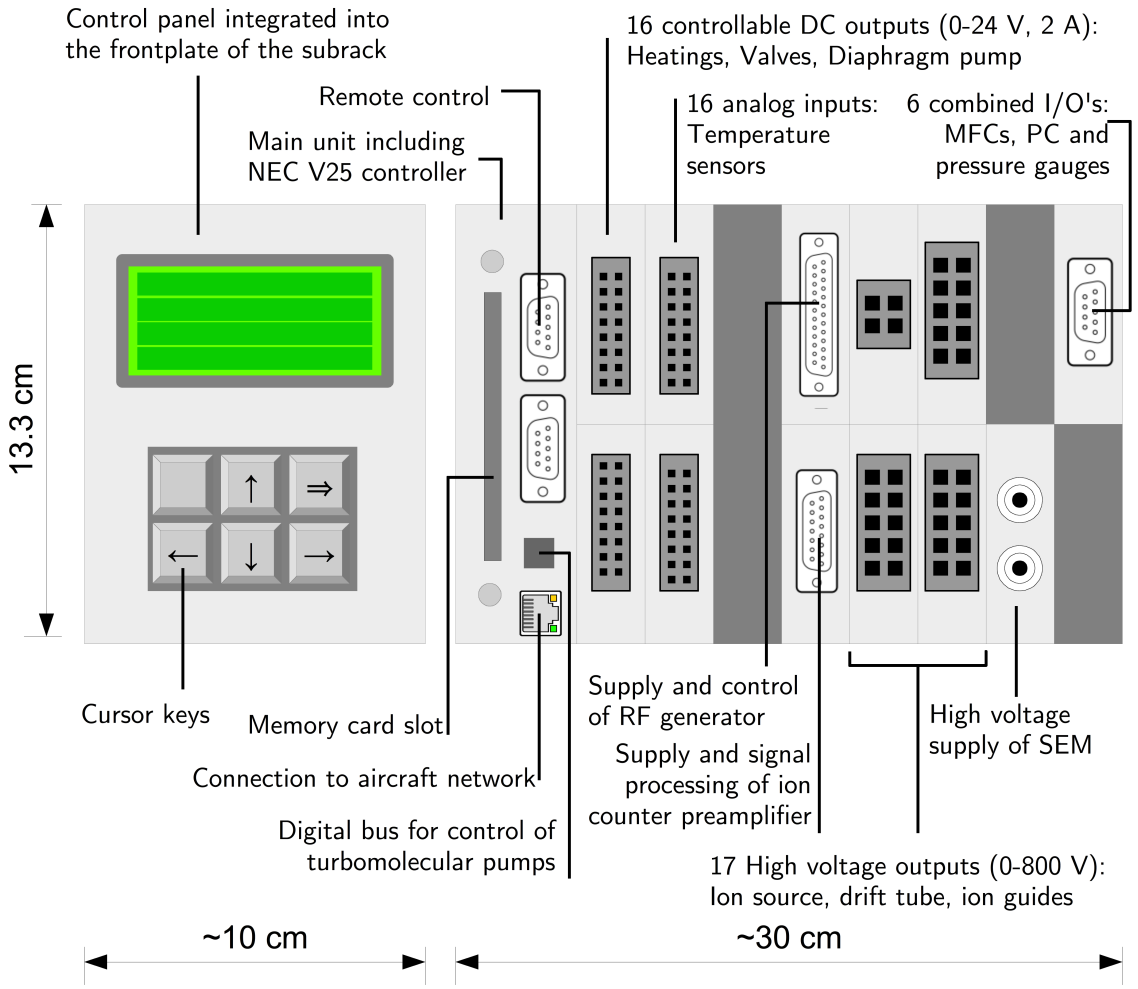

Figure 3.9.: Schematic illustration of the main components of the V25 system used in PTRMS-HALO. The control panel (left side) is installed in the front plate of the control unit, whereas the main unit and the I/O modules (right side) are installed in the inside.

of the subrack, from where shielded cables lead to the individual instrumental components.

Two identical modules provide in total 16 separately controllable DC outputs (0–24 V) to supply the diaphragm pump, heatings, cooling fans and to actuate the valves in the gas inlet system. Another two identical modules have the same number of analog inputs, used to read out temperature sensors. A newly developed module supplies and controls the RF generator of the quadrupole mass spectrometer and processes the signals from the ion detector. In total five modules provide the high voltages for the ion source, drift tube, ion lenses and detector. The last module has 6 channels, which combine power supply (24 V DC), a controllable DC output (0–10 V) and an analog input (0–10 V). Three of them are used to power and regulate the MFCs and

the PC in the gas inlet system. The other 3 channels take over the power supply and signal acquisition of the pressure gauges.

One great advantage of this custom-made modular system is, that modules can be easily replaced or added by the user. This is particularly important during airborne campaigns, where time-consuming repairs of defective hardware are not possible. Furthermore, the possibility to extend the system offers great potential with regard to future modifications (e.g. the ion-funnel enhanced DT)

3.3.3. Control software

A key component, to which the author contributed considerably, is the instrument software, controlling all components and parameters and handling the data acquisition. In contrast to commercial systems, the software is available in the form of a source code, which has the great advantage that all processes and interfaces can be adapted by the user. This flexibility opens up entirely new possibilities for a customized intelligent instrument control, commercial instruments are unable to provide. Furthermore, it allows the user to directly implement changes in the process workflows, which might become necessary after modifications.

The source code itself can be divided into two parts: In the first one, variables and functions are declared and the menu structure of the visual interface is defined. The visual interface is displayed on the control panel (see Figure 3.9) and allows the operator to monitor all system parameters (e.g. pressures, temperatures, flow rates) and to view the recorded measurement data. Furthermore, it enables the operator to manually control the instrument and to change the measurement and control settings.

The second part of the program contains the process workflows. As soon as the V25 is supplied with power, a comprehensive workflow is started, which successively switches on the individual components of the instrument and activates different control procedures to avoid unstable measuring conditions and to prevent damages of the mass spectrometer components in case of malfunctions (e.g. leakages in the vacuum system).

Before the HALO campaign OMO, the existing control software had to be adapted to the needs of airborne operation. The prime objective was to achieve a fully automated operation. Even though 3–4 scientists (operators) are onboard HALO to operate

all (typically 12–15) instruments, a highly automatized instrument relieves their workload and simultaneously avoids potential loss of data due to delayed or wrong user inputs and other user errors. However, also a fully automated instrument is not safe from failures and an early detection is essential during a campaign, as flights cannot be repeated. Therefore, a sophisticated and intelligent software that realizes malfunctions is required.

Start-up procedure

In Figures 3.10 and 3.11, the workflow during start-up of the instrument is schematically illustrated. In previous versions, not all operational parameters were read out or logged, which complicated trouble-shooting. During the MUSICA campaign, for instance, the turbo pumps shut down due to high temperatures, but the temperature sensors of the pumps were not read out by the software. This was changed in the latest version. As soon as the control unit is switched on, all acquired system parameters are periodically written into a log file, if not deactivated by the user.

At this early stage, also the (not yet implemented) activation of the heatings was integrated into the workflow to ensure that all components are heated up to their operation temperature before the instrument reaches the measurement mode. Furthermore, a new procedure continuously checks whether the inlet pressure is below 900 hPa. If this is the case, the software assumes that a measurement flight takes place and MFC I is opened to allow flushing of the inlet line (see Figure 3.7).

As a next step, the diaphragm pump (MD1; Vacuubrand, Wertheim, Germany) is started to generate the pre-vacuum necessary for operation of the turbomolecular pumps (HiPace 80; Pfeiffer Vacuum, Asslar, Germany). A threshold of 12 hPa, below the maximum permitted pre-vacuum (22 hPa) specified by the manufacturer, was implemented. If the threshold pressure is not obtained within 2.5 minutes, everything points to a leakage in the system and the start-up procedure is automatically aborted.

A similar control mechanism is implemented during the start of the three turbomolecular pumps (see Figure 3.10). To avoid unnecessary power consumption, the pumps are sequentially turned on. The first one is the turbo pump evacuating the drift tube and the subjacent pressure stage. If the pressure in the drift tube drops below 10^{-3} hPa within 5 minutes, which indicates that the pump has reached its full speed (1500 Hz), the two remaining turbo pumps are switched on to pump the mass

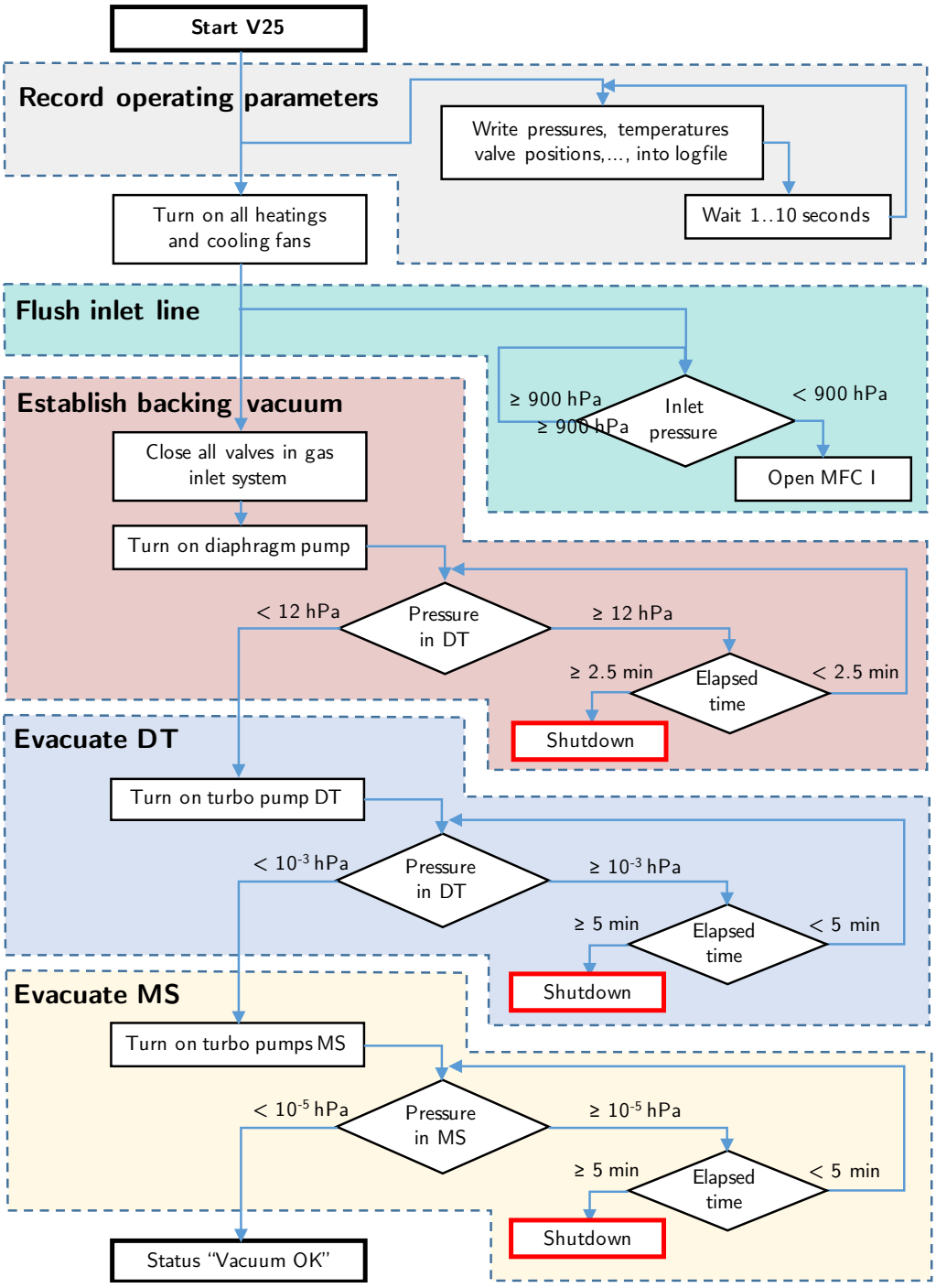

Figure 3.10.: Flow chart of the first processes after starting the software. The pumps are switched on one after another if the pressure condition of the respective level is fulfilled. As soon as all pumps are running and the pressure in the mass spectrometer (MS) region falls below 10^{-5} hPa, the instrument turns into a status named "Vacuum OK". If a condition is not fulfilled in the given time, the start-up procedure is aborted.

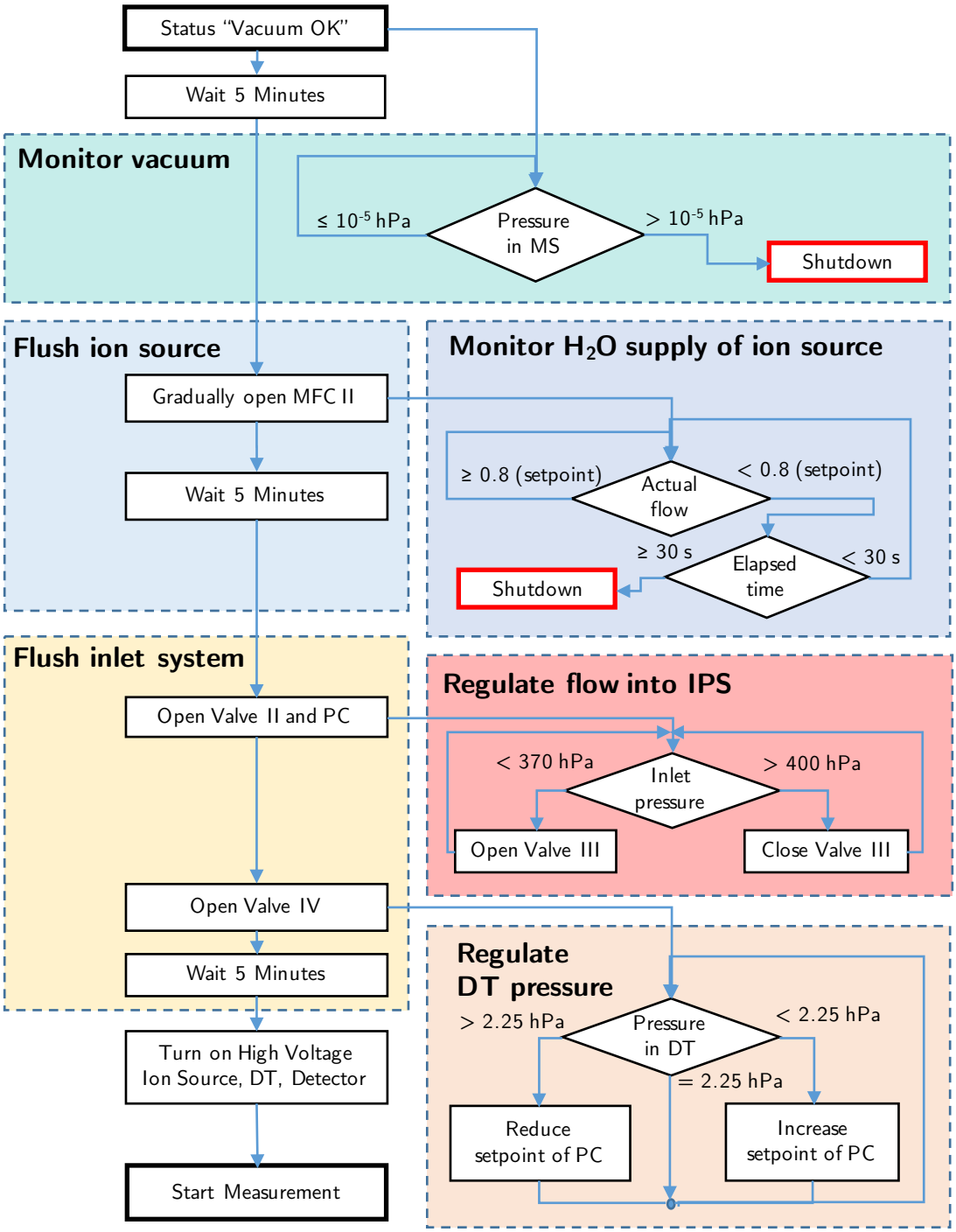

Figure 3.11.: Program flow chart of the processes after evacuation (status "Vacuum OK") until a measurement can be started.

spectrometer (MS). These two pumps are operated at rotation speeds of 1300 Hz. At this stage, a pressure of at least 5 10^{-5} hPa must be reached within 5 minutes to continue the workflow. If this condition is fulfilled, the instrument switches into a status called "Vacuum OK".

This status also activates a continuous pressure monitoring of the mass spectrometer (see cyan box in Figure 3.11) to ensure that the pressure in the MS is kept below the maximum operation pressures of the quadrupole (10^{-4} hPa) and ion detector (10^{-5} hPa). When operated at higher pressures, both components can be severely damaged due to the occurrence of electric arcs and gas discharges between the rods of the quadrupole or the dynodes of the detector. Therefore, the control software switches off the entire instrument if the pressure in the MS exceeds 10^{-5} hPa.

After 5 minutes, MFC II is gradually opened to remove air in the water vapor supply of the ion source. This is done to ensure that only pure water vapor enters the ion source during subsequent operation. Starting at this point, also the actual flow rate of the MFC is continuously monitored to recognize if the reservoir runs out of water. In this case, the actual flow through the MFC declines, as the pressure in the reservoir adapts itself from the vapor pressure of water (23 hPa at 20°C) to the pressure in the ion source ($\sim$1 hPa). To prevent the ion source from running dry, the control software automatically shuts down the instrument if the actual flow rate falls below 80 % of the set value (7 sml min^{-1}) for more than 30 seconds.

In the last step of the start-up phase, the gas inlet system and drift tube are flushed with zero air for 5 minutes to remove potential wall impurities before measurement. To ensure a sufficient flow into the IPS regardless of the aircraft's altitude, a pressure-dependent actuation of valve III (red box in Figure 3.11) has been added to the latest version of the control software. As soon as the drift tube is flushed, also the PID-controlled regulation of the DT pressure (orange box in Figure 3.11) becomes activate. After the flushing procedure, the high voltage is applied to the ion source, DT and mass spectrometer, and the instrument is ready for measurements.

Acquisition of QMS mass spectrum

Only if the start-up procedure is completed without errors, the control software starts the measurement process illustrated in Figure 3.12. As knowledge of the instrumental background is essential, this process involves time-controlled actuation of valves I and II in the gas inlet system (see Figure 3.7) so that ambient air is fed through the

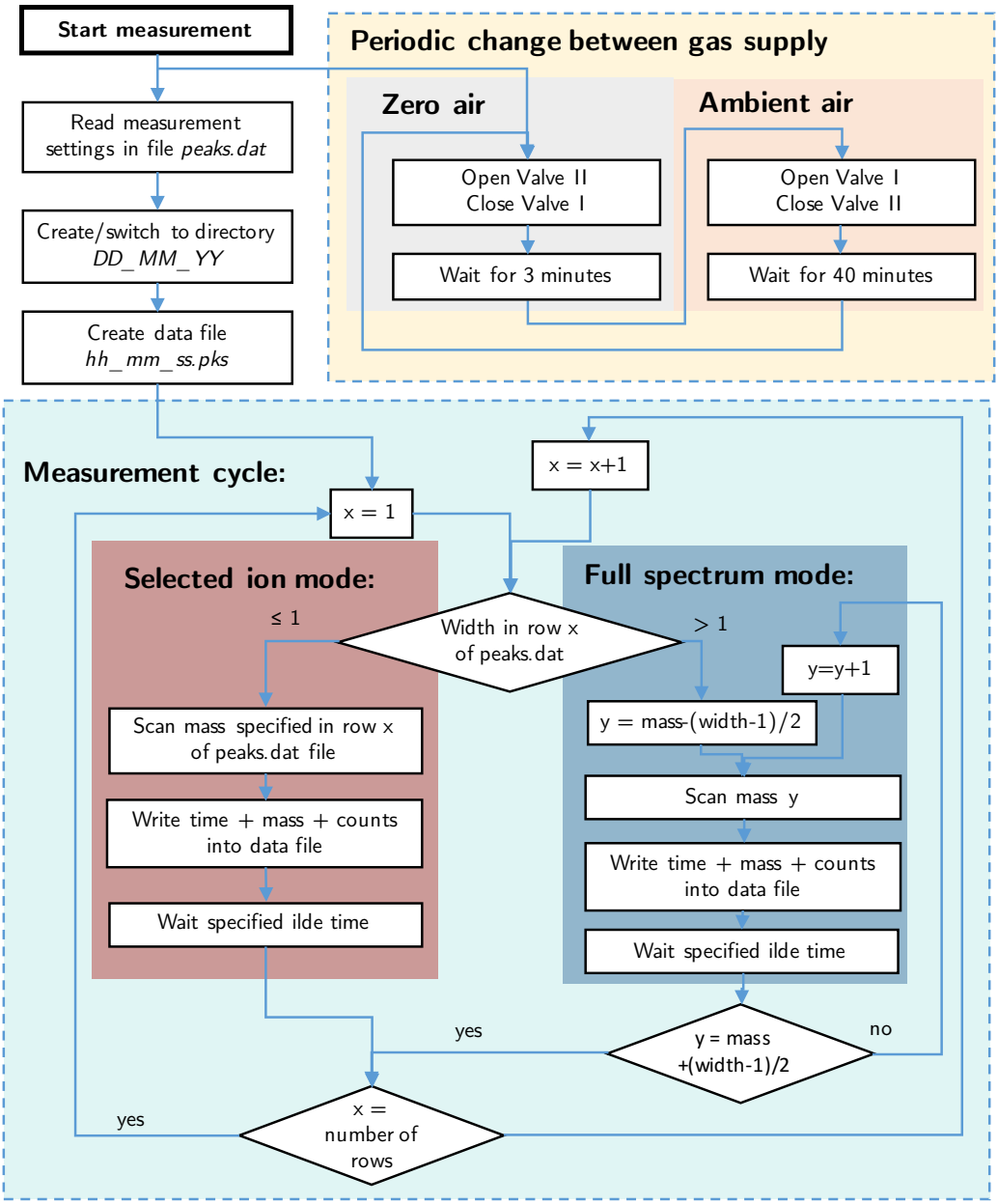

Figure 3.12.: Flow chart of the measurement process.

1	number	name	mass	width	dwelltime	dwellwait
	1	H3O	21.0	0.25	125	100
3	2	Formaldehyde	31.0	0.25	125	100
	3	Oxygen	32.0	0.25	12	100
5	4	Methanol	33.0	0.25	125	100
	5	Dimer	37.0	0.25	12	100
7	6	Acetonitrile	42.0	0.25	125	100
	7	Acetaldehyde	45.0	0.25	125	100
9	8	Acetone	59.0	0.25	125	100
	9	DMS	63.0	0.25	125	100
11	10	spectrum	50.0	61.0	125	100

Figure 3.13.: Example of a *peaks.dat* file

catalytic converter for 3 minutes every 40 minutes (or any other interval specified by the user; see yellow box in Figure 3.12).

All parameters required to control the data acquisition of the quadrupole mass spectrometer (QMS) are stored in an ASCII file named *peaks.dat*, read in before the first data acquisition. In Figure 3.13, the structure of a *peaks.dat* file is exemplarily shown. Each row contains a specific instruction, which can be the measurement of a specific mass (selected ion mode) or the subsequent measurement of adjacent masses (continuous spectrum mode). During measurement, these instructions are sequentially executed in a continuous loop as illustrated in the cyan box in Figure 3.12.

Selected ion mode

In the selected ion mode, the quadrupole sequentially measures the masses of interest, regardless whether they are adjacent or not. This mode becomes active, if the widths w specified in the *peaks.dat* file are less or equal unity (see lines 2-10 in Figure 3.13). In this case, the measurement of each mass m is divided into 8 steps at

$$m_i = m + \left(i - \frac{9}{2}\right) \cdot \frac{w}{8}, \quad i = 1, ..., 8, \quad 0.125 < w \leq 1, \tag{3.1}$$

where w is the associated width. If the width is set to its minimal value of 0.125 amu, the measurement at m is simply repeated 8 times (F. Helleis, personal communication). Each single measurement is performed for the variable dwell time t_{dwell} (in milliseconds) specified in the*peaks.dat* file, resulting in an overall measurement time of $8 \cdot t_{\text{dwell}}$ per mass. If all 8 measurements have been made, the software writes the following output

```
CurTime CurMass CountInt Counts1 Counts2 Counts3 ... Counts8
```

into the data file and jumps to the next mass. *CurTime* states the V25 time at the end of the 8 measurements corresponding to $CurMass$. The signal of each measurement is given as *Counts1* to *Counts8*, whereas *CountInt* states the sum. The correct start and halfway time of all 8 measurements can be calculated as follows, using the dwell time t_{dwell}:

$$\begin{aligned} t_{\text{start}} &= CurTime - 8 \cdot t_{\text{dwell}} \\ t_{\text{mean}} &= CurTime - 4 \cdot t_{\text{dwell}}. \end{aligned} \tag{3.2}$$

If the masses to measure are not close to each other, the manufacturer recommends to give the hardware some waiting time (dwellwait, also in milliseconds)

$$t_w \approx 2 \text{ ms} + |m_2 - m_1| \cdot 0.02 \frac{\text{ms}}{\text{amu}} \tag{3.3}$$

to "jump" from mass m_1 to m_2 and stabilize (Pfeiffer Vacuum, 2001).

Continuous spectrum mode

To measure a continuous mass spectrum over a certain mass range, the center mass m and an uneven integer width w larger than 1 amu must be specified in the *peaks.dat* file (see line 11 in Figure 3.13). In this case, the above-mentioned 8 measurements are sequentially done for each nominal mass within the range

$$\left[m - \frac{w-1}{2}, m + \frac{w-1}{2}\right]. \tag{3.4}$$

In-flight data downlink to ground

Since 2014, HALO is equipped with a Satcom interface enabling communication between aircraft and the scientific crew on ground via instant messaging and data transfer. This feature is extremely useful, as the downlink can be directly accessed by the instruments, connected to the Satcom interface via the onboard network. During OMO, the principal investigator of the mission requested real-time acetone data to be able to direct HALO according to the observations. Until then, the V25 did not buffer the raw counts, but directly wrote them into the output file.

In the new version, the V25 preprocesses the raw counts and computes preliminary concentrations of acetone and acetonitrile. This preliminary data is not background-corrected and based on the set sensitivities (usually inferred from the last calibration). However, with the framework provided by the author, an automatic (but preliminary) background subtraction should be easily integrated in future.

The V25 control program generates an ASCII string with these preliminary data and additional operational parameters in the following prescribed format (defined in the PLANET Technical Notes):

```
NAME,yyyy-mm-ddThh:mm:ss,value,value,value,value,value,value
```

Pos.	Parameter 1	Parameter 2
1	Flag [1]	Flag [2]
2	Signal of H_3O^+ [10^6 cps]	Flow through bypass [sml min^{-1}]
3	Ratio of O_2^+ and H_3O^+ [%]	Flow into the ion source [sml min^{-1}]
4	Ratio of $H_2OH_3O^+$ and H_3O^+ [%]	Pressure at the sample inlet [hPa]
5	Concentration of acetonitrile [ppb]	Pressure in the drift tube [10^1 Pa]
6	Concentration of acetone [ppb]	Concentration of acetone [ppb]

Table 3.2.: Parameters sent by the PTR-MS via Satcom interface.

According to the `NAME` variable (the PTR-MS uses `HKMS` as identifier), the Satcom software assigns the strings to the individual instruments and collects the data in separated ASCII files for each instrument. As the data rate of the satellite connection is limited, it was decided to alternately send two strings with different parameters and use the first value as flag. Table 3.2 lists the parameters, their units and position in the string for both packages.

During the OMO campaign, the string with flag 1 was provisionally triggered by the measurement at $m/z = 21$ (i.e. the last cycle was complete), whereas the second string was triggered by the measurement at $m/z = 37$. In the following, a typical sequence of ASCII strings sent by the PTRMS-HALO during flight is shown:

```
HKMS,2015-08-06T06:21:23,1,12.4,1.47,1.44,0.36,1.04
HKMS,2015-08-06T06:21:36,2,991.,7.00,492.,2251,1.04
HKMS,2015-08-06T06:22:02,1,12.3,1.48,1.47,0.36,1.32
HKMS,2015-08-06T06:22:15,2,991.,7.00,500.,2250,1.32
HKMS,2015-08-06T06:22:41,1,12.6,1.43,1.40,0.37,1.27
HKMS,2015-08-06T06:22:54,2,991.,7.00,501.,2250,1.27
```

In this example, the inlet pressure was between 492 hPa and 501 hPa and the inlet line was flushed with 991 sml min^{-1} (not considering the flow through the instrument). The pressure in the drift tube and the flow of water vapor into the ion source were controlled to 2.25 hPa and 7 sml min^{-1}, respectively.

Pos.	Parameter	Condition
1	All pressures in given limits	VacuumState = Ready
2	Alternating sample and background measurements	Process = on
3	High voltage applied to IS/DT/MS	HV = on
4	Operational parameters are recorded	Logger = on
5	Spectrum acquisition is active	ACQMode = Peak
6	Ion source is active	m21 $> 2 \cdot 10^6$ cps
7	Negligible photon signal	m25 < 10 cps
8	Negligible oxygen-to-primary ion ratio	m32 < 5 %
9	Negligible dimer-to-primary ion ratio	m37 < 5 %

Table 3.3.: List of automatically monitored parameters

Status indication and monitoring

A new subroutine gives feedback to the operator that the instrument is in the correct measurement mode. If all conditions specified in Table 3.3 are met, the light of the status photodiode, installed in the front panel of the electronics subrack, turns to green. In all other cases, it is red.

In addition, monitoring of all temperature sensors used for controlling heatings was implemented. In the past, overheating was possible when a negative temperature coefficient (NTC) thermistor was broken or disconnected, as the software interpreted the infinite resistance as low temperature. In consequence, the heat output was permanently set to the maximum. To prevent such scenarios, the new software offers the possibility to define temperature ranges for each sensor. If the actual value is out of range, the corresponding heating is automatically switched off.

3.3.4. Electromagnetic compatibility

Any electrical component emitting electric or magnetic fields (radiated via air and/or conducted via cables) is a potential source of electromagnetic interference (EMI) with other electronic devices. A device is referred to as being electromagnetically compatible, when the electromagnetic field interactions are tolerable within the specific environment.

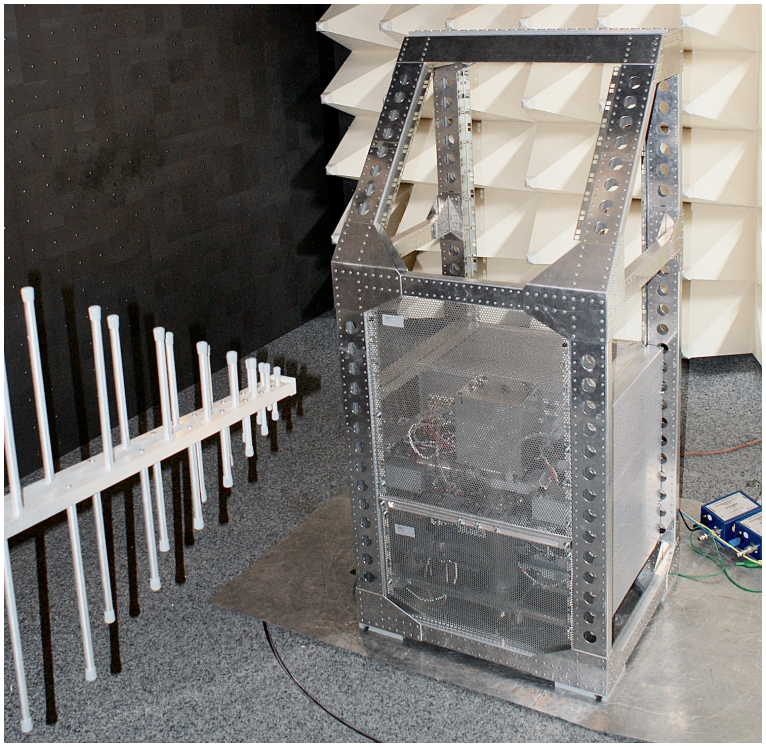

Figure 3.14.: Measurement of vertical radiated emissions from the rear side of the instrument in the anechoic chamber of the test laboratory Mectronic Prüflabor GmbH, Weiterstadt, Germany. The test was done according to the DO-160 standard, version G (RTCA, 2010).

In aircraft, disturbances of onboard electrical systems and the radio communication between cockpit and ground directly affect the safety of the aircraft and must therefore be avoided in any case. Stringent requirements are imposed to any electrical component to be installed onboard aircraft. The test procedures and limits are specified in the DO-160 regulation, which is regularly updated by the Radio Technical Commission for Aeronautics (RTCA). The different versions are denoted by ascending characters beginning with the letter A (first revision of the initial regulation) to G (currently valid version, published in 2010).

Within the scope of their certification, all scientific instruments used in HALO have to be tested for conducted (via the power cables) and radiated emissions in an accredited test laboratory according to the DO-160 standard prior to installation. Figure 3.14 shows PTRMS-HALO in such a laboratory (Mectronic Prüflabor GmbH, Weiterstadt, Germany) in an anechoic test chamber.

When the author took charge of the PTRMS-HALO, the instrument did not fulfill the specifications of the DO-160. The radiated emissions with frequencies between 0.1 GHz

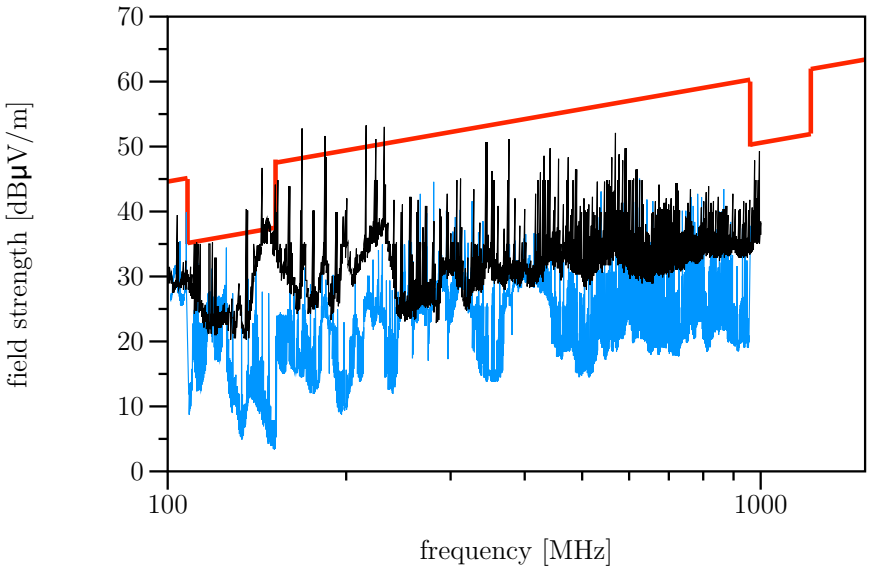

Figure 3.15.: Radiated emissions of HALO PTR-MS before (black) and after (blue) the changes made by the author (see text). The threshold of the DO-160 regulations is shown in red. Data courtesy of Mectronic Prüflabor GmbH.

and 1 GHz exceeded the threshold of the DO-160 at many frequencies (136, 144, 152, 168, 184, 216, 224, 232 MHz, see black spectrum in Figure 3.15). Please note that the threshold is lower for the bandwidths used for radio communication and aeronautical radio-navigation (108–152 MHz and 960–1215 MHz). The field strength E in Figure 3.15 is given as level L relative to 1 µV/m in decibel (dB):

$$L = 20 \lg \left(\frac{E}{1 \frac{\mu V}{m}} \right) \text{dB}. \tag{3.5}$$

Electromagnetic interferences are typically caused by electronic components operating with a certain frequency. In this case, the threshold overruns occurred at intervals of 8 MHz (or multiplies thereof), corresponding to the working frequency of the quartzes used in the modular V25 system to synchronize different digital circuits. As a consequence, all redundant quartzes were removed and the V25 main board was put in a separate shielded housing. However, this measure did not solve the problem completely, also as not all oscillators could be removed. Thus, further improvements were required.

To understand them, it is necessary to know how high-frequent parasitic currents propagate. The load current propagates in the differential mode, i.e. the magnetic

fields of the bidirectional currents cancel each other out (e.g. Ozenbaugh and Pullen, 2016). In contrast, the high-frequent parasitic currents propagate in the common mode and produce an impedance (e.g. Vasilescu, 2005). A ferrite toroid enhances this impedance (at higher frequencies above ∼100 MHz) and thus, suppresses the common-mode noise, whereas the impedance of the differential-mode current remains unaffected (e.g. Mardiguian et al., 2014). Therefore, ferrite toroids were implemented at the output of each DC/DC converter. In addition, capacitors were installed at the outputs to short-circuit the interferences against ground. The capacitors simply return the noise to its source and prevent its propagation (e.g. Martin, 2013). These measures mainly reduced inferences from the converters. The remaining radiated emissions originated to a large extent from the cables between the different units. In particular, the coaxial cables were critical as the components were grounded. Therefore, the overall shielding was improved by using additional grids on each side of the rack.

Unfortunately, all these changes increased the conducted emissions for frequencies greater than 1 MHz (see Figure 3.16). This problem was solved by replacing the inlet filter (Procond Oy GFHF) by a more efficient version (Schaffner FN2090). With all of these measures, the instrument passed the EMI test without objections on 9 October 2014. The aeronautical certification was completed in November 2014.

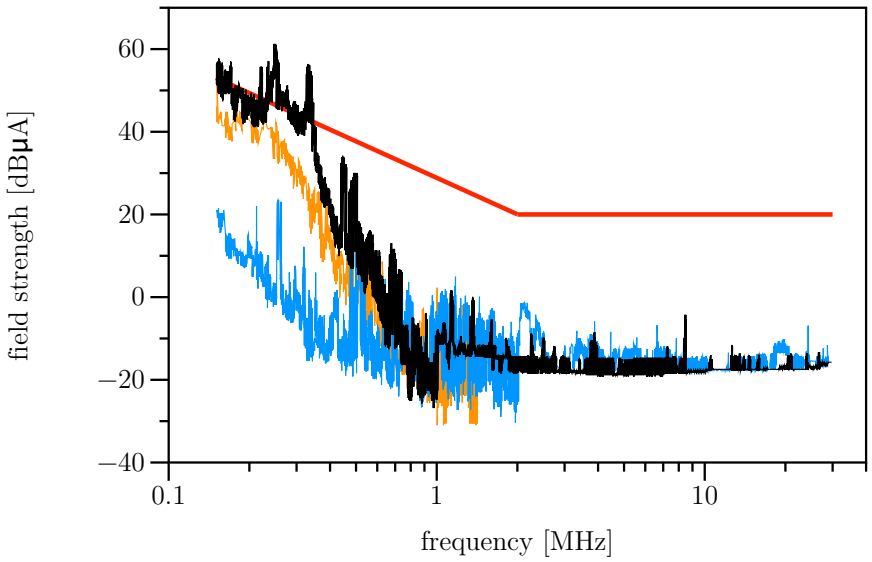

Figure 3.16.: Conducted electromagnetic emissions of PTRMS-HALO before (orange) and after (black) the changes made to reduce the radiated emissions compared to the threshold of the DO-160 regulations (red). Exchanging the instrument's net filter led to the final spectrum (blue). Data courtesy of Mectronic Prüflabor GmbH.

3.4. First airborne deployment

After attaining its aeronautical certification, PTRMS-HALO was first deployed onboard aircraft within the framework of the scientific HALO (see Section 1.3.2) mission Oxidation Mechanism Observations (OMO).

In the following section, the scientific objectives and the time schedule of the mission are addressed. The second part (Section 3.4.2) focuses on the VOC measurements made during OMO. Based on the data of an individual flight, the very good performance of PTRMS-HALO and the scientific value of the measurement data are demonstrated. A more comprehensive evaluation of the data will be objective of a separate manuscript (in preparation).

3.4.1. The OMO campaign

Main objective of the OMO mission was to improve the understanding of the oxidation processes in the UTLS downwind of the Asian summer monsoon. Within the monsoon, deep convection leads to a rapid uplift of polluted boundary layer air into the UTLS, where much of the pollution is confined in a strong anticyclonic vortex, spanning from Asia to the Middle East (e.g. Randel et al., 2010).

The rates at which the air pollutants are removed from the UTLS strongly depend on the abundance of HO_x radicals, which in turn affects the lifetime and thus, distribution of many air pollutants and greenhouse gases. Various studies revealed considerable discrepancies between measured and modeled HO_x levels, indicating that radical chemistry is still poorly understood (e.g. Jaeglé et al., 1998, Wennberg et al., 1998; Jackson et al., 2009; Stone et al., 2012; Regelin et al., 2013). Consequently, a major objective of the OMO campaign was to constrain the levels, sources and sinks of HO_x radicals in the Asian summer monsoon anticyclone. In addition, the influence of convective and long-rang transport of air pollutants on the composition and oxidation capacity of the atmosphere was addressed.

The PTRMS-HALO contributed to these objectives by measuring VOCs that are either precursors of HO_x (e.g. acetone, formaldehyde) or allow conclusions about the origin or age of air mass (e.g. acetonitrile, benzene, toluene). In Figure 3.18, the final cabin installation of PTRMS-HALO together with the ozone measurement device of KIT (Zahn et al., 2012) is shown. Due to the low weight and compact size of PTRMS-HALO, the ozone instrument could be mounted into the same rack, which

was positioned in first place behind the cockpit (see right picture of Figure 3.18). Both instruments shared a trace gas inlet (TGI; Enviscope, Frankfurt, Germany) mounted on top of the aircraft's fuselage on one of the various aperture plates. The cabin-internal interface of the aperture plate is also depicted in Figure 3.18.

In January 2015, a short test campaign was carried out. Three flights were conducted outbound of Oberpfaffenhofen (Germany) to test the only recently completed instrumentation under airborne conditions. Due to the experimental nature of these flights and the fact that flights were restricted to Europe, this part of the campaign is also referred to as OMO-EU/-Test.

The intensive main phase of the OMO campaign (OMO-Asia) took place in July and August 2015. In total 19 measurement flights were performed over the Eastern Mediterranean, the Arabian Peninsula and the Arabian Sea. Except for a period of 10 days, during which HALO was stationed on Gan (Maledives), the mission base was in Paphos (Cyprus).

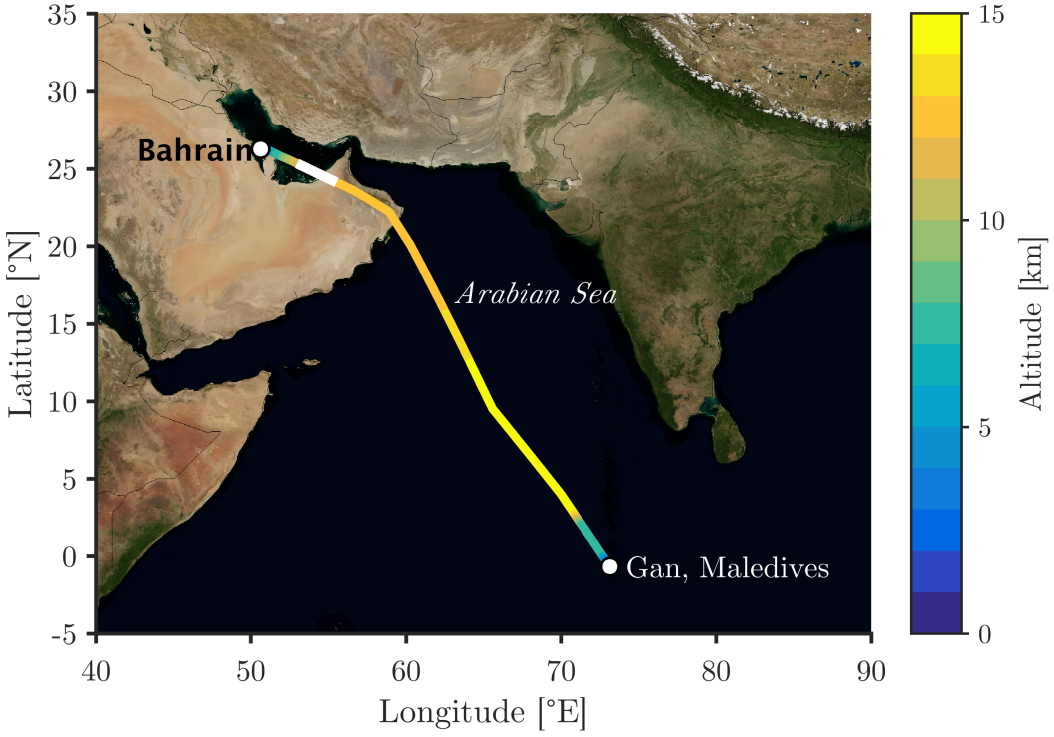

Figure 3.17.: Flight track of HALO performing a flight from Bahrain to Gan (Maledives) on 6 August 2015 (colorcoding: flight altitude). The part of the flight, in which measurements were not permitted, is shown in white. Satellite image courtesy of NASA's Earth Observing System (EOS).

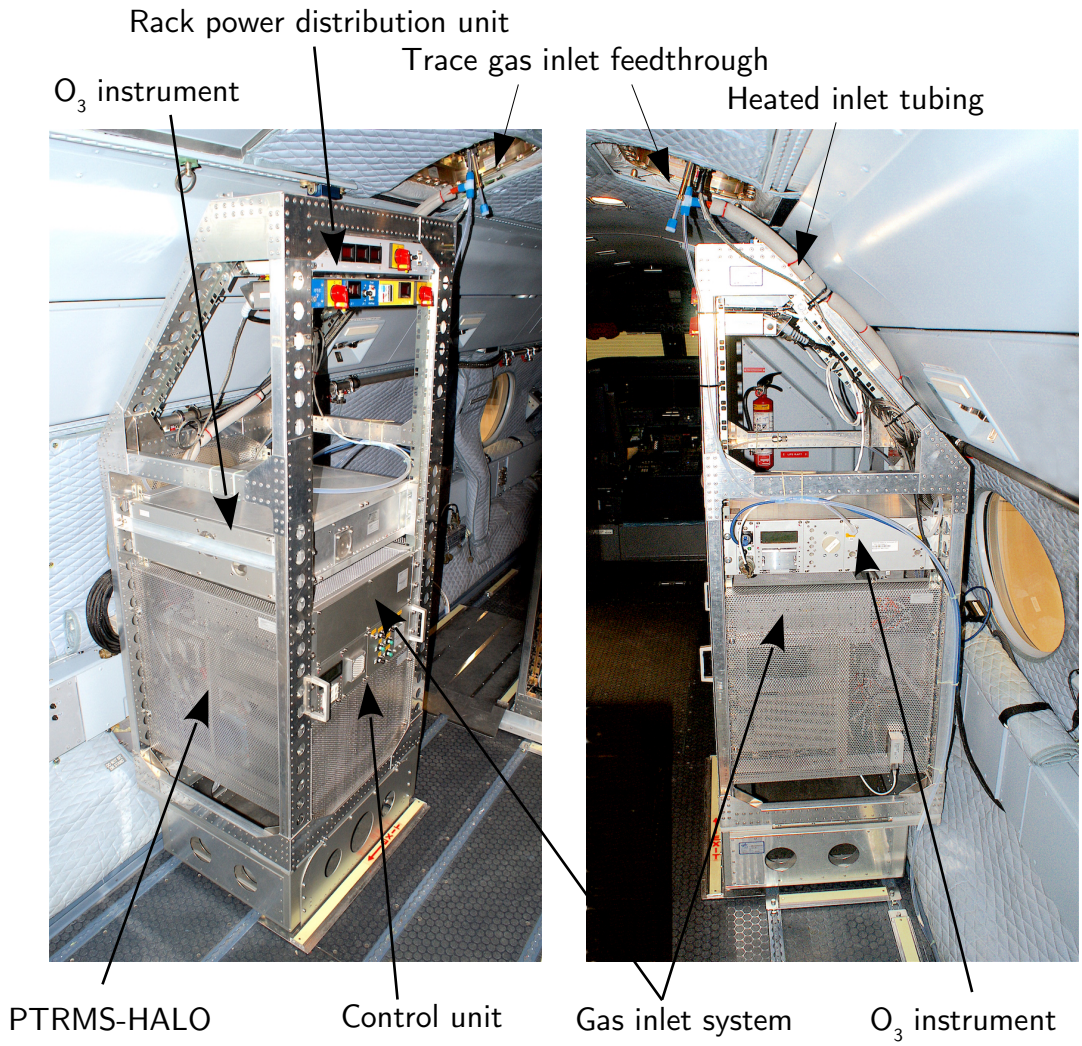

Figure 3.18.: Installation of PTRMS-HALO (and the ozone instrument of KIT) in the cabin of HALO during the campaign OMO.

The stopover in Gan had been initially planned as starting point for flights into the Asian monsoon over the Gulf of Bengal. However, due to construction work at the airport of Gan, the full length of the runway was not available and HALO could not take off with the fuel amounts required for extended flights over the Gulf of Bengal. Instead, flights were carried out over the Arabian Sea including refueling stops in Bahrain (for an exemplary flight track see Figure 3.17). The mission was completed on 27 August 2015 when HALO returned to its home base in Oberpfaffenhofen.

3.4.2. Flight from Bahrain to Gan

PTRMS-HALO conducted successful measurements during all mission flights, which is a remarkable achievement for the first airborne deployment of a newly developed instrument. Here, the very good performance is shown based on an individual flight from Bahrain to Gan on 6 August 2015. The corresponding flight track and altitude profile are illustrated in Figure 3.17 and 3.19a, respectively.

HALO took off in Bahrain at 07:45 and landed in Gan at 12:55 (all times are given in Universal Time Coordinated, UTC). No measurements were permitted between 08:12 and 08:35, when HALO crossed the air space of the United Arab Emirates.

Technical performance of PTRMS-HALO

PTRMS was switched on at 08:00 to avoid contamination during taxiing and take-off (see Figure 3.19a). However, the start-up procedure of PTRMS-HALO (see Section 3.3.3) was completed well before measurements were (again) permitted at 08:35, as can be seen from the temporal evolution of the DT pressure (see Figure 3.19b). The first pressure increase (08:07) is attributed to the opening of MFC II, which supplies the ion source with water vapor (see Figure 3.7). The second and larger pressure increase (08:12) is due to the last step of the start-up procedure. The inlet system is flushed for 5 minutes after opening Valve IV (see Figure 3.7) and activating the DT pressure regulation (set value: 2.25 hPa).

However, accurate (i.e. background-corrected) measurements are only possible when the VOC catalyst reaches its operating temperature (here 300°C). This was the case at 08:23 (see Figure 3.19a). Furthermore, the DT temperature and pressure have to be kept as constant as possible, as both parameters affect the instrumental sensitivity $\alpha \propto p^2/T^2$ (this relationship emerges from inserting Equation 2.20 into 2.11 in Section 2.1). The excellent performance of the temperature- and pressure-regulation is displayed in Figure 3.19b and 3.19c. The relative standard deviation (RSD) of the DT pressure and temperature is only 0.03 % and 0.11 %, respectively. These values are ∼30 times lower than the ones of the CARIBIC-PTRMS, which will be soon replaced by a version similar to PTRMS-HALO (see Section 3.5). The visible swings in the DT pressure of PTRMS-HALO are except for one case solely caused by the valve actuation when switching between ambient and zero air.

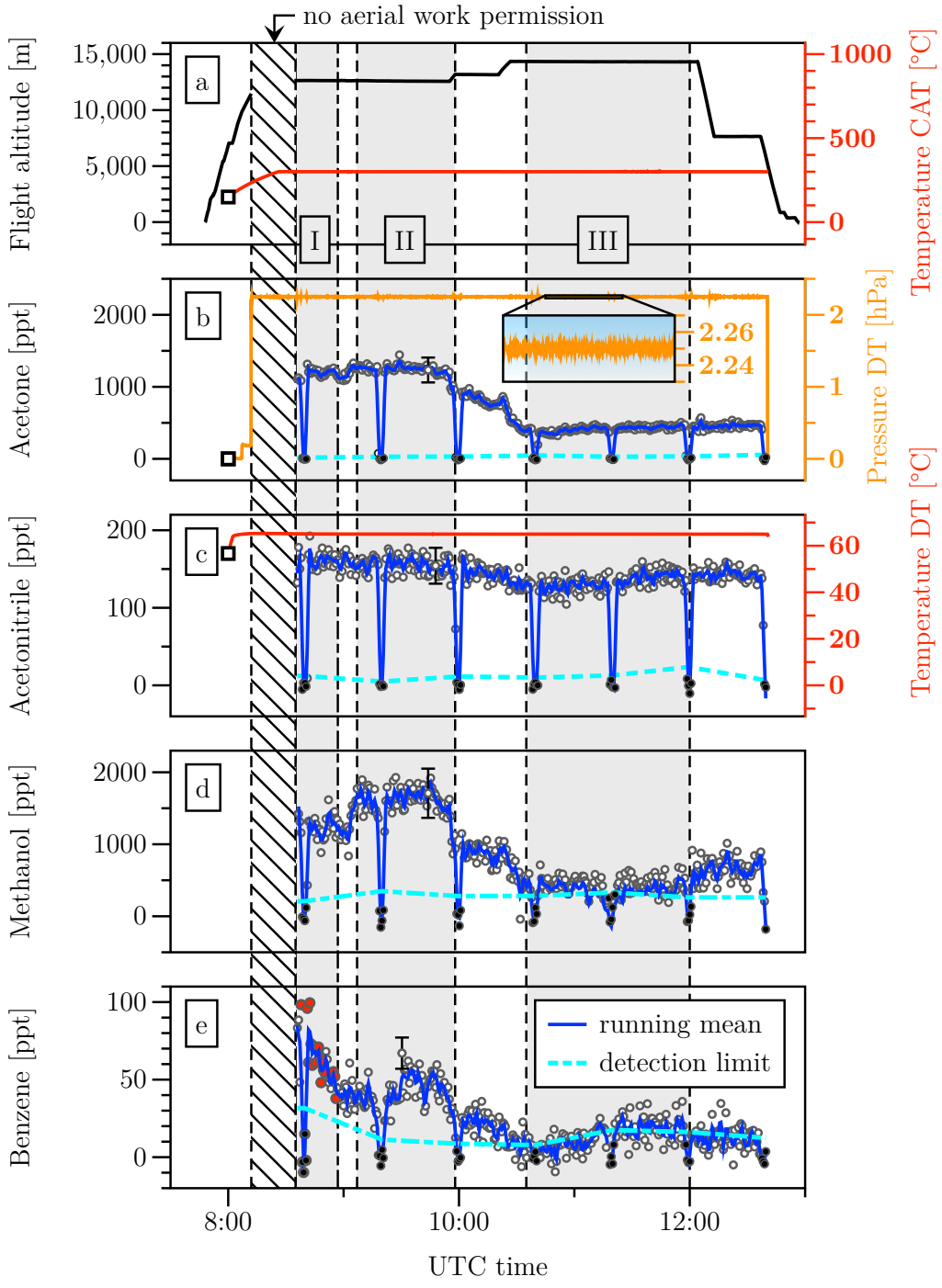

Figure 3.19.: Time series of background-corrected VMRs and parameters during a mission flight from Bahrain to Gan on 6 August 2015.

Ambient VMRs are displayed as open circles and oriented on the left-hand axis. Background measurements are marked in black (filled circles). The estimated overall uncertainty of VMRs is exemplarily shown for one measurement per substance. The dark blue solid and cyan dashed line represent the running mean over 5 measurements and the detection limit ($S/N = 3$), respectively. (a) Altitude profile of HALO (black line) and temperature of the VOC catalyst (red line, right axis). (b) Acetone VMR (open circles, left axis) and DT pressure (orange line, right axis). (c) Acetonitrile VMR (open circles, left axis) and DT temperature (red line, right axis). (d) Methanol VMR. (e) Benzene VMR. Measurements coinciding with methane VMRs larger than 1879.8 ppb (see Equation 3.6) are marked in red. The grey shaded segments of the flight (I, II and, III) are used for trajectory analysis (see Figures 3.20 and 3.21).

In panel b–e of Figure 3.19, the background-corrected VMRs of acetone, acetonitrile, methanol and benzene are shown. During ambient measurements, the instrumental background was estimated using a (step-wise) linear interpolation based on the means of each background measurement. This procedure is commonly used (e.g. Custer and Schade, 2007; Jordan et al., 2009b; Vlasenko et al., 2010), as there is no indication for a physical process that leads to a specific temporal course of the background. To illustrate the timing of the background measurements (3 minutes at intervals of 40 minutes), the respective measurements (subtracted by the interpolated background) are also displayed. Please note that due to the background correction and finite precision of the measurements also negative VMRs initially occur. However, this is not a problem, as values below the LOD (see Section 2.2.4) are in any case excluded from further analysis.

For each substance, the LOD (dashed light blue line in Figure 3.19) was calculated as three times the standard deviation of the background measurements during flight and linearly interpolated in between. For acetone and acetonitrile, all ambient measurements are above the LOD. Methanol VMRs are close to the LOD between 10:30 and 12:00, when the aircraft's altitude was 14300 m. At the same time, the measured benzene VMRs are almost evenly distributed around the LOD. However, in contrast to methanol, benzene does not show an increase in VMRs after HALO descended to 7600 m at 12:10. In total, 6 and 32 % of the methanol and benzene measurements were below the LOD. In theory, the LOD can be still retrospectively improved – on the expense of the temporal resolution – by merging successive measurements. However, further analysis, which would have gone beyond the scope of this study, is required to process the data this way.

Air mass characterization

To determine the approximate origin and age of sampled air masses, 12-day backward trajectories were calculated using the atmospheric transport and dispersion model HYSPLIT 4 (Hybrid Single-Particle Lagrangian Integrated Trajectory model) (Draxler and Hess, 1997 and 1998; Draxler, 1999; Stein et al., 2015). The model was integrated with 3-hourly meteorological fields derived from the Global Data Assimilation System (GDAS) of the National Center for Environmental Prediction (NCEP), provided on 55 hybrid sigma-pressure surfaces and a $0.5^\circ \times 0.5^\circ$ horizontal grid.

In order to automatically calculate a large number of trajectories (as required when analyzing one or more complete flights), the author developed a Matlab script, which processes the flight track data of HALO and directly controls the HYSPLIT model using its batch mode (for the respective code see Appendix B). Trajectories were started along the flight path at intervals of 1 min (minimum time step of the model), while the output frequency of trajectory points was set to 1 hour.

Nevertheless, for reasons of clarity and due the scope of this section, not all trajectories calculated for flight on 6 August 2015 can be shown here. Instead, three interesting flight segments (gray-shaded sections in Figure 3.19) have been selected. The first segment is characterized by elevated VMRs of benzene, the second shows the highest methanol and acetone VMRs of the flight and the third one stands out with relatively low concentrations for all species measured with PTRMS-HALO. In the following, the pathways of the backward trajectories calculated for the three segments (see Figures 3.20 and 3.21) are discussed:

Segment I: During this part of the flight, elevated benzene VMRs (50–100 ppt) coincide with enhanced methane concentrations (see Figure 3.19e). Due to the high contribution of anthropogenic sources to its total emissions, benzene is often used as tracer for anthropogenic pollution (e.g. Holzinger et al., 2007). Major sources of methane include emissions from livestock farming and rice cultivation, biomass burning and natural gas production and handling (e.g. Johnson and Johnson, 1995; Garg et al., 2001). Tomsche et al. (2016b, 2017) showed that due to its long atmospheric lifetime in the order of years, methane is well suited to determine whether sampled air was influenced by the Asian summer monsoon or not. Based on the mean and standard deviation of observed free tropospheric background VMRs of methane over Europe (Cyprus, Italy and Germany) they derived a threshold value

$$[\mathrm{CH_4}]_{\mathrm{threshold}} = \overline{[\mathrm{CH_4}]_{\mathrm{bgnd}}} + 2\ \sigma([\mathrm{CH_4}]_{\mathrm{bgnd}}) = 1879.8\ \mathrm{ppb} \tag{3.6}$$

to tentatively assess whether an air parcel corresponding to a specific VMR was affected by deep convection in the Asian summer monsoon (see also Bourtsoukidis et al., 2017). With a likelihood (confidence level) of 95 %, methane VMRs above this threshold cannot be explained by the natural variability of the free tropospheric background and are thus, associated with rapid upward transport in the Asian summer monsoon.

In Figure 3.19, the benzene VMRs coinciding with methane VMRs exceeding this threshold are marked in red. During this flight, the threshold was only exceeded in

this segment. About 70 % of the methane VMRs measured in the segment (data courtesy of Tomsche et al., 2016a, not shown here) are higher than the threshold. The trajectory analysis reveals that 48, 40, 36 and 26 % of the trajectories corresponding to this flight segment crossed the 550, 650, 750 and 850 hPa pressure level, respectively, within the last 12 days.

According to the trajectory pathways shown in Figure 3.20a, the majority of air masses, which had contact with the planetary boundary layer within this period, originated from Bangladesh and Myanmar. Deep convection frequently occurs over these countries during the Asian summer monsoon due to the southwesterly monsoonal flow encountering the Himalayan foothills in this region. Orographic lifting of the potentially unstable flow then triggers convection (e.g. Li et al., 2005; Medina et al., 2010; Reeve, 2015).

Further analysis of the trajectory data shows that the affected air masses were transported into the free troposphere on average 7.9 (±1.1) days ago (± standard deviation). While methane has such a long atmospheric lifetime that only negligible amounts degrade within this period, the short atmospheric lifetime of benzene in the order of ∼10 days suggests that substantially more benzene has been injected into the free troposphere than measured here. Still, the benzene VMRs observed in theses relatively aged air masses exceed the mean VMR (∼10 ±4 ppt) of CARIBIC observations over this region and during this time of the year (Baker et al., 2014) at least by a factor of five.

Segment II: In this flight segment, consistently higher methanol VMRs (1500–2000 ppt) than during the rest of the flight were observed (see Figure 3.19d). Methanol is known to be emitted by biogenic and anthropogenic sources including biomass burning (see Table 1.2) and is also produced in the atmosphere by the oxidation of other VOCs and methane (e.g. Razavi et al., 2011). While the emissions from anthropogenic sources and biomass burning only constitute a minor source (∼10 %), methanol is the second largest contributor to the total biogenic VOC source after isoprene (Guenther et al., 2012). However, due to its longer lifetime (∼5–22 days compared to ∼1–2 hours), it is more abundant in the troposphere than isoprene and any other non-methane VOC (Tie et al., 2003; Jacob et al., 2005; Millet et al., 2008). Therefore, the VMRs observed here are not unusually high. Although biogenic emissions are thought to be the largest terrestrial source of methanol, elevated VMRs are not per se an indicator of strong biogenic contributions, as other sources may dominate on regional scales. Enhancements due to biogenic emissions would imply

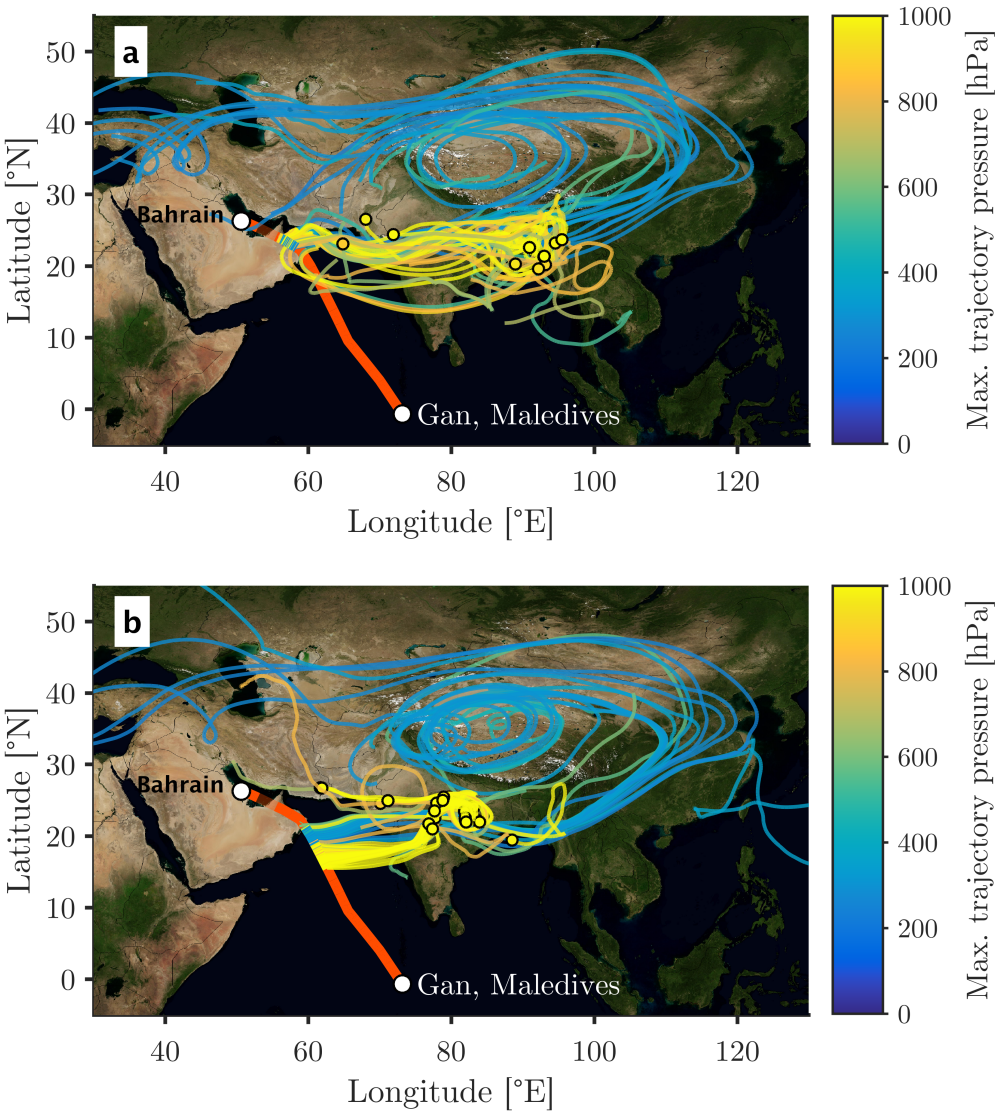

Figure 3.20.: Backward trajectories for air masses sampled on 6 August 2015 between 8:35 and 8:56 UTC (panel a) and between 9:07 and 9:58 UTC (panel b). For the corresponding measurements see Figure 3.19 (segments I and II). Colorcoding denotes the maximum pressure of the trajectory. If applicable, trajectories have been cut at 850 hPa (= assumed mean pressure height of the planetary boundary layer). The positions of these cut-offs are highlighted as color-filled circles. The flight track of HALO is shown in red. Satellite image courtesy of NASA's Earth Observing System (EOS).

that also other biogenically emitted species such as acetone (see Section 5.1) are likewise elevated. However, the acetone VMRs measured here remain on the same level as observed in segment I (see Figure 3.19b).

Also, a contribution from biomass burning is unlikely, as this would be accompanied with elevated VMRs of acetonitrile being a common tracer of biomass burning (see Chapter 6). Here, regional anthropogenic emissions might have been the cause for the enhancement. This is supported by the concurrent measurements of benzene and CO, which are common tracers for air masses of anthropogenic origin. In this segment, measured VMRs of CO (data courtesy of Tomsche et al., 2016; not shown here) increase from ∼80 ppb to ∼130 ppb, well above the regional tropospheric background of 82 (± 14) ppb determined from CARIBIC observations (Baker et al., 2014).

The trajectory analysis particularly agrees with the CO measurements but does not show a completely unambiguous picture with regard to the methanol measurements. In the first half of the segment, the mean atmospheric pressure level of the trajectories is on average 265 (±64) hPa (± standard deviation). Except for one trajectory originating from the marine boundary layer of the Gulf of Bengal (∼90° E, 20° N, see Figure 3.20b), maximum pressure values of the trajectories indicate that air masses sampled in this part did not ascend from the planetary boundary layer within the last 12 days. However, in the second half of the segment, where also the CO VMRs are highest, the trajectories suggest that 93 % of the air masses had recently contact with the planetary boundary layer, on average 3.3 (±1.9) days before the measurements (mean ± standard deviation). Most of the trajectories originate from central India and the Indo-Gangetic Plain (see Figure 3.20b), where one seventh of the world's population lives (Sinha et al., 2014). In this region, Sinha et al. (2014) found surface VMRs of methanol consistently higher than observed in urban environments elsewhere in the world. The authors concluded that the high methanol concentrations were likely due to the emission from anthropogenic sources such as water treatment and chemical plants (Galbally and Kirstine, 2002; Tata et al., 2003).

Segment III: In this segment, VOC VMRs reach their minimum values for this particular flight. Likewise, the concentrations are on the lower side of the range of what has been measured during the campaign (data courtesy of Safadi and Neumaier, 2016). Also, the VMRs of CO observed in this segment are exceptionally low (∼50–60 ppb). It can therefore be readily assumed that very clean air masses have been sampled and that the measured VMRs (acetone: ∼500 ppt; acetonitrile: ∼150 ppt; methanol: ∼500 ppt; benzene: ∼20 ppt) reflect tropospheric background concentrations. In general, this is also supported by the trajectory analysis shown in Figure 3.21.

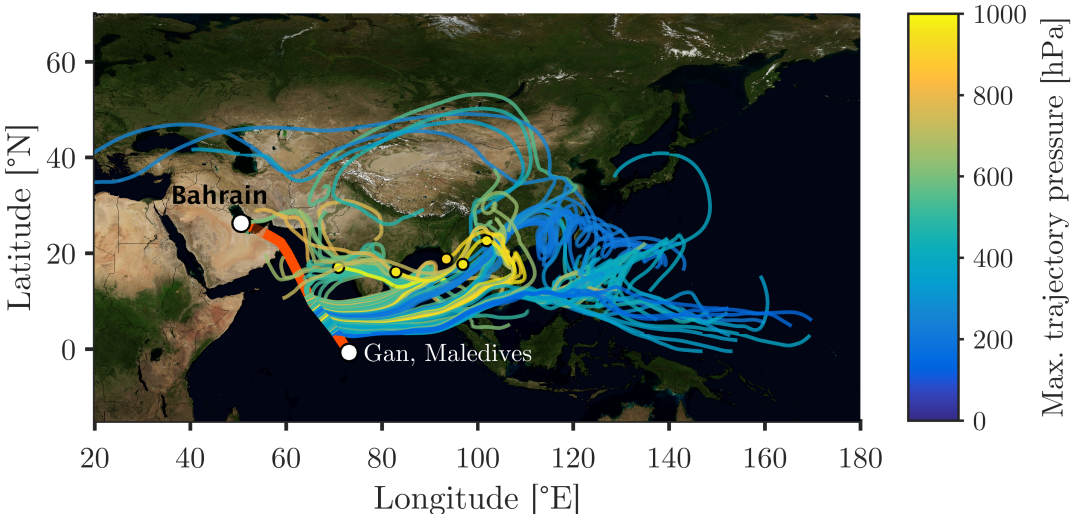

Figure 3.21.: Same as Figure 3.20, but for the time period between 10:36 and 12:00 UTC (segment III in Figure 3.19). Satellite image courtesy of NASA's Earth Observing System (EOS).

The mean/maximum pressure level of the trajectories calculated for this segment is 316 hPa and 487 hPa, respectively, on average. Only 6 % of the trajectories indicate that air masses had contact with the planetary boundary layer within the last 12days. These air masses originated from central India and Myanmar and left the boundary layer on average 8.2 (±1.1) days ago (mean ± standard deviation). The other trajectories, which constitute the great majority, end at pressure levels of on average 395 (±169) hPa 12 days before the flight. Unfortunately, it is not discernible in Figure 3.21 that about 35 % of them end over the Arabian Sea (mean position at 65° E, 15° N) after having made a larger turnaround over the Gulf of Bengal. The remaining 65 % are not affected by this change in direction and mostly end over the remote Pacific Ocean (mean position: ∼125° E, 15° N).

3.5. Outlook: The new PTRMS-CARIBIC

Since 2005, a strongly modified version of a commercial PTR-MS instrument (Ionicon, Innsbruck, Austria) has been regularly deployed onboard the CARIBIC passenger aircraft (see Section 1.3.1) for VOC measurements with high time resolution (Sprung and Zahn, 2010). In contrast to the commercial version, it is e.g. equipped with a more light-weight backing pump, a 24–28 V DC power supply system and a LabVIEW-based software (National Instruments, Austin, Texas), controlling all

instrumental components and thus, enabling an unattended deployment (for details see Sprung and Zahn, 2003 and 2005; Zahn et al., 2013). However, it soon turned out that only ∼2–3 VOCs (acetone, acetonitrile and to some extend methanol) can be readily measured with this device in the UTLS. Nevertheless, instrumental changes to fix this problem were hardly possible during regular operation of the container, which had just started then. This is partially due to certification issues, the short time periods between subsequent flight series and also due to the complexity of the control software, which made any adaption difficult and lengthy.

Therefore, in 2012 the construction of a completely new instrument was started, using the PTRMS-HALO described in Section 3.3 of this chapter as standard. As the completion of PTRMS-HALO was not finished before the end of 2014 (see Section 3.3.4), also the construction of the new PTRMS-CARIBIC had been delayed. In 2013, a first prototype was deployed within the framework of the MUSICA aircraft campaign to test the V25-based control unit under airborne conditions (see Section 3.2.1), but it was clear from the very beginning that still a lot of engineering was necessary to adapt the prototype shown in Figure 3.4 to the installation and deployment conditions of the CARIBIC container (e.g. with respect to the rack dimensions and envelope).

Although the final completion of PTRMS-HALO was done by others, the planning thereof was to large extent made in this work and greatly benefitted from the experiences gained during the MUSICA campaign and the subsequent completion and operation of PTRMS-HALO.

During troubleshooting, it e.g. turned out that the compact height of the 19" subracks used in PTRMS-HALO and the prototype of PTRMS-CARIBIC considerably complicated removal and insertion of I/O modules. The exchange of modules was hardly possible without removing the cabling of all modules and disassembling the subrack to a certain extent.

In addition, the space-constrained installation in the subrack led to an overheating of the electronics during deployment onboard aircraft (see Section 3.2.1), as the air could not circulate sufficiently around the modules. Therefore, larger subracks with an additional height of ∼4.5 cm are used in the final version of PTRMS-CARIBIC. The resulting additional space enables sufficient air ventilation for cooling and allows for the easy exchange of all modules including the microcontroller unit.

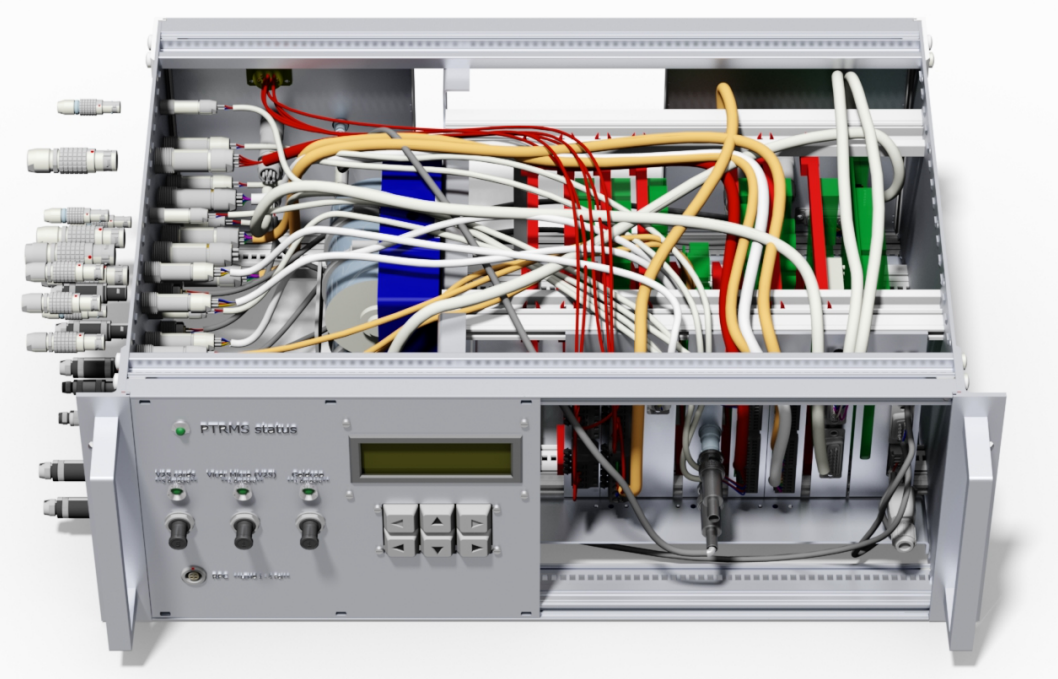

Figure 3.22.: CAD drawing of the modified electronics subrack used in the new PTRMS-CARIBIC. Please note that the picture is not complete. Some parts and accessories are missing to give a better insight, e.g. the missing front panel enables the view at the I/O interface of the V25 control system. The main unit comprising e.g. the V25 microcontroller and the memory card slot is installed on the very right. The individually combined I/O modules are mounted to the left of it. The majority of their inputs and outputs is connected by cable with the sockets on the left exterior side of the subrack. Image courtesy of Simon Heger (KIT).

Further operating difficulties originated from the connectors on the rear side of the electronics subrack. These connectors were difficult to access in the prototype, as the above mounted subrack (the "flowbox") had a greater depth. Therefore, the connectors have been relocated to the left side of the subrack, where they are more easily accessible. In Figure 3.22, a CAD drawing of the resulting new electronics subrack is shown. A drawing of the complete instrument, installed in the instrument rack, is presented in Figure 3.23.

Another deficiency of the prototype was that largely identical sockets and plugs were used directly next to each other. In particular, there was the risk that a sensor cable is accidentally plugged in a power output. To avoid this, only non-interchangeable plugs (LEMO, Ecublens, Switzerland) are used next to each other in the final version of PTRMS-CARIBIC.

Although the subracks of PTRMS-CARIBIC and -HALO are not interchangeable, attention was paid to mainly use the same electrical components in both instruments. As a result, the control software of PTRMS-HALO, which has been extensively elaborated in this work (see Section 3.3.3), also runs on the new PTRMS-CARIBIC. Only the part controlling the satellite-based transmission of preliminary data in HALO had to be adopted to the network communication with the master PC in the CARIBIC container (Brenninkmeijer et al., 2007).

Besides the above-mentioned improvements, the new PTRMS-CARIBIC is the first instrument equipped with a technically more sophisticated version of the unheated permeation device originally presented by Brito and Zahn (2011). While the hitherto used CARIBIC instrument could only be calibrated in the laboratory, this new device enables quasi-continuous in-flight calibration and thus, contributes to a reduction of uncertainties. As will be shown in Chapter 6, these becomes crucial when comparing observations of different years with each or with the results of model simulations in order to assess bottom-up emission estimates of VOCs.

The first airborne deployment of the new device is expected to take place in October 2017. A picture of the instrument, readily installed in the CARIBIC container, is shown in Figure 1.5 (Section 1.3.1).

3.6. Conclusion

Within this work, the development and aeronautical certification of a fully customized, innovative PTRMS system for airborne VOC measurements has been finalized. The resulting two new instruments, PTRMS-HALO and PTRMS-CARIBIC, are by far the most compact and lightweight PTRMS instruments deployed onboard aircraft and can easily compete with larger devices.

The most striking feature of the new development is the customizable control unit and software. For the first time, the entire instrument including the commercial quadrupole mass spectrometer, is controlled by one and the same system. Due to its modular and open design, the new system can be easily adapted to various deployment conditions and upgraded if new instrumental developments become available.

Moreover, the presented results of the first scientific airborne deployment demonstrate that the new device is fully capable of the envisaged VOC measurements in the upper

Figure 3.23.: CAD drawing of the new PTRMS-CARIBIC installed in the instrument rack. Please note that the picture is not complete. Some parts and accessories are missing to give a better insight. In contrast to the hitherto used PTRMS, the new device saves so much space and weight that a further instrument can be installed in the rack. Image courtesy of Simon Heger (KIT).

troposphere and lower stratosphere. Due to its enhanced sensitivity and reduced detection limits, more species can be detected than has hitherto been the case. The instrument also turned out to be highly reliable. PTRMS-HALO was one of the few instruments within the payload of OMO, that delivered data for all mission flights in consistently high quality. The promising results will be objective of a separate paper, currently in preparation.

Besides further missions onboard HALO, the new system will soon replace the currently deployed PTRMS onboard the CARIBIC passenger aircraft. Combined with the high spatial coverage and long-term operation of CARIBIC, the enlarged set of detectable species will significantly contribute to a better understanding of the composition and processes of the UTLS.

4. Instrumental characterization of PTRMS-HALO

Instrumental performance is commonly assessed in terms of precision, accuracy, sensitivity and limit of detection and determining these characteristics is not only important for comparison purposes. Although many scientists refrain from publishing these parameters along with their data, they are crucial for correct interpretation of the data. However, please note that the characterization presented here has been done under laboratory conditions, which may be not comparable to the conditions during airborne measurements. Nevertheless, such a characterization is of great value, e.g. as a reference for future calibrations. Here, it is used to document the final state of the instrument after its long-term development and to assess it by comparing the results with the ones of former development stages of PTRMS-HALO as well as others instruments.

4.1. Reagent ion signals

Typical count rates of reagent ions as observed in November 2016 are summarized in Table 4.1. To prolong the lifetime of the detector (e.g. Taipale et al., 2008) and because of possible saturation effects observed at high count rates (Ammann et al., 2004), the primary ion signal (H_3O^+, $m/z = 19$) is typically obtained from the count rates of its ^{18}O-isotope on $m/z = 21$ multiplied by a factor of 500 reflecting the isotope ratio. This factor is commonly used in the PTR-MS literature, but there are a few studies, which also consider less abundant combinations of isotopes, including hydrogen. Using the on-line isotope pattern calculator of Junhua (2001), Taipale et al. (2008) derived a factor of 487. However, as long as a factor is consistently applied to all measurements including calibrations, it does not matter which value is used.

m/z	Reagent ion	Mean count rate [cps]	Ratio to H_3O^+ [%]	Comments
19	H_3O^+	1.6×10^7	100.0	calculated value
21	$H_3{}^{18}O^+$	3.1×10^5	0.2	used to determine H_3O^+
25		12.6	0.0	detector noise, photons
30	NO^+	3.0×10^4	0.2	parasitic reagent ion
32	O_2^+	4.6×10^5	2.9	parasitic reagent ion
37	$H_3O^+(H_2O)$	2.6×10^5	1.7	1st water cluster

Table 4.1.: Typical count rates of reagent ions affecting the performance of the instrument. Shown are mean values as observed in November 2016 and their percentages relative to the primary ion signal.

The signal at $m/z = 25$ is used as an indicator of 'pure' detector noise, as no compound or any fragment ion has been reported at that mass (e.g. Steinbacher et al., 2004; Custer and Schade, 2007; Amann et al., 2010). The background signals of other masses typically comprise of the detector noise and of ions originating from impurities inside the mass spectrometer, but it is impossible to separate the individual contributions.

Energetic photons, which are produced in the glow discharge ion source, are held responsible for the detector noise (e.g. Mikoviny et al., 2010; Kalogridis et al., 2014) and it is therefore reasonable to assume that the noise is also present on other masses. However, any avoidable noise on masses, which are assigned to compounds of interest, is disadvantageous, as a high noise level impedes the distinction of a weak compound signal from the background. As such, the noise determines the detection limit, i.e. a lower noise level enables the detection of lower VOC concentrations. The transmission of the photons into the detector region strongly depends on the geometry of the ion source and drift tube and can be e.g. reduced by tilting the drift tube (Brito, 2011). The detector noise observed here for the PTRMS-HALO is relatively high compared to other devices (e.g. Amann et al., 2010). Therefore, further counteractions should be considered in the future (e.g. a different bending of the ion source).

The observed NO^+ and O_2^+ ions are generated in the ISDR by charge transfer from H_2O^+ ions to O_2 and NO molecules originating from the DT or, if they reach the discharge region, by electron ionization in the source. As both have lower ionization energies than H_2O, they are unable to undergo charge-transfer reactions with H_2O in the ISDR and will be retained within the PTR-MS (Lindinger et al.,1998). However,

they can undergo unwanted reactions with many analyte molecules, leading to a potential underestimation of their VMRs and interferences on masses affected by the product ions of NO^+- and O_2^+-reactions (e.g. Knighton et al., 2009). Therefore, it is common practice to tune the parameters of the ion source in such a way that the contribution of NO^+- and O_2^+ are negligible. It has been recommended elsewhere to keep the O_2^+/H_3O^+-ratio below 3 % (ACTRIS, 2014), which the instrument complies with.

In the drift tube, the presence of water vapor from the ion source or the analyte air leads to the formation of water dimers $H_3O^+(H_2O)$, which have a high proton affinity (808 ± 6 kJ mol^{-1}; Goebbert and Wentold, 2004) and can undergo other reactions than proton transfer (e.g. ligand switching). Furthermore, the sensitivity of those compounds that do not react with $H_3O^+(H_2O)$ potentially decreases when more primary ions are tied up in the formation of the less reactive water ion clusters (Warneke et al., 2001; Ellis and Mayhew, 2014). Effects on the determination of concentrations are expected whenever the abundance of water dimers varies greatly between sampling and calibration.

Please note, that the percentages of reagent ions relative to H_3O^+ shown in Table 4.1 are not transmission-corrected. As will be shown in Section 4.5, H_3O^+ ions are less efficiently transmitted through the quadrupole than O_2^+, NO^+ and $H_3O^+(H_2O)$ ions. Consequently, the abundance of these ions in the DT compared to H_3O^+ is actually lower than specified.

4.2. Sensitivity

Determination of the instrumental sensitivity is essential for accurate measurements of VMRs, as it is used to convert measured ion count rates into VMRs. The proper definition of sensitivity is that of an instrumental response measured per amount of VOC molecules in the analyzed sample air (Busch, 2002).

As shown in Section 2.2.4, a high sensitivity improves the precision of the measurements. Consequently, a specific precision can be obtained in a shorter time interval, which improves the temporal resolution. In addition, the signal-to-noise ratio increases with sensitivity (see Equation 2.29), which means that signals of lower VMRs can be distinguished from the background noise and thus, be detected (see Section 4.4).

Both effects are particularly useful for airborne measurements in the upper troposphere and lower stratosphere, where VMRs of VOCs are in the ppt-range and fast measurements are necessary to resolve the high spatial variation, because of the high speed of aircraft.

4.2.1. Calibration method

For the determination of the sensitivity, calibration against appropriate gas standards continues to be the method of choice, although it relies on the temporal stability of the gas standard and the instrument's sensitivity (de Gouw et al., 2003b; Ammann et al., 2004; Ellis and Mayhew, 2014).

In this study, a gas standard containing 13 VOCs in known concentrations (Apel Riemer Environmental Inc., Denver, Colorado, USA; stated accuracy: ±5 % per compound) was dynamically diluted in synthetic air (Alphagas; AirLiquide, Paris, France) to VMRs between 0.5 and 30 ppb per compound. In Figure 4.1, the corresponding set-up is shown.

The gas standard and the synthetic air are connected with the inputs of the mass flow controllers MFC1 and MFC2, respectively. The regulated gas flows are then mixing at the subsequent t-piece, which is connected to the gas sample inlet of the "flowbox" of PTRMS-HALO. To obtain an approximate pressure of 950 hPa in the sample line, the flow through the bypass was manually adjusted by alternating the setpoint of MFC3 until a steady-state was reached. All tubes used in the set-up were made of PFA (Perfluoroalkoxy alkane). In principle, the same set-up was also used during the OMO campaign, but with much longer tubing between the external MFCs (Bronkhorst, Ruurlo, Netherlands) and gas bottles, as the latter had to be positioned outside of the aircraft.

The VMRs of the compound inside the diluted VOC mixture are defined by the flows through the mass flow controllers MFC1 and MFC2. The above-mentioned range of 0.5–30 ppb was chosen according to typical VMRs of VOCs during actual measurements (Ellis and Mayhew, 2014), i.e. in the free troposphere. For the exact composition of the gas standard please refer to Table 4.2.

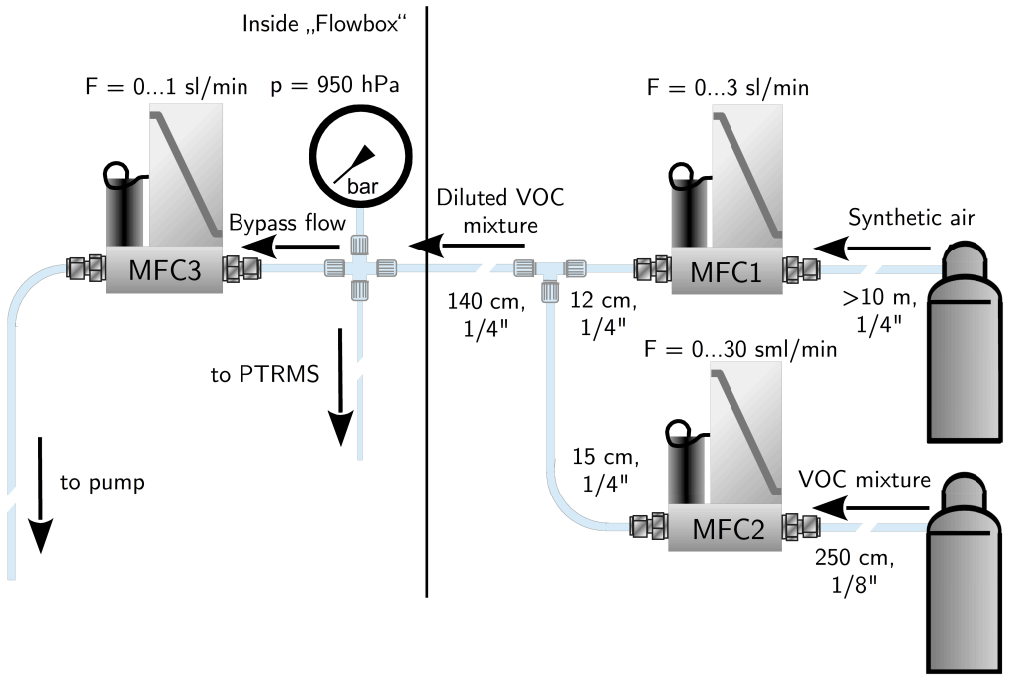

Figure 4.1.: Simplified diagram of the calibration set-up consisting of two external mass flow controllers (MFC) regulating the flow of synthetic air and the gas standard, respectively. The outputs of the MFCs are connected to the sample inlet of the flowbox via a t-piece and PFA tubing.

For each chosen mixing ratio, the diluted gas standard was measured sufficiently long enough to obtain stable count rates (see Figure 4.2a). The means of these (stable) count rates for each dilution step were plotted over the respective VMRs and linearly fitted (see Figure 4.2b). The slope of the resulting line represents the absolute sensitivity.

Here, the Williamson-York fit algorithm (York, 1966; Williamson, 1968) was applied as recommended by Cantrell (2008). In contrast to the standard least-squares fit, it considers the uncertainties in x- and y-direction and, hence, leads to more reliable results. Please note, that only the (equally distributed) statistical uncertainties of the dilution process and count rates should be considered in the linear fit, as a deviation of the VMRs in the gas standard leads to a shift of all calculated VMRs into the same direction. To estimate the uncertainty for this case, the linear fit was repeated using minimal and maximum possible VMRs (worst case analysis).

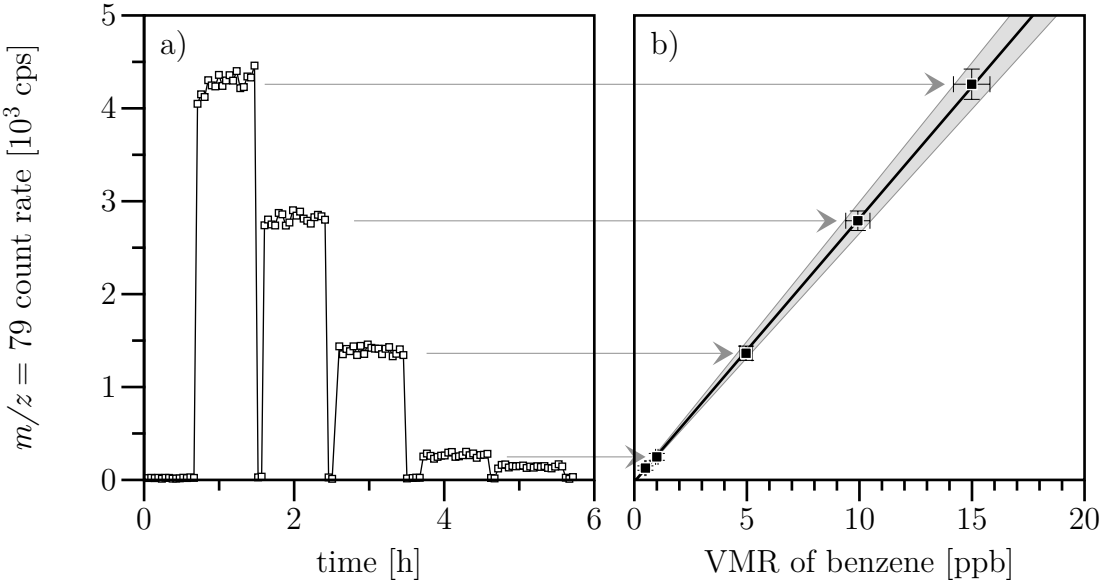

Figure 4.2.: Calibration measurement and subsequent determination of the sensitivity exemplarily shown for benzene: (a) Time series of count rates on $m/z = 79$ (protonated benzene) including hourly changes of the dilution ratio of the calibration gas. Before each dilution ratio change, zero air was measured to determine the instrumental background. For reasons of clarity only every 10th measurement is shown; (b) Plot of means of count rates for each dilution ratio over the corresponding VMRs. The horizontal error bars represent the uncertainty of the VMRs including the accuracy of the gas standard and the uncertainty related to the dilution process. The grey-shaded area indicates the possible range of regression lines as estimated by a worst-case analysis.

4.2.2. Normalized vs. absolute sensitivity

The above-mentioned procedure for determining sensitivities is often be done with normalized count rates resulting in normalized sensitivities. The choice whether to use absolute or normalized sensitivities heavily depends on the objective.

To assess the performance of an instrument, its unaltered response to a known concentration or VMR (commonly expressed in cps ppb^{-1}) is of interest. As shown in Section 2.1 (Equation 2.9), this absolute sensitivity is directly proportional to the primary ion signal $i(H_3O^+)$ and thus, only valid for a particular $i(H_3O^+)$ value.

However, it is well known that the $i(H_3O^+)$ signal can vary considerably with time (Ellis and Mayhew, 2014). Due to this fact, a once determined absolute sensitivity is not suited to accurately derive VMRs from count rates measured over longer time periods.

To avoid this dilemma, sensitivities and count rates are commonly normalized to a particular ion count rate (10^6 cps) and one can assume that these values remain valid even if the absolute primary ion signal changes (Ellis and Mayhew, 2014). Therefore, it is practical to use the normalized sensitivities for calculation of the VMRs.

4.2.3. Results

With the previously described method the current absolute sensitivities of the PTRMS-HALO were quantified for each compound of the calibration gas standard. In Table 4.2, the results are summarized and compared with mean sensitivities found in the literature and the one of the other PTRMS in the group, which was deployed onboard the CARIBIC aircraft between 2005 and 2016. Please note that the ensemble of considered studies may neither be complete nor representative, but on the other hand studies were not selected according to the reported sensitivities. As the latter mainly represent snapshots (or even upper limits) of instrumental sensitivity (e.g. they are based on the maximum primary ion signal instead of the primary ion signal during measurement or the sensitivity for fragment ions was added to the ones of the protonated parent ion), the sensitivities of the PTRMS-HALO and the old PTRMS-CARIBIC presented here are solely based on a single calibration, whereas the reproducibility is discussed in the next section.

The results show that the new PTRMS-HALO is on average twice as sensitive as PTR-MS instruments that have been characterized in the literature. However, it has to be pointed out that publications usually lag behind technical advances, i.e. the majority of currently available studies was conducted with less sensitive instruments.

This may also be related to the increasing deployment of PTR-Time-of-flight (TOF) instruments, which are known for their lower sensitivity compared to quadrupole-based PTR-MS. Warneke et al. (2015) found that their PTR-TOF is on average by a factor of ~ 20 less sensitive than their quadrupole instrument. However, this drawback could be recently compensated by implementing a quadrupole or hexapole ion guide between the drift tube and mass spectrometer (Sulzer et al., 2014; Yuan et al., 2016, Ionicon, 2017).

With such an instrument, Yuan et al. (2016) reached sensitivities similar to the quadrupole instrument described in Warneke et al. (2011, 2015), which represents the current benchmark for PTR-MS (to the author's knowledge). Sulzer et al. (2014)

reported even 5–6 times higher sensitivities for benzene, toluene and xylene taking advantage of the fact that the transmission of a TOF-MS steadily increases with mass whereas the one of a quadrupole passes a maximum at typically 60–100 amu and decreases afterwards (Taipale et al., 2008; Kim et al., 2009; Halbritter, 2011). The general progress in PTR-MS sensitivity over the last two decades and a comparison of the different types of PTR-MS is well illustrated in Yuan et al. (2016).

It should be pointed out that the PTRMS-HALO was not designed to compete with the latest laboratory instruments and the comparison of sensitivities only may be misleading in this case. The development of the PTRMS-HALO aimed at constructing an instrument being perfectly adapted to the limitations and conditions of airborne deployment, but still sensitive enough to reach the intended scientific goals. These criteria were perfectly fulfilled as will be shown later.

The quadrupole- or hexapole-enhanced PTR-TOF-MS are 2-3 times as heavy as the PTRMS-HALO and require about 3 times more space and power (Ionicon, 2017), making a deployment on common airborne platforms questionable.

As the PTR-MS deployed onboard the CARIBIC passenger aircraft is soon to be replaced by a version based on PTRMS-HALO (see Section 3.5), the sensitivities of the two instruments are also compared with in Table 4.2. The values of the CARIBIC-PTR-MS do not exceed the literature averages except for isoprene, which is not relevant in the UTLS due to its short lifetime. The PTRMS-HALO is on average by a factor of 2.7 more sensitive, which clearly justifies the replacement of this instrument by a version based on the high sensitivity PTRMS-HALO. Besides that, there are further reasons for the exchange: The hardware of the CARIBIC instrument is already 13 years old and becomes increasingly susceptible to failures. A problem that already became apparent in the last few years, is a periodical shift of the reference potential of most analog signals. As these signals are used to control the conditions of the drift tube (e.g. pressure) and ion source (water flow into the ion source), the oscillations are also visible in the data and increase the noise levels. Identifying the causes for this behavior would require a complete disassembly of the electronics and extensive troubleshooting. Moreover, for many components spare parts are not available anymore and the companies do not repair them.

It is also noteworthy that the sensitivity of the PTRMS-HALO could be considerably improved during the last 6 years, to large extent within this project by carefully optimizing the drift tube parameters and ion lens voltages. In Figure 4.3, the overall increase in sensitivity between 2010 and 2016 is exemplarily shown for 6 compounds.

Calibration gas standard			Sensitivities [cps ppb^{-1}]		
m/z	Compound	VMR [ppb]	**HALO**†	CARIBIC‡	Literature*
31	Formaldehyde	1040.3	**217**		92
33	Methanol	476.9	**234**	91	124
42	Acetonitrile	514.9	**553**	164	169
45	Acetaldehyde	494.0	**491**	160	260
59	Acetone	483.4	**571**	201	267
63	DMS	488.6	**369**	136	173
69	Isoprene	486.3	**200**	83	98
71	MVK	450.1	**521**		229
73	MEK	512.1	**521**		308
79	Benzene	494.6	**341**	123	158
93	Toluene	491.0	**362**	133	186
107	p-Xylene	478.2	**368**	135	200
137	α-Pinene	494.1	**117**		79

Table 4.2.: Composition of the calibration gas standard used in this study (left) and compilation of compound-specific sensitivities for different instruments (right). The sensitivities of the PTRMS-HALO (bold) as derived within this study are compared with the ones of the group's PTR-MS deployed onboard the CARIBIC aircraft between 2005 and 2016 and means of sensitivities found in the literature.

† Sensitivities taken from calibration on 20 November 2016.
‡ Sensitivities derived from calibration on 25 September 2015. Please note that a different gas standard containing less compounds was used. Due to instrumental modifications, the given sensitivities are not representative for the whole operation period of the CARIBIC-PTR-MS.
* Averages based on 16 randomly selected studies providing instrumental sensitivities, namely: Sprung et al. (2001), de Gouw et al. (2003b), Karl et al. (2009), Jordan et al. (2009a), Vlasenko et al. (2009), Graus et al. (2010), Inomata et al. (2010), Warneke et al. (2011), Fares et al. (2012), Beauchamp et al. (2013), Yang et al. (2013), Karl et al. (2013), Müller et al. (2014), Jardine et al. (2015), Shaw et al. (2015), and Yuan et al. (2016). Normalized sensitivities were converted into cps ppb^{-1} by multiplication with the given mean primary ion signal.

This restriction is mainly caused by the fact that previous studies did not provide sensitivities for all compounds. The first sensitivities of the PTRMS-HALO were reported by Brito (2011), who used an ion funnel enhanced drift tube to increase ion transmission and, thus, sensitivity. The lowest sensitivities were observed during the UBWOS campaign in 2012 (Geiger, 2015), with values not only below the literatures averages, but also below the sensitivity of the CARIBIC instrument (see Table 4.2). The removal of the ion funnel may have contributed to the strong decrease, but since Brito (2011) attributed only a 30 % sensitivity boost to the ion funnel, it can be assumed that other circumstances led to the poor performance. In 2014, the instrument was taken over by the author and the sensitivity could be subsequently improved.

Before the OMO-Asia campaign, the orifice in the exit plate of the drift tube (0.9 mm ⌀) was replaced by a larger one (1.2 mm ⌀) to enhance ion transmission into the quadrupole. As a result, the sensitivities obtained with the ion funnel (Brito, 2011) could be reproduced without it. The recent boost in sensitivity between 2015 and 2016 could be partially archived by further fine-tuning of the instrument settings, but may be also due to more favorable measurement conditions in the laboratory compared to the field (e.g. in the laboratory instruments can be operated continuously and calibrations can be performed after much longer running-up times). Differences in the calibration procedure might have also contributed to the differences.

The achievement of this PhD project becomes particularly clear when comparing the results of this study with the sensitivities of the instrument during UBWOS, when the instrument was fielded for the first time. The sensitivity could be increased on average by a factor of 4 dependent on species. For toluene (not shown in Figure 4.3) the detection sensitivity is 5 times higher than during UBWOS, whereas for acetone an increase by a factor of 3.3 could be achieved. In absolute terms, the sensitivity could be enhanced from values well below average to outstanding ones, which can compete with other PTR-MS instruments deployed onboard aircraft. Due to the work of all involved, the lengthy and challenging development could be turned into a very successful one. The new level of sensitivity offers new opportunities, e.g. more sophisticated measurements, and thus, ensures the ability to compete with the top of international science.

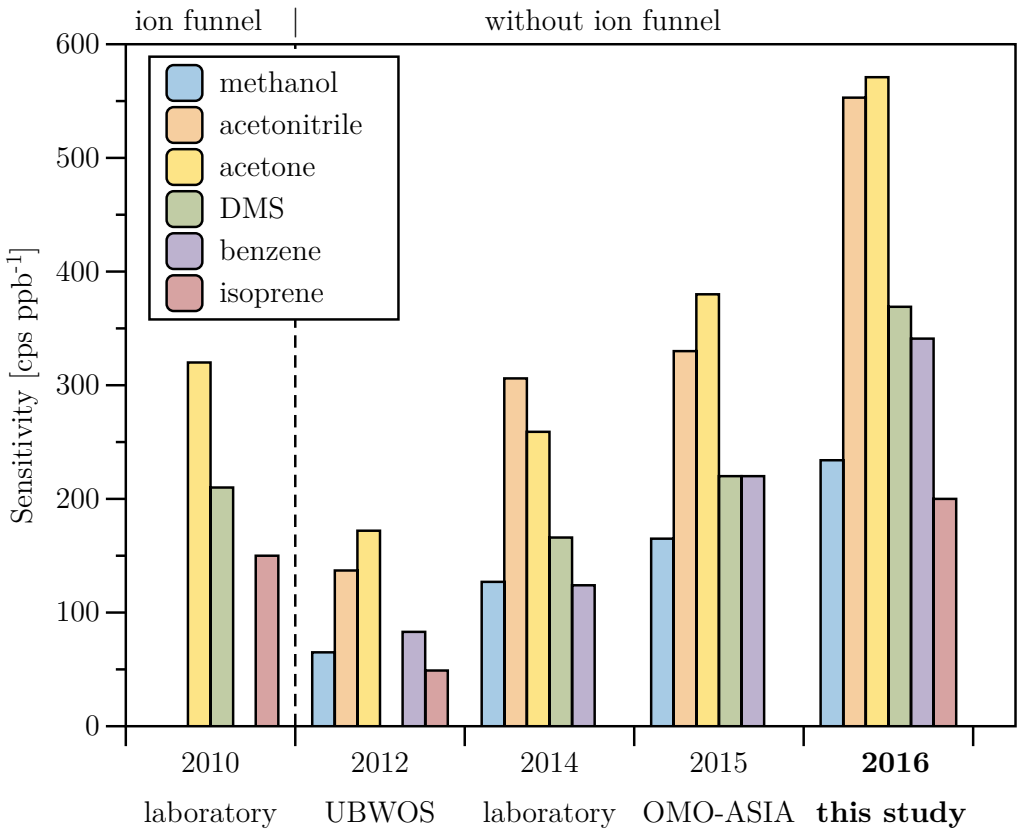

Figure 4.3.: Absolute sensitivity of the PTRMS-HALO for methanol, acetonitrile, acetone, DMS, benzene and isoprene measured during different development phases of the instrument. The sensitivities in 2010, 2012 and 2015 are taken from Brito (2011), Geiger (2015) and Safadi (PhD thesis in preparation). The ion funnel enhanced drift tube was removed between 2010 and 2012 (dashed vertical line). Before the laboratory measurement in December 2014, the instrument was taken over by the author.

4.3. Reproducibility

The accuracy of measurements strongly relies on the reproducibility of calibration results. To achieve a high reproducibility, it is essential to know which systematic errors affect calibration and which are negligible. This question also emerged when defining the calibration procedure needed for instrumental characterization. Here, the discussion is limited to initial observations, as the focus of this study and chapter lies on the characterization of the instrument. More sophisticated experiments, which are out of the scope of this study, are required to fully identify systematic errors and to rule out misinterpretations of the observations. However, it is believed that the discussion, although not being conclusive, can provide valuable suggestions for further investigations and raise the awareness for potential errors during calibration.

4.3.1. The choice of flow rates

As shown in Section 4.2.1, the calibrations within this study are based on dynamic dilution of the gas standard. As different combinations of the flow rates for the calibration gas and zero air lead to the same dilution mixing ratio, at the beginning the question was raised whether the choice of flow rates has an influence on the calibration result. Therefore, the first calibrations were done with different flow rates: The first one with low flow rates of zero air (197 sml min^{-1}) and calibration gas (0.9–6.2 sml min^{-1}) and the second one with maximal possible flows (967 sml min^{-1} and 1.9–30 sml min^{-1}, respectively).

In Figure 4.4, the results of this experiment are exemplarily shown for acetone and methyl ethyl ketone, but the picture is similar for all compounds (see Table 4.3). The observed count rates increased with the analyte flow to the instrument and the increase was larger for high VMRs, leading to apparently higher sensitivities at first sight.

Compound	Sensitivity [cps ppb^{-1}] low flow	high flow	Increase [%]
Formaldehyde	75 ± 2	175 ± 8	136
Methanol	119 ± 21	120 ± 5	1
Acetonitrile	355 ± 20	488 ± 1	37
Acetaldehyde	405 ± 2	456 ± 4	12
Acetone	438 ± 7	529 ± 4	19
Dimethyl Sulfide	313 ± 2	345 ± 1	10
Isoprene	166 ± 1	182 ± 1	9
Methyl Vinyl Ketone	361 ± 2	460 ± 6	24
Methyl Ethyl Ketone	386 ± 2	469 ± 3	24
Benzene	283 ± 2	313 ± 1	11
Toluene	315 ± 14	333 ± 2	6
p-Xylene	282 ± 4	331 ± 3	16
α-Pinene	92 ± 1	103 ± 0	12

Table 4.3.: Derived Sensitivities (standard deviation in parentheses) from two preliminary calibrations on 11 November 2016, and their relative differences are given. The former was conducted with inlet flow rates of 198–278 sml min^{-1} ("low flow") and the latter with ones of 967–997 sml min^{-1} ("high flow").

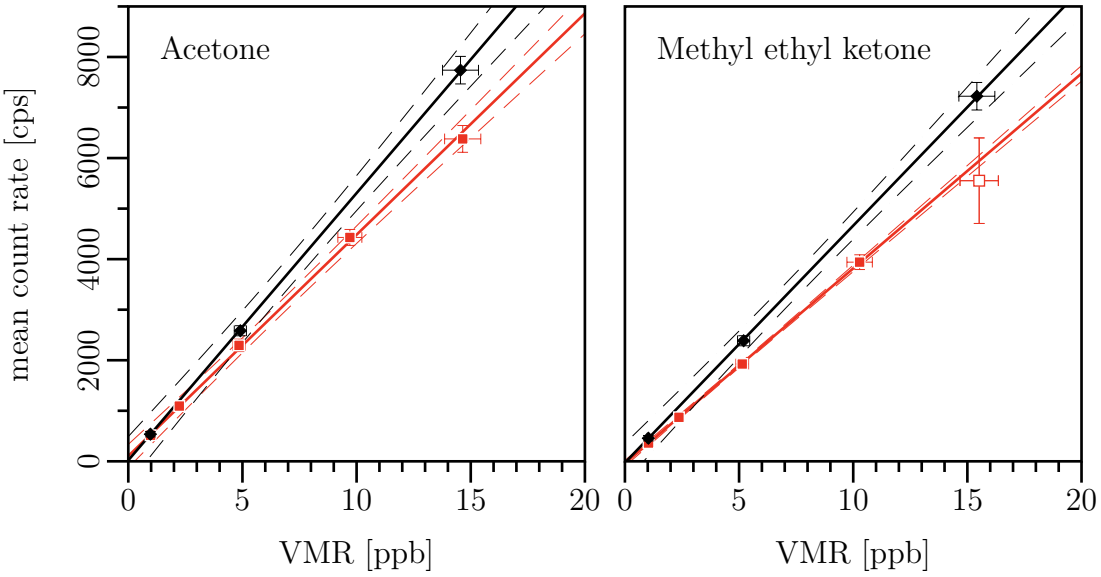

Figure 4.4.: Calibration scatter plots for acetone (left) and methyl ethyl ketone (right) and two different inlet flow regimes: (198 – 278) sml min^{-1} (red squares) and (969 – 997) sml min^{-1} (black diamonds). The horizontal error bars represent the uncertainty of the calculated VMRs including the accuracy of the gas standard and the uncertainty related to the dilution process. The vertical error bars represent the 95 % confidence interval of the count rates observed during each dilution step. The dashed lines indicate the 95 % confidence interval of the Williamson-York-fit (solid lines). The open red square labeled measurement was discarded from the fit as the observed count rates were not in steady state.

The strongest increases were observed for formaldehyde (136 %) and acetonitrile (28 %), whereas for methanol, the count rates were evenly shifted to higher values at the higher flow rate, resulting in a very similar slope of the regression line.

As a dependence of the instruments sensitivity on the inlet flow rate is unlikely (e.g. Hayward et al., 2002), sampling line losses due to surface-VOC interactions are more plausible. Physical adsorption on surfaces or dissolution of soluble compounds in condensed water are an issue in trace gas analytics (e.g. Neuman et al., 1999). A higher flow rate decreases the time of interaction with the surfaces and, thus, wall losses. In turn, more molecules per time reach the instrument resulting in higher count rates, whereas the sensitivity stays the same. For this reason, the higher flow rate regime was selected for all subsequent measurements. However, further investigations (e.g. of a possible temperature and pressure dependence or interferences from previous measurements), which are out of the scope of this study, are necessary to review this effect. In particular, the critical surfaces in the used set-up need to be identified and

subsequently minimized.

In other studies, PFA tubing did not lead to significant wall losses and memory effects (Karl et al., 2003; de Gouw and Warneke, 2007; Schnitzhofer et al., 2009; Hu et al., 2011). Kajos et al. (2015) found apparently larger sensitivities when adjusting the flows with needle valves instead of mass flow controllers. The stainless steel surfaces of flow controllers are suspected to cause such deviations (de Gouw et al., 2003b; Taipale et al., 2008; Mikoviny et al., 2010).

For this reason, de Gouw et al. (2003b) maintained a constant flow of the calibration gas through the pressure reducer, tubing and flow controller, even when no calibration was performed. During calibration, only the zero air flow rate was varied to change the dilution mixing ratio. With these measures, the authors achieved a very good reproducibility of calibration results, even for problematic compounds.

However, the advantages of continuous purging of the calibration gas line with the expensive gas standard must be carefully weighed against the costs. It might be only justified when calibrations are done regularly and frequently (e.g. during continuous field measurements).

The variation of the zero air flow rate instead of the calibration gas flow rate or both seems reasonable, but unfortunately this could not be realized with the present set-up, as the pressure at the instrument's inlet is not actively controlled. Instead the pressure has to be manually adjusted by balancing the inlet and bypass flow. Any significant change of one of the flow rates could disturb the balance to such an extent that the pressure runs out of the operation range and causes an unwanted shut-down. However, this could be easily changed in future by implementing a function in the software that holds the inlet pressure constant.

4.3.2. The choice of measurement times

The calibration measurements also revealed that the equilibration times, being the time until count rates were in steady state, varied considerably between the compounds and different calibration measurements. In general, the longest equilibration times were found for methanol, but also other compounds showed a similar behavior at high VMRs (> 10 ppb).

The first methyl ethyl ketone measurement of the experiment shown in Figure 4.4 (open red square) had to be discarded, as the count rates were not stable. This

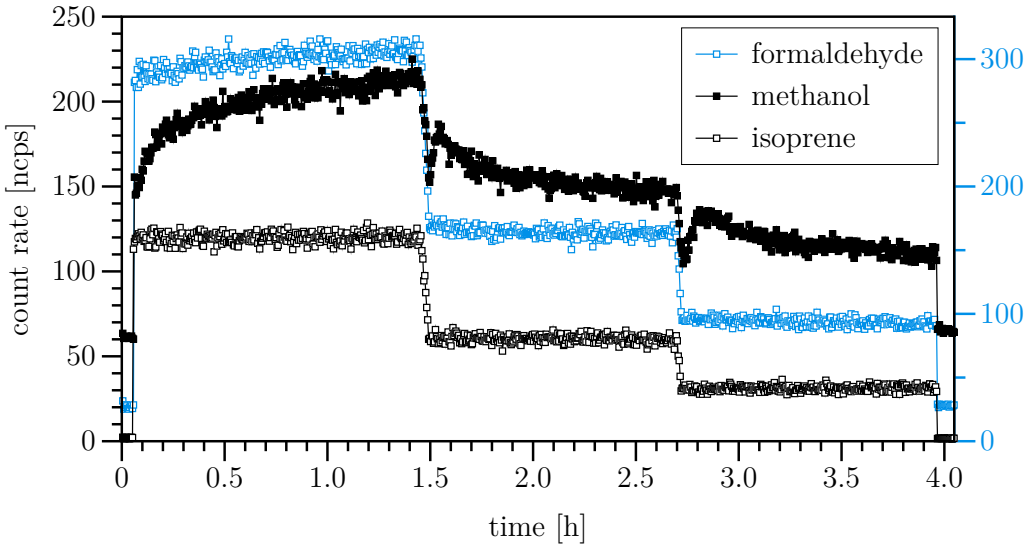

Figure 4.5.: Time series of normalized count rates during calibration (shown here are 3 dilution steps) for formaldehyde (scaled to avoid overlap), methanol and isoprene. For formaldehyde, the scale on the right side) was used.

becomes already evident from the large standard deviation, which rather reflects the range of the count rate as its statistical noise.

In Figure 4.5, a typical temporal evolution of count rates during an extended calibration is shown for formaldehyde, methanol and isoprene. For most compounds of the gas standard (see Table 4.2), count rates were found to be very stable throughout the different dilution steps, as it is exemplarily shown here for isoprene.

Methanol shows a very slow and pronounced transient response for all three dilution steps. As discussed in the previous section, surface effects might be related to this and methanol is known to be particularly affected (de Gouw et al., 2003b). Another cause might be the low humidity of the diluted calibration gas. Apel et al. (2008) stated that methanol is not efficiently transferred through tubing under dry conditions. This is consistent with the findings of Eerdekens et al. (2009), who observed substantially lower methanol calibration factors for dry conditions. Calibrations using humidified zero air, which will be part of another PhD thesis (by L. Safadi), will help to understand such issues in more detail.

It is also noteworthy that the direction from which the methanol count rates approach the steady state changes after the first step. At the beginning of the second and third step, count rates peak shortly and then converge to lower count rates. This suggests that the sequence of VMRs (from high to low values) might play a role. However, the

same behavior was observed when calibrating in reverse order (Sonderfeld, 2014). For formaldehyde, only the count rates of the first dilution step ($\sim$ 20 ppb) show a trend, but in contrast to the methanol signal, the drift is more linear and less pronounced. It can be assumed that such a drift could be not derived from significantly shorter measurements.

Although these observations might be not transferable to other calibration set-ups and instruments and further investigations are essential, it is still conspicuous and should be pointed out that such calibration time series are rarely shown in the literature. Instead, only the mean count rates of dilution steps are frequently presented and plotted versus the respective VMRs to demonstrate the linearity of the instrument's response. However, without the disclose of standard deviations for the mean count rates and the measurement times per dilution step, it is hardly possible to assess the quality of the calibration from these plots. The very good linearity and high correlation coefficient may discard from the fact that the measurements can still be affected by systematic errors.

Kajos et al. (2015) recommended to adjust the duration of each dilution step to the compound with the longest equilibration time. However, as the flow rates were manually adjusted in this set-up, significantly longer calibration measurements as the ones shown in Figure 4.5 were not feasible. In consequence, the number of dilution steps was reduced to 3, as accuracy was considered more important than quantity.

4.3.3. Results of recurring calibrations

As mentioned earlier, the use of discontinuous calibration methods relies strongly on the assumption that the instrumental sensitivity does not change between calibrations (Ammann et al. 2004). However, there is no agreement about the frequency of calibrations. For continuous field measurements, reported calibration intervals vary between hours (Custer and Schade, 2007; Brito, 2011; Fares et al., 2012) and weeks (Jordan et al., 2009b; Kontkanen et al., 2016; Rantala et al., 2016; Hellen et al., 2017). There are also studies, which rely on a few calibrations and the argument that other PTR-MS instruments were reported to be very stable (e.g. Sarkar et al., 2016).

Besides this huge discrepancy, it is conspicuous that the variation of derived sensitivities and the handling of data between the calibrations is rarely discussed in the literature. The studies of de Gouw et al. (2003), Custer and Schade (2007) and Taipale et al. (2008) constitute exemplary exceptions in this regard.

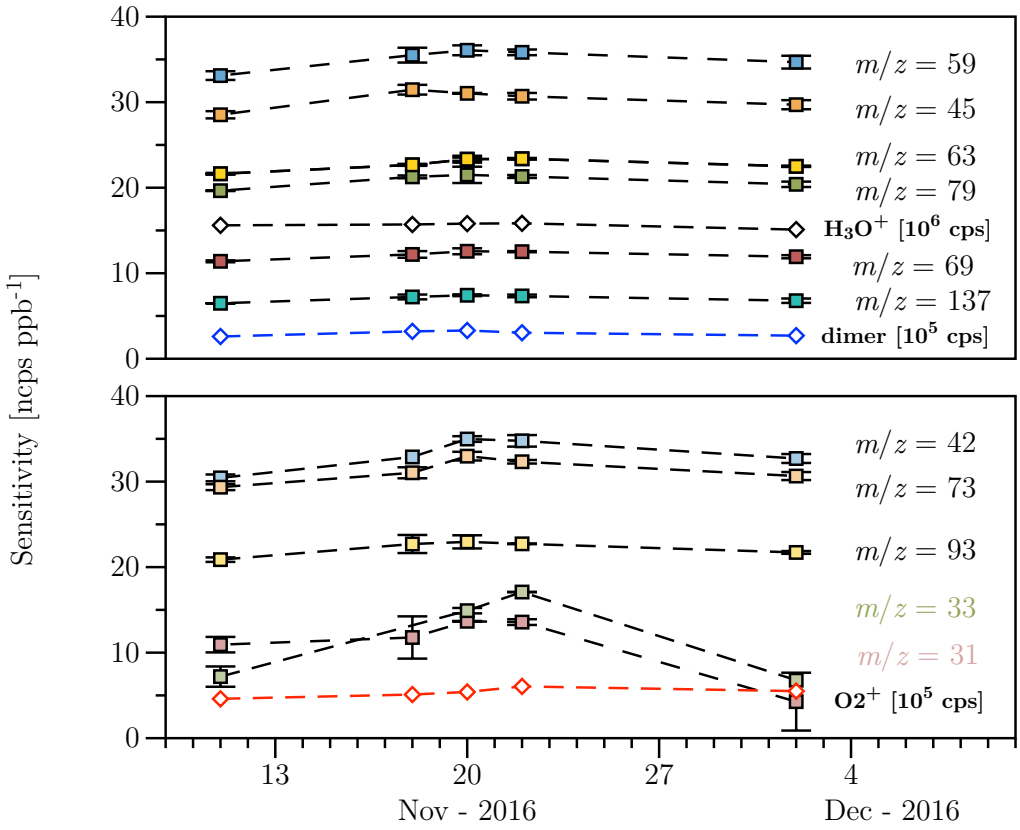

Figure 4.6.: Normalized sensitivities derived from 5 calibrations in November – December 2016. The sole purpose of the dashed lines is to show which data belong together. The data of methyl vinyl ketone ($m/z = 71$) and *p*-Xylene ($m/z = 107$) are not displayed, as they are almost identical to the ones of methyl ethyl ketone ($m/z = 73$) and toluene ($m/z = 93$), respectively. No data is available for methanol on 18 November, as the count rates did not reach equilibrium within the dilution steps. Error bars indicate the 95 % confidence interval of the Williamson-York-fit results. The open diamonds show the mean count rates of H_3O^+ (black), the dimer $(H_2O)H_3O^+$ (blue) and O_2^+ (red) during the respective calibrations.

To assess the reproducibility, the instrument was calibrated 5 times within one month at intervals of 2 – 10 days. However, in contrast to the above-mentioned studies, the instrument did not run continuously and was even transported by car between the first two calibrations, which may have negatively influenced the instrumental stability.

The results of the recurring calibrations are shown in Figure 4.6. Here, the normalized sensitivity was used to correct for slight performance drifts of the ion source over the reviewed time period. However, the picture for the raw count rates is similar, as the

mean primary ion signal hardly changed.

For most compounds, the calibrations show a good reproducibility with sensitivities varying by 3 – 6 % relative standard deviation (RSD). There is an apparent increase in sensitivity between the first two calibrations and a decrease between the last two calibrations. The sensitivities of methanol ($m/z = 33$) and formaldehyde ($m/z = 31$) follow this general trend, but stand out with much higher differences between the first two (methanol) and the last two calibrations (methanol and formaldehyde). For these compounds, the overall variability is found to be considerably higher with 46 % and 36 % RSD, respectively.

The results of the 3 successive calibrations conducted at 2 day intervals around 20 November 2016 show substantially less variability. Excellent agreement is found for benzene (0.6 % RSD), toluene (0.6 % RSD) and acetone (0.8 % RSD). Methanol and formaldehyde again stand out with 10 % and 8 % RSD. The sensitivities of all other compounds vary by 1 – 3 % RSD from the 4-day average.

The reasons for the higher variability in formaldehyde and methanol sensitivities are difficult to assess retrospectively. The recorded operational parameters provide no indication for instrumental changes, e.g. the primary ion yield, the percentages of other reagent ions and the conditions of the drift tube were stable over the considered time period.

Changes in humidity of the analyte air could be an issue, as the detection sensitivity for formaldehyde (Hansel et al., 1997; de Gouw et al., 2003a; Vlasenko et al., 2010; Warneke et al., 2011) and the transport efficiency of methanol through tubing (Apel et al., 2008; Eerdekens et al., 2009; Hanson et al., 2009) are known to be humidity dependent. However, for all calibration zero air of the same quality was taken from gas cylinders and the percentage of water dimers, a known proxy for ambient water concentration (Ammann et al., 2006), did not change between calibrations.

As the count rates of both compounds were affected by long and varying equilibration times during calibration (see Section 4.3.2), it is only reasonable to suspect that the variance is related to systematic errors during calibration. This assumption is also shared by several studies reporting high variations in methanol and formaldehyde calibration results.

Already Spanel and Smith (1997) reported of problems in obtaining reliable mixture concentrations of methanol due to an unpredictable degree of adsorption on stainless steel surfaces in selected ion flow tube experiments. De Gouw et al. (2003b) observed

erroneously high and strongly varying calibration results for methanol during the first days of a field campaign, which they attributed to impurities in the pressure regulator and/or mass flow controller in the calibration gas line.

Custer and Schade (2007) observed a considerable structure in methanol sensitivities, when performing calibrations every 8 hours over a period of 3 weeks. Despite some abrupt shifts related to changes of the instrumental settings, the overall precision of the methanol sensitivity was estimated to be only 20–30 %.

Hanson et al. (2009) reported that methanol sensitivities for different humidities were not reproducible when using stainless steel fittings in the calibration set-up. Also Sonderfeld (2014) observed large differences in methanol calibrations results. Normalized sensitivities varied between 9.4 and 17.5 ncps ppb^{-1} without showing a clear trend.

Kajos et al. (2015) were the first ones investigating the problem more systematically by comparing a calibration set-up with mass flow controllers to one using stainless steel needle valves to adjust the flow rates. Subsequent calibrations of two PTR-MS revealed that the methanol sensitivities were apparently higher for the set-up consisting of needle valves, which supports the assumption of large wall losses in the mass flow controllers. Furthermore, the subsequent calibrations with the mass flow controller set-up showed on average a higher variability in methanol sensitivities (44 % RSD) compared to the set-up with needle valves (17 % RSD), which substantiates the unpredictability of the wall effects.

Formaldehyde was not measured in the above-mentioned studies, but Wisthaler et al. (2008) found a 40 % difference in calibration factors obtained during two successive days following identical calibration procedures.

Further measurements, which would have gone beyond the scope of this study, are absolutely necessary to clarify the problem of reproducibility for methanol and formaldehyde calibration factors.

Continuous calibration methods, simultaneous measurements with another PTR-MS and measurements with different tubing materials may help to diagnose the problem. In any case, the known reproducibility and the required uncertainty of the measurements have to be taken into account when determining the frequency of calibrations and the usability of collected data. When measuring these compounds in the field, short calibration intervals are necessary.

4.4. Limit of detection

According to Equation 2.24 in Section 2.2.4, the statistical noise can be expressed as

$$\sigma_{\text{blank}} = \sqrt{\frac{\bar{x}_{\text{blank}}}{t_{\text{dwell}}}} \tag{4.1}$$

where $\bar{x}_{\text{blank}}$ is the mean count rate of the background measurement. Substituting Equation 4.1 into 2.31 and using $\bar{x}_{\text{blank}} = \alpha \times \text{VMR}(\bar{x}_{\text{blank}})$ leads to the important relationship

$$\text{VMR}(x_{\text{LOD}}) \propto \; k \sqrt{\frac{\text{VMR}(\bar{x}_{\text{blank}})}{t_{\text{dwell}} \cdot \alpha}}, \tag{4.2}$$

indicating that the LOD can be in generally reduced in three different ways:

- Reduction of the chemical background $\text{VMR}(\bar{x}_{\text{blank}})$
- Extension of the measurement time t_{dwell}
- Enhancement of the instrumental sensitivity α

In the following, the individual options are discussed with regard to their use in PTRMS-HALO.

Minimizing the chemical background

As the LOD is approximately proportional to the square root of the background signal, it is essential to keep the chemical background of the instrument as low as possible. For this reason, the gas inlet system of PTRMS-HALO has been designed so that the sampled air is not exposed to mass flow or pressure controllers, which have some non-passivated surfaces (see flow paths in Figure 3.7 and discussion in Section 4.3.1). In addition, only relatively inert and impermeable tubing and fitting materials (PFA, PEEK, PVDF) have been used. To remove remaining organic residues (e.g. human skin oils) from the surfaces, the entire system was purged several hours with O_3-enriched air (500–1000 ppb) to oxidize contaminants attached at the inner surfaces of the sampling system (cf. Wisthaler et al., 2005; Wisthaler and Weschler, 2010).

The chemical background can be further minimized by continuous pumping. However, for airborne instruments like PTRMS-HALO, this is hardly possible, as aircraft power is only available for a limited time before and after flights. To avoid that contaminants

enter the vacuum system and settle on the surfaces while the instrument is switched off, filling the vacuum system with clean air represents a viable alternative. However, the effect strongly depends on the purity of the air. To improve this, the previous version of gas inlet system has been modified so that air used for venting is passed through the catalytic converter before entering the mass spectrometer. Furthermore the design and the position of the catalytic converter have been changed so that the degradation process of VOCs, which could settle down on the surfaces, is more effective (see Section 3.3.1).

Extending the measurement time

Lower detection limits can always be obtained by enhancing the measurement or dwell time t_{dwell}. As the statistical noise is inversely proportional to the square root of t_{dwell}, the LOD can be ideally reduced by half when increasing the dwell time by a factor of 4. Although this can be easily realized, the considerable drawback of such changes is the lower time resolution of measurements. A decrease of the dwell times for all masses reduces the time resolution by the same factor.

Here, most stationary ground-based measurements benefit from the rather slow alterations of ambient VOC concentrations. However, there are a few exceptions: For the determination of surface–atmosphere fluxes, sampling frequencies in the order of 5–20 Hz are necessary to resolve all eddies contributing to the vertical transport (Lenschow, 1995; Langford et al., 2009).

Similar time resolutions are required for measurements onboard driving vehicles (Roger et al., 2006; Zavala et al., 2006; Geiger, 2015). Roger et al. (2006) used dwell times of 0.1 s, resulting in a temporal resolution of ∼1 Hz and detection limits between 1 ppb (toluene) and 5 ppb (methanol). Still, these detection limits were more than sufficient to detect the intercepted diluted exhaust plumes of cars driving in front of the mobile laboratory.

However, the challenge of airborne measurements in the upper troposphere lies in the coincidence of low VMRs (from a few hundred ppt to less than 10 ppt) and the high speed of aircraft (50–260 m s^{-1}). The latter directly converts the time resolution of the device into the spatial resolution of the measurements.

As the HALO and CARIBIC aircraft are both jet aircraft with normal cruising speeds of 236 and 251 m s^{-1}, a high sampling frequency is particularly crucial. Therefore,

a general extension of the dwell times to achieve lower detection limits is not an option for instruments like PTRMS-HALO, as it significantly deteriorates the spatial resolution of the measurements.

Maximizing the sensitivity

As shown in Section 4.2, the sensitivity of PTRMS-HALO could be significantly improved within the last years due to modifications of the ion source design, orifice diameters and optimization of electrode voltages. According to Equation 4.2, the on average achieved fourfold increase of the sensitivity reduced the LOD by a factor of 2, from a purely mathematical point of view. If this is indeed the case, this is a substantial step forward towards expanding the number of species detectable in the upper troposphere and lower stratosphere.

Looking at all above-mentioned options, it also becomes clear that the only possibility to further improve the LOD, if the chemical background is reduced to its minimum, is to find new measures to enhance the instrumental sensitivity.

4.4.1. Measurement method

According to the definition of the IUPAC, the LOD can be experimentally obtained by measuring the background signal (see Equation 2.31). However, a few considerations are necessary:

To determine the LOD for a specific measurement, sample air must be fed through the catalytic converter of the gas inlet system for the same measurement times t_{dwell} per mass as for sample measurement. However, as the objective of this chapter is not to determine the LOD of individual measurements, but to characterize the current status of the instrument in a reproducible manner, synthetic air (Alphagas; AirLiquide, Paris, France) was fed through the catalytic converter and t_{dwell} was set to 5 seconds for all masses. Furthermore, it must be decided on the signal-to-noise-ratio k of interest (see Equation 2.31). Although ratios of 2 and 3 are commonly used in the PTR-MS community to determine the LOD, here, the more conservative factor 3 is used, corresponding to a confidence interval of 99.7 (Ellis and Mayhew, 2014).

When determining the LOD, the duration of the considered background measurement may also influence its value, as drifts in the signal increase the LOD.

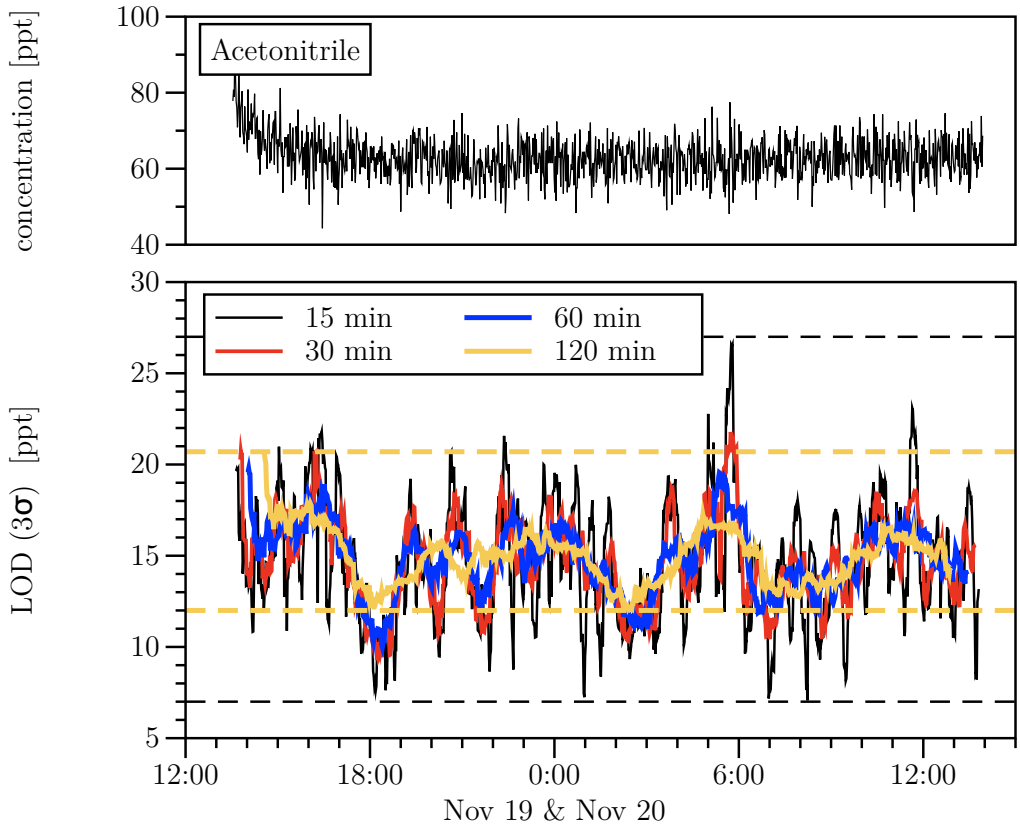

Figure 4.7.: Time series of a one-day acetonitrile background measurement (upper panel) using synthetic air fed through the internal catalytic converter ($t_{\mathrm{dwell}} = 5$ s). In the lower panel, 3 times the moving standard deviation is shown for 4 different window length (15, 30, 60, 120 minutes).

Taipale et al. (2008) chose a "representative period" of 48 successive measurements, corresponding to a duration of 30 minutes.

As the choice seems to be somewhat arbitrary, a one-day measurement was conducted to investigate the variation of the LOD with time and the number of selected measurements. The temporal evolution of the LOD was calculated using a moving standard deviation with window lengths of 12, 24, 48 and 96 subsequent 5s-measurements (corresponding to overall time periods of 15, 30, 60 and 120 minutes, as several compounds were measured in a "duty cycle").

In Figure 4.7, the results are exemplarily shown for acetonitrile. As expected, the overall variability decreases with the number of measurements considered for each LOD. When using only a small number of measurements, but having the choice to select a period within a longer measurement series, it can be tempting to choose one of the periods with lower noise. However, it is evident that such a minimum

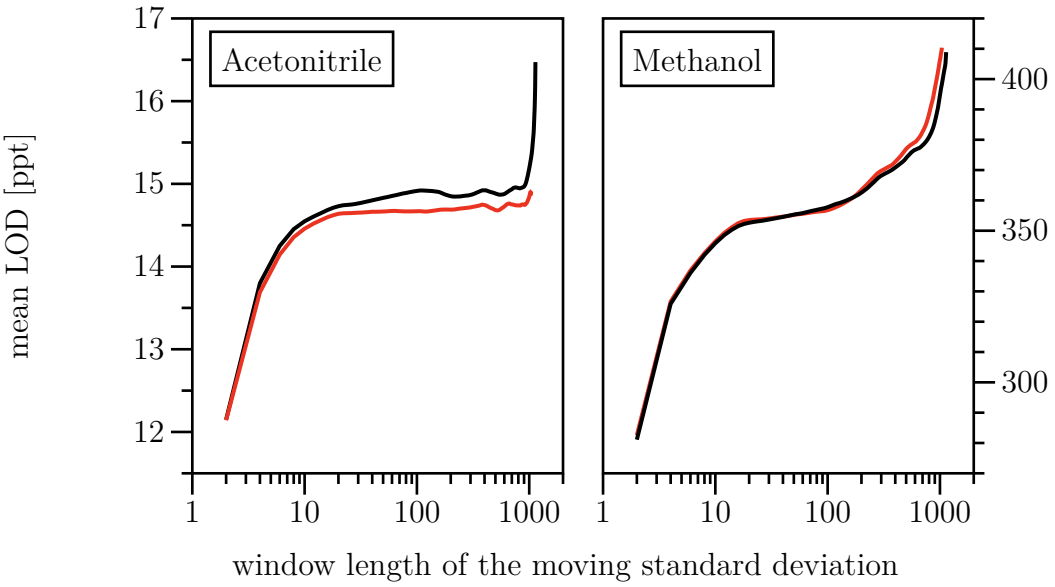

Figure 4.8.: Variation of the mean LOD with the window length of (i.e. the number of adjoined 5s-measurements included in) the moving standard deviation for acetonitrile (left panel) and methanol (right panel). The calculation of the mean LODs are based on a one-day background measurement, including the first two hours (black curves) and without the first two hours (red curves).

LOD is not applicable to most measurements and thus not representative of the overall instrumental performance, in particularly during a field measurement, which typically lasts several hours. The same is true when selecting only the period showing the highest noise, although this would lead to a conservative estimate of the LOD.

Here, the on average obtained LOD seems to be the appropriate parameter to describe the true performance of the instrument over a longer measurement. In contrast to the minimum and maximum LOD, the mean value is also less sensitive to the window length of the moving standard deviation.

In Figure 4.8, the variation of the mean LOD with the window length is exemplarily shown for acetonitrile and methanol. For both compounds, the mean shows a strong increase at small window lengths and reaches a plateau at ∼20 measurements. Changes in the background signal lead to a further increase at larger window lengths.

For acetonitrile, the abrupt increase at very large window lengths is caused by the decline of the background signal during the first two hours, as the analysis without the first two hours shows (red curve). For methanol, the plateau ends earlier at a windows length of ∼100 5s-measurements, which indicates that the background signal

is affected by drifts of the same time scale (∼2 hours). In contrast, too small windows lengths are mainly affected by poor statistics, as the large changes show. Therefore, the window length corresponding to the begin of the plateau (20 measurements) seems to be an adequate choice.

4.4.2. Results

The mean LOD was calculated for each compound based on the moving standard deviation of 20 measurements. In Table 4.4, the results are shown and compared with literature values and typical background concentrations observed in the upper troposphere.

Compound	LOD [ppt] **HALO**	CARIBIC	Literature⋆	UT Background VMRs [ppt]
Formaldehyde	**170**		318	20–230
Methanol	**353**	619	428	200–2000
Acetonitrile	**15**	50	76	100–200
Acetaldehyde	**42**	108	255	60–200
Acetone	**27**	72	85	200–900
DMS	**18**	53	44	< 5
Isoprene	**32**	60	86	< 20
MVK	**14**		47	< 10
MEK	**19**		112	< 15
Benzene	**19**	42	73	< 30
Toluene	**18**	44	97	< 8
p-Xylene	**33**	73	122	< 4
α-Pinene	**48**		218	< 20

Table 4.4.: Mean detection limits of PTRMS-HALO, the hitherto used CARIBC-PTRMS and of other PTR-MS reported on in the literature. All values refer to 5 s dwell time and a S/N ratio of 3.

⋆ Averages based on 14 randomly selected studies providing limits of detection, namely: Warneke and de Gouw et al. (2001), de Gouw et al. (2003), Karl et al. (2009), Taipale et al. (2008), Vlasenko et al. (2009), Graus et al. (2010), Inomata et al. (2010), Sjostedt et al. (2011), Fares et al. (2012), Brilli et al. (2014), Copeland et al. (2014), Müller et al. (2014), Jardine et al. (2015), and Yuan et al. (2016). Dwell times t_{dwell} were extrapolated to 5 seconds using a correction factor of $\sqrt{t_{\mathrm{dwell}}/5\,\mathrm{s}}$, as derived from Poisson counting statistics.

The PTRMS-HALO stands out with detection limits of only a few tens of ppt for most compounds, which is considerably lower than the average of values reported for PTR-MS in the literature. The higher detection limits of PTR-MS described in the literature are not surprising; Most PTR-MS instruments are used for ground-based measurements, where VMRs are at least 1–2 orders of magnitude higher than in the upper troposphere and, thus, the necessity of lower detection limits is not given.

Quantification of the background VMRs in the UTLS is particularly important to derive climatologies. When comparing the detection limits of the PTRMS-HALO to known background VMRs in the upper troposphere, it becomes clear, that for acetonitrile, acetaldehyde, acetone and benzene the atmospheric background can be quantified with high certainty for all seasons and regions. The detection limits for formaldehyde and methanol lie in the range of reported background VMRs. It is therefore worth considering to enhance the dwell times of the latter species, whereas the dwell times of acetonitrile and acetone could be decreased (e.g. to 1 second) without great disadvantages except a larger noise. For the shorter-lived species, detection limits are mainly below the background VMRs. Measurement of these species in the UTLS are rare and the stated background values partly rely on very few measurements.

With the current detection limits for the shorter-lived species, only events of strong convection might be observed in the UTLS. But even if it is not possible to detect the upper tropospheric background of these compounds at all times, the detection in pollution plumes with elevated VMRs provides valuable information about the sources of the pollution. In this regard, toluene might be particularly interesting, as it has a considerably longer atmospheric lifetime ($\sim$ 2 days) compared to the other short-lived compounds in the calibration gas and the same emission sources as the longer-lived benzene ($\sim$ 10 days), namely vehicle exhaust and fuel evaporation (Bravo et al., 2002; Li et al., 2011; Correa et al., 2012). Due to the known emissions ratios, but different atmospheric lifetimes, the ratio of benzene and toluene in photochemically aged pollution plumes can be used to derive the age of air mass (e.g. Roberts et al., 1984; de Gouw et al., 2005; Vlasenko et al., 2009; Warneke et al., 2013).

4.4.3. Interferences on $m/z = 33$

The by far highest detection limit was encountered for methanol (353 ppt). The main reason for this is the high background signal ($\sim$ 3800 cps) at the mass of

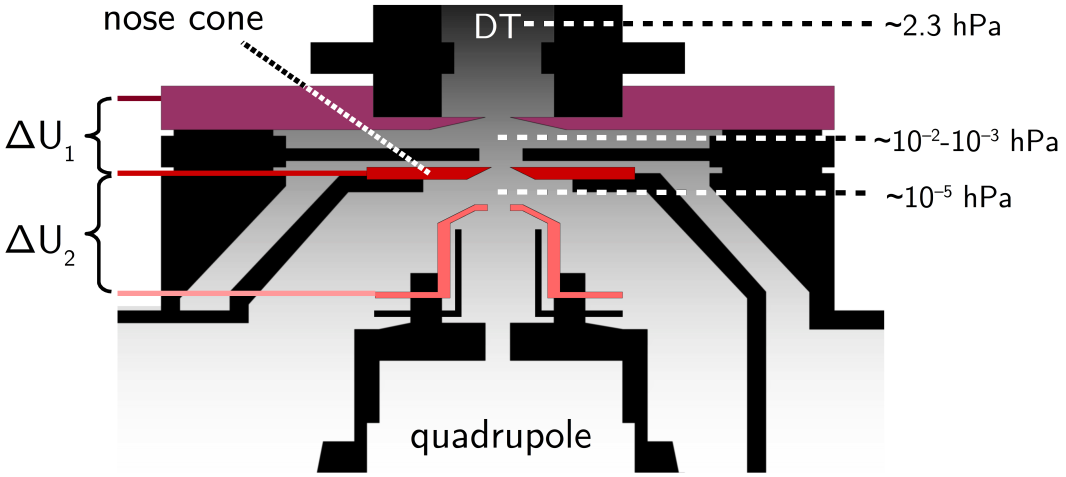

Figure 4.9.: Schematic section through the region between the drift tube (DT) and the entrance of the quadrupole. The electrodes, whose voltages were alternated, are colored differently.

protonated methanol ($m/z = 33$), which has been also observed for other PTR-MS (Ruuskanen, 2009; Misztal et al., 2011). Using a high resolution PTR-TOF, Müller et al. (2014) identified protonated molecular oxygen, HO_2^+, as the main contributor to the background signal on $m/z = 33$. The $^{16}O^{17}O^+$ isotopologue could not be resolved from the HO_2^+ peak, but its contribution to the HO_2^+-signal was estimated to be in the order of 15 %. For PTRMS-HALO, the $^{16}O^{17}O^+$ contribution was calculated to be about 11 % of the background signal based on the $^{16}O^{17}O^+/^{16}O_2^+$-ratio and the observed count rate of $^{16}O_2^+$.

As oxygen has a lower proton affinity than that of water, HO_2^+ can only be formed endothermically. Therefore, the production must take place in one of the extraction regions underneath the drift tube (see Figure 4.9), where the pressure is sequentially reduced from 2.3 hPa to values below 10^{-5} hPa (Müller et al., 2014; Li et al., 2014). In PTR-MS, there are two stages of ion extraction, one directly at the exit of the drift tube and another one at the nose cone.

In order to investigate the effect of HO_2^+ formation in this regions, the electric fields in the two stages were varied, whereas all other fields were left constant. So far, the "standard settings" resulted in a potential difference $\Delta U_1 = 16.5$ V between the drift tube exit and nose cone and $\Delta U_2 = 104$ V between the nose cone and first ion lens. For variation of ΔU_1, the voltages of the nose cone and the quadrupole's reference potential were changed to the same extent. For variation of ΔU_2, only the reference

potential of the quadrupole was changed.

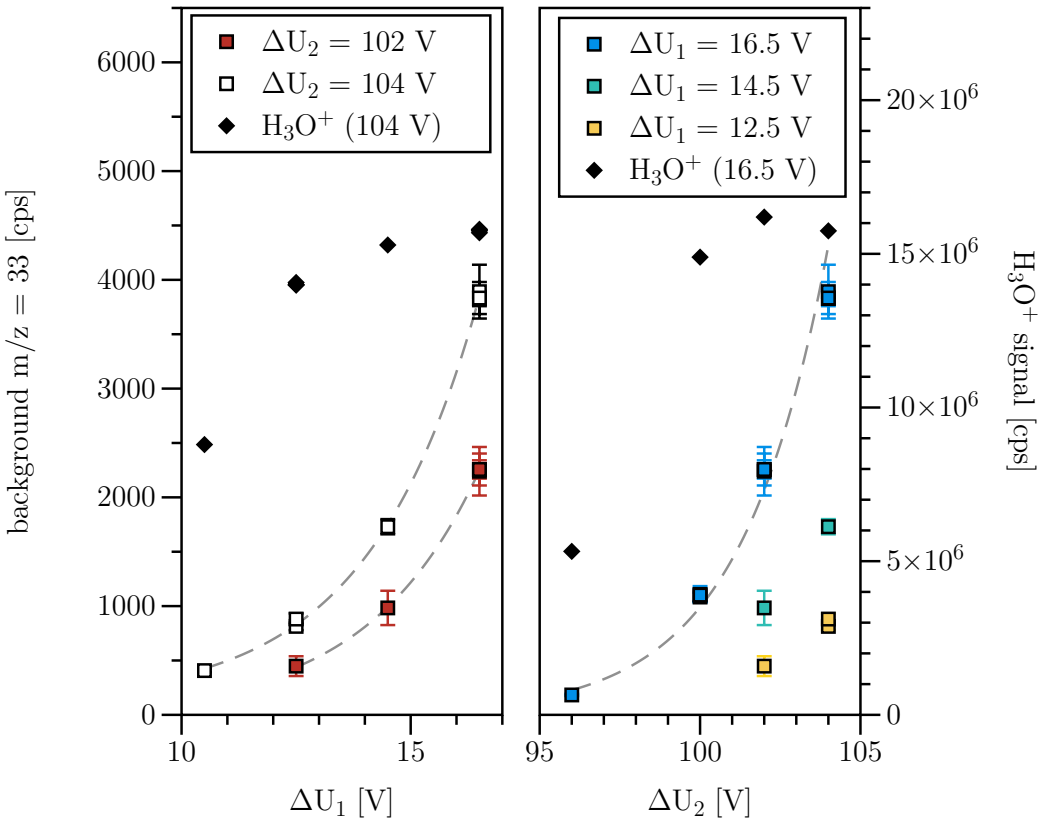

Figure 4.10.: Variation of the background signal on $m/z = 33$ and the H_3O^+ signal for different potential differences between the drift tube exit and nose cone (ΔU_1) and between the nose cone and first ion lens (ΔU_2).

In Figure 4.10 it is shown how the background signal at $m/z = 33$ varies when ΔU_1 (left panel) or ΔU_2 (right panel) are reduced compared to the standard values, which have been found to be optimal for the detection of acetone. The signal shows a clear dependence on both ΔU_1 and ΔU_2 and decreases strongly (assumably with an exponential rate) when ΔU_1 or ΔU_2 is reduced. A decrease of either ΔU_1 or ΔU_2 by 4 V or decreasing both by 2 V has a similar effect on the background.

In general, the decrease can be a cumulative effect of two causes: The reduction of the fields can decrease the production of HO_2^+ and the overall ion transmission. To investigate, which effect dominates, the transmission of other ions has to be analyzed. Therefore, in Figure 4.10, the loss in transmission is exemplarily shown for the primary ions, but all other masses were affected likewise. For both ΔU_1 and ΔU_2, the ion transmission shows a plateau towards higher field strengths, which is attained at 12.5 V and 100 V, respectively. Consequently, also the contribution

Compound	Sensitivity [cps ppb^{-1}]			Relative change [%]	
ΔU_1 =	16.5 V	12.5 V	10.5 V	16.5–12.5 V	16.5–10.5 V
Formaldehyde	217	195	114	10	48
Methanol	243	218	119	10	51
Acetonitrile	553	453	260	19	58
Acetaldehyde	491	396	209	19	58
Acetone	571	426	229	25	60
DMS	369	284	151	23	59
Isoprene	200	169	91	15	54
MVK	521	393	204	25	61
MEK	521	375	191	28	63
Benzene	341	235	123	31	64
Toluene	362	243	115	33	68
p-Xylene	368	214	105	42	72
α-Pinene	117	72	35	39	70

Table 4.5.: Variation of the sensitivities for different potential differences ΔU_1 between the drift tube exit and nose cone.

of the $^{16}O^{17}O^+$ isotopologue (not shown in the figure) to the background signal is relatively stable ($\sim$ 375 cps) for $\Delta U_1 > 12.5$ V and $\Delta U_2 > 100$ V. Therefore, it can be concluded that the strong changes of the background signal between 12.5–16.5 V (ΔU_1) and 100–104 V (ΔU_1) are mainly related to changes in the production rate of HO_2^+.

As the detection limit is closely linked to both the background level and the transmission efficiency, a compromise between the reduction of the HO_2^+ production and the decrease in transmission, which affects the instrument's sensitivity for all compounds, has to be found. In order to fully assess the impact, calibrations were conducted for three values of ΔU_1 (10.5 V, 12.5 V, 16.5 V). The absolute sensitivities and relative changes are given in Table 4.5.

The decrease in sensitivity due to a reduced electrical field was lowest for light-weight compounds and increased with mass. The same behavior was observed for calibrations with different values of ΔU_2. However, due to the instability of the methanol signal, the latter calibration measurements could not be fully evaluated and, thus, are not shown here.

Compound	LOD [ppt]		
$\Delta U_1 =$	16.5 V	12.5 V	10.5 V
Formaldehyde	170	162	237
Methanol	353	188	270
Acetonitrile	15	23	41
Acetaldehyde	42	54	83
Acetone	27	36	61
DMS	18	33	64
Isoprene	32	54	101
MVK	14	22	47
MEK	19	26	54
Benzene	19	39	79
Toluene	18	37	81
p-Xylene	33	59	108
α-Pinene	48	114	272

Table 4.6.: Variation of the detection limits for different potential differences ΔU_1 between the drift tube exit and nose cone.

The alteration of both electrical fields probably changed the ion beam shape at the entrance of the quadrupole. According to Muntean (1995), a larger beam divergence at the quadrupole entrance shifts the maximum transmission to small values, which is consistent with the results.

In the following, the sensitivities were used to calculate the mean detection limits using 12-hour background measurements for each ΔU_1. The results are summarized in Table 4.6. Except for methanol and formaldehyde, all detection limits considerably increased when ΔU_1 was reduced. As the background signals of the other compounds were not affected by HO_2^+ and thus did not significantly alter with ΔU_1, the increase of the detection limit is mainly caused by the lower sensitivities.

For methanol, the initial reduction of ΔU_1 by 4 V led to a decrease in LOD by a factor of $\sim$2. Further reduction of ΔU_1 led to an increase of the LOD, as the transmission loss starts to dominate over the reduction of HO_2^+. Therefore, a further improvement of the LOD for methanol due to adjustment of the electrical fields in the extraction region seems to be unlikely. However, adjusting the electrical fields to improve the detection limits for the compounds of interest should be considered

in the future. Changing ΔU_1 to 12.5 V should not affect UTLS measurement of acetonitrile, acetaldehyde and acetone, but detection of benzene and toluene becomes even more challenging (see Table 4.4). An alternative might be to switch between 12.5 V and 16.5 V within the measurement cycle, but response times have to be carefully evaluated.

4.5. Detection of other compounds

As shown in Section 4.2, the sensitivities of many VOCs can be inferred by calibration relative to a standard, without knowing the proton transfer reaction rate coefficients k or transmission efficiencies Γ of these VOCs (cf. Equation 2.10). However, this limits quantification to the compounds contained in the gas standard. Ideally, it contains all species of interest. Unfortunately, there are compounds, which are either not stable in gas cylinders or not compatible with other gases of the mixture. In such cases, calibration with permeation tubes is an alternative (Wyche et al., 2009; Brito and Zahn, 2011; Haase et al., 2012), but requires a more sophisticated set-up and proper handling.

Another, in the early days of PTR-MS frequently applied, but less accurate way to determine the sensitivity, is to use reaction rate constants reported in the literature and instrument-specific transmission coefficients. The latter can be experimentally determined using a calibration with a gas standard. For the compounds present in the standard, the relative transmission coefficients can be calculated by rearranging Equation 2.10 as follows:

$$\Gamma[\mathrm{MH^+}]_{\mathrm{rel}} = \frac{\Gamma[\mathrm{MH^+}]}{\Gamma[\mathrm{H_3O^+}]} = \frac{R\ T}{k\ t_r\ p\ N_A\ \mathrm{VMR(M)}} \cdot \frac{i(\mathrm{MH^+})}{i(\mathrm{H_3O^+})} \tag{4.3}$$

The relationship between the VMR of M and the count rates of $\mathrm{MH^+}$ and $\mathrm{H_3O^+}$ is determined by the calibration. The reaction time t_r is calculated according to Equation 2.20 and the compound-specific reaction rate constant k_{M} is taken from the literature (Zhao and Zhang, 2004). The reaction rate constants used here are summarized in Table 4.7.

The derived transmission coefficients are then used to determine the relative transmission curve, which describes how the transmission varies with m/z for the given instrument. For quadrupole mass spectrometers, this relationship can be approxi-

m/z	Compound	$k[10^{-9}$ cm^3 s$^{-1}]$
31	Formaldehyde	2.92
33	Methanol	2.33
42	Acetonitrile	4.74
45	Acetaldehyde	3.36
59	Acetone	3.00
79	Benzene	1.97
93	Toluene	2.12
93	*p*-Xylene	2.27
137	α-pinene	2.44

Table 4.7.: Proton transfer reaction rate constants for different VOCs (taken from by Zhao and Zhang, 2004).

mated with a curve of the empirical form

$$\Gamma[\mathrm{MH}^+]_{\mathrm{rel}} = \frac{c\left(1 + a^{x-b}\right)^{-0.25}}{1 + \exp(\frac{x-b}{d})} \tag{4.4}$$

with $x = m/z$ (Halbritter, 2011). Figure 4.11 shows the typical form of this curve for quadrupole mass spectrometer (Halbritter, 2011) and the ones derived for the PTRMS-HALO based on three different calibrations. The calculated relative transmissions of the PTRMS-HALO agree moderately well with the known transmission behavior of quadrupole mass analyzer. Nevertheless, for some compounds, deviations of at least ∼30 % are observed between the fitted curve and the underlying calculated transmission coefficients (filled squares and open diamonds).

Based on the relative transmission curve and zero air measurements it is e.g. possible to estimate the detection limits of compounds, which are not present in the gas standard, but planned to be measured in the future. For the instruments of the author's group, this includes acetic acid, formic acid and peroxyacetyl nitrate (PAN), which are important photoproducts of other trace gases and have been measured by PTR-MS in other studies.

In Table 4.8, the used reaction rate constants, derived transmission coefficients and the resulting sensitivities as well as detection limits are summarized. Protonated PAN has a m/z value of 122, but Hansel and Wisthaler (2000) found that ∼95 % of

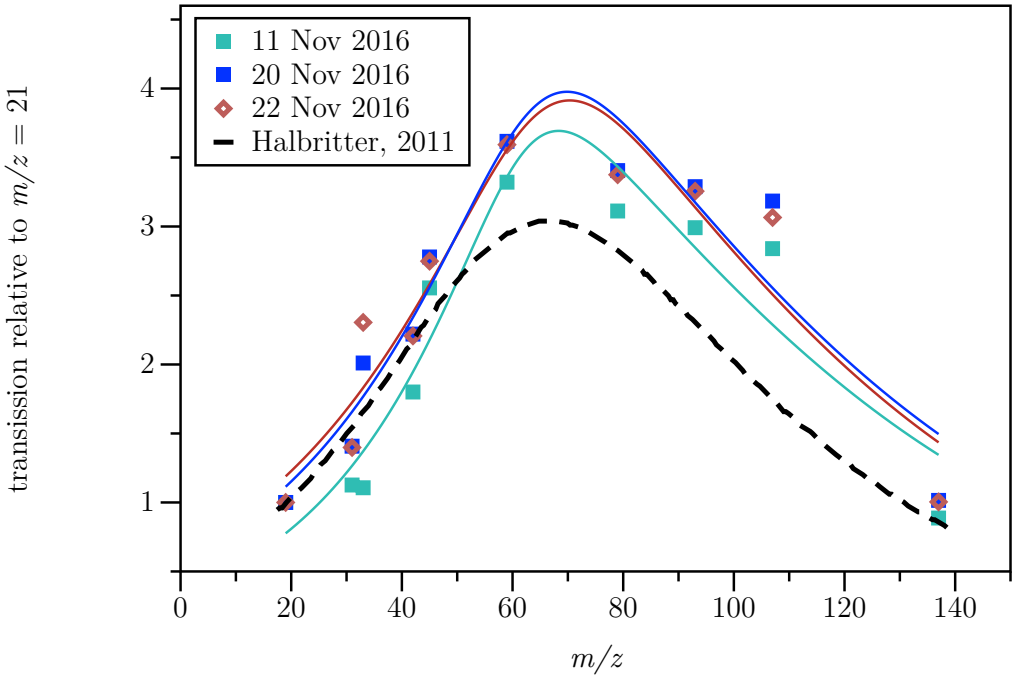

Figure 4.11.: Relative transmission curves: The black dashed line shows the transmission behavior of another quadrupole-based PTR-MS (Halbritter, 2011). The colored solid lines are the result of fitting Equation 4.4 to the transmission values (filled squares and open diamonds) calculated with Equation 4.3 using the reaction rate constants in Table 4.7.

m/z	Compound	$k_{H_3O^+}$ [10^{-9} cm^3 s^{-1}]	T_{rel}	bgnd [cps]	Sensitivity [cps ppb^{-1}]	LOD [ppt]
47	Formic acid	2.02	2.6	834	327	117
61	Acetic acid	2.27	3.6	78	513	27
77	Peroxyacetyl nitrate	4.50	3.7	28	1046	5

Table 4.8.: Calculation of sensitivities and detection limits based on the fundamental physical conditions in the drift tube for selected compounds, which are not present in the currently used gas standard. The relative transmission coefficients were determined from a mean transmission curve. The proton transfer reaction rates are taken from Zhao and Zhang (2004), except for the one of peroxyacetyl nitrate, which was taken from Hastie et al. (2010). The detection limits are stated for a S/N ratio of 3 and dwell times of 5 s.

the protonated PAN reacts with water in the drift tube to form $CH_3C(O)OOHH^+$, which can be detected at $m/z = 77$.

The derived detection limit for formic acid (117 ppt) suffers from a large chemical background on the channel, where protonated formic acid ($m/z = 47$) is detected, consistent with the finding of de Gouw et al. (2003b). Reported VMRs of formic acid are comparable to or below the estimated LOD. For the upper troposphere at Northern Hemisphere mid latitudes, Grutter et al. (2010) derived mean monthly formic acid VMRs of 100-110 ppt in summer and ∼45 ppt in winter from MIPAS spectra, which is consistent with the ACE-FTS observations (González Abad et al., 2009). Reiner et al. (1999) measured mean UTLS VMRs of 59–216 ppt during an aircraft campaign in fall 1999 over Germany. To observe the upper tropospheric background of formic acid during all seasons, it is therefore important to eliminate the high instrumental background or to further increase the sensitivity.

For the other two compounds, the chemical background is 10–30 times smaller and estimated detection limits are considerably lower. For the case of acetic acid, the derived LOD is 27 ppt. In the free troposphere, acetic acid is present in amounts comparable to or larger than formic acid (Madronich et al., 1990; Seinfeld, 1999; Treadaway, 2015). Talbot et al. (1990) found concentrations of 200 ppt in the free troposphere above the Amazonian rain forest. Reiner et al. (1999) observed mean values of 110-357 ppt in the UTLS. This is in good agreement with recently obtained vertical profiles above the US (Treadaway, 2015). As the estimated LOD is significantly lower than the reported values, acetic acid can be probably detected with PTRMS-HALO.

The same is true for PAN, which has been more frequently measured in the UTLS than acetic acid. Moore and Remedios (2010) used MIPAS measurements of 2003 to retrieve PAN VMRs between 300–600 ppt in the Northern Hemisphere UTLS in summer and mean VMRs of less than 250 ppt in winter. The VMRs derived from ACE-FTS measurements are generally lower with zonal means of 200-300 ppt in summer and 50 ppt in winter at Northern Hemisphere midlatitudes (Tereszchuk et al., 2013b). The summer value is in good agreement with the in-situ measurements of Alvarado et al. (2010) and Roiger et al. (2011), who observed PAN VMRs of ∼300 ppt in the upper troposphere. A few studies have demonstrated that PAN can be detected by PTR-MS at $m/z = 77$ (Hansel and Wisthaler, 2000; de Gouw et al., 2003b; Kaser et al., 2013). As the typical VMRs in the UTLS are much higher than the estimated LOD, PAN should be detectable with the HALO PTR-MS, but

calibration must be given particular attention. Due to the instability of PAN, it needs to be synthesized in-situ.

4.6. Summary and conclusions

In this chapter, the performance of the final version of PTRMS-HALO is determined and compared to other instruments in terms of compound-specific sensitivities and detection limits.

Comparisons with earlier development stages of PTRMS-HALO reveal that the sensitivities could be improved by a factor between 3 and 5, depending on species. In general, the completed instrument features sensitivities, which are twice as large as the averages of sensitivities reported in the literature.

This achievement is of great importance for the intended airborne measurements in the UTLS. This is due to the fact that an increase in sensitivity is commonly accompanied by an improvement of the signal-to-noise ratio, which in turn is beneficial for two reasons. First, measurements with a specific precision can be obtained more rapidly and secondly, the detection limits become smaller. Both effects are of great significance for airborne measurements in the UTLS, where VOC concentrations are particularly small. A high time resolution directly implies a high spatial resolution, enabling the detection of small-scaled atmospheric processes, while lower detection limits allow for the measurement of further species, which have been not quantifiable so far. The final version of PTRMS-HALO stands out with detection limits below 50ppt (using a dwell time of 5 s and a confidence level of 99.7 %) for all considered species except formaldehyde (170 ppt) and methanol (353 ppt).

As much of the knowledge about the atmosphere so far has been driven by what can be measured and, if so, how fast it can be measured (Williams and Koppmann, 2007; Roscoe and Clemitshaw, 1997), the new airborne PTRMS-HALO is of great value for the community of atmospheric sciences and its ongoing striving for a better understanding of the atmosphere.

Besides the instrumental characterization of PTRMS-HALO, the existing calibration set-up und procedure is evaluated with regard to potential error sources. Subsequent calibrations performed on 5 days within a time period of 3 weeks show that apparently the sensitivities for formaldehyde and methanol vary considerably with time (36–46 % RSD). However, as the signals of these compounds also need significantly more

time to stabilize after a change in concentration, it is assumed that uncontrollable wall losses of these species led to this situation. Further investigations as well as a modification of the calibration set-up, if the assumption turns out to be true, are strongly recommended.

5. Acetone–CO enhancements in the upper troposphere

The presence of acetone (CH_3COCH_3) in the UTLS was first detected in the early 1980s by Arnold and coworkers (Hauck and Arnold, 1984; Arnold and Hauck, 1985; Arnold et al., 1986). Since then it has been measured during several research aircraft campaigns (e.g. Singh et al., 1994, 1995; Scheeren et al., 2003). Besides being the second most abundant non-methane VOC in the troposphere after methanol (Koppmann and Wildt, 2007), it is considered to be a key species in UT chemistry (Singh et al., 1995; Arnold et al., 1997; Fischer et al., 2012; Neumaier et al., 2014).

In the dry extratropical UT, acetone constitutes an important source of HO_x radicals (e.g. Singh et al., 1995; McKeen et al., 1997; Folkins and Chatfield, 2000; Neumaier et al., 2014). At high-NO_x levels, acetone can form peroxyacetyl nitrate (PAN), which acts as a temporary reservoir for NO_x and thus, enables long-range transport of reactive nitrogen (Singh et al., 1986, 1992; Folkins and Chatfield, 2000; Fischer et al., 2014).

Consequently, acetone has an important impact on the budgets of HO_x and NO_x, which both play a central role in atmospheric processes, including the formation of tropospheric ozone, the production of secondary organic aerosols and the removal of greenhouse gases (e.g. Monks, 2005). However, to assess these effects, the spatial and temporal variability of tropospheric acetone must be well known.

During several research aircraft campaigns, a high variability of acetone VMRs has been observed. Nevertheless, due to the limited temporal and spatial coverage of the campaigns, it was not possible to derive a global acetone climatology.

To tackle this problem, efforts have been made to retrieve acetone from ACE-FTS (Coheur et al., 2007; Harrison et al., 2011; Tereszchuk et al., 2013; Dufour et al., 2016) and MIPAS (Moore et al., 2012) satellite data, but the signature of acetone is hard to detect (Stiller et al., 2004; Waterfall et al., 2004) and the vertical resolution

of the respective instruments is limited to 2–3 km (Moore et al., 2012; Dufour et al., 2016). Therefore, limited acetone data have been provided this way.

By contrast, all these deficiencies do not apply to the CARIBIC project (see Section 1.3.1). Already since 2006, atmospheric acetone is regularly measured onboard the CARIBIC passenger aircraft with high spatial resolution and coverage. As a result, the knowledge about the seasonal and spatial distribution could be significantly improved (Sprung and Zahn, 2010; Elias et al., 2011; Baker et al., 2014). In general, acetone VMRs are highest in the Northern hemisphere with mean values between 200 ppt in winter and 1200 ppt in summer in the extratropical UT (Sprung and Zahn, 2010; Neumaier et al., 2014; Dufour et al., 2016).

Despite these achievements, studies about the global acetone budget diverge considerably with regard to their source and sink estimates (e.g. Jacob et al., 2002; Fischer et al., 2012; Khan et al., 2015). Current global source estimates range from $42.5\,\mathrm{Tg\,a^{-1}}$ (Arnold et al., 2005) to $127\,\mathrm{Tg\,a^{-1}}$ (Elias et al., 2011). Therefore, it is important to further constrain the total acetone source and its contributors. In this chapter, the large CARIBIC in-situ data set of acetone and CO is used for this purpose. During several research aircraft campaigns in the 1990s, a good correlation between acetone and CO VMRs has been observed (de Reus et al., 2003). To the author's knowledge, Singh et al. (1994) were the first that reported on this correlation and utilized it to better assess the acetone sources.

In Section 5.1, the current knowledge about the sources and sinks of acetone is reviewed. The concept of enhancement ratios is introduced in Section 5.2. In Section 5.3, a new approach to detect physically meaningful correlations of acetone and CO in the CARIBIC data set is presented. The temporal evolution of acetone-CO enhancement ratios is discussed in Section 5.4. The sections thereafter comprise the results of the comprehensive data analysis including top-down estimates for the North American (Section 5.8) and Southeast Asian (Section 5.9) acetone sources. The study is concluded in Section 5.10 by providing a summary and outlook.

Please note that this study has been published under the title "Acetone–CO enhancement ratios in the upper troposphere based on 7 years of CARIBIC data: new insights and estimates of regional acetone fluxes" by Fischbeck et al. (2017) in the Journal of Atmospheric Chemistry and Physics (ACP)[†]. The following parts of this chapter have been therefore mainly adopted from this publication.

[†]The interactive discussion (review process) is available on the following website: https://www.atmos-chem-phys.net/17/1985/2017/acp-17-1985-2017-discussion.html

5.1. Sources and sinks of acetone

Acetone is directly emitted into the atmosphere by anthropogenic and biogenic sources as well as formed in situ by the oxidation of precursor compounds (e.g. Jacob et al., 2002)

Biogenic sources (including secondary production from biogenic precursors) are believed to account for ∼50–70 % of the total acetone emissions (Jacob et al., 2002; Fischer et al., 2012; Hu et al., 2013; Khan et al., 2015). This is also supported by CARIBIC observations in the extratropical UTLS (see Figure 5.1). The observed mean VMRs of acetone follow the same seasonal cycle as the biogenic emissions provided in the MEGAN-MACC inventory (Sindelarova et al., 2014).

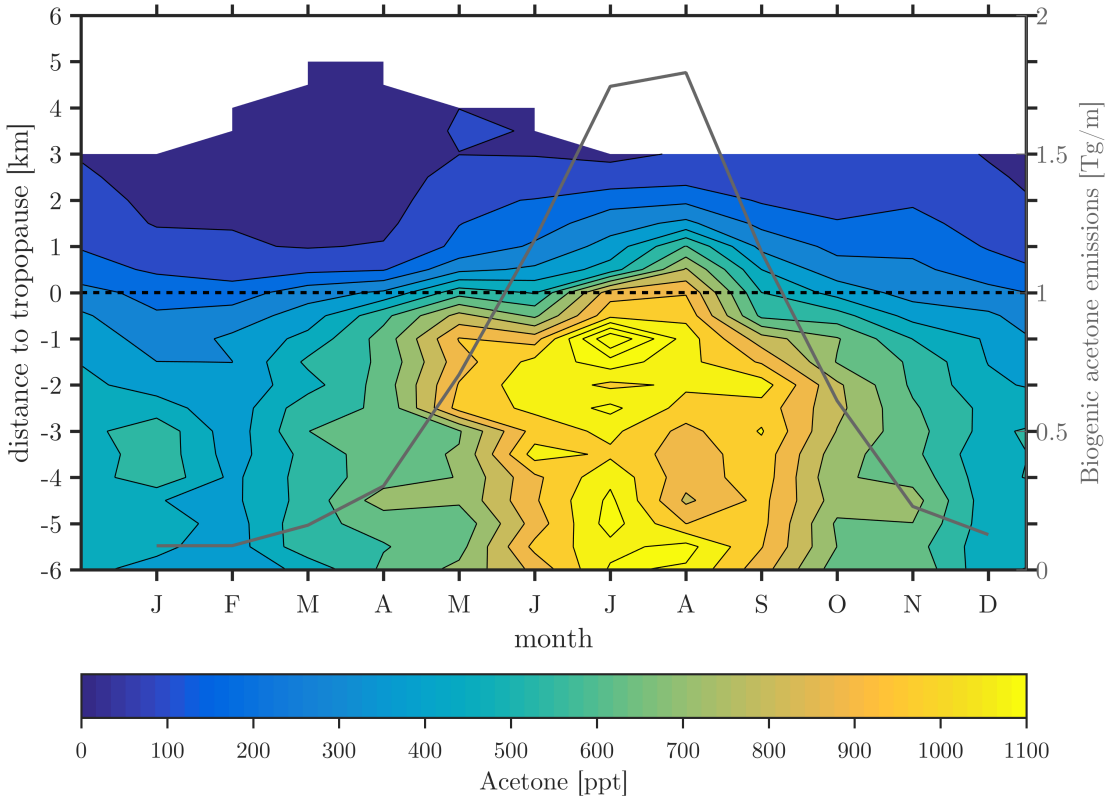

Figure 5.1.: Seasonal variation of acetone VMRs around the chemical tropopause (dashed line) as observed with IAGOS-CARIBIC at Northern Hemisphere midlatitudes (23.5°N – 66.5°N). The underlying data are monthly averages using 500 m altitude bins. Superimposed, the seasonal cycle of biogenic acetone emissions (grey line) is shown as derived from the MEGAN-MACC (Sindelarova et al., 2014) averaged over the period 2000–2010. Figure adopted from Sprung and Zahn (2010).

Direct biogenic emissions have been identified from trees (Isodorov et al., 1985), grasslands (Kirstine et al., 1998) and decaying plant matter (Warneke et al., 1999). The terrestrial biosphere also emits methylbutenol (Goldan et al., 1993; Harley et al., 1998) and large amounts of monoterpenes (Guenther et al., 2012), which are rapidly oxidized in the atmosphere and lead to the production of secondary acetone. Several laboratory studies have been conducted to determine the acetone yields from biogenic precursors (e.g. Calogirou et al., 1999; Orlando et al., 2000; Lee et al., 2006).

Direct anthropogenic emissions of acetone include contributions from solvent use (Singh et al., 1994), landfills (Brosseau and Heitz, 1993), car exhaust (Smith et al., 2002, 2004) and industrial processes, that produce or use acetone to manufacture plastics, fibers and other chemicals. The direct emissions are however considered to account for less than 5 % of the total acetone source (Singh et al., 1994, 2000; Jacob et al., 2002). Most anthropogenic acetone is produced in-situ in the atmosphere by the OH oxidation of isoalkanes. Until recently, propane was thought to be the dominant acetone precursor accounting for $\sim 30\,\%$ of the total acetone budget (Fischer et al., 2012). However, the latest STOCHEM-CRI model calculations by Khan et al. (2015) suggest that oxidation of short-lived biogenic monoterpenes such as α-pinene and β-pinene could account for more than 60 % of atmospheric acetone with propane oxidation being much less important ($\sim 12\,\%$). The contribution from C_4- to C_5-alkanes is expected to be 6–7 % (Jacob et al., 2002; Fischer et al., 2012).

Beside the above-mentioned sources, acetone and its precursors are also emitted from biomass burning (BB) (Holzinger et al., 1999, 2005) with an estimated contribution of ~ 4–$10\,\%$ to the global source (Jacob et al., 2002; Singh et al., 2004; Fischer et al., 2012). Furthermore, several studies inferred a large oceanic source of acetone (Kieber et al., 1990; Nemecek-Marshall et al., 1995; Zhou and Mopper, 1997; Singh et al., 2001). Meanwhile, the role of the ocean as a source has been reconsidered (Marandino et al., 2005). It was found that the ocean can be a source and sink of acetone, but on a global scale, it is thought to be in near-equilibrium with the atmosphere (Fischer et al., 2012).

The main tropospheric sinks of acetone are oxidation by OH and photolysis. Dry deposition is considered to be a further relevant sink (e.g. Jacob et al., 2002). Altogether, the sinks lead to an overall tropospheric mean lifetime (Equation 6.2) in the range of 14–35 days (Jacob et al., 2002; Schade and Goldstein, 2006; Fischer et al., 2012; Hu et al., 2013; Khan et al., 2015; Weimer et al., 2017).

5.2. Emission and enhancement ratios

A powerful tool for quantifying emissions is the analysis of enhancement ratios (EnRs) in plumes (e.g. Singh et al., 2004; Lai et al., 2011). The EnR is obtained by dividing the plume enhancement of a species X (above to the background) by the enhancement of another species Y (Lefer et al., 1994; Lee et al., 1997; Mauzerall et al., 1998):

$$\mathrm{EnR} = \frac{[X]_{\mathrm{plume}} - [X]_{\mathrm{bgnd}}}{[Y]_{\mathrm{plume}} - [Y]_{\mathrm{bgnd}}}. \tag{5.1}$$

In practice, it is either determined by measuring the VMRs of X and Y inside and outside the plume (e.g. Simpson et al., 2011) or from continuous airborne measurements during plume passage (see Figure 5.2) (Yokelson et al., 2013). With

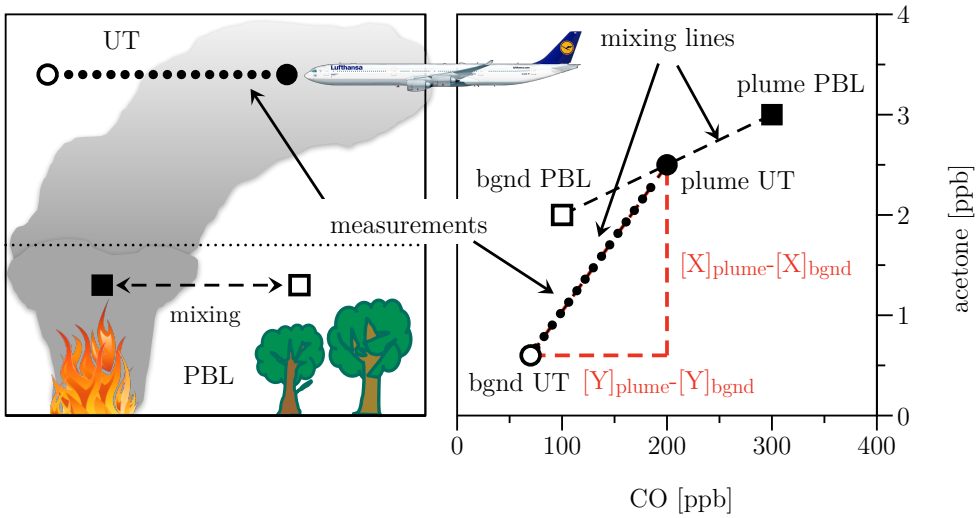

Figure 5.2.: Left: Schematic drawing of a biomass burning plume and its transport from the planetary boundary layer (PBL) into the upper troposphere (UT), where sampling takes place. Adapted from Mauzerall et al. (1998). Right: Acetone plotted versus CO concentrations. Black-filled square (plume PBL): acetone–CO concentration in the fresh plume near the ground, which initially mixes with adjacent background (bgnd) air of the PBL (open square, bgnd PBL). When the resulting plume (full circle) rises into the UT, the enhancement of acetone and CO are reduced as the plume mixes with background air of the UT (open circle, bgnd UT). In an ideal case, concentrations measured during plume passage lie on the UT mixing line. The slope of the mixing lines, equivalent to EnR (see Eq. 5.1), may differ considerably in the PBL and the UT. Adopted from Fischbeck et al. (2017).

ER [ppt ppb^{-1}]	Air mass, location, time	References
0.06–0.25	Biofuel burning	Andreae and Merlet (2001)
0.84	Vegetation from the southwest USA; laboratory experiment	Warneke et al. (2011)
1.1	Indonesian Peat fires	Stockwell et al. (2016)
1.2	Savanna biomass burning	Akagi et al. (2011)
1.6	Canadian boreal forest fire	Simpson et al. (2011)
1.7–2.05	North American wildfires	Friedli et al. (2001)
1.9–4.6	Savanna and grassland biomass burning	Andreae and Merlet (2001)
2.3–2.7	Extratropical forest biomass burning	Andreae and Merlet (2001)
1.93	Vegetation from the southeast USA; laboratory experiment	Warneke et al. (2011)
1.94	Pines spruce; laboratory experiment	Warneke et al. (2011)
2.1	Peat burning, laboratory experiment	Stockwell et al. (2015)
2.2	Rocket cook stove, laboratory experiment	Stockwell et al. (2015)
2.8	Boreal forest biomass burning	Akagi et al. (2011)
2.9	Peatland burning	Akagi et al. (2011)
2.9	Tropical forest biomass burning	Andreae and Merlet (2001)
2.9	Charcoal burning	Andreae and Merlet (2001)
2.9	Residential heating	Kaltsonoudis et al. (2016)
3.0	Extratropical/boreal forest biomass burning	Akagi et al. (2011)
3.3	Tropical forest biomass burning	Akagi et al. (2011)
4.1	Temperate forest fire	Müeller et al. (2016)
4.5	Boreal forest wood, laboratory experiment	Stockwell et al. (2015)
4.8	Fresh African savannah fire	Jost et al. (2003b)
5.4	Savanna grass, laboratory experiment	Holzinger et al. (1999)
2.5 ± 1.4	Mean acetone–CO ER ($\pm$ standard deviation)	

Table 5.1.: Literature values of acetone–CO emission ratios (ERs). Adopted from Fischbeck et al. (2017).

regard to acetone, it has become common practice to use CO as reference species Y, because both gases are emitted during incomplete combustion (Andreae and Merlet, 2001; Wisthaler et al., 2002; Greenberg et al., 2006; Warneke et al., 2011).

When an EnR is measured at the source, it equals its molar emission ratio (ER) (Yokelson et al., 2013) (see Table 5.1 for a compilation of acetone–CO emission ratios reported in the literature). Downwind from the source, the EnR remains equal to the ER as long as production or removal of X and Y in the plume are negligible and as long as the plume mixes in the same fixed background (Mauzerall et al., 1998; Yokelson et al., 2013). This is due to the fact that dividing the enhancement of X by the enhancement of Y normalizes for dilution, as both species dilute at the same rate (Akagi et al., 2012; Yokelson et al., 2013). Whenever it cannot be excluded that the ratio has changed since emission, the term EnR should be preferred over the term ER. As shown in Figure 5.2, this is particularly the case for measurements in the UT. Plume air initially mixes with planetary boundary layer (PBL) air and subsequently enters the "cleaner" UT. Plume ratios observed in the UT significantly differ from the PBL EnR value simply because the UT background has a different acetone–CO ratio as the PBL background.

The most comprehensive overview of acetone–CO EnRs to date has been given by de Reus et al. (2003), using data of five research aircraft campaigns. For each campaign, the authors split the data into measurements from the marine boundary layer (0–1 km), free troposphere (1–12.5 km) or lower stratosphere ($O_3 > 150$ ppb, $CO < 60$ ppb) and derived one EnR per layer. Please note, that in this way, data of different flights, i.e. data of "unrelated" measurements in terms of distance and time span, were used to derive a single EnR estimate. The authors found different EnRs for the different layers, but, surprisingly, consistent values among the campaigns. Since then, EnRs have been frequently reported for individual plumes and various conditions.

In Tables 5.3 and 5.2, an overview is given of literature acetone–CO EnRs reported for non-biomass burning plumes and those impacted by biomass burning (without any claim to completeness). It is worth noting that ERs (see Table 5.1) are only available for biomass and biofuel burning and are generally lower (mean: 2.5 ppt ppb^{-1}) than the observed free-tropospheric EnRs, which are on average 9.9 ppt ppb^{-1} for biomass burning plumes and 12.5 ppt ppb^{-1} for other plumes.

In order to understand the underlying processes that change the EnR, it is worth estimating how fast plumes usually mix with background air masses. In simple models, this mixing is prescribed with a constant dilution rate. In a few studies, dilution rates were determined experimentally; the results are summarized in Table 5.4.

EnR [ppt ppb^{-1}]	Air mass, location, time	References
1.57	Urban air, central eastern China, March–April 2011	Yuan et al. (2013)
3.18	Urban air, London, winter 2012	Valach et al. (2014)
3.4	Free troposphere, Indian Ocean, February–March 1999	Reiner et al. (2001)
3.59	Urban air (with vehicular emissions), Sao Paolo, February–April 2013,	Brito et al. (2015)
5.0	Mount Tai, China, June 2006	Inomata et al. (2010)
5.8	Fresh urban plumes, eastern USA, July–August 2004	Warneke et al. (2007)
6.12	High-altitude (> 9km), Pacific Ocean, February–March 1994	McKeen et al. (1997)
13–16	Marine boundary layer	De Reus et al. (2003)
13.4–17.2	Ship measurements, Indian Ocean, March 1999	Wisthaler et al. (2002)
14	Marine boundary layer, Indian Ocean, March 1999	Reiner et al. (2001);
14.2	Los Angeles, April–May 2002	Warneke et al. (2007)
18.3	Urban plumes, summer 2008	Singh et al. (2010)
19.5	Aged high-altitude plumes, Surinam, March 1998	Andreae et al. (2001)
21–25	Free troposphere	De Reus et al. (2003)
~ 22	Los Angeles Basin, May–June 2010	Warneke et al. (2012)
30	Troposphere, eastern Canada, July–August 1990	Singh et al. (1994)
12.5 ± 8.6	Mean acetone–CO EnR ($\pm$ standard deviation)	

Table 5.2.: Literature values of acetone–CO enhancement ratios (EnRs) in air masses unaffected by biomass burning in ppt ppb^{-1}. Adopted from Fischbeck et al. (2017).

EnR [ppt ppb^{-1}]	Air mass, location, time	References
4.7	Fresh biomass burning plume, summer 2008	Singh et al. (2010)
5.0	Biomass burning plumes, Canada, June–July 2008	Hornbrook et al. (2011)
5.7	Aged boreal biomass burning plumes from North America, July–August 2011	Tereszchuk et al. (2013)
6.0	Biomass burning plumes, California, June–July 2008	Hornbrook et al. (2011)
6.2	Aged boreal biomass burning plumes from Siberia, July–August 2011	Tereszchuk et al. (2013)
6.3	Aged plumes of Alaskan and Canadian forest fire, July 2004	de Gouw et al. (2006);
6.6	Aged Biomass burning plumes, Yucatan, March 2006	Yokelson et al. (2009)
6.6–22	Aged biomass burning plumes, free troposphere, winter/spring 2001	Jost et al. (2003b)
7.2–10.3	Biomass burning plumes, South Atlantic, September–October 1992	Mauzerall et al. (1998)
7.1	Biomass burning plumes, Canada, June–July 2008	Hornbrook et al. (2011)
7.5	Biomass burning plumes, Pacific, winter/spring 2001	Singh et al. (2004)
7.7	Forest Fire Lake Baikal, April 2008	Warneke et al. (2009)
9.0	Asian biomass burning plumes, June–July 2008	Hornbrook et al. (2011)
10.6	Aged (1–5 days) biomass burning and urban plumes, summer 2008	Singh et al. (2010)
11.3	Fresh savannah fire plumes (0–125 min plume age), Africa	Jost et al. (2003b)
11.7	Agricultural fires Kazakhstan, April 2008	Warneke et al. (2009)
14.3	Fresh boreal biomass burning plumes from Siberia, July–August 2011	Tereszchuk et al. (2013)
16.8	Fresh boreal biomass burning plumes from North America, July–August 2011	Tereszchuk et al. (2013)
18	Aged biomass burning plumes, Crete, August 2001	Holzinger et al. (2005)
20.4	Young biomass burning plume, Tanzania, October 2005 (using background VMR over Pacific Ocean)	Coheur et al. (2007)
9.9 ± 4.6	Mean acetone–CO EnR ($\pm$ standard deviation)	

Table 5.3.: Literature values of acetone–CO enhancement ratios (EnRs) in biomass burning plumes. Adopted from Fischbeck et al. (2017).

Dilution rate [day^{-1}]	Location, time	References
0.1	Atlantic air masses, summer	Arnold et al. (2007)
0.1	Inside smoke plume, July	Pisso et al. (2009)
0.16 (0.05–0.2)	Biomass burning plume, North Atlantic, summer	Real et al. (2007)
0.24	Free troposphere, April	Price et al. (2004)
1	Outside smoke plume, July	Pisso et al. (2009)
1.44	Planetary boundary layer, South Africa, winter	Igbafe et al. (2006)
1.5	Mexico City plateau, March	Voss et al. (2010); Shrivastava et al. (2011)
5.5	Planetary boundary layer, California, summer	Dillon et al. (2002)
4.8–10.3	Planetary boundary layer, Germany	Kramp and Volz-Thomas (1997)
2.0 ± 2.7	Mean dilution rate ($\pm$ standard deviation)	

Table 5.4.: Dilution rates reported in the literature. Adopted from Fischbeck et al. (2017).

5.3. Data analysis

Data from the individual IAGOS–CARIBIC instruments are combined into single "merge" files for each flight with a time binning of 10 s. Data with a sampling frequency greater than 0.1 Hz, such as the CO measurements (1 Hz), are averaged over the 10 s intervals, whereas low-frequency data (< 0.1 Hz), like the acetone measurements (0.03 Hz), are assigned to the corresponding 10 s interval. The correlation analysis is restricted to UT air masses. Data from ascend and descend are rarely available because of the long run-up time of the PTR-MS after take-off and an automatic equipment shutdown procedure well before landing. Stratospheric acetone–CO correlations are not well suited for the intended investigation of source patterns, because of the long transport times. To exclude stratospheric data, the threshold of the chemical tropopause as proposed by Zahn and Brenninkmeijer (2003) and Zahn et al. (2004) and verified by Thouret et al. (2006) and the concomitant CARIBIC ozone data are used. Air masses with an ozone concentration above the threshold value of

$$[O_3]^{TP}_{ppb} = 97 + 26 \sin\left(2\pi \frac{doy - 30}{365}\right), \tag{5.2}$$

where doy denotes day of the year, are identified as stratospheric and excluded. In the rare event of ozone data being unavailable, potential vorticity (PV) calculated from the ECMWF model is used. Measurements of air masses associated with a PV greater than 2 pvu, a value commonly used to define the dynamical tropopause (e.g. Hoskins et al., 1985; Holton et al., 1995), are discarded. In this way, 42 % of the acetone–CO data were identified as stratospheric.

In the remaining dataset, physically meaningful correlations are searched for in all possible subsets of data fulfilling the following two requirements adapted from

Zahn et al. (2002) and Brito (2011): (i) The subset consists of at least 10 successive measurements that are no further apart from each other than 50 km and cover less than 500 km flight path; (ii) The range of CO VMRs in the subset is greater than 10 times the average measurement uncertainty of CO. These criteria ensure that only temporal and spatial coherent events with a "fresh" source signature are considered and will be discussed in more detail in Section 5.4. For each possible subset, Pearson's linear correlation coefficient r and corresponding p value are calculated. A good linear correlation is assumed in the event $r > 0.5$ and $p < 0.05$ (5 % significance level). In such a case, the slope is calculated using the bivariate least-squares method of Williamson–York (York, 1966; Williamson, 1968; York et al., 2004) as suggested by Cantrell (2008). The Williamson–York fit has the advantage in that it accounts for the different uncertainties of both acetone and CO measurements and precludes a dependence of EnR on the axis assignments.

A high Pearson's correlation coefficient can also arise when respective acetone–CO VMRs form two clusters. To exclude such physically meaningless correlations, a cluster analysis based on Gaussian mixture models (GMMs) was implemented (Everitt and Hand, 1981; McLachlan and Peel, 2000). In this way, two GMMs are fitted to the acetone–CO subset. The first model expects only one cluster and the second two clusters. In order to choose the best-fitting model, the corrected Akaike's information criterion ($\mathrm{AIC_C}$) (Sugiura, 1978; Hurvich and Tsai, 1989) is used. Subsets with an $\mathrm{AIC_C}$ suggesting two clusters ($\mathrm{AIC_{C,}}_{n=2} < \mathrm{AIC_{C,}}_{n=1}$) are discarded.

Figure 5.3 shows two exemplary subsets; the first subset shows no clustering, whereas the second is affected by a strong clustering into two groups with no measurements in-between to support the correlation. Although the correlation coefficient ($r = 0.79$) suggests a good correlation, the cluster analysis reveals that two well-separated air masses were measured. Such a subset is excluded from further analysis as the above-mentioned rejection criterion is fulfilled.

In general, the EnR-based approach used here differs from the "classical" straightforward approach in that the diagnosed correlations are by definition limited to temporally and spatially coherent events. The enhancement ratios detected with the EnR-based approach mainly characterize the mean partitioning of acetone and CO sources in the boundary layer on a regional scale. The spread of these source regions depends on the time the analyzed air parcel spends in the boundary layer before it is released into the free and upper troposphere. Therefore, one could interpret the correlations derived from the approach presented here as "event-based" EnRs,

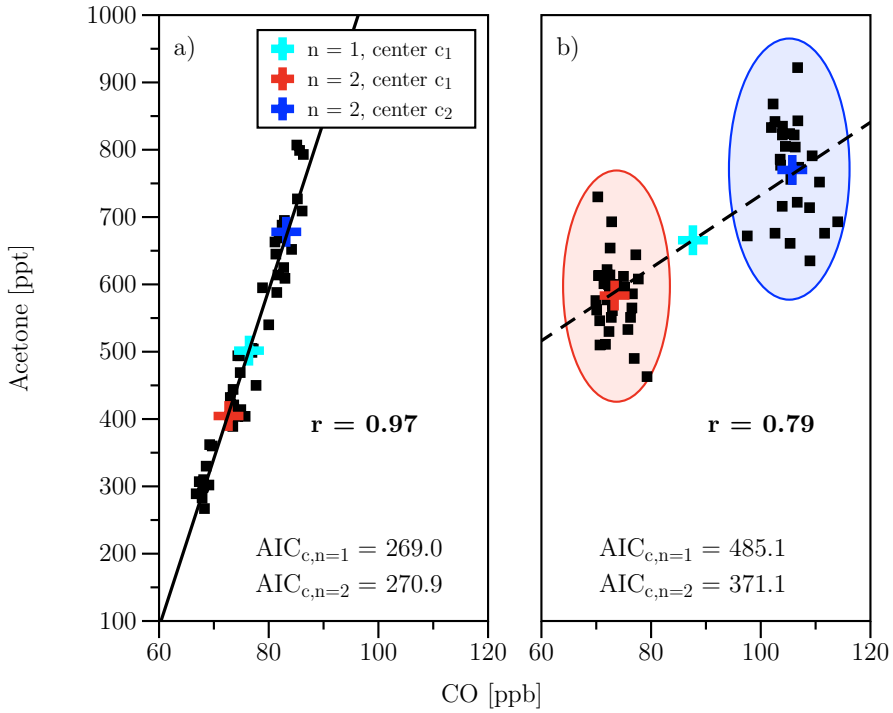

Figure 5.3.: Scatter plots of two exemplary subsets of subsequently measured acetone and CO VMRs. **(a)** Shows a subset with highly correlated data ($r = 0.97$) and no visible clustering, which is also confirmed by the cluster analysis ($\mathrm{AIC}_{\mathrm{C},n=1} \leq \mathrm{AIC}_{\mathrm{C},n=2}$). **(b)** Two distinct clusters are visible and automatically identified by the cluster analysis ($\mathrm{AIC}_{\mathrm{C},n=1} > \mathrm{AIC}_{\mathrm{C},n=2}$). Although the Pearson's correlation coefficient indicates a good correlation ($r = 0.79$), this subset is rejected for determination of EnR. Adopted from Fischbeck et al. (2017).

whereby the "event" is the release of an individual air parcel out of the boundary layer into the free troposphere. In contrast to this analysis, non-coherent correlations detected in former studies will often mirror spatial (e.g. latitudinal) gradients of acetone and CO, respectively, or imply differences of the trace gas composition of different air masses, but not enhancement ratios that characterize pollution sources and the chemical processing between emission in the boundary layer and sampling in the upper troposphere. For this reason, it is believed that this approach is best suited for the analysis of source patterns utilizing tropospheric EnRs.

In Figure 5.4, the differences between the two approaches and fit algorithms are illustrated based on the data of 17 selected flights. The flights were chosen in such a way that larger overlaps of data were kept at a minimum. The diversity of the event-based EnRs, ranging from 1.3 to 77.2 ppt ppb^{-1}, is clearly visible. Furthermore, it is shown that initial averaging over the total data (classical approach) instead

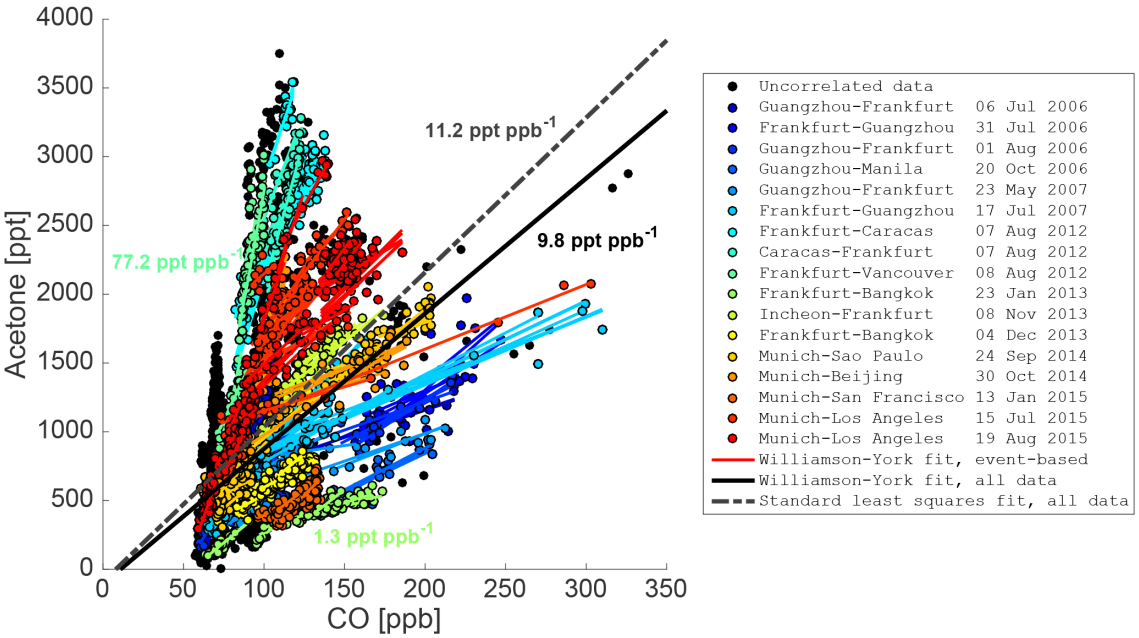

Figure 5.4.: Scatter plot of tropospheric acetone and CO data of 17 selected CARIBIC flights. Detected correlations are shown as regression lines plotted in the range of the underlying data. Color coding denotes to which flight data and correlations belong to. Data, which did not fall into the event-based correlation criteria, are shown as filled black circles regardless of their flight affiliation. The solid black and the grey dashed line represent the results of a Williamson–York fit (EnR: 9.8 ppt ppb^{-1}) and of a standard least-squares fit (EnR: 11.2 ppt ppb^{-1}), respectively, applied to all data of the 17 flights. The minimum, mean and maximum value of the event-based EnRs are 1.3, 18.6 and 77.2, respectively (all values in ppt ppb^{-1}). Adopted from Fischbeck et al. (2017).

of averaging over the individual EnRs of coherent events makes a difference. The mean of the individual EnRs (18.6 ppt ppb^{-1}) is a factor of 1.9 larger than the slope of the classical approach (9.8 ppt ppb^{-1}). In addition, the EnR of the Williamson–York fit (9.8 ppt ppb^{-1}) is smaller than the one of the standard least-squares fit (11.2 ppt ppb^{-1}), as the former puts (more) weight on the small VMRs due to their lower uncertainties. Less weight is put on the large VMRs, in particular the acetone VMRs, as they have larger uncertainties than the CO VMRs.

5.3.1. Emission inventories

In this study, surface emission data from different inventories is used, available in the ECCAD (Emissions of atmospheric Compounds & Compilation of Ancillary Data)

database (Granier et al., 2013) of the French Atmospheric Chemistry Data Centre ESPRI (formerly Ether; `http://eccad.sedoo.fr/`). The objective is to derive the total acetone flux from the boundary layer into the upper troposphere for different regions and compare this flux with the acetone source strengths derived from the enhancement ratios and CO inventory data.

The ideal case would be to use inventory data of exactly the same years for which CARIBIC data were used in this study (2006–2008; 2012–2015), but not all data in the ECCAD database is yet available for the full period. Therefore, the last 6 years with complete data coverage (2005–2010) were chosen as reference period. This period has a similar duration as the CARIBIC periods and at least covers the first CARIBIC data period. Except for biomass burning emissions, there is currently only one possible inventory for each source type for the given period. Hence, anthropogenic emissions are taken from the MACCity inventory (van der Werf et al., 2006; Lamarque et al., 2010; Granier et al., 2011; Diehl et al., 2012) and biogenic emissions from MEGAN-MACC (Sindelarova et al., 2014). For biomass burning emissions, it was decided to use the GFED3 inventory (van der Werf et al., 2010) instead of GFASv1.0 for reasons of easier data handling, as GFED3 data in ECCAD has the same temporal and spatial resolution as MACCity and MEGAN-MACC. Furthermore, Kaiser et al. (2012) found that the budgets of GFED3(.1) are consistent with GFASv1.0.

As the interest here lies on the total fluxes of acetone, i.e. primary emissions and secondary production, also emission data from the major precursors of acetone and CO are included. According to Jacob et al. (2002) and Fischer et al. (2012), the three dominant precursors of acetone are propane (13–22 $\mathrm{Tg\,a^{-1}}$ acetone), higher alkanes (4–7 $\mathrm{Tg\,a^{-1}}$ acetone) and monoterpenes (5–6 $\mathrm{Tg\,a^{-1}}$ acetone).

In order to estimate the acetone source from propane oxidation, propane emission data from MACCity and GFED3 and a molar acetone yield of 72 % (Jacob et al., 2002; Pozzer et al., 2010) are used. For isobutane and isopentane, the "butanes and higher alkanes" data of MACCity are taken. The respective mass proportion of the two species (5.7 % for isobutane and 9.7 % for isopentane) is calculated according to the VOC speciation of Passant (2002) and Calvert et al. (2008). The resulting amount of acetone is derived using the means of the yields suggested by Jacob et al. (2002) and Pozzer et al. (2010), which are $0.96\,\mathrm{mol\,mol^{-1}}$ for isobutane and $0.72\,\mathrm{mol\,mol^{-1}}$ for isopentane.

For the monoterpenes, the emission data for the sum of monoterpenes are taken from MEGAN-MACC inventory (Sindelarova et al., 2014). To calculate the emissions of the individual monoterpene species (α-pinene, β-pinene, limonene, trans-β-ocimene, myrcene, sabinene and 3-carene), the relative contributions provided in Sindelarova et al. (2014) are used. For each species, a mean acetone yield is derived based on the available literature. In this respect, the two main degradation processes of monoterpenes, reaction with OH and O_3, are considered, i.e. the yields are weighted according to the respective reaction rates.

For the secondary production of CO, only precursors with an annual global contribution of more than 25 Tg CO (according to the inventory of Duncan et al., 2007) and an atmospheric lifetime shorter than that of acetone are considered. This includes isoprene, methanol, monoterpenes, ($\geq C_4$) alkanes, ($\geq C_3$) alkenes and ethene. The respective CO production yields are taken from the same study and do not account for loss of intermediate trace gases by deposition, which might over-predict the contribution from longer-lived precursors (Duncan et al., 2007). As uncertainties are not provided for all yields and emission inventory fluxes, it is refrained from performing a comprehensive uncertainty analysis. However, considerable uncertainties might exist and estimates based on these data have to be taken with care. In the analysis, performed here, at least the statistical uncertainties of fluxes are strongly reduced by averaging over large regions and time periods.

5.4. Temporal evolution of EnR between emission and sampling

For the CARIBIC measurements in the UT, it is important to consider the possible temporal evolution of the EnR, because transport timescales and typical tropospheric lifetimes of acetone and CO are of a comparable range. So far, the combined influence of dilution and chemical transformation on acetone–CO EnRs has not been addressed in previous studies.

In order to better assess their impact, the temporal evolution of EnRs is initially examined from a theoretical point of view. A simple one-box model is applied, in which the box represents the volume of the plume at time $t = 0$. Whereas the plume expands with time, the considered box volume is held constant to take dilution into account. The temporal evolution of the mixing ratio of a compound X inside the

plume can then be approximated by (McKeen and Liu, 1993; McKeen et al., 1996)

$$\frac{\mathrm{d}\,[X]_{\mathrm{plume}}}{\mathrm{d}t} = -L_X\,[X]_{\mathrm{plume}} - D\left([X]_{\mathrm{plume}} - [X]_{\mathrm{bgnd}}\right) + P_{Z,X}\,[Z]_{\mathrm{plume}}\,, \qquad (5.3)$$

where L_X is the overall chemical loss rate of X, D is the first-order dilution rate and $P_{Z,X}$ is the production rate of X from the oxidation of the precursor compound Z. The overall chemical loss rate L_X is the sum of all loss mechanisms, which are for acetone reaction with OH and photolysis ($L_{\mathrm{Ac}} = k_{\mathrm{Ac}}\,[\mathrm{OH}] + J_{\mathrm{Ac}}$) and for CO reaction with OH ($L_{\mathrm{CO}} = k_{\mathrm{CO}}\,[\mathrm{OH}]$). As the lifetimes of both species are at least weeks, it can be assumed that the reaction and diluted rates are constant over the considered time period. Consequently, daily averaged photolysis rates obtained from the tropospheric ultraviolet and visible radiation model (TUV version 5.0; Madronich and Flocke, 1999; Madronich et al., 2010) are used. Quantum yields for the photodissociation of acetone are taken from Blitz et al. (2004). For the concentration of OH, the monthly means provided in Spivakovsky et al. (2000) are used. The OH reaction rates and uncertainties thereof are taken from the latest recommendations of the IUPAC (International Union of Pure and Applied Chemistry) Task Group on Atmospheric Chemical Kinetic Data Evaluation (Atkinson et al., 2004 and 2006). The latter are reported to be $\sim 20\,\%$. The same was assumed for the acetone photolysis rate (see Neumaier et al., 2014).

As the evolution of $[X]_{\mathrm{plume}}(t)$ is of interest, Equation 5.3 needs to be integrated. However, this is impeded by the additional time-dependent variable $[Z]_{\mathrm{plume}}$. In order to derive an analytical solution, the following steps are, therefore, shown without the production term $P_{Z,X}\ [Z]_{\mathrm{plume}}$. However, in the examples given in Figure 5.5, the full equation including $P_{Z,X}\ [Z]_{\mathrm{plume}}$ has been solved numerically, by progressively calculating the changes of $[X]_{\mathrm{plume}}$ and $[Z]_{\mathrm{plume}}$ at hourly intervals, which are short compared to the net reaction rates. Integration of Equation 5.3 without the production term $P_{Z,X}\ [Z]_{\mathrm{plume}}$ leads to

$$[X]_{\mathrm{plume}}\,(t) = \left([X]_{\mathrm{plume},t=0} - \frac{D}{L_X + D}\,[X]_{\mathrm{bgnd}}\right) e^{-(L_X+D)t} + \frac{D}{L_X + D}[X]_{\mathrm{bgnd}}. \quad (5.4)$$

Since the function does not consider the quasi-equilibrium of the background, it allows for unphysical low mixing ratios in the plume ($[X]_{\mathrm{plume}} < [X]_{\mathrm{bgnd}}$). Thus,

Equation 5.4 is only valid for times

$$0 < t < t_{\max} = \frac{\ln\left(\frac{[X]_{\text{plume},t=0}}{[X]_{\text{bgnd}}}\left(1+\frac{D}{L_X}\right)-\frac{D}{L_X}\right)}{L_X+D}. \tag{5.5}$$

Placing Equation 5.4 into the definition of EnR in Equation 5.1 leads to the time-dependent function:

$$\text{EnR}\,(t) = \frac{\left([X]_{\text{plume},t=0}-\frac{D}{L_X+D}[X]_{\text{bgnd}}\right)e^{-(L_X+D)t}-\frac{L_X}{L_X+D}[X]_{\text{bgnd}}}{\left([Y]_{\text{plume},t=0}-\frac{D}{L_Y+D}[Y]_{\text{bgnd}}\right)e^{-(L_Y+D)t}-\frac{L_Y}{L_Y+D}[Y]_{\text{bgnd}}}. \tag{5.6}$$

In the case of no chemical processing ($L_X = L = 0$) or if $L_X, L_Y \ll D$, Equation 5.6 simplifies to

$$\text{EnR} = \frac{[X]_{\text{plume},t=0}-[X]_{\text{bgnd}}}{[Y]_{\text{plume},t=0}-[Y]_{\text{bgnd}}} = \text{const.}, \tag{5.7}$$

i.e. in contrast to the ratio $[X]_{\text{plume}}/[Y]_{\text{plume}}$, the EnR remains constant as long as the plume mixes into the same background. In turn, any temporal change of EnR points to chemical processing inside the plume. However, as soon as chemical decomposition takes place, the assumption $L_X = L_Y = 0$ used in Equation 5.7 is no longer valid and the combined impact of both chemical transformation and dilution has to be taken into account in the model.

In contrast to most previous studies, both processes are considered here. Moreover, the background reservoir is excluded from any chemical degradation (quasi-steady-state), as changes in the total balance of all sources and sinks are negligible on these short timescales. Based on the evaluation of the model, it is found that the direction of change of EnR without secondary production not only depends on the chemical lifetimes of X and Y, as stated in former studies, but also strongly depends on the initial concentrations of X and Y relative to their background (see Equation 5.6). If the enhancement of X approaches zero faster than the enhancement of Y, the EnR decreases and ultimately becomes zero. For the opposite case, the EnR increases and tends towards infinity when approaching the singularity caused by the denominator.

In Figure 5.5, the temporal evolution for two initial EnR values at different conditions (season, atmospheric layers and secondary production of acetone) is illustrated. For reasons of clarity, the range of uncertainty based on the uncertainties of the main

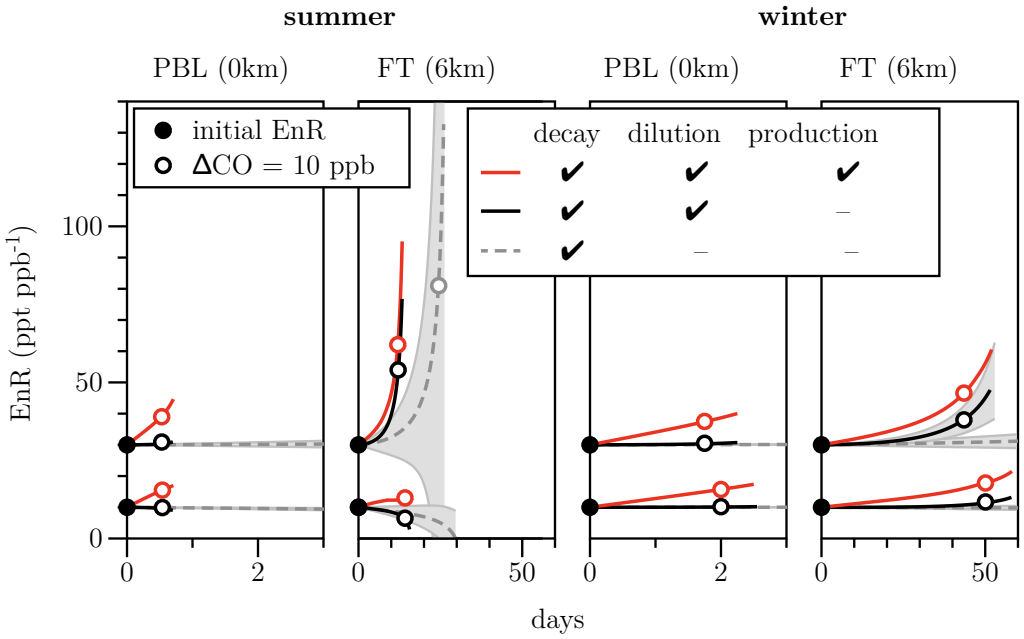

Figure 5.5.: Evolution of acetone–CO enhancement ratios (EnRs) in the mid-latitudinal planetary boundary layer (PBL) and free troposphere (FT) for summer and winter in the Northern Hemisphere calculated numerically (full equation including production term). In the grey dashed lines, only chemical decay of acetone and CO is considered. In the solid black lines dilution is considered in addition. The red lines represent the EnR evolution if acetone is additionally produced by the oxidation of propane. For selected curves, the range of uncertainty is exemplarily shown in light grey color. The terminating condition for the EnR calculation is a CO enhancement of 5 ppb. The open circles indicate an CO enhancement of 10 ppb. The underlying rates and concentrations are given in Table 5.5. Adopted from Fischbeck et al. (2017).

reaction rates is provided only for selected curves. The underlying mixing ratios and rates are given in Table 5.5. The free-tropospheric background concentrations are derived from CARIBIC data (see also Figure 5.8). For the PBL, estimates based on year-round measurements in Minnesota (Hu et al., 2013), California (Schade and Goldstein, 2006) and at Mace Head (Novelli et al., 2003) are used. The plume enhancements are scaled according to the selected EnR values. The chemical degradation rates are calculated as described above for 44° N, 1000 hPa (PBL) and 500 hPa (FT) for January (winter) and July (summer). The dilution rates are taken from Table 5.4 except for the value displayed for the FT in winter, which had to be estimated (as half the value reported for the FT in summer), as no observational data was available. Propane volume mixing ratios are estimated using data from Pozzer et al. (2010), Lewis et al. (2013) and Baker et al. (2014).

		Summer		Winter	
		PBL	FT	PBL	FT
Background [ppb]	Acetone	2.0	0.6	0.5	0.3
	CO	100	70	150	80
	Propane	0.1	0.1	1.0	0.2
Enhancement [ppb]	Acetone	4.2/2.0			
	CO	140/200			
	Propane	0.5			
Chemical loss rate [d^{-1}] (lifetime [weeks])	Acetone	0.029 ± 0.004 (5.0 ± 0.7)	0.049 ± 0.007 (2.9 ± 0.4)	0.002 ± 0.000 (82.9 ± 11.8)	0.004 ± 0.001 (37.0 ± 5.2)
	CO	0.026 ± 0.005 (5.5 ± 1.1)	0.039 ± 0.008 (3.6 ± 0.7)	0.002 ± 0.000 (94.0 ± 18.8)	0.003 ± 0.001 (49.3 ± 9.9)
	Propane	0.111 ± 0.023 (1.3 ± 0.3)	0.154 ± 0.031 (0.9 ± 0.2)	0.005 ± 0.001 (26.7 ± 5.3)	0.009 ± 0.002 (15.2 ± 3.0)
Dilution rate [d^{-1}]		4.80	0.10	1.44	0.05

Table 5.5.: Mixing ratios, chemical loss and dilution rates used for the simulation of the temporal evolution of acetone–CO EnRs shown in Figure 5.5. Adopted from Fischbeck et al. (2017).

In the PBL, EnR (without secondary production) hardly changes until dissolution of the plume, as dilution is the dominant loss process and the approximation used in Eq. 5.7 is valid. Taking the dilution rates (Table 5.5) as best estimate, the initially applied enhancements ratios will be completely dissolved in the PBL within less than 1 day in summer and 3 days in winter. Consequently, it is very likely that emissions of different adjacent sources may have mixed before the release into the free troposphere. This means that the free-tropospheric EnR as observed during IAGOS–CARIBIC flights will largely reflect a mean value representing the release of regionally well-mixed PBL air into the troposphere and not the emission ratios of single point sources of acetone and CO. In other words, the mixing in the PBL ensures that air masses released into the free troposphere have a specific signature that on average represents the general proportion of acetone and CO emissions within a certain radius. As already noted in Section 5.3, the spread of this source region depends on the residence time of the air mass in the PBL. Furthermore, the footprint is not restricted to sources that simultaneously emit both acetone and CO, but includes sources emitting only acetone or CO and also secondary production from precursors, if the residence time in the PBL is long compared to their lifetime.

As this study focuses on the pure signatures, which are necessary to assess the sources, the question arises as to how long the unaltered EnR is conserved in the free troposphere. The examples given in Figure 5.5 clearly show that the EnR changes

stronger and faster in summer due to shorter lifetimes. In any case, changes become largest in aged plumes, in which the CO enhancements in the denominator of the EnR become small. As the EnR tends towards infinity when the denominator converges towards zero, the CO enhancement is more sensitive than the acetone enhancement and, therefore, better suited, e.g., to define the dissolution of the plume. In Figure 5.5, a CO enhancement of 5 ppb is used as dissolution criterion for the calculated evolution of EnRs. In the given examples for the free troposphere in summer, the change of EnR is as high as $\sim 300\,\%$ at the time of dissolution, strongly depending on the initial CO enhancement and the presence of secondary acetone production.

As no information about the actual age of the plumes observed in CARIBIC is available, it is not possible to correct for the temporal changes. Therefore, the analysis done here is limited to plumes with a CO enhancement greater than 10 ppb (more specifically, 10 times the mean measurement uncertainty of CO; see Section 5.3). This threshold (open circles in Figure 5.5) clearly represents a trade-off between maximizing the number of detected correlations to achieve good statistics and minimizing the consideration of EnRs, which have been changed by chemistry and dilution to such an extent that conclusions about the source signature are not possible anymore. This problem and the sensitivity of results to the chosen threshold are further addressed in Appendix A.

In former studies, the observation of high acetone–CO EnRs was often associated with secondary production of acetone in the plume (Wisthaler et al., 2002; Holzinger et al., 2005). Propane is considered as the major precursor in this context, as it is co-emitted by biomass burning (Jacob et al., 2002; Fischer et al., 2012). If this source of acetone is considered in the model presented here, the loss of acetone is partly compensated and may lead to an increase in EnR. For plumes in the PBL, the temporal increase in EnR is therefore an indicator for secondary production of acetone. In the free troposphere, the situation is more complex and the model predicts an increase of EnR in three of four cases even without the presence of propane, although one has to admit that the range of uncertainty is very large in one case. Especially in summer, when the curves of the higher EnR with and without secondary production do not differ significantly, it seems to be hardly feasible to distinguish between the different reasons of increasing EnRs.

As mentioned earlier, another reason for possible changes in EnR between emission and measurement is the subsequent mixing with different backgrounds (e.g. Mauzerall et al., 1998; Yokelson et al., 2013). Equation 5.6 is only valid as long as the terms

$[X]_{\mathrm{bgnd}}$ and $[Y]_{\mathrm{bgnd}}$ are constant. Whenever the background mixing ratios change, e.g. the plume enters the free troposphere, the EnR becomes larger under the condition

$$\left([X]_{\mathrm{bgnd,old}} - [X]_{\mathrm{bgnd,new}}\right) > \mathrm{EnR}_{\mathrm{old}} \left([Y]_{\mathrm{bgnd,old}} - [Y]_{\mathrm{bgnd,new}}\right) \tag{5.8}$$

and smaller for the reverse inequality. Figure 1 illustrates this common scenario and the resulting change of the slope of the mixing line.

5.5. Observation of EnR within IAGOS–CARIBIC

5.5.1. Temporal and spatial distribution of data

The analysis of acetone–CO EnR relies on the availability of the simultaneous measurement of acetone and CO in the troposphere. At the time of this study, tropospheric acetone data were available for 105 CARIBIC flights between 20 February 2006 and 13 December 2008 and for 109 CARIBIC flights between 6 March 2012 and 16 July 2015. The gap is due to a larger modification of the instrument and subsequent re-certification.

As shown in Figure 5.6, about 90 % of simultaneous tropospheric acetone and CO measurements were carried out in the Northern Hemisphere, mainly in the subtropics and mid-latitudes along the routes between Germany and Caracas/Bogota, Sao Paolo, Chennai, Bangkok and Guangzhou/Hong Kong. Although IAGOS–CARIBIC flights to North America took place frequently, mainly stratospheric air was sampled due to the lower tropopause heights there. To obtain statistically reliable results, the following evaluation is therefore constrained to the subtropics and mid-latitudes.

5.5.2. Frequency distribution of EnR

In Figure 5.7, frequency distributions of the acetone–CO EnR are compared for summer (JJAS) and winter (DJFM). The commonly used months JJA (June–July–August) and DJF (December–January–February) are extended by the subsequent month to improve the statistics.

Compared to the airborne and ground observations by others (see Tables 2–3), the CARIBIC observations provide a surprisingly clear picture. To quantify the

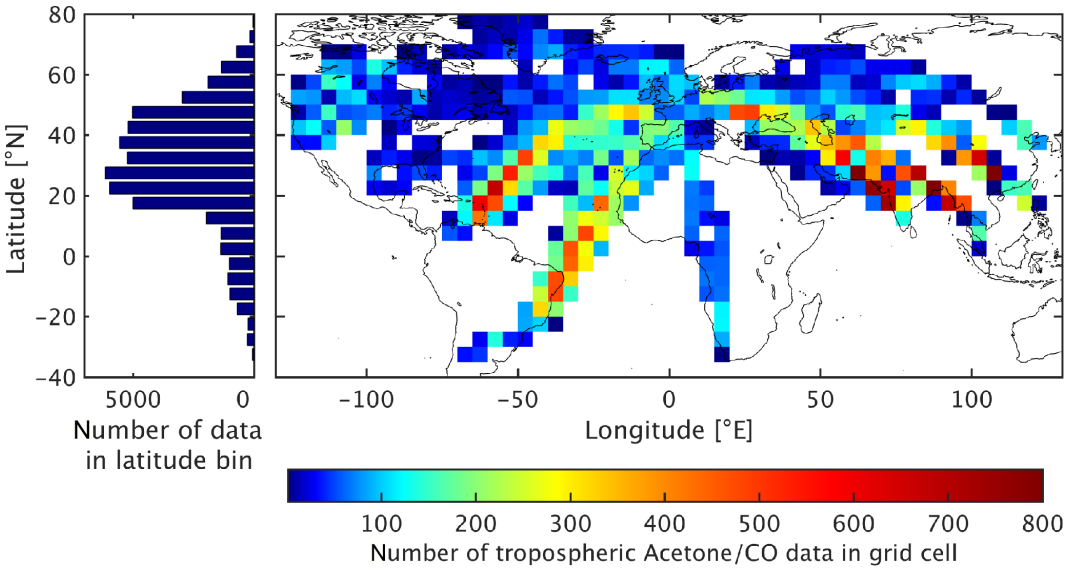

Figure 5.6.: Latitudinal (left) and geographical distribution (right) of simultaneous tropospheric acetone and CO measurements in the time periods February 2006–December 2008 and March 2012–July 2015. Grid cells without data are left bank. Adopted from Fischbeck et al. (2017).

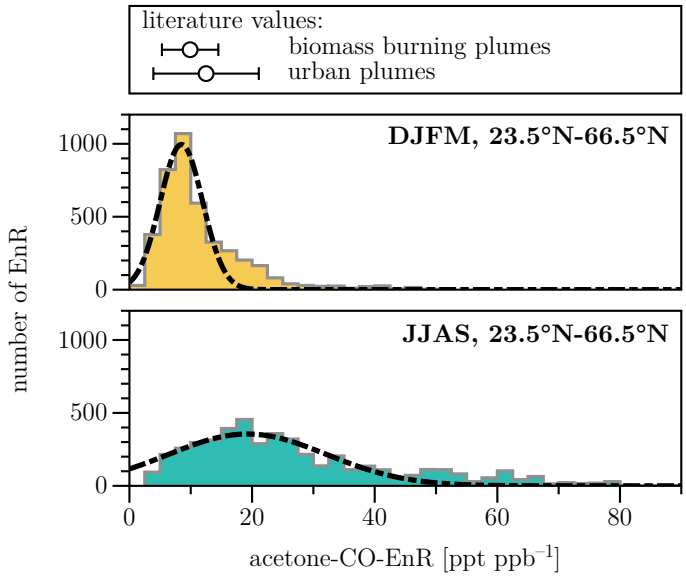

Figure 5.7.: Comparison of **(a)** the mean literature values for biomass burning plumes and for plumes of other origin with the distribution of EnR observed with CARIBIC in the Northern Hemisphere subtropics and mid-latitudes (23.5–66.5° N) in **(b)** winter (DJFM) and **(c)** summer (JJAS). The grey lines represent Gaussian curves fitted to the histograms. The values of the most important statistical variables describing the distributions are given in Table 5.6. Adopted from Fischbeck et al. (2017).

	Season	JJAS	DJFM
Slope/EnR [ppt ppb^{-1}]	Arithmetic mean $\pm\sigma$	27.2 ± 17.0	11.6 ± 7.2
	Median	22.9	9.4
	Gaussian line center $\pm\sigma$	19.3 ± 12.9	8.5 ± 3.5
	Number of correlated measurements	4747	4137
	Number of all measurements	12896	10311

Table 5.6.: Mean and median values of EnR frequency distributions and center of the fitted Gaussian distributions. Adopted from Fischbeck et al. (2017).

distributions, Gaussian profiles are used. In Table 5.6, the parameters resulting from the curve fitting are summarized. In winter, the approximated Gaussian profile has its center at 8.5 ppt ppb^{-1} (Full Width at Half Maximum (FWHM) = 8.2 ppt ppb^{-1}). Thus, the center is slightly lower than the mean literature values derived for plumes with and without biomass burning influence (9.9 and 12.5 ppt ppb^{-1}, respectively; see Table 5.3–5.2), but both values lie within the 1σ range. It is clear that the real distribution differs from a normal distribution, as 33 %/21 % of the EnRs exceed the $1\sigma/2\sigma$ range of the Gaussian profile. This asymmetry is probably a result of the sampling of aged plumes as discussed in Section 5.4.

In summer, observed EnRs are on average $\sim$2.3 times larger compared to winter. The center of the Gaussian profile (19.3 ppt ppb^{-1}) is higher than the mean literature values, but again the values lie within the 1σ range. The FWHM of the Gaussian profile is even $\sim$3.7 times greater ($\sim$30.4 ppt ppb^{-1}), reflecting the larger natural variability in summer. As in winter, the real distribution of CARIBIC EnRs is shifted towards larger values (mean: 27.2 ppt ppb^{-1}). About 30 %/$\sim$16 % of the EnRs exceed the $1\sigma/2\sigma$ range of the Gaussian profile. The great majority of high EnRs in summer was sampled in air masses measured above or originating from North America (see next section).

To identify the reason for the considerable seasonal variation of the acetone–CO EnR in the upper troposphere, the regression lines for the mean and median parameters (as derived from the observed EnR distributions, see Table 5.6) are plotted alongside the VMRs of the total measurements (see Figure 5.8). It becomes clear that the factor of $\sim$2.3 between summer and winter EnR is mainly the consequence of the considerable seasonality of acetone. The mean CO VMRs between JJAS and DJFM differ by only 6 %, simply as the CO maximum and minimum in the UT occur in March–April and September–October, respectively (Zahn et al., 2002; Zbinden et al., 2013; Petetin et al., 2016; Osman et al., 2016).

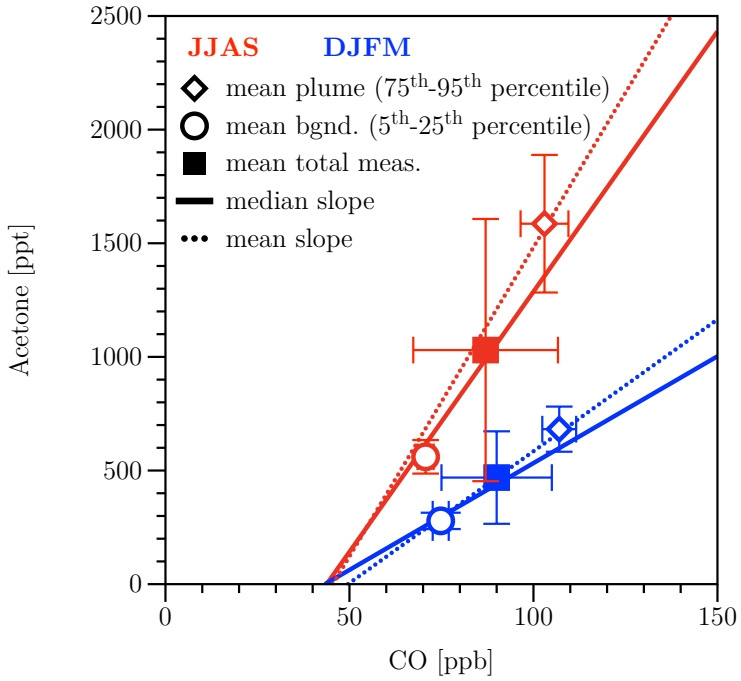

Figure 5.8.: Regression lines for summer (red) and winter (blue), using mean slope (solid line) and median slope (dotted line) given in Table 5.6. The filled squares represent the mean VMRs of the total measurements, whereas the open circles (diamonds) are the mean of all values lying in the 5th to 25th (75th and 95th) percentile, respectively. Adopted from Fischbeck et al. (2017).

5.6. Regional differences in EnR

In this subsection, sample location and 5-day ECMWF backward trajectories calculated every 3 min along the flight track (van Velthoven, 2016) are used to assign EnR to specific source regions. If a correlation is found in a subset of data (see Section 5.3), the derived EnR is assigned to each acetone–CO data pair of the subset and to the closest 5-day back trajectory thereof.

According to the box model (see grey dashed line in Figure 5.5), in the free troposphere chemical decay (no dilution) does not significantly alter the EnR within 5 days; in the given examples, changes are below 5 % in summer and below 1 % in winter. Therefore, each EnR is assigned to the full path of the corresponding 5-day back trajectory, which is given with a temporal resolution of 1 h. In practice, this means that for each hourly waypoint of the trajectory, the assigned EnR is duplicated and the coordinates of the sample location are exchanged by the ones of the waypoint.

This domain-filling technique is also known as trajectory mapping and has been applied elsewhere for similar in-situ datasets (Stohl et al., 2001; Osman et al., 2016). In Figure 5.9, the resulting geographical distribution and frequency of EnRs duplicated this way are shown based on a $5^\circ \times 5^\circ$ grid. It is recognized that the back trajectories have limited reliability. However, random trajectory errors should be negligible here, with respect to the large number of trajectory-mapped EnRs.

The assignment of EnRs to source regions is done as follows. In a first step, longitude–latitude boxes are defined for the regions of interest. In this case, North America, Europe, East Asia and Southeast Asia have been selected (see Figure 5.9). All EnRs with coordinates inside a box, including the duplicates from the trajectory mapping, are assigned to the corresponding region. This means, that an EnR is initially assigned to a region regardless of whether the trajectory passed through the box only for 1 h or the entire 5 days. However, when it comes to averaging over all EnRs of a certain region, the different situations shall be considered. For this purpose, the duplicates created by the trajectory mapping are not eliminated. Consequently, an EnR associated with a trajectory passing the box only for 1 h, is represented only once in the regional subset, whereas an EnR with a trajectory staying in the box for 5 days is represented in the subset 120 ($= 5 \times 24$ h) times. When averaging over EnRs of a certain region, this naturally leads to a weighting based on the trajectory's residence time above the region.

The altitude of the trajectory is not considered here, simply due to the fact that not all transport processes are represented by single trajectory calculations (e.g. convection; see Stohl et al., 2002). Furthermore, in single trajectory calculations infinitesimally small air parcels are assumed (e.g. Stohl et al., 2002), whereas the volumes of sampled air masses are extended. For these reasons, it is believed that even though a trajectory passes a region at high altitudes, there is a certain likelihood that the sampled air mass had contact with convected air masses from the boundary layer of the underlying region. As the probability of such an incident increases with time, weighting according to the trajectory's residence time over the region seems to be the most reasonable choice.

In Figure 5.10, the weighted-mean EnRs and box plots are shown for each source region and the months JJAS and DJFM, respectively. The numbers of the underlying, unique (i.e. non-duplicated) EnRs and percentages of the total number of EnRs are given in Table 5.7. Please note that single EnRs can be assigned to multiple regions, when the trajectories pass through more than one region.

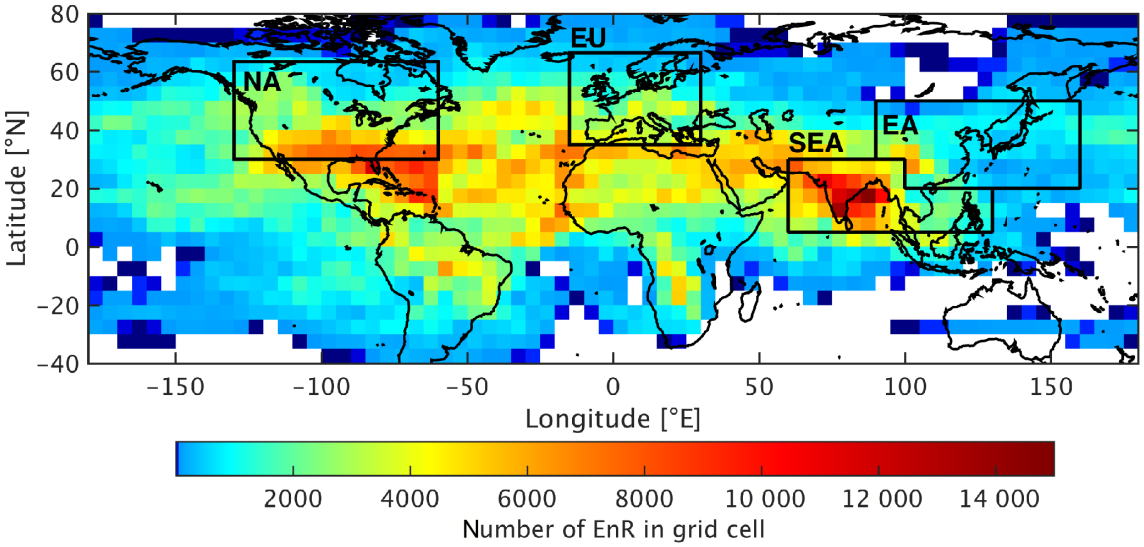

Figure 5.9.: Geographical distribution of EnRs duplicated along the waypoints of the assigned 5-day back trajectories. Grid cells without data are left bank. Four areas of interest (rectangles) are considered: North America (NA), Europe (EU), Southeast Asia (SEA) or East Asia (EA). Adopted from Fischbeck et al. (2017).

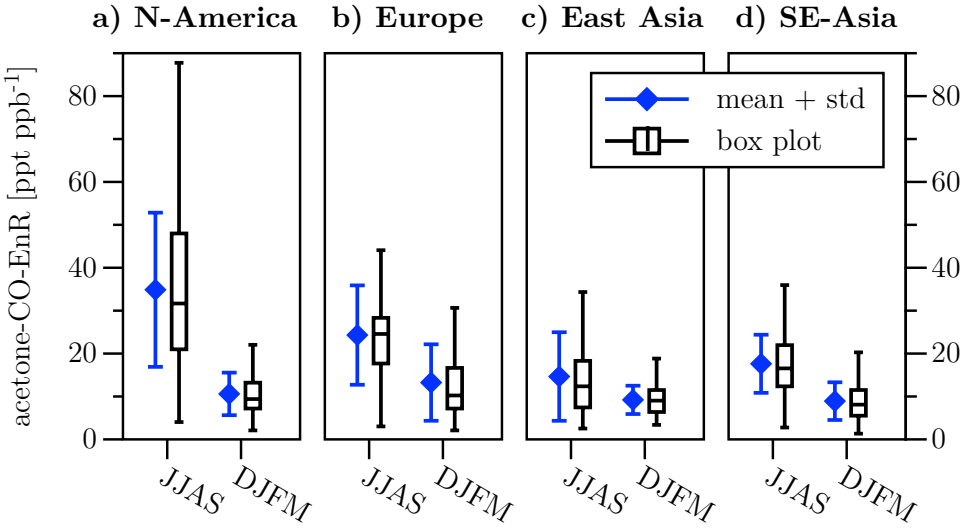

Figure 5.10.: Mean and standard deviation (SD) (blue) and box plots (black) of EnR summer (JJAS) and winter (DJFM) distributions for four selected regions as shown in Figure 5.9. In the underlying distributions, individual EnRs have been duplicated along the hourly waypoints of the assigned 5-day back trajectories to consider the residence time of the samples above the region. The numbers of individual, unique EnRs as well as percentages related to the total number of EnRs are given in Table 5.7. Adopted from Fischbeck et al. (2017).

	North America		Europe		East Asia		Southeast Asia		Global	
JJAS	3060	15 %	1218	6 %	1272	6 %	992	5 %	6535	32 %
DJFM	1725	8 %	1688	8 %	685	3 %	2255	11 %	7686	37 %
Other months	2085	10 %	1344	7 %	1343	7 %	2262	11 %	6431	31 %
All months	6870	33 %	4250	21 %	3300	16 %	5509	27 %	20 652	100 %

Table 5.7.: Numbers and percentages of individual EnRs for different months and regions. EnRs are associated with a specific region, when the assigned trajectory passes through the box of the region. For the assignment it does not matter whether only one waypoint or the entire trajectory lies inside the box. Assignment to multiple regions occurs, when the trajectory crosses more than one box. The boxes of the respective regions are indicated in Figure 5.9. Adopted from Fischbeck et al. (2017).

The best coverage is archived for North America (33 %) and Southeast Asia (27 %), which is also why these regions are evaluated in more detail in the following sections.

North America stands out with the highest EnRs observed in IAGOS–CARIBIC. In summer, the median EnR (31.7 ppt ppb^{-1}) is $\sim$3.4 times larger than in winter (9.4 ppt ppb^{-1}) and the interquartile range is even $\sim$5.4 times larger compared to winter. The significantly higher EnR in summer compared to winter can be explained by the following reasons: (i) the much stronger biogenic source strength in summer, (ii) the more frequent sampling of younger (acetone-rich) plumes due to strong convection and (iii) the faster increase in EnR due to shorter chemical lifetimes (see Section 5.4 and Figure 5.5). The seasonality is less pronounced (in descending order) above Europe, Southeast Asia and East Asia. In contrast to the mean EnRs, individual low EnRs are observed throughout the year in all regions, as can be seen from the overlap of the lower whiskers in Figure 5.10. Low EnR in summer might be an indication of rapidly ascended plumes from sources with low acetone–CO emission ratios, such as smoldering fires and other incomplete combustion processes (see Table 5.1).

5.7. Acetone emission rates in North America

As a next logical step towards identifying the cause for the high EnRs over North America in summer, bottom-up source estimates provided by emissions inventories (see Section 5.3.1) are utilized. In general, these inventories provide separate emission estimates for the major sources (e.g. anthropogenic, biogenic and biomass burning emissions) and thus, allow for an assessment of the individual contributions of the

individual sources to the total emissions (the same was done in Section 1.1 to determine the contributions specified in Table 1.1). It is exactly this information that might provide a decisive hint for further interpretation of the observed seasonal variability in EnR.

To enable comparisons with observed EnR, the ratio of total emissions of acetone and CO provided in the inventories needs to be calculated in terms of volume. For reasons of simplicity, this ratio is referred to as Total Emissions volume Ratio (TER) in the following. It is defined as

$$\mathrm{TER} = \frac{M_{\mathrm{CO}}}{M_{\mathrm{Ac}}} \cdot \frac{\sum\limits_i S_{\mathrm{Ac},i}}{\sum\limits_i S_{\mathrm{CO},i}}, \tag{5.9}$$

where M is the molar mass of the respective compound and S is the emission flux of the individual source averaged over the reference time period 2005–2010.

In Figure 5.11, the seasonal variation of (a) the acetone emission rates, (b) the CO emission rates and (c) the monthly means of TERs and EnRs are shown. The emissions of acetone and CO are in phase with maxima in summer and minima in winter, but the seasonal amplitude for acetone is much stronger due to the larger proportion of biogenic emissions. In Figure 5.11c, the inventory-based TER (with and without the consideration of biomass burning emissions) is compared with the monthly means of IAGOS–CARIBIC EnR identified during the two time periods 2006–2008 and 2012–2015.

It is important to note here that a direct comparison of both ratios makes only sense if the considered CARIBIC EnRs are not significantly altered by dilution and chemical processing. As discussed in Section 5.4, the effects of these processes are not negligible and for this reason, the analysis is limited to events with a CO enhancement of at least 10 times the measurement uncertainty of CO ($\sim 10\,\mathrm{ppb}$). In the ideal case, this restriction ensures that CARIBIC EnRs primarily reflect the chemical signature of the source regions.

The highest EnR are found in June and September ($\sim 40\,\mathrm{ppt\,ppb^{-1}}$) with a temporary decline in-between. On the first view, this seems to be an insignificant feature, but there are some further observations that identify biomass burning as the most likely reason:

1. Elevated acetonitrile VMRs were observed during this time period. In $\sim 53\,\%$

of the air masses with correlated acetone and CO measurements, acetonitrile VMRs were greater than 200 ppt, which according to Sakamoto et al. (2015) presents a threshold for the detection of biomass burning plumes. EnRs in June appear to be unaffected by biomass burning, supported by the consistently lower acetonitrile VMR level (< 200 ppt) compared to the following month.

2. The EnR decline is also apparent in TER with a shift of 1 month ahead, which can be attributed to biomass burning (orange diamonds in Figure 5.11c). The reason lies in the low acetone–CO emission ratio of boreal forest fires of 1.6–3.0 ppt ppb^{-1} (see Table 5.1). Warneke et al. (2006) found various plumes attributed to biomass burning during flights along the US east coast in July and August 2004 and concluded that 30 % of the CO enhancement is related to forest fires in Alaska and Canada, which is in good agreement with the emission inventory data (~ 32 %). It is therefore assumed that the lower EnRs in July and August (~ 30 ppt ppb^{-1}) are related to a then larger influence of biomass burning.

In July, a mean ($\pm$standard deviation) EnR of (28.0 ± 14.0) ppt ppb^{-1} is found, comparable to the ones observed during aircraft campaigns over eastern Canada, e.g. by de Reus et al. (2003) during STREAM (Stratosphere Troposphere Experiment by Airborne Measurements) in July 1998 (24.4 ppt ppb^{-1}) and by Singh et al. (1994) during ABLE3B (Arctic Boundary Layer Experiment) in July and August 1990 (30 ppt ppb^{-1}). The higher variability in the IAGOS–CARIBIC EnR is presumably due to the large regional and annual variations in emissions, which are only resolved when considering local correlations over a longer time interval such as in IAGOS–CARIBIC.

5.8. Estimation of North American acetone source

Emission and enhancement ratios are frequently used to estimate global acetone emissions from biomass burning (e.g. Holzinger et al., 1999, 2005; Jacob et al., 2002; Wisthaler et al., 2002; Singh et al., 2004; van der Werf et al., 2010; Akagi et al., 2011). Singh et al. (2010) denoted that this top-down approach is often useful in assessing the accuracy of emission inventories that are generally derived from bottom-up data. Since the analysis was not restricted to biomass burning plumes, the IAGOS–CARIBIC EnRs should reflect the total acetone source. In order to derive the total acetone flux S_{Ac} from the observed EnRs, the mass-corrected CARIBIC

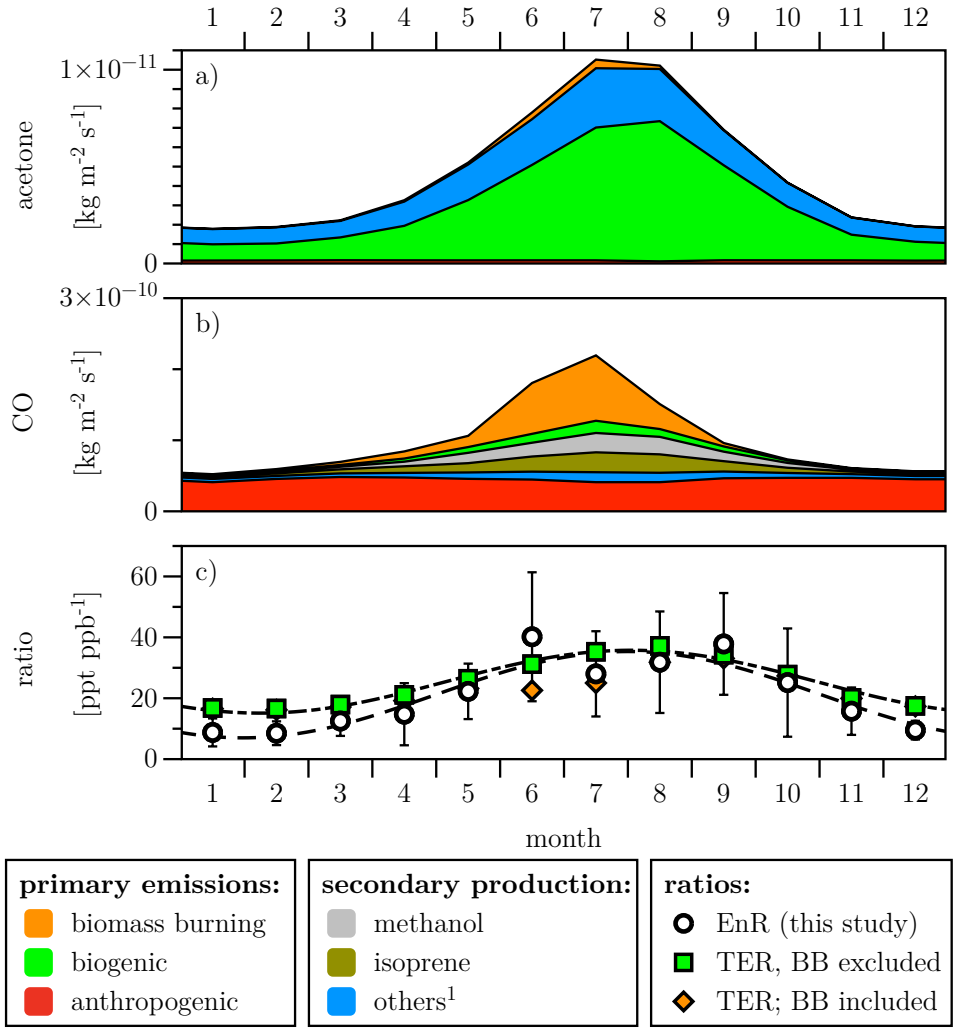

Figure 5.11.: North American emission rates of **(a)** acetone and **(b)** CO according to the ECCAD inventory database, averaged over the time period 2005–2010. **(c)** Mean EnRs derived from IAGOS–CARIBIC measurements are compared to ECCAD total emissions volume ratios (TERs) of acetone and CO with and without consideration of biomass burning (BB). The dashed lines show sinusoidal functions fitted to the monthly means of EnR and TER (biomass burning excluded). [1] Includes propane, isobutane, isopentane, seven monoterpene species and methylbutenol as precursors of acetone and ethene, ($\geq C_4$) alkanes, ($\geq C_3$) alkenes and monoterpenes as precursors of CO. Adopted from Fischbeck et al. (2017).

EnR is multiplied by the total flux of CO derived from inventories:

$$S_{\mathrm{Ac}} = \mathrm{EnR} \cdot \frac{M_{\mathrm{Ac}}}{M_{\mathrm{CO}}} \cdot \sum_i S_{\mathrm{CO},i}. \tag{5.10}$$

For North America, a mean annual flux of $(53 \pm 27)\,10^{-13}\,\mathrm{kg\,m^{-2}\,s^{-1}}$ is estimated, corresponding to total emissions of $(6.0 \pm 3.1)\,\mathrm{Tg\,a^{-1}}$. This is in very good agreement with the bottom-up estimate of $5.8\,\mathrm{Tg\,a^{-1}}$, which is the result of summing up the mean acetone emissions given in the source-specific emission inventories (see Section 5.3.1).

In contrast, Hu et al. (2013) determined a North American acetone source of $10.9\,\mathrm{Tg\,a^{-1}}$ from tall-tower measurements and inverse modeling, consisting of 5.5 Tg from biogenic sources and 5.4 Tg from anthropogenic sources. Whereas the biogenic source is similar to the estimate of this study, simply because the same a priori source is used (4.8 Tg), they assume a much higher anthropogenic source based on the US EPA NEI 2005 (NEI-05) inventory (12 % primary, 88 % secondary). Please note that anthropogenic emissions of acetone, propane and CO in NEI-05 are ~ 3, ~ 2 and ~ 1.5 times higher, respectively, than the ones given by the MACCity inventory used in this study. Several studies stated that NEI-05 overestimates anthropogenic emissions of CO and other species (Brioude et al., 2011, 2013; Kim et al., 2013; Li et al., 2015), whereas Stein et al. (2014) reported that the anthropogenic emissions of CO in MACCity underestimate the source in Northern Hemisphere industrialized countries in winter. The latter would be in accordance with the observation of lower EnR compared to TER in winter in Figure 5.11c. A larger anthropogenic acetone source would push EnRs in the opposite direction and is not supported by IAGOS–CARIBIC EnR results. Further investigations are required to resolve the discrepancy between the above-mentioned model result of Hu et al. (2013) and the bottom-up and top-down estimates.

5.9. Acetone emission in Southeast Asia

The focus of this section is to assess regional acetone sources to the Southeast Asia region. Due to its increasing role in global air pollution and the current shortage of in-situ studies regarding the emissions of this region, Southeast Asia stands out as a highly interesting region (Jaffe et al., 1999; de Laat et al., 2001; Lelieveld et al., 2001, 2015). The rapid industrialization is accompanied by widespread biomass burning resulting in a significantly different pollution source profile compared to North America (e.g. de Laat et al., 2001). Here the focus is on the region of Southeast Asia (including Pakistan, India, Bangladesh, Bhutan, Myanmar, Thailand, Laos, Cambodia, Vietnam and the Philippines) as defined in van der Werf et al. (2006).

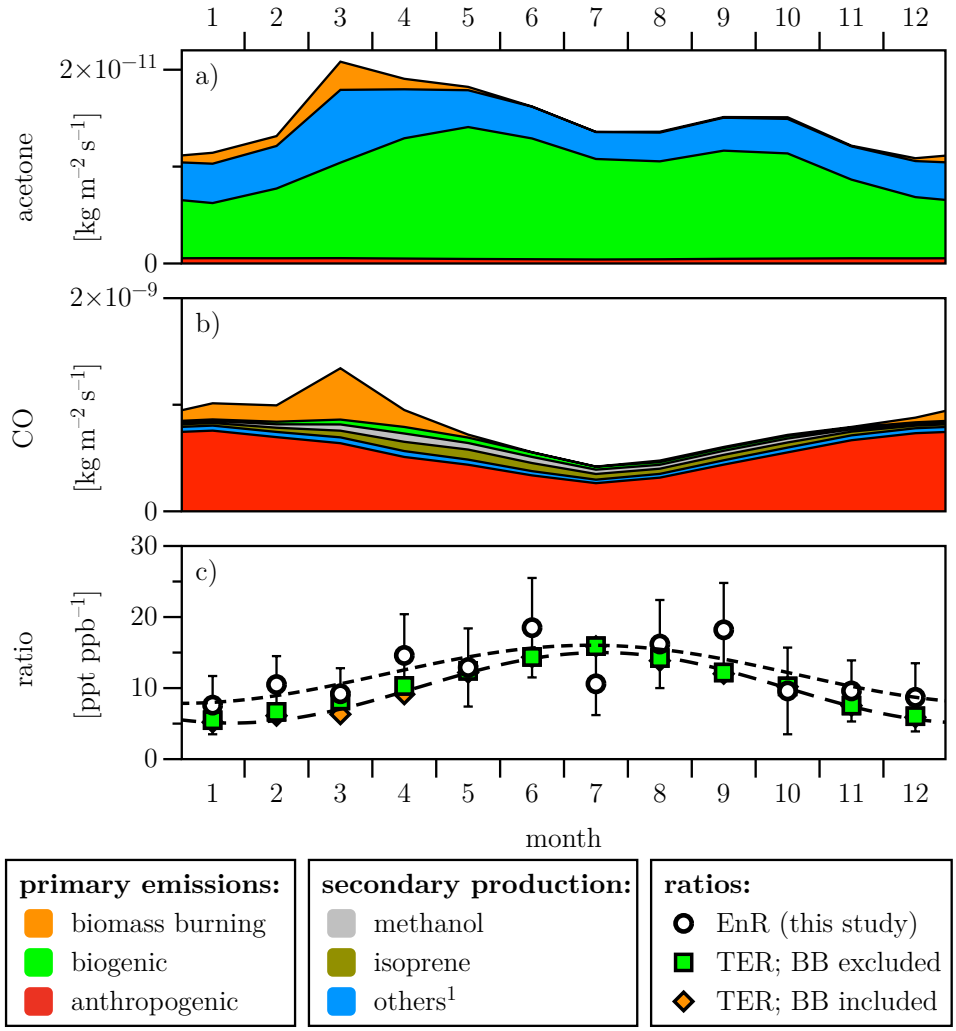

Figure 5.12.: Southeast Asian emission rates of **(a)** acetone and **(b)** CO according to the ECCAD database for the time period 2005–2010. **(c)** Volume ratio of total emissions of acetone and CO displayed for three different scenarios and compared to EnR derived from IAGOS–CARIBIC in-situ data. A sinusoidal function (dashed line) is fitted to the monthly means of EnR and total emissions volume ratio (TER), respectively (see Figure 5.11). [1] Includes propane, isobutane, isopentane and seven monoterpene species as precursors of acetone and ethene, ($\geq C_4$) alkanes, ($\geq C_3$) alkenes and monoterpenes as precursors of CO. Adopted from Fischbeck et al. (2017).

In this region, the acetone emission fluxes given in the inventories (Figure 5.12a) are on average $\sim$3 times higher than in North America and show a different seasonality due to the different (i.e. mainly wet tropical and humid subtropical) climate. Emissions of CO (Figure 5.12b) are mainly assigned to anthropogenic sources throughout the year, showing a maximum in March due to biomass burning emissions and a minimum in

July.

In Figure 5.12c, TER and IAGOS–CARIBIC EnR are plotted for comparison. As for North America, both are in the same range and show the same seasonal variation when fitting a sinusoidal function to the monthly TER and EnR, but EnR (annual mean: 12.2 ppt ppb^{-1}) are on average $\sim$3 ppt ppb^{-1} higher than TER (annual mean: 9.2 ppt ppb^{-1}). EnR values derived from the research aircraft campaign INDOEX (INDian Ocean EXperiment) conducted over the Indian Ocean in February–March 1999 are even higher than mean CARIBIC EnRs for February and March (9.7 ppt ppb^{-1}).

De Reus et al. (2003) found a mean EnR of 21.6 and 16.2 ppt ppb^{-1} when integrating over all flights in the free troposphere and in the marine boundary layer air, respectively. De Gouw et al. (2001) derived an EnR of 14 ppt ppb^{-1} using data from the same campaign, but averaged acetone and CO values for level flight tracks before applying the correlation analysis. The results are consistent with the EnRs of 13.4–17.2 ppt ppb^{-1} found in individual plumes in the marine boundary layer over the Indian Ocean (Reiner et al., 2001; Wisthaler et al., 2002).

The reasons for the high EnRs in INDOEX compared to the mean TER of Southeast Asia ($\sim$7.7 ppt ppb^{-1}) and the mean CARIBIC EnR (9.7 ppt ppb^{-1}) can be manifold. Besides this comprehensive campaign in 1999, little data have been published on acetone emissions in this region.

Based on the IAGOS–CARIBIC EnR and inventory data for CO and its precursors, a mean ($\pm$ standard deviation) acetone flux of $(185 \pm 80)\,10^{-13}$ kg m^{-2} s^{-1} is derived, corresponding to total emissions of (4.8 ± 2.1) Tg a^{-1}. Langford et al. (2010) observed a mean acetone flux of $(33 \pm 181)\,10^{-13}$ kg m^{-2} s^{-1} above a tropical rainforest in Malaysia in 2008, whereas Karl et al. (2004) reported a mean midday flux of 250×10^{-13} kg m^{-2} s^{-1} above a tropical rainforest in Costa Rica. All three fluxes are in the same range, but hardly comparable, because of the different spatial and temporal scopes of the measurements. Whereas the in-situ flux measurements at individual locations reflect local conditions, the mean CARIBIC EnRs are representative of extended heterogeneous source regions and also capture secondary acetone production during transport.

The inventory data for acetone and its precursors suggests a mean annual flux of 149×10^{-13} kg m^{-2} s^{-1} and an annual source of 3.7 Tg a^{-1} for Southeast Asia, which is lower than our estimates, but well within the standard deviation.

5.10. Summary and conclusions

This chapter provides a major update on enhancement ratios of acetone and CO in the upper troposphere. A new method to detect coherent correlations being physically more meaningful than correlations based on spatially or temporally distant measurements is presented.

This method is applied to the IAGOS–CARIBIC dataset of acetone and CO and the concept of enhancement ratios is successfully utilized for interpretation. In former studies, free-tropospheric acetone–CO enhancement ratios were often compared directly with emission ratios of individual sources, although enhancement ratios are only equivalent to the emission ratio when measured at the source. For EnRs higher than the ERs, the respective authors assumed secondary production of acetone in the plume.

In this work, however, it is shown that an increase in EnR is not inevitably caused by secondary production of acetone, but strongly depends on the initial quantities of acetone and CO in the plume. Dilution rates from other studies indicate that common enhancements are rapidly mixed in the PBL and rather contribute to the PBL background than being directly transported into the free troposphere. It is concluded that an uplift of these air masses leads to tropospheric EnRs that can be interpreted as chemical signatures of the boundary layer air, therefore rather reflecting larger regional source patterns than distinct emissions from single point sources.

As the sources vary by season, the seasonality of EnR is investigated. It is found that in the Northern Hemisphere mid-latitudes EnRs are on average 2.3 times larger in summer than in winter. Given the coverage and representativeness of the IAGOS–CARIBIC dataset, it is also possible to investigate regional differences in EnR and its seasonality. When comparing the seasonality of EnRs observed over North America, Europe, East Asia and Southeast Asia, it is found that the general behavior is the same, but the amplitude of the seasonal cycle differs from region to region. It is assumed that these differences are mainly caused by regional differences in acetone and CO sources and therefore enable the comparison of EnR with emission estimates of inventories. The monthly ratios of the total acetone and CO bottom-up source estimates lie well within the standard deviation of mean EnR observed over the respective region and show the same seasonal course as EnR.

Regional acetone fluxes are subsequently calculated using well-constrained CO emission data and monthly averaged EnR. For North America and Southeast Asia, mean annual acetone fluxes of $53 \times 10^{-13}\,\mathrm{kg\,m^{-2}\,s^{-1}}$ and $185 \times 10^{-13}\,\mathrm{kg\,m^{-2}\,s^{-1}}$, respectively, are estimated. These values reflect the dominance of biogenic acetone emissions that are larger in tropical to subtropical Southeast Asia.

With the EnR-based approach, it will be also possible to estimate regional acetone fluxes for other regions in the future. First preliminary evaluations for tropical South America show that EnRs are significantly lower than the monthly total emission ratios derived from inventories, except for months with high biomass burning emissions. It could well be that the large biogenic source of the Amazon rainforest does not provide sufficiently strong regional gradients (plumes) to be captured by the event-based detection algorithm. However, the detected EnRs might be related to biomass burning or polluted air masses from the highly populated coastal regions. Further investigations, e.g. analysis of other tracers or evaluation of the box model adapted to the particular conditions, are necessary to understand this potential discrepancy. In addition, further measurements over this region would be of great value.

It is concluded that free-tropospheric EnR data with a large spatial and temporal coverage are a powerful tool to investigate the regional and seasonal differences in sources, to estimate the total acetone flux of specific regions and potentially to assess the quality of acetone emission inventories.

6. Global atmospheric budget and distribution of acetonitrile

Acetonitrile (CH_3CN) is the second most abundant cyanide in the atmosphere after hydrogen cyanide (HCN) and omnipresent in the UTLS (Singh et al., 2003). Due to its relatively long tropospheric lifetime in the order of ∼6 months (e.g. Harrison and Bernath, 2013) and the fact that it is almost exclusively emitted by biomass burning, it is an ideal, unique tracer for biomass burning (Lobert et al., 1990; Holzinger et al., 1999; Warneke et al., 2006; Akagi et al., 2011). Such tracers are essential to study the transport to and impact of biomass burning emissions on remote atmospheric regions, which react most sensitive to changes.

Despite the great significance of CH_3CN as tracer, its atmospheric budget is subject to considerable uncertainty. The current knowledge is based on the data of a few field campaigns with limited spatial and temporal coverage. In the last years, CH_3CN measurements have been mainly used to identify encountered biomass burning plumes. This allows to investigate the composition and temporal evolution of such plumes.

However, to understand the impact of biomass burning on atmospheric regions, e.g. the UTLS, regular, longer-term measurements of CH_3CN are required. Within the CARIBIC project, CH_3CN has been measured for 7 years in the UTLS. So far, the data has only been used to identify biomass burning plumes, but the unique spatial and temporal coverage of the data set has far more potential. Comparisons with model simulations would allow to assess the current knowledge of the CH_3CN budget and to estimate emissions from a top-down perspective.

As CH_3CN does not belong to the suite of reactive species emitted by biomass burning, it has been rarely taken into account in model simulations and emission inventories. Despite the large uncertainties in the budget of CH_3CN, only one model study has been conducted so far (Li et al., 2003), where evaluation is limited to a time period of 2 months in 2001.

Before this study, none of the chemistry transport models used at the IMK included CH_3CN and only one emission inventory containing CH_3CN data was available. However, the inventory data is only available for the first three years of the CARIBIC operation and will not be continued.

To remedy these deficiencies, CH_3CN was preliminarily implemented into the model ICON-ART. Furthermore, the integration of the most recent available biomass burning emission inventory was realized. This new CH_3CN inventory has several advantages, which will substantially improve the simulation of biomass burning emissions in ICON-ART, not only with regard to CH_3CN. In this chapter, the current status of the implementation is described and first results of the model simulations are shown.

6.1. Current knowledge about the CH_3CN budget

In the troposphere, typical abundances of CH_3CN are in the range of 50 to 200 ppt (e.g. Hamm et al., 1989; Schneider et al., 1997; Crutzen et al., 2000; Singh et al., 2003; Scheeren et al., 2003; Traub et al., 2003; Kleinböhl et al., 2005). Biomass burning is believed to be by far the dominant source of atmospheric CH_3CN (Lobert et al., 1990; Holzinger et al., 1999; Li et al., 2003), with minor contributions from car exhausts (Arijs and Brasseur, 1986; Holzinger et al., 2001; Moussa et al., 2016). Emission estimates based on molar emission ratios (relative to CO) and CO emission data, which both have large uncertainties, vary from 0.4 to 2.2 Tg per year (Lobert et al., 1990; Hamm and Warnek, 1990; Holzinger et al., 1999; Andreae and Merlet, 2001; Singh et al., 2003; Li et al., 2003).

The sinks of CH_3CN are less well known. It is well established that the reaction with OH is the main loss mechanism in the UTLS (Arijs and Brasseur, 1986), leading to lifetimes of 17–26 months (Singh et al., 2003; Li et al., 2003; de Gouw et al., 2003c). In the stratosphere, the lifetime is thought to be considerably longer. Arijs and Brasseur (1986) estimated a lifetime of 20 years at 20 km, which is consistent with the findings (10–20 years in the lower stratosphere) of Kleinböhl et al. (2005). Recently, Harrison and Bernath (2013) determined a stratospheric lifetime of 73years using the linear correlation between CH_3CN and CFC-11 and the lifetime of the latter.

In the lower troposphere, the lifetime might be significantly shorter as the above-

mentioned 17–26 months, due to oceanic uptake of CH_3CN. This sink was first suggested by Hamm et al. (1984) and again proposed by Hamm and Warneck (1990) to balance the known emissions and the observed VMRs. Although there is no direct evidence of this sink (Singh et al., 2003), observed vertical gradients of CH_3CN in the marine boundary layer support the presence of the proposed sink (Jost et al., 2003a; de Gouw et al., 2003c; Singh et al., 2003). Including the oceanic sink in their calculations, Hamm and Warneck (1990), Singh et al. (2003) and Li et al. (2003) found overall tropospheric lifetimes in the range of 5.4 – 6.6 months.

6.2. Acetonitrile in the model ICON-ART

Chemistry transport models are a powerful tool to investigate the budget of trace gases like CH_3CN, its distribution and variability in the atmosphere on a global and seasonal scale. To the author's knowledge, only one global modeling study of CH_3CN has been conducted so far in order to improve the understanding of the atmospheric CH_3CN budget (Li et al., 2003). They used measurements over the Pacific Ocean during the TRACE-P campaign between February and April 2001 to constrain the oceanic sink of CH_3CN and extrapolated the observations in time and space to derive a global budget, but also noted that far more measurements are required to determine a more accurate and reliable global budget.

Meanwhile, CH_3CN has been measured over a period of 7 years onboard the CARIBIC passenger aircraft and at a few ground-based stations (e.g. Jordan et al., 2009b; Hu, 2014; Patokoski et al., 2015). This long-term data sets and in particularly the good spatial coverage of the CARIBIC data set are well suited to further constrain the global budget of CH_3CN when comparing them with model simulations. Therefore, a first attempt was made to implement CH_3CN into the ART (Aerosols and Reactive Trace gases) extension of the ICON (ICOsahedral Nonhydrostatic) model.

ICON is the result of a collaboration between the German weather forecasting service DWD (Deutscher Wetterdienst, Offenbach, Germany) and the Max Planck Institute of Meteorology (MPI-M; Hamburg, Germany) to develop a unified model for global and regional weather forecasting and climate simulations (Bonaventura, 2004; Zängl et al., 2015). It is non-hydrostatic and makes use of an icosahedral grid.

Here, only the most important details about ICON are presented. For additional information, please refer to the extensive literature about ICON (e.g. Wan et al.,

2013; Zängl et al., 2015, Reinert et al., 2017, Heinze et al., 2017). The usage of the unfiltered, non-hydrostatic Navier-Stokes equations, equations allows ICON to be operated at scales, where the hydrostatic assumption is no longer valid ($\leq$10 km, see Daley, 1988). As a result, physical processes such as cumulus convection can be directly simulated and do not need to be parameterized anymore (e.g. Tomita and Satoh, 2004)

Also the icosahedral grid has a number of advantages: As it divides the sphere into nearly equal elements with regard to area and shape, it is better suited to numerically integrate the motion equations in the global domain than other grids (Sadourny et al., 1968). Furthermore, it is not affected by over-sampling near the poles as it is the case for a conventional longitude-latitude grid. For detailed information about the ICON model, the reader may refer to the extensive literature.

The ART module, which is currently developed at IMK, extends ICON to a chemistry transport model by incorporating a full gas-phase and aerosol chemistry (Rieger et al., 2015; Schröter et al., 2016; Weimer et al., 2017).

6.2.1. Implementation of sinks

In the atmosphere, the removal of a compound at a certain location commonly depends on the abundance of the reaction partner (e.g. OH radicals) and physical properties (pressure, temperature, light). Therefore, removal rates can vary considerably with location and time. In this first model approach, removal of CH_3CN was implemented more simple by assuming temporally constant removal rates for the marine boundary layer, troposphere and stratosphere. The corresponding lifetimes are summarized in Table 6.1.

A description of the technical implementation of the sinks is provided in Section C.1 of Appendix C. To distinguish between troposphere and stratosphere, the tropopause

Atmospheric Layer	Lifetime
Stratosphere	70 years
Free troposphere and continental boundary layer	22.3 months
Marine boundary layer	21 days

Table 6.1.: Implemented lifetimes of CH_3CN for different atmospheric layers in ICON-ART.

height according to the WMO definition was determined for each model time step and column.

The removal rate in the stratosphere was set to the inverse of 70 years similar to the 73 years estimated by Harrison and Bernath (2013). The lifetime in the free troposphere and the planetary boundary layer was estimated using the temperature-dependent reaction rate recommended by the IUPAC (Atkinson et al., 2004)

$$k(T) = 8.1 \times 10^{-13} \exp^{(-\frac{1080}{T})} \text{cm}^3 \text{ molecule}^{-1} \text{ s}^{-1}, \tag{6.1}$$

a mean tropospheric temperature of 273 K (Seinfeld and Pandis, 2016) and a mean tropospheric OH abundance of 1.1×10^6 molecules cm^{-3} (Spivakovsky et al., 2000; Lelieveld et al., 2016). These assumptions result in an OH-driven tropospheric lifetime of 22.3 months, which is close to the 23 months determined by Singh et al. (2003). The inverse of this lifetime was used as removal rate for the whole troposphere, except for the lowest 8 model layers (0–750 meter) above the oceans, where oceanic uptake is supposed to lead to significantly lower lifetimes. Hamm and Warneck (1990) determined a minimum lifetime of 15 days in the marine boundary layer. Here, 21 days were used, resulting in an overall tropospheric lifetime of 6.5 months, consistent with the estimates of Singh et al. (2003) and Li et al. (2003).

The overall tropospheric lifetime $\bar{\tau}$ emerges from the consideration of the globally integrated tropospheric sink of CH_3CN

$$L = \int \frac{[\text{CH}_3\text{CN}](\vec{x})}{\tau(\vec{x})} \, \text{d}V = \frac{1}{\bar{\tau}} \int [\text{CH}_3\text{CN}](\vec{x}) \, \text{d}V, \tag{6.2}$$

where $\tau(\vec{x})$ is the lifetime and $[\text{CH}_3\text{CN}](\vec{x})$ the concentration of CH_3CN at the position $\vec{x}$. Integrating the latter over the tropospheric volume gives the total amount of CH_3CN, which is also referred to as tropospheric burden B. Rearranging of Equation 6.2 leads to the definition of the overall tropospheric lifetime

$$\bar{\tau} = \frac{\int [\text{CH}_3\text{CN}](\vec{x}) \, \text{d}V}{\int \frac{[\text{CH}_3\text{CN}](\vec{x})}{\tau(\vec{x})} \, \text{d}V} = \frac{B}{L}, \tag{6.3}$$

which does not only depend on the spatial distribution of the sinks, but also on the spatial distribution and amount of CH_3CN in the troposphere (Plumb et al., 2013). Whereas the former is prescribed, the latter is typically not known from measurements. Therefore, the estimate of $\bar{\tau}$ is a model-based value using the simulated distributions of CH_3CN. The resulting tropospheric lifetime of 6.5 month for CH_3CN is the mean of

the values calculated for each monthly model output over a time period of 10 years.

6.2.2. Sources

Biomass burning is the dominant source of atmospheric CH_3CN. Due to the high spatial–temporal variation of biomass burning, a good knowledge of the geographical and temporal occurrence of fires and the emitted amounts of CH_3CN are necessary to represent the biomass burning emissions in the model. Such information can be obtained from emission inventories, which commonly use global satellite-derived burned area information, vegetation fuel load models and compound-specific emission factors to estimate emissions (van der Werf et al., 2010). The output of the inventories are gridded emission fluxes (in kg m^{-2} s^{-1}) for a suite of compounds, whereby the temporal and spatial resolution, the covered time period and the number of included trace gases varies from inventory to inventory. The capability of the model to simulate the distribution of trace gases and their temporal evolution strongly depends on these parameters and the quality of the emission data.

As CH_3CN is a relatively inert trace gas, it is not often modeled and, therefore, commonly not represented in emission inventories. In 2003, when Li et al. (2003) conducted their model study about CHN and CH_3CN, there was no inventory including emission data of the respective species. Therefore, they derived the emission fluxes by multiplying observed (emission) ratios of the respective gases relative to CO with emission data of CO. For CH_3CN, they used a molar ratio of 0.15 %, consistent with the observations of Lelieveld et al. (2001). Holzinger et al. (1999) found emission ratios between 0.04 and 0.25 % when burning different savannah grasses in laboratory fire experiments. The broad range as well as the fact that emission ratios change with fuel type and the combustion efficiency of the fire make this type of estimation relatively uncertain.

ACCMIP–MACCity inventory

In 2008, the ACCMIP–MACCity (Atmospheric Chemistry and Climate Model Intercomparison Project–Monitoring atmospheric composition and climate) inventory was released (Lamarque et al., 2010; Heil and Schultz, 2014). A thorough search of the relevant literature yielded that this is currently the only publicly available inventory containing emission fluxes of CH_3CN. As the authors use the fuel-type specific

emission factors from Andreae and Merlet (2001, with updates until 2008), the flux data should have a better quality than the estimates with a constant CO/CH_3CN emission ratio for all fires. Data are available on a $0.5° \times 0.5°$ grid with a monthly resolution covering the years 1960–2008. The years 1960 to 1996 are based on raw data (amount of biomass burned) of the RETRO wildland fire emission inventory (Schultz et al., 2008), whereas for the years 1997 onwards the amount of burned biomass was taken from the GFED2 inventory (Global Fire Emissions Database) (Randerson et al., 2005 and 2006; van der Werf et al., 2006; Giglio et al., 2006).

GFED inventory

Meanwhile, the emission factors have been continuously refined and the GFED data has been updated twice (Giglio et al., 2013). In GFED3, daily and 3-hourly resolved emissions data became available (Mu et al., 2011). The latest version (GFED4.1s) was further enhanced by including emissions from small fires (Randerson et al., 2012) and by a better spatial resolution ($0.25° \times 0.25°$) (van der Werf et al., 2017a). The GFED project is being continued and recent data is regularly added to the existing data set.

However, in contrast to ACCMIP–MACCity or other inventories, ready-to-use emission fluxes for trace gases are not provided. Instead, the amount of dry matter burned per area is given for different fuel types (van der Werf et al., 2017b). This data is the raw product of any biomass burning emission inventory and it has the great advantage that it enables to derive emission fluxes of species, which are not included in ready-to-use emission data sets.

The author developed a tool, which fulfills this task for CH_3CN (or any other species) and provides the derived emission fluxes in a format, which can be readily imported into ICON-ART. With the resulting Matlab script it is possible to use the most recent GFED inventory data in ICON-ART and to simulate emissions of species, which are not included in ready-to-use inventory outputs. The source code of the script is provided in Section C.4 of Appendix C.

Prior to this new development, biomass burning simulations in ICON-ART were generally restricted to the years before 2013. Model simulations including CH_3CN were only possible until the end of 2008, as the ACCMIP-MACCity inventory is not continued.

The developed Matlab script also allows to simulate more recent years (meanwhile until the end of 2016), which is of great scientific value with regard to the ongoing CARIBIC measurements. Thus, a much larger data set of in–situ measurements is available for model validation and in return, model simulations covering the entire period of CARIBIC flights add more value to the data set and its scientific evaluation.

In addition, usage of the script in combination with the GFED4.1s data provides the following advantageous opportunities compared to ready-to-use emission fluxes of other inventories:

- The user can choose between different compilations of emission factors and derived emission fluxes can be easily updated, if new emission factors become available.
- The impact of different emission factors on emission estimates and modeled VMRs can be investigated.
- The uncertainty in emission estimates due to the large spatial and temporal variability (van Leeuwen et al., 2013) of emission factors can be assessed.

Processing of the GFED4.1s raw data

The Matlab script takes over all necessary steps to convert the amount of burned dry matter into emission fluxes for the trace gases of interest. In a first step, it checks for updates on the GFED website and, if necessary, downloads the most recent GFED4.1s raw data, which are provided in the hierarchical data format HDF5 (HDF, 2017). Each file contains data for one year. Table 6.2 shows an excerpt of the file structure and the location of the variables needed for the emission calculations (printed in bold). All these variables represent fields with 720 rows (latitude) and 1440 columns (longitude) according to a $0.25^\circ \times 0.25^\circ$ grid. The variable DM contains the amount of dry matter burnt in the respective month and cell in kg m^{-2}. Element-wise multiplication with each of the fields in the daily fraction folder (contribution of the particular day x to the monthly amount) gives the amount of burnt dry matter on the day x. The fuel-type specific amounts are calculated by element-wise multiplication with each of the fields in the partitioning folder.

/emissions				
	/<month>			
		/**DM**		
		/daily fraction		
			/**day_1**	
			/**day_2**	
			⋮	
			/**day**_n (number of days in month)	
		/partitioning		
			/**DM_SAVA**	(Savannah, grassland)
			/**DM_BORF**	(Boreal forest)
			/**DM_TEMF**	(Temperature forest)
			/**DM_DEFO**	(Tropical forest)
			/**DM_PEAT**	(Peat)
			/**DM_AGRI**	(Agricultural waste)

Table 6.2.: Section of the hierarchical structure of the GFED4.1s raw data (adapted from van der Werf et al., 2017b)

For many fuel-types and trace gases, emission factors

$$EF_{x,\text{fuel-type}} = \frac{M_{x,\text{fuel-type}}}{M_{\text{biomass,fuel-type}}}, \tag{6.4}$$

defining the amount of a compound emitted ($M_{x,\text{fuel-type}}$) per amount of dry biomass matter consumed ($M_{\text{biomass,fuel-type}}$), have been derived from laboratory fire experiments or in-situ observations (for a compilation, see Andreae and Merlet, 2001, or Akagi et al., 2011). For acetonitrile, the reported fuel-type emission factors are summarized in Table 6.3. Using a set of these emission factors, the daily emissions

Biome/Fire type	Used Abbreviation	Andreae and Merlet 2001	Akagi et al. 2011	Stockwell et al. 2015
Savannah	EF_{SAVA}	0.11	0.11 ± 0.06	0.15 ± 0.14
Boreal Forest	EF_{BORF}	0.19	0.61	0.13 ± 0.11
Temperate Forest	EF_{TEMF}	0.19	–	–
Extratropical Forest		–	0.61	–
Tropical Forest	EF_{DEFO}	0.18	0.41 ± 0.10	–
Peat	EF_{PEAT}	–	3.70 ± 0.90	0.60 ± 0.26
Agricultural Waste	EF_{AGRI}	0.18	0.21 ± 0.06	0.23 ± 0.17

Table 6.3.: Compilation of CH_3CN emission factors reported in the literature. All values are given in g CH_3CN per kg consumed dry matter.

E_x in kg m^{-2} of a species x can be expressed as

$$\begin{aligned} E_x = \text{Dayfraction} \cdot \text{DM} \; (&EF_{x,\text{SAVA}} \cdot \text{DM\_SAVA} + EF_{x,\text{BORF}} \cdot \text{DM\_BORF} \\ &+EF_{x,\text{TEMF}} \cdot \text{DM\_TEMF} + EF_{x,\text{DEFO}} \cdot \text{DM\_DEFO} \\ &+EF_{x,\text{PEAT}} \cdot \text{DM\_PEAT} + EF_{x,\text{AGRI}} \cdot \text{DM\_AGRI}). \end{aligned} \tag{6.5}$$

with element-wise multiplication of the fields. In this study, the mean emission factors provided in Akagi et al. (2011) were used, as they are most complete. For temperate forest fires, the emission factor of extratropical forest fires was used. However, for future studies, other emission factors can also be considered and it is possible to investigate the effect of the uncertainties of the emission factors on the atmospheric distribution.

Implementation of the emissions into ICON-ART

Before emissions can be read by the ICON model, they need to be converted from the longitudinal–latitudinal grid to the native ICON grid. This is done by a script of the DWD ICON tools, which are provided by the DWD for remapping, extracting and querying data files.

For each year between 2004 and 2015, two GFED4.1s CH_3CN emissions files were generated: The first one containing monthly resolved emissions and the second one daily emissions.

The further import of the emissions files is done by the emissions interface of ICON-ART, which has been developed and described by Weimer et al. (2017). In short, the emissions interface controls, which emission inventory is used for the individual trace gases and emission types, interpolates the emissions to each model time step, converts the emission fluxes to VMRs and adds them to the VMRs present in the surface-near model layer(s).

The parameters related to the import of the CH_3CN data are mostly fixed and their usage is well described in Weimer et al. (2017). However, it might be relevant for further model studies of CH_3CN to change the emission inventory, the model resolution and the number of lowest model layers into which emissions are inserted. Therefore, the configuration of the emission interface as used here is described in detail in Section C.2 of Appendix C.

The ACCMIP-MACCity inventory has the peculiarity of distinguishing between

forest fires and grassland/savanna fires. As the emissions of the two fuel types are provided in separate variables, the emissions interface sums up both variables.

In this study, the emissions were only added to the lowest model layer. However, due to the heat of the fires, the warm air masses are often directly injected into the free troposphere (e.g. Crutzen and Andreae, 1990; Leung et al., 2007). To simulate this effect, it can be reasonable to insert the emissions into more surface-near layers in future studies.

6.3. CH_3CN global source estimates

As the emission inventory data are the key input of the model simulations, the simulated abundance and temporal-spatial distribution of CH_3CN will likely depend on the choice of the emission inventory. In previous studies, CH_3CN emissions were solely based on extrapolated CO emissions using an observed (constant) molar emission ratio of CH_3CN and CO as scaling factor (Singh et al., 2003; Li et al., 2003). Here, for the first time, CH_3CN emissions based on fuel-type specific emission factors are used. Therefore, it is necessary to compare the results of the two approaches – direct (EF) and indirect (CO) – for both inventories with previous source estimates.

For this purpose, gridded emission fluxes of CH_3CN and CO (in kg m^{-2} s^{-1}) were derived from the GFED4.1s raw data using the script developed in this work (see Section 6.2.2) and the emission factors of Akagi et al. (2011). In a next step, the fluxes were converted into total emissions for each cell (in Tg a^{-1}) and summed up. For the indirect (CO) approach, the total CO emissions were multiplied with a factor corresponding to the molar emission ratio of 0.15 % used in the studies of Singh et al. (2003) and Li et al. (2003). The same was done for the ACCMIP-MACCity inventory, with the difference that the gridded emission fluxes of CH_3CN and CO were already calculated by the authors of the inventory.

In Table 6.4, the resulting annual emissions of CH_3CN and their means are summarized for each inventory and approach. In the case of the direct (EF) approach, the ACCMIP-MACCity data yields a mean annual source (2.4 Tg) twice as high as the GFED4.1s data (1.2 Tg). In contrast, the results of the indirect (CO) approach are in better agreement (0.9 Tg and 0.8 Tg), indicating that the large discrepancy in the fuel-type specific CH_3CN emissions of both inventories is not related to the underlying fire product, but rather a result of different emission factors used for

CH_3CN.

In Table 6.5, literature values of the annual CH_3CN emissions are compiled. The very first estimates were based on rather crude assumptions and involved no direct measurements of acetonitrile. Since then, estimates have been considerably revised upwards due to new constraints from further atmospheric measurements and the detection of CH_3CN in the emissions of controlled laboratory fires. Although there have been no new studies since 2003, the latest estimates suggest a global source of 1.0–1.4 Tg.

Despite being based on CO emission estimates, the latest estimates of the global CH_3CN source are larger than the results of the indirect (CO) approach derived in this study. This is due to the fact that Andreae and Merlet (2001), Singh et al. (2003) and Li et al. (2003) included CO emissions from the combustion of biofuels and charcoal burning in their CO emissions estimates, which are not included in the ACCMIP-MACCity and GFED4.1s biomass burning inventories.

The combustion of biofuels mainly refers to small fires in stoves for cooking and heating (Akagi et al., 2011), which cannot be resolved by satellites. Andreae and Merlet (2001) assumed a CH_3CN source from biofuel burning of 0.5 Tg. However, the recently reported emission factors of CH_3CN from open cooking and cookstoves are 1–3 magnitudes smaller than the ones from other fire types (Stockwell et al., 2015), suggesting that the source from biofuel burning is considerably smaller or even negligible.

Comparison of the literature values with the results of the direct (EF) approach reveals that the global CH_3CN source derived from the GFED4.1s data is consistent with previous estimates, although biofuel emissions are not included. The reason for this presumably lies in the larger emission factors of Akagi et al. (2011) compared to

Inventory & approach		1998	1999	2000	2001	2002	2003	2004	2005	2006	2007	2008	**Mean**
MACCity	direct (EF)	3.9	2.0	1.6	1.9	3.0	2.1	2.4	2.7	3.0	1.8	1.5	**2.4 ± 0.7**
	indirect (CO)	1.4	0.9	0.8	0.8	1.0	0.9	0.9	1.0	0.9	0.9	0.7	**0.9 ± 0.2**
GFED	direct (EF)	1.5	1.0	0.8	0.8	1.7	1.3	1.3	1.2	2.1	1.0	0.8	**1.2 ± 0.4**
	indirect (CO)	1.0	0.8	0.6	0.6	0.9	0.8	0.8	0.8	0.8	0.7	0.6	**0.8 ± 0.1**

Table 6.4.: Annual emissions of CH_3CN in Tg based on the ACCMIP-MACCity and GFED4.1s inventory. The results of the direct (EF) approach are based on fuel-type specific emission ratios, whereas the indirect (CO) approach refers to the source estimates based on CO emissions of the respective inventory and a constant molar CH_3CN/CO emission ratio of 0.15 %.

CH_3CN [Tg a^{-1}]	Type of Measurement	References
0.02–0.17	assessment of total BB emissions	Arijs and Brasseur (1986)
0.05	observed VMR in the LS	Knop and Arnold (1987)
0.4–2.2	controlled laboratory fires	Lobert et al. (1990)
0.8 ± 0.5	literature review & assessment	Hamm and Warnek (1990)
0.4–1.0	controlled laboratory fires	Holzinger et al. (1999)
1.0	literature review & assessment	Bange and Williams (2000)
1.3	literature review & assessment	Andreae and Merlet (2001)
1.2	ratio observed over the Pacific	Singh et al. (2003)
1.4	ratio observed over the Pacific	Li et al. (2003)

Table 6.5.: Literature estimates of the global annual CH_3CN biomass burning source in Tg. The table has been adopted from Singh et al. (2003) and Li et al. (2003).

the ones of Andreae and Merlet (2001) used in previous studies (see Table 6.3).

For the ACCMIP-MACCity inventory, the direct (EF) approach (corresponding to the provided emission fluxes of CH_3CN) yields a considerably higher source than the literature values. Only the upper range (2.2 Tg) reported in Lobert et al. (1990) comes close to the derived mean annual source of 2.4 Tg (see Table 6.4). Therefore, this inventory should be considered as an upper limit of CH_3CN emissions. This is also confirmed later by comparing the VMRs of the model simulations with the ones measured onboard the CARIBIC aircraft (see Section 6.5). Further investigations, which were out of the scope of this study, are recommended to clarify the high CH_3CN emissions in the ACCMIP-MACCity inventory. However, due to the fact that the ACCMIP-MACCity inventory ends in 2008 and the IAGOS-CARIBIC project continues its operation, the ACCMIP-MACCity inventory will likely play only a secondary role in future studies.

6.3.1. Variability of the global CH_3CN source

Due to its different driving forces including meteorological conditions and human activities, biomass burning is subject to substantial seasonal and interannual variability (e.g. Duncan et al., 2003; Pechony and Shindell, 2010; Dong and Fu, 2015). In Table

6.4, the interannual variability of the global CH_3CN source within the time period 1998 – 2008, when data of both inventories (ACCMIP-MACCity and GFED4.1s) are available, is shown.

In Figure 6.1, the derived monthly CH_3CN emissions of both inventories and approaches (direct and indirect) are plotted against time. As stated earlier, the GFED emissions have been derived within this study, whereas for the ACCMIP-MACCity inventory fluxes were provided for CO and CH_3CN.

When comparing the emissions based on the fuel-type specific emission factors (direct approach), two features stand out:

1. The monthly emissions of the ACCMIP-MACCity are on average 0.1 Tg larger.

2. The strongest emissions in both inventories coincide, but the temporal evolution of the emissions in ACCMIP-MACCity shows more structure compared to the GFED inventory. In the GFED data set, the emissions peak once a year around August and September, but the ACCMIP-MACCity emissions show another smaller peak around the turn of each year. In the displayed period, this second annual peak is particularly prevalent at the beginning of 1998 and of 2005.

The CO-based emissions (indirect approach) follow the same annual cycle for both inventories, but the absolute values slightly differ: For the case of the MACCity inventory, the extrapolated emissions always stay below the direct (EF) estimates and the differences are particularly high for months with strong emissions. On average, the CO-based emissions are 0.12 Tg below the estimates deduced from the provided CH_3CN emission fluxes.

For the GFED inventory, the emissions derived from the different approaches are in better agreement. Deviations are only visible for the months with strong emissions, but not for all years. On average, the monthly emissions based on the indirect (CO) approach are 0.04 Tg lower than the ones based on the direct (EF) approach.

Both inventories have in common, that the largest discrepancies between the different approaches occur in the months with high biomass burning emissions. This leads to the conclusion that mainly the fires contributing to the globally enhanced fire activity in these months emit more CH_3CN relative to CO as assumed by the ratio of 0.15 %. As the interannual variability is to a large part driven by the peak annual emissions, it is considerably and unrealistically lower when using the CO-based approach (see

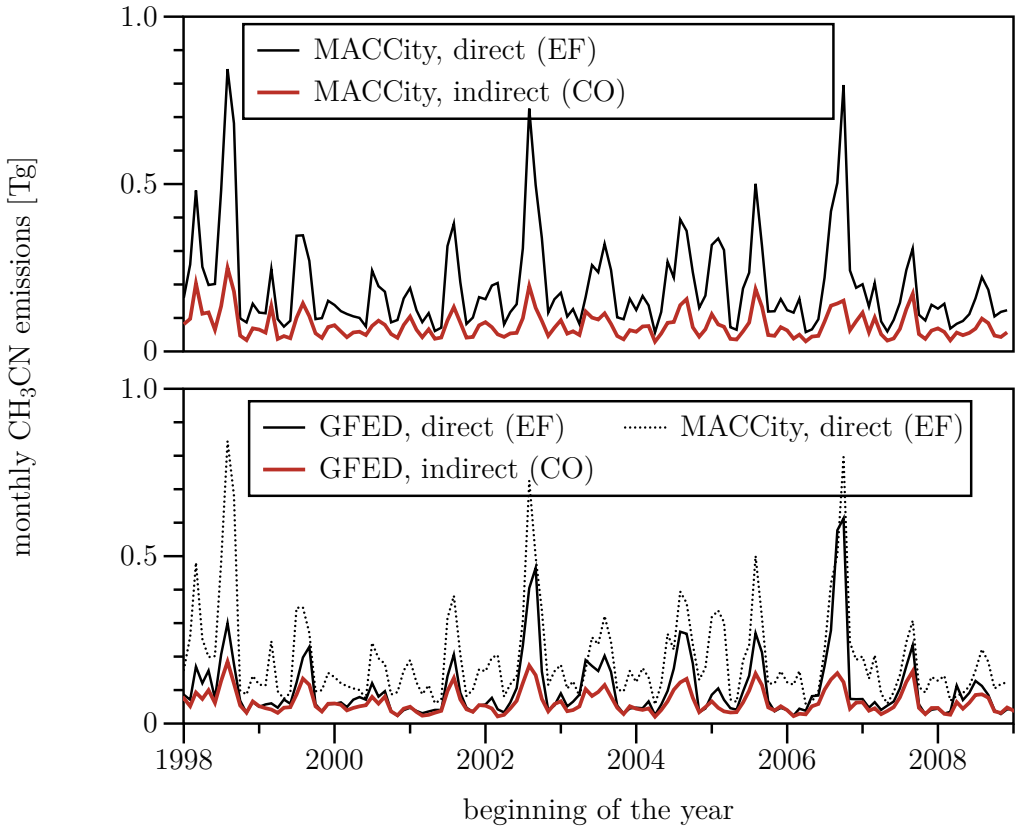

Figure 6.1.: Temporal evolution of monthly CH_3CN emissions for the period 1998 – 2008. In the upper panel, the original ACCMIP-MACCity CH_3CN direct (black) and the CO-based indirect emission estimates (red) are shown. In the lower panel, the same comparison is made for the GFED4.1s inventory. For better comparison of the two inventories, the ACCMIP-MACCity data are overlaid as dotted line.

also Table 6.4).

6.4. Volume mixing ratios in model simulations

The previous section revealed that the mean annual CH_3CN emissions of the two inventories (ACCMIP-MACCity and GFED4.1s) differ by a factor of 2 (see Table 6.4). To assess the different estimates with regard to in-situ measurements, the resulting amounts of CH_3CN in the atmosphere, i.e. the mean VMRs in the troposphere, need to be determined. As a first step, global mean tropospheric VMRs are estimated using a one-compartment model.

6.4.1. One-compartment model

The change of the total mass m of CH_3CN can be expressed by the differential equation

$$\dot{m}(t) = S - \lambda\, m(t), \tag{6.6}$$

where S is the emission mass flow of CH_3CN into the troposphere and λ the mean removal rate. Assuming a constant emission flux and removal rate, the equation can be solved numerically and the time dependence of the total mass is described by

$$m(t) = \left(m_0 - \frac{S}{\lambda}\right) \exp^{-\lambda t} + \frac{S}{\lambda} = (m_0 - S\ \tau) \exp^{-\frac{t}{\tau} t} + S\ \tau, \tag{6.7}$$

where m_0 is the total mass at time zero and $\tau = \lambda^{-1}$ is the tropospheric lifetime. In steady state ($t \gg \tau$), the total mass equals the product of the emissions rate and the lifetime ($S\ \tau$). This can be converted into a VMR

$$\mathrm{VMR}_{\mathrm{CH_3CN}} = \frac{n_{\mathrm{CH_3CN}}}{n_{\mathrm{air}}} = \frac{m_{\mathrm{CH_3CN}} \cdot M_{\mathrm{air}}}{m_{\mathrm{air}} \cdot M_{\mathrm{CH3CN}}} = \frac{M_{\mathrm{air}}}{m_{\mathrm{air}} \cdot M_{\mathrm{CH3CN}}}\ S\ \tau, \tag{6.8}$$

where n is the amount of moles and M is the molar mass. The total mass of the atmosphere is ∼5140 Pg (Trenberth and Guillemot, 1994). Given that the troposphere contains about 80 % of the mass and the mean molar mass of air is ∼29 g mol^{-1}, the fraction on the right side of Equation 6.8 is equivalent to 171.7 ppt per Tg CH_3CN. The overall tropospheric lifetime of CH_3CN was estimated to be 6.5 months (see Section 6.2.1). Substituting the annual emissions of MACCity (2.4 Tg a^{-1}) and GFED (1.2 Tg a^{-1}) inventories into the Equation 6.8 results in the following tropospheric VMRs:

$$\begin{aligned} &\text{MACCity:} && 223 \pm 65 \text{ ppt} \\ &\text{GFED:} && 112 \pm 37 \text{ ppt,} \end{aligned}$$

where the range reflects the interannual variability of the annual source. Whereas the former is slightly above the range of previously observed tropospheric background VMRs (50–200 ppt; Hamm and Warneck, 1990; Singh et al., 2003; de Gouw et al., 2003c), the latter lies well within the range. Without considering the presumed ocean sink, the estimated VMRs would be unrealistically high (765 ppt for MACCity and 383 ppt for GFED).

Nevertheless, for comparison with in–situ measurements, simulations with a chemical transport model such as ICON-ART are indispensable, e.g. to resolve the observed

vertical gradient of CH_3CN in the troposphere.

6.4.2. ICON-ART

To investigate the effects of the discrepancy between MACCity and GFED more closely, ICON-ART model simulations were performed with both inventories. The model was operated on a horizontal grid referred to as R2B04 (for a detailed description of the notation see Zängl et al., 2015) corresponding to an effective grid resolution of 157.8 km. In the vertical, the smooth level vertical (SLEVE) coordinate (Schär et al., 2002, Leuenberger et al., 2010) with 90 height-based levels was used.

Model simulations were performed for the time period between 1 January 2004 and 31 October 2014 to cover the majority of IAGOS-CARIBIC CH_3CN measurements starting in 2006. As the model domain was not filled with CH_3CN at the start, the spin-up period took about one year. The meteorological conditions were once initialized on 1 January 2004 (00:00 UTC) using ERA-Interim reanalysis data and then left free-running. The model time step was set to 8 min. At monthly intervals, the output of each model layer was interpolated to a $0.5^\circ \times 0.5^\circ$ longitude-latitude grid and saved in a NetCDF (Network Common Data Form; Unidata, 2014) file.

In Figure 6.2, the monthly global emissions of CH_3CN (lower panel) are compared to global mean VMRs of CH_3CN (upper panel) at the surface (solid lines) and 1 km below the tropopause (dotted lines). The latter was chosen to exclude stratospheric air masses. For the comparison with in–situ aircraft measurements, the VMRs in the upper troposphere are of main interest.

As the MACCity inventory only contains data until the end of 2008, the emissions interface of ICON-ART repeatedly used the monthly emissions of 2008 for the following years. The resulting VMRs are not shown in Figure 6.2 and have been excluded from the following analysis to avoid a bias. In Table 6.6, the global mean VMRs of the two model simulations and for the surface and upper troposphere are compared with each other.

The absolute values are lower than the ones from the one-compartment model. This is expected due to the fact that tropospheric-stratospheric exchange is not included in the one-compartment model although the stratosphere represents a reservoir for CH_3CN. Mean VMRs of the MACCity simulation are only 1.7–1.8 times higher than in the GFED simulation, remaining below the factor of 2 derived from the

one-compartment model. The VMRs in the upper troposphere are on average larger than at the ground, as large amounts of CH_3CN are effectively transported into the upper troposphere, where the lifetime is almost two years (see Table 6.1). The spatial variability of the VMRs in the upper troposphere is on average ±20 % (RSD) of the mean values for both inventories.

Near the surface, the oceanic sink reduces the global mean lifetime, which explains the on average lower VMRs at the ground. However, as the lifetime in the continental boundary layer is the same as in the free troposphere, this effect strongly depends on the amount of CH_3CN being transported into the marine boundary layer, which in turn depends on the location of the fire and the prevailing meteorological conditions. The spatial variability of the surface VMRs is considerably higher than in the UT and therefore not displayed in Figure 6.2.

Figure 6.2 also reveals that the VMRs both at the surface and in the UT follow a distinct annual cycle, which is prescribed by the emissions at the surface and shifted by 1–2 months in the UT due to the upward transport time scales. The amplitude of this cycle in the VMRs is more pronounced in the GFED simulation, which is due to the different emissions pattern. As discussed in the previous section, the global emissions in GFED only peak once a year in August–September, whereas the MACCity emissions have another, yet smaller peak around the turn of each year, which reduces the amplitude in the emissions and VMRs.

Besides the quantities and temporal evolutions of the emissions, also the source locations within the two inventories are of great importance, as they predetermine the propagation of the plumes and thus, the spatial distribution of CH_3CN. Most biomass burning worldwide occurs in the tropics (e.g. Seiler and Crutzen, 1980, Crutzen and Andreae, 1990; Duncan et al., 2003). However, due to the subtropical transport barriers (e.g. Haynes and Shuckburgh, 2000; Stohl et al., 2002), exchange

	MACCity		GFED	
time period	surface	below TP	surface	below TP
2005–2008	163 ± 26	190 ± 28	97 ± 18	107 ± 23
2009–2014			91 ± 24	98 ± 18

Table 6.6.: Global mean volume mixing ratios of CH_3CN (in ppt) at the model surface and 1 km below the model tropopause (TP) for the respective time periods and emission inventories. The shown uncertainties represent the temporal variability (standard deviation).

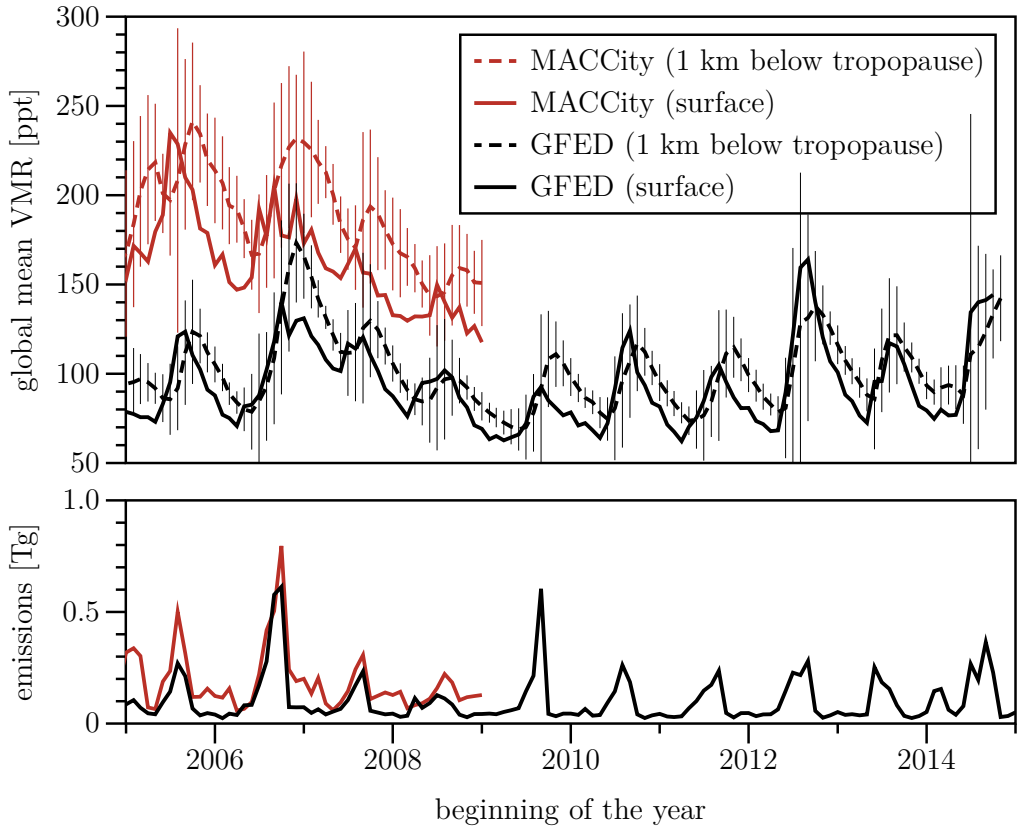

Figure 6.2.: Monthly emissions (lower panel) and global mean VMRs of CH_3CN in the model simulations (upper panel) at the surface (solid lines) and 1 km below the tropopause (dashed lines). The spatial variability of the upper tropospheric VMRs is indicated by vertical lines. For reasons of clarity, the one of the surface VMRs is not shown.

of air masses between the tropics and the extratropics is slow (weeks to months) compared to mixing within the tropics and extratropics (days to weeks) (Bowman, 2006).

When comparing the results of the model simulations with CARIBIC measurements, as it is done in the next section, it is therefore important to consider that CH_3CN VMRs in the midlatitudes, where most of measurements have been done, will be most immediately affected by emissions in the midlatitudes and to a much lesser extent by emissions in the tropics and vice versa (Cooper et al., 2007).

6.5. Comparison with CARIBIC measurements

The model simulations of this study do not allow for a one-to-one (spatially and temporally coherent) comparison of simulated VMRs and the ones measured onboard the CARIBIC aircraft. Such a comparison would require frequent adjustments of the simulated meteorological conditions to observations (a so called "nudging") and an output mechanism, which stores the simulated VMRs at high frequency along the flight paths during flight. However, frequent nudging over longer time periods is not yet possible within ICON-ART and such an individual output mechanism still has to be developed.

Despite these limitations, comparisons with CARIBIC observations are most promising, as they comprise the worldwide largest set of upper tropospheric CH_3CN measurements available at the moment. Moreover, the CARIBIC data set is unique in terms of its spatial and temporal coverage. As the observations have been made remote from the sources, they are also representative for much larger regions compared to ground-based measurements. Therefore, model-measurement comparison of the annual means and the frequency distribution of VMRs seems to be an adequate analysis method.

6.5.1. Annual distributions

In contrast to the model, the CARIBIC data set is limited to the flight altitude and the spatial coverage of the flight routes (see Figure 1.4). With regard to the spatial variability, which can be considerable, it is not reasonable to compare mean VMRs, which were mainly measured in the Northern Hemisphere with globally averaged VMRs of the model. Therefore, a volume needs to be selected, which on the one hand has a good data coverage in both data sets (model and measurements) and on the other hand is well suited to assess the source strength of biomass burning emissions.

About 50 % of the CARIBIC measurements have been done in the stratosphere. However, as the stratosphere is far away from the sources and advection is very slow compared to the troposphere (e.g. Plumb, 2002), it does not represent a well-mixed reservoir for CH_3CN and the spatial variability will be rather driven by differences in the age of the air mass than by the sources (Jobson et al., 1999). Consequently, stratospheric observations are not well suited to estimate the surface emissions of

CH_3CN. Furthermore, the simulated stratospheric VMRs have to be taken with care, as the stratospheric domain needs considerably more spin-up time than the time period considered in the simulation.

Conversely, surface-near concentrations of CH_3CN are dominated by local emissions and sinks, which likewise impedes the estimation of a global biomass burning source strength. A large number of measurements at various places would be required to assess the high spatial variation of fires, but the CARIBIC data set only contains very few surface-near measurements made during ascent and descent confined to the proximity of some airports.

Therefore, the atmospheric region best suited for the intended comparison and source assessment lies in between: The upper troposphere constitutes a well-mixed reservoir for CH_3CN and is regularly probed by the CARIBIC aircraft. To distinguish between tropospheric and stratospheric measurements, the concomitant ozone data and the threshold of the chemical tropopause are used (for details see Section 5.3). The few measurements during ascent and descent are excluded with an upper pressure limit of 280 hPa.

In the model, the WMO tropopause was used to either assign the tropospheric or stratospheric lifetime of CH_3CN to the respective model layers. Therefore, the height relative to the WMO tropopause is also used here to define the lower and upper limit of the reference volume in the model environment. As a first approach, the limits are set to 3 km and 1 km below the tropopause.

With regard to the spatial coverage of the flight routes, it seems most reasonable to restrict the horizontal expanse of the volume to the Northern Hemisphere midlatitudes (23.5°N–66.5°N) and the longitudinal range between -135°E to 135°E. This covers the majority of the CARIBIC measurements and excludes the Pacific Ocean, which was not sampled by the CARIBIC aircraft.

In Figure 6.3, the annual distributions of VMRs contained in the defined reference volume are shown for the CARIBIC measurements and the model simulations. All distributions lie within the same range of VMRs starting from 50 ppt to 300 ppt, but differ from each other with regard to the shape, center and width.

In general, the distributions of the CARIBIC measurements are more symmetric than the ones of the simulated VMRs. All distributions are skewed to the right (positive skewness factor, see Table 6.7), but this shape is much more pronounced

year	data set	number of data points	skew-ness	mean VMR ($\pm1\sigma$) [ppt] all values	background	proportion of bgnd. [%]
2006	CARIBIC	2783	1.2	107 ± 32	100 ± 24	75
	GFED	3059347	4.0	115 ± 36	89 ± 6	38
	MACCity	3059347	3.1	196 ± 26	178 ± 13	52
2007	CARIBIC	3331	0.3	122 ± 36	117 ± 33	80
	GFED	3059347	1.4	119 ± 20	108 ± 12	54
	MACCity	3059347	1.1	182 ± 27	158 ± 9	37
2008	CARIBIC	8185	0.6	125 ± 36	114 ± 27	71
	GFED	3059347	7.2	98 ± 25	91 ± 8	71
	MACCity	3059347	6.1	152 ± 20	143 ± 9	58
2012	CARIBIC	6153	1.3	148 ± 34	122 ± 15	43
	GFED	3059347	3.5	122 ± 54	86 ± 6	37
2013	CARIBIC	8616	2.5	160 ± 29	155 ± 20	79
	GFED	3059347	20.1	109 ± 29	92 ± 6	31
2014	CARIBIC	5558	1.7	212 ± 61	157 ± 18	29
	GFED	2353347	5.8	121 ± 45	91 ± 6	47
2015	CARIBIC	6720	0.3	185 ± 45	178 ± 40	78

Table 6.7.: Parameters of the distributions shown in Figure 6.3 and additionally included the CARIBIC measurements in 2015 (not shown). The mean background CH_3CN VMRs were determined as center μ of a Gaussian function fitted to the left flank of the distributions. The proportion of background (bgnd.) VMRs was defined as the percentage of VMRs lower than the sum $\mu + 1\sigma$ of the Gaussian fit parameters.

for the simulated distributions. The latter have a distinct maximum at low VMRs, which can be related to the atmospheric background reservoir of CH_3CN, and an extended tail towards elevated VMRs caused by in-mixing of fresh biomass burning plumes into the UT background. In some years (e.g. 2007, 2012, and 2014), this tail has 1–2 local maxima, which are most likely the result of temporally and spatially extended biomass burning episodes.

In the CARIBIC measurements, such clearly resolved structures are not visible except for 2014, where a local peak is present at ∼210 ppt. In the other years, including also measurements from 2015 (not shown), the shape of the distributions is close to a normal distribution with a flat tail towards enhanced VMRs observed within

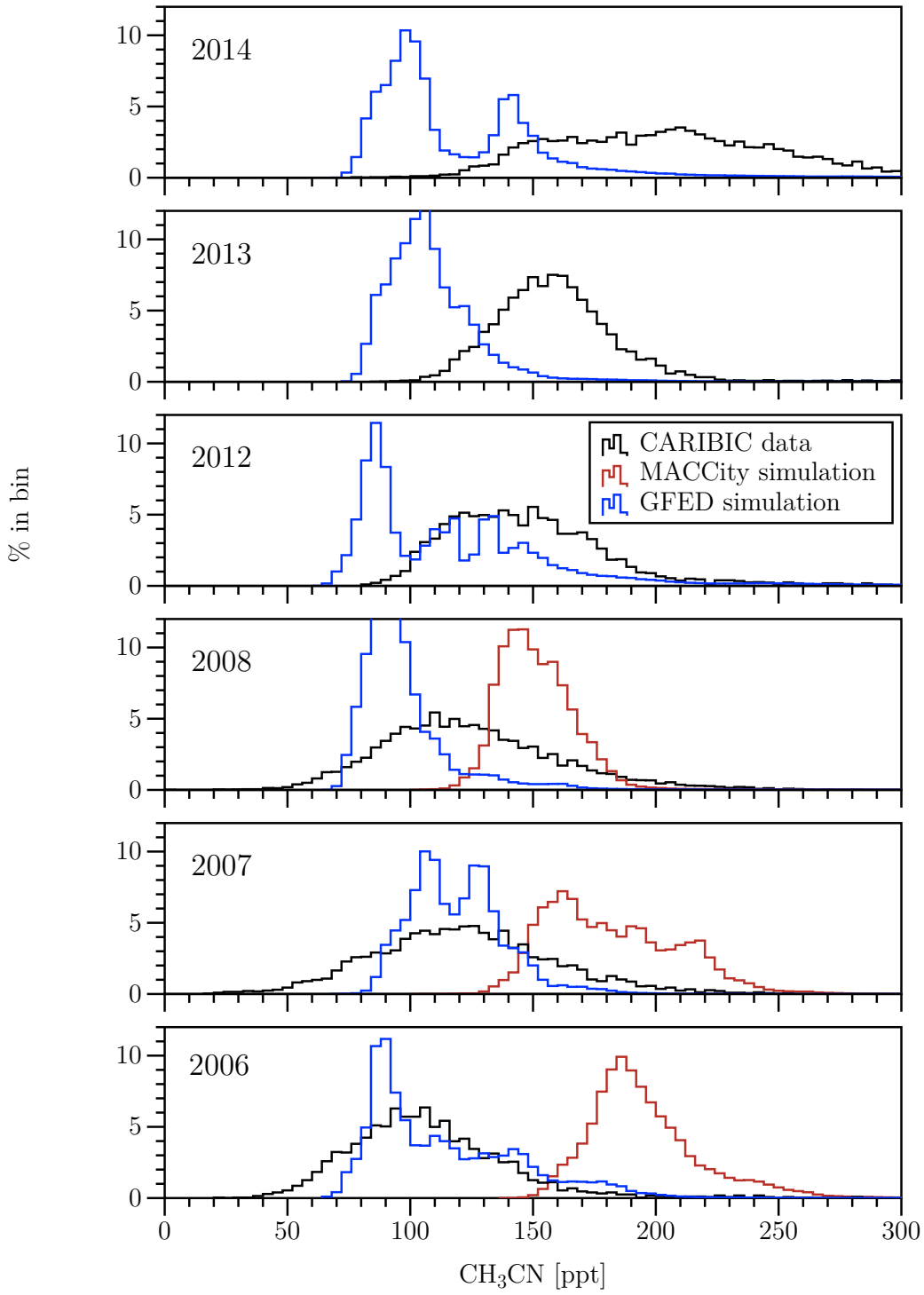

Figure 6.3.: Annual distribution of CH_3CN VMRs measured with CARIBIC (black) and simulated using the MACCity (red) or GFED (blue) emission inventory. All three data sets were restricted to the upper troposphere in the Northern Hemisphere midlatitudes (see text for details). Statistical parameters of the distributions are summarized in Table 6.7.

encountered biomass burning plumes.

Depending on the frequency of observed plumes and their degree of mixing, the tail is more or less pronounced and the arithmetical mean may be shifted towards higher VMRs and deviate from the maximum of the distribution. However, one has to consider that the frequency of fresh biomass burning plumes encountered by the CARIBC aircraft strongly depends on the selected flight routes, as global fire activities are subject to a distinct seasonal and spatial pattern. Likewise, the propagation of biomass burning plumes in the model may be distorted, as emissions are currently only injected into the lowest model layer neglecting the influence of pyroconvection. Consequently, the annual means do not provide a profound basis to assess the global source and discrepancy between the two inventories.

By contrast, the background VMRs should be much more robust and less affected by the chosen flight routes and plume propagation in the model, as the hemispheric mixing timescales (few months) are short compared to the UT lifetime of CH_3CN ($\sim$2 years). Several methods exist to estimate the atmospheric background VMR. In Section 5.5.2, air masses with acetone and CO VMRs between the 5th and 25th percentile were attributed to the background.

For CH_3CN, the longer lifetime suggests a higher proportion of background measurements. However, the high variability in emissions makes it difficult to specify a constant inter-percentile range for all years. Therefore, a Gaussian function fitted to the left flank of the distributions is used here to determine the mean background VMR (center μ of the Gaussian function) and the proportion of measurements attributed to the background (all VMRs lower than $\mu + 1\sigma$).

In Figure 6.4, the approach is exemplarily shown for the CARIBIC measurements in 2012 and 2014, which were affected by a considerably higher variation in VMRs compared to other years. The widths of the overall distributions suggest another mode with enhanced VMRs, which were comparably often (2012) or even more often (2014) sampled as the clean background. Also the distributions of the GFED model simulation (see Figure 6.3) are much broader in the two years and show at least one further mode of elevated VMRs, indicating the occurrence of strong biomass burning. Accordingly, the derived percentage of background air sampled with CARIBIC are relatively low (43 % in 2012 and 29 % in 2014).

In all other years, the shape of the CARIBIC distributions is much closer to a normal distribution suggesting that mostly clean or well-mixed, aged air masses with VMRs

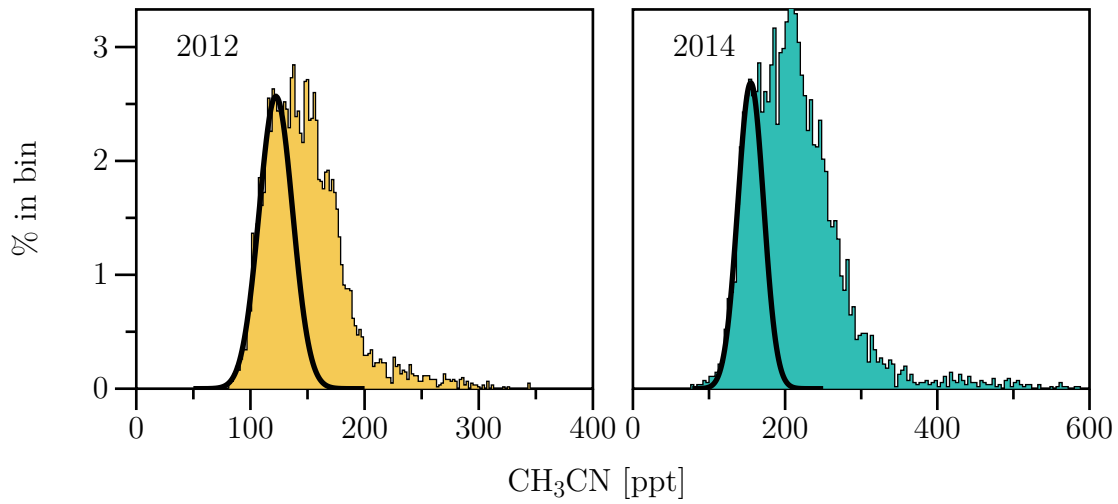

Figure 6.4.: Histograms of the CARIBIC CH_3CN data for 2012 (left panel, yellow) and 2014 (right panel, green).

close to the background value were sampled. This is also reflected in the derived background proportions ranging between 70–80 %.

In Table 6.7, the results for all years and data sets (CARIBIC, GFED and MACCity) are summarized together with the annual means. In the years 2006–2008, the background of the CARIBIC measurements (on average 110 ppt) and of the GFED simulations (on average 96 ppt) do not show significant differences within the 1σ-range of the Gaussian fit. However, one has to consider that the observed and simulated VMRs are also subject to the accuracy of the measurements and the uncertainties associated with the sinks included in the model, respectively. With regard to the former, an upper limit of 15 % can be assumed, whereas the latter is assessed as follows:

For the lifetime τ_{OH} against reaction with OH, an uncertainty of 5.6 months, corresponding to 23 %, is found when considering the uncertainties of the mean annual OH density (15 %; Spivakovsky et al., 2000; Lawrence et al., 2001) and the temperature-dependent reaction rate (20 % resulting from the uncertainty of the parameterization and the mean temperature $\pm 10^\circ$ C).

The lifetime τ_{ocean} against oceanic uptake depends on the deposition velocity of CH_3CN and the assumed height of the marine boundary layer. The range of published values indicates an uncertainty of 20.5 days.

As both sinks affect well-separated atmospheric layers, the mean tropospheric lifetime

$\bar{\tau}$ derived from the model results can be considered as weighted sum of the two lifetimes:

$$\bar{\tau} = x_{\mathrm{OH}} \cdot \tau_{\mathrm{OH}} + (1 - x_{\mathrm{OH}})\ \tau_{\mathrm{ocean}}, \tag{6.9}$$

where x_{OH} denotes the proportion of the reaction with OH relative to the total tropospheric sink of CH_3CN. Rearranging of Equation 6.9 and inserting the lifetimes (see Section 6.2.1) yields a proportion of $x_{\mathrm{OH}} \approx 0.27$, meaning that most of the CH_3CN is removed by oceanic uptake.

Nevertheless, the oceanic sink has only a very limited influence on the mean tropospheric lifetime and thus, the VMR in steady-state (see Equation 6.8). This is due to the fact that the difference in lifetimes of the two sinks is much larger than the difference in their contributions to the total sink. Consequently, the weighting of the two sink terms on the right side of Equation 6.9 is dominated by the lifetimes. As τ_{OH} is 33 times larger than τ_{ocean}, the mean tropospheric lifetime is mainly driven by the OH sink.

This also holds true for the model uncertainty, which is ∼30 % based on linear error propagation. According to Equation 6.8, this uncertainty can be directly transferred to the simulated VMRs. With regard to the comparison with CARIBIC observations (see Table 6.7), the determined uncertainty enables the following conclusions:

For the time period 2006–2008, the CARIBIC observations support the mean annual background VMRs of the GFED simulation and thus, the biomass burning source strength included in this inventory. In contrast, the high background VMR of 178 ppt in the MACCity simulation in 2006 is in contradiction to the CARIBIC measurements. Comparison of the annual emissions with previously reported estimates already revealed that the MACCity inventory has to be taken with care and considered as an upper limit for CH_3CN emissions. The high discrepancy between observed and simulated VMRs in 2006 seems to confirm this. However, in the following two years, the simulated background VMRs decrease and fall into the range, which can be explained by the measurement accuracy and uncertainty of the sinks.

In the second period beginning in 2012, the comparison is restricted to the CARIBIC measurements and the GFED model simulations. The mean background VMRs in the simulation continue to be around 90 ppt, whereas the CARIBIC observations suggest a continuous increase. The mean background VMR changed from 122 ppt in 2012 to 155 ppt in 2013 and from 157 ppt in 2014 to 178 ppt in 2015. Except for 2012, the large differences between model and observations cannot be explained by

the considered uncertainties.

Possible reasons for this are: a) The GFED inventory underestimates the emissions in 2012–2014, b) the background determined from the observations is not representative, c) the measurements accuracy is lower than expected or d) the uncertainty associated with the sinks implemented in the model is higher than estimated.

In this context, it has to be mentioned that the CARIBIC instrument was strongly modified between 2008 and 2012. Before the modification, the instrument was frequently calibrated in-flight by diluting a gas standard into the sample line at intervals of 35 minutes. However, as a matter to save weight, the gas cylinder containing the gas standard was removed during the modification and calibrations were subsequently done in the laboratory between flights. This enlarges the overall uncertainty of the measurements, as instrumental drifts may occur and not be corrected for.

Another important aspect is the change in flight routes between the two periods. In the first one (2006–2008), the CARIBIC container was primarily deployed on flights to Asia, whereas in the 2nd period (2012–2014), flights to North or South America dominate depending on season. Consequently, the seasonal sampling is very different between the two periods and may explain the different VMRs. Based on this finding, the seasonal variability of CH_3CN within the model simulations and observations is examined more closely in the next section.

6.5.2. Annual cycle

In the previous section, only the annual CH_3CN distributions were compared regardless of a seasonal variability due to the limited number of CARIBIC measurements in each individual month. If such a variability exists, it might explain the observed rather broad distributions of measured VMRs and the different modes in the distributions of the simulated VRMs.

To investigate the seasonal variability in the CARIBIC data set, it is again important to focus on a region with good data coverage. In accordance with the previous section, the analysis is thus restricted to the Northern hemisphere midlatitudes (23.5°–66.5°N). Furthermore, to obtain a statistically sufficient number of measurements per month, the monthly data of several years have to be merged. This was done for the two continuous periods 2006–2008 and 2012–2016. The data set of the first period is

consistent and measurements were frequently calibrated in-flight. The data set of the second period is characterized by generally increasing VMRs and two leaps in VMRs due to instrumental maintenance and changes, which complicate the merging of data of different years.

The leaps, which occurred between September and October 2012 (change of detector and adjustments of the ion lens voltages) and between November 2014 and January 2015 (re-adjustment/calibration of the mass axis), are clearly related to instrumental issues. The questions, why the maintenance and modification caused such leaps in the 2012–2015 time series of the CARIBIC CH_3CN measurements despite calibrations (in total 16 calibrations were done at irregular intervals in the considered time period) and whether the observed increase is related to this, is certainly worth investigating but is out of the scope of this study. However, to combine the monthly data of different years for analysis, it is inevitable to correct the data for the two leaps and the resulting temporal trend in the 2012–2016 CH_3CN time series.

For this purpose, a linear function $f(t) = a \cdot t + b$ was fitted to each subset of the data (i.e. all data before the first leap, between the leaps and after second leap). To remove the temporal trend and to normalize all VMRs to a comparable level (the mean VMR observed in the period 2006–2008), the following correction was applied to each measurement $x_{i,\mathrm{meas}}$ conducted at the time $t_{i,\mathrm{meas}}$:

$$x_{i,\mathrm{corr}} = x_{i,\mathrm{meas}} - (a \cdot t_{i,\mathrm{meas}} + b) + \bar{x}_{\mathrm{meas,2006–2008}}. \tag{6.10}$$

In Figure 6.5, the resulting seasonality is shown relative to the chemical tropopause for both periods. With regard to the considerable differences in the histograms (see Figure 6.3), the good agreement of the annual cycle between the two periods is remarkable.

In both periods, there is a distinct maximum of median tropospheric VMRs around May (∼145 ppt) and a minimum in the winter months (∼85 ppt). In the years 2006–2008, the period of enhanced VMRs lasts until July, whereas in the 2nd period it continues until September. In August, higher VMRs were measured directly above the tropopause. The lowest tropospheric VMRs are found in January and December, which is consistent with the observations during the first period.

In the lowermost stratosphere (LMS), a seasonal variation is only visible during the second period. The lowest VMRs are obtained in late spring. This is consistent with

the concurrent observation of maximum ozone and minimum CO VMRs indicating that aged stratospheric air masses control the composition of the LMS at this point of the year. In late summer CH_3CN-rich air masses penetrate into the LMS, where the distribution of CH_3CN is largely influenced by transport as a result of the long chemical lifetime of ∼70 years. As transport is slow in the stratosphere, the injected amounts of CH_3CN are not effectively removed from the LMS in the following months.

In Figure 6.6, a similar plot is shown for the GFED model simulation. In the interest of comparability, the data was restricted to the same latitude (23.5°–66.5°N) and longitude range (-135°–135°E) of the CARIBIC measurements. However, due to the completion of the simulation at the end of 2014, the second period of the CARIBIC measurements is not fully covered.

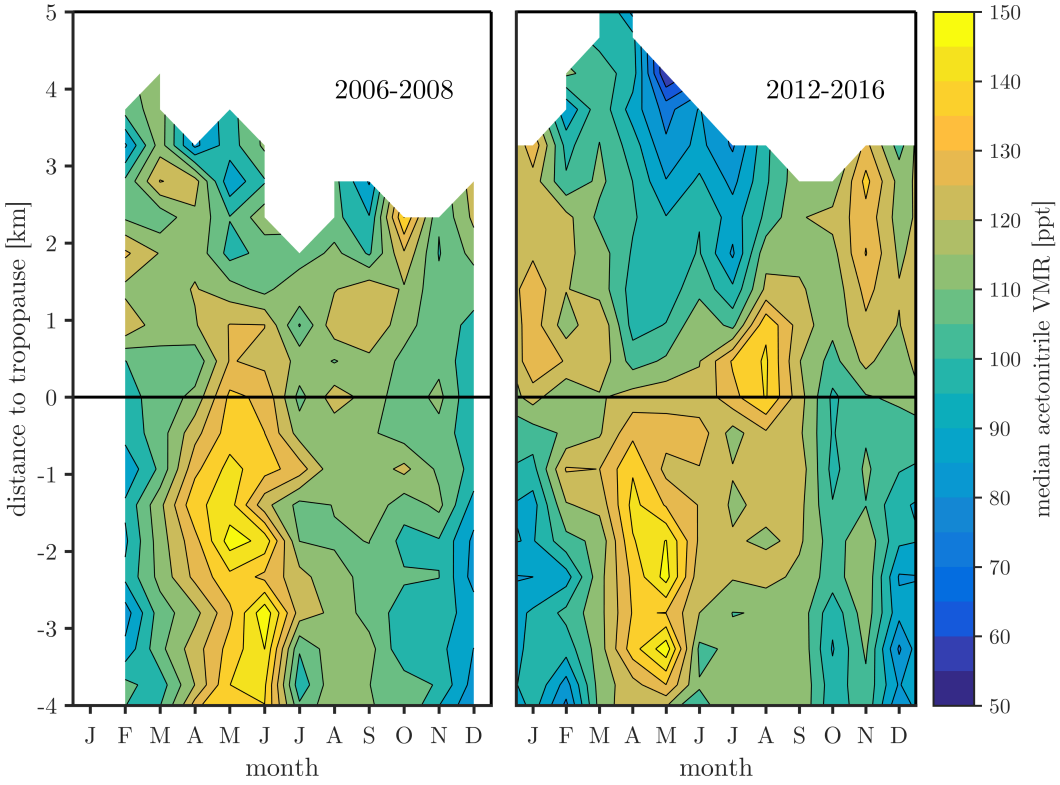

Figure 6.5.: Median CH_3CN VMRs relative to the chemical tropopause measured with the CARIBIC aircraft in the time periods 2006–2008 (left panel) and 2012–2016 (right panel). The data of the latter period has been corrected for a linear trend and shifted to the mean VMR observed between 2006 and 2008 (see text for details). Only measurements in the Northern hemisphere midlatitudes (23.5°–66.5°N) have been included.

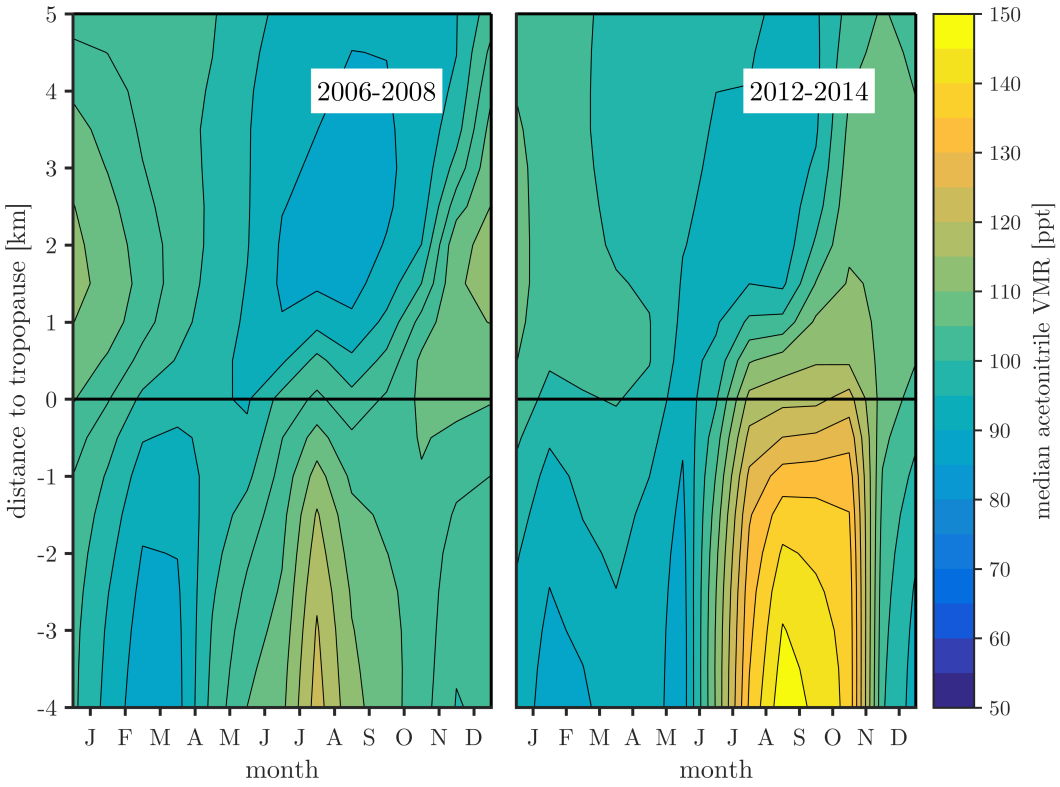

Figure 6.6.: Median CH_3CN VMRs relative to the WMO tropopause in the GFED model simulation. The underlying data is restricted to the Northern hemisphere midlatitudes (23.5°–66.5°N) and the longitude range (-135°–135°E) covered by the CARIBIC measurements.

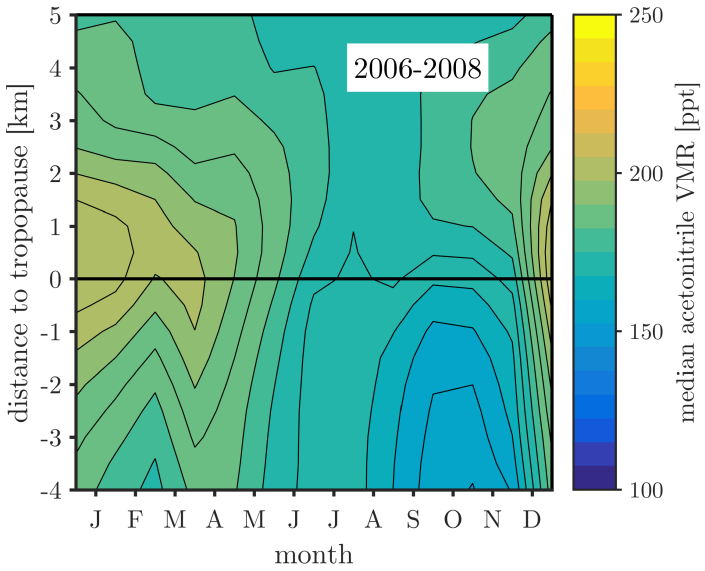

Figure 6.7.: Same as Figure 6.6, but for the MACCity model simulation. Please note the different scale of the colorbar.

Compared to the CARIBIC measurements, the distributions of the simulated VMRs show significantly less small-scaled structures. Reasons for this are the homogeneous distribution of sinks in the model, the coarse resolution of the model compared to the measurements and the better statistics of the underlying data. The GFED model simulation also show a seasonal variation in upper tropospheric CH_3CN VMRs, but the occurrence of minima and maxima is very different compared to the measurements.

In the years 2006–2008, there is a minimum (∼90 ppt) around March and a maximum (∼120 ppt) in July–August. The second period (2012–2014) is characterized by low VMRs (∼95 ppt) from January to June and an extended period of enhanced VMRs (∼135 ppt) between July and the end of October. Between both periods strong gradients are present.

The distributions of both periods have in common that the amplitude of the annual cycle decreases towards the tropopause, which can be explained by the increasing distance to the dominating sources and sinks. Moreover, this negative vertical gradient suggests that the VMRs in the northern hemisphere UT are largely influenced by regional emissions.

The strong annual increase of CH_3CN VMRs in spring, as observed with CARIBIC, is not present in the GFED model simulation. Likewise, the extended period of enhanced VMRs in fall, which occurs in the GFED model simulation between 2012 and 2014, coincides with the period of decreasing VMRs in the CARIBIC measurements.

For the model simulation using the MACCity inventory, a comparison is only possible for the first period of CARIBIC measurements, as the inventory data is only available until 2008. In Figure 6.7, the resulting distribution of median VMRs is shown. Please note that due to the generally higher VMRs in the MACCity simulation, the colorbar was adjusted.

In contrast to the GFED simulation, the median VMRs are highest at the turn of the year (∼195 ppt) and have a minimum around October (∼160 ppt) in the UT. In the first months of the year, the VMRs increase towards the tropopause and maximum VMRs are found directly above the tropopause in the LMS. This is a strong indication that the enhancement during this period of the year was not caused by emissions in the considered area (Northern hemisphere midlatitudes), but by transport of polluted air masses from the tropics into the extratropical UTLMS. As the transport processes are the same for the GFED and MACCity simulation,

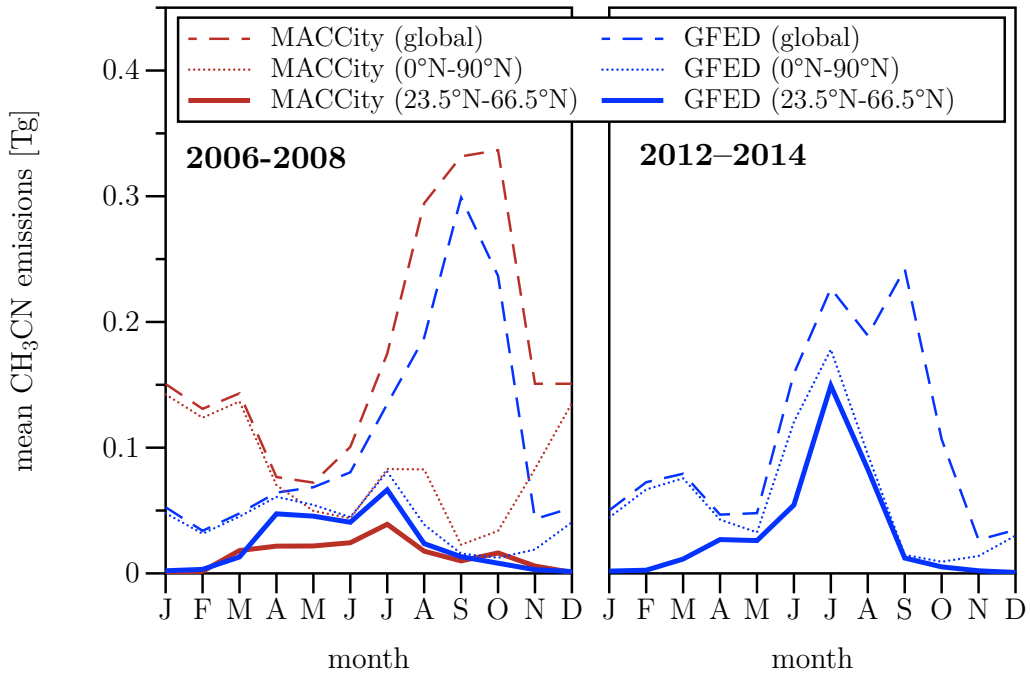

Figure 6.8.: Mean monthly emissions of CH_3CN in 2006–2008 (left panel) and 2012–2014 (right panel) for the MACCity (red lines) and GFED (blue lines) inventory.

not only the quantities of emissions must be different between both inventories, but also their geographical and temporal distribution.

To further investigate this, the mean monthly emissions in GFED and MACCity are compared for three different latitude ranges (global, entire NH and NH midlatitudes) in Figure 6.8. Interestingly, the GFED emissions in the NH midlatitudes between 2006 and 2008 are higher than the corresponding MACCity emissions, but in the model simulations, the VMRs of the NH midlatitudinal UT/LMS show the opposite behavior. This is a further indication that in the selected region – the midlatitudinal UT/LMS – the VMRs in the MACCity simulation are less influenced by regional emissions, but seem to be dominated by emissions in the tropics.

For the overlapping period (2006–2008), both inventories have in common that the emissions in the NH midlatitudes are negligible between November and February. They start to increase in March and have their annual maximum in July. However, between April and July the NH midlatitudinal emissions in the GFED inventory are on average twice as large as in MACCity. Also the relation between the total NH emissions and the midlatitudinal ones is different between the two inventories.

In the GFED inventory, 80 % of the NH emissions between April and October are released in the midlatitudes, whereas in the MACCity inventory, the midlatitudes only contribute 40 % to the total NH emissions in this period. However, the strongest difference between the two inventories occurs between November and March. In this period, the NH emissions in the MACCity inventory are three times larger than in the GFED inventory. The additional quantities of CH_3CN are released in the NH tropics and subsequently mix into the extratropical UTLS.

Compared to these amounts, the midlatitudinal emissions are small (18 % of the annual emissions in the NH). Therefore, the VMRs in the MACCity simulation rather follow the annual cycle of the emissions in the entire NH (red dotted line in Figure 6.8) than the one of the midlatitudinal emissions.

In the GFED inventory, the tropical emissions are lower and the simulated VMRs in the midlatitudinal UT/LMS indicate that they are linked to the regional emissions. For the period 2006–2008, the annual increase of simulated VMRs in April and the maximum VMRs in July match with the annual cycle of the regional emissions. In 2012–2014, there are less emissions in spring and considerably more emissions in July and August according to the inventory. This is also reflected by the median VMRs of the GFED simulation in Figure 6.6.

To illustrate the differences between both inventories further, the geographical distribution of the GFED-based emissions and their deviations from the emissions in the MACCity inventory are shown in Figure 6.9. In the NH winter months, the higher MACCity emissions in NH Africa are the main difference. In NH spring, global emissions are almost balanced, but the MACCity inventory does not capture the intense Russian wild fires to the same extent as GFED. This is also the case for the majority of fires in the southeastern part of Russia in boreal summer, whereas emissions from fires in the more northern regions of Russia are larger in the MACCity inventory. During the same period of the year, emissions from Canadian forest fires are strongly underestimated in the MACCity inventory compared to GFED-based values. In autumn, this statement may be reversed, at least for the region at the Canadian west coast, where the only major deviation is present. During this time of the year, however, strong deviations occur in Africa, where the MACCity emissions are generally higher. In South America, there are deviations in the magnitude of local emission fluxes, but otherwise emissions seem to be rather balanced on the continental scale.

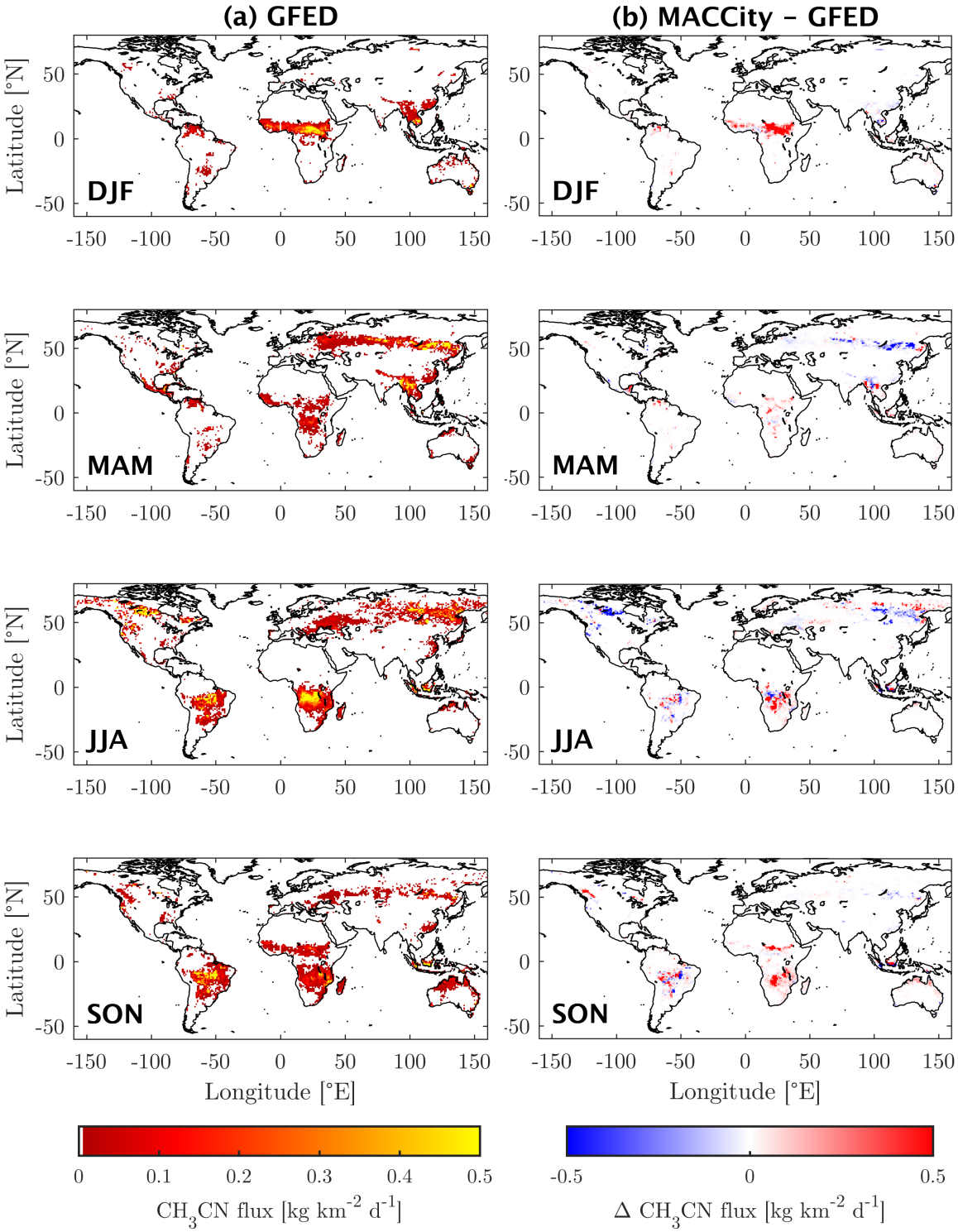

Figure 6.9.: (a) Geographical distribution of GFED-based CH_3CN emissions averaged over the respective months (DFJ, MAM, JJA, SON) in 2006–2008. (b) Differences between the three-month seasonal mean emission fluxes of the MACCity and GFED inventory.

With respect to the CARIBIC measurements, both model simulations do not fully reproduce the annual cycle observed within CARIBIC. Although the midlatitudinal biomass burning emissions included in both inventories coincide with the period of elevated CH_3CN VMRs observed by CARIBIC in the midlatudinal UTLS, the annual cycles of the model simulations deviate from the observations in terms of absolute values (MACCity) and the occurrence of maxima and minima (GFED and MACCity).

Regardless of the selected inventory, the observed maximum of UT CH_3CN VMRs around May, which is clearly visibly in both periods of CARIBIC observations, is not reproduced by the model simulations. At least for the GFED inventory and the time period 2006–2008, the NH midlatitudinal emissions around May are comparable to the ones, coinciding with the maximum of the simulated annual cycle in July. A potential reason for this might be the missing pyroconvection in the model. In summer, there is more regular convection, so that the biomass burning emissions, injected into the lowest model layer, are more efficiently transported in the UTLS.

Comparing the annual cycle derived from the CARIBIC observations with the one of the MACCity simulation reveals that the CH_3CN emissions in MACCity are not only shifted to higher VMRs, but also subject to a very different geographic distribution with considerably more emissions in the tropics and SH (see Figure 6.9b). In contrast, the VMRs observed within CARIBIC seem to be more influenced by regional emissions.

6.6. Daily resolved emission data

The majority of available biomass burning emission inventories provides data with monthly resolution, although the duration and the spatial expansion of fires commonly change on much shorter time scales. In the model simulation, the emissions data are interpolated to the time steps of the model. This means that the monthly emissions of each grid cell are uniformly distributed over the month, which should also lead to a more uniform distribution of trace gases in the modeled compared to the real atmosphere. Furthermore, in the case of monthly resolved emissions, large quantities of trace gases and aerosols may be released under meteorological conditions that considerably differ from those that were prevalent during the time of the fires (Mu et al., 2011).

To overcome this issue, inventories with daily and hourly resolution have been developed (Heald et al., 2003; Mu et all, 2011; Giglio et al., 2013). Also the GFED4.1s inventory used in this study provides daily-resolved emissions data (see Section 6.2.2). To investigate the effect of the temporal resolution on the simulated VMRs, another simulation using the daily-resolved GFED emissions was conducted. The set-up of this simulation was identical to the one with the monthly-resolved GFED emissions, i.e. the simulation started on 1 January 2004 with the same homogeneous CH_3CN distribution of 1 ppt in the entire model domain and was left free-running. Furthermore, the provision of daily fractions in the GFED raw data (see Table 6.2) ensures that in total the same amounts of CH_3CN are released each month in both simulations, regardless of the temporal resolution of the emissions.

This is also evident when comparing the global mean tropospheric VMRs of both simulations accessed at monthly intervals over a time period of 10 years (see Figure 6.10). The minor deviations can be explained by the fact that the monthly outputs of the simulation with daily emissions are influenced by the presence or absence of recent fire activities whereas the ones of the monthly emissions reflect the homogenous release of CH_3CN over the month.

Although the mean tropospheric VMRs are very similar, the differences in the spatial distribution of CH_3CN at the dates of the model outputs are remarkable (see lower panel in Figure 6.10). On average, the standard deviation of the global mean VMRs is 13 % higher in the troposphere when using the daily instead of the monthly resolved emissions. However, fluctuations are high and for a full assessment, the output intervals (once per month) are too large compared to the temporal resolution of the emissions, at least in the case of daily resolved emissions.

Therefore, the simulations based on daily and monthly emissions were repeated with the same set-up, except that the output interval was reduced to one day for a selected period of two months starting on 31 August 2005. However, this also means that the spatial distribution of CH_3CN is already different between the two simulations (daily vs. monthly resolved emissions) at the beginning of the two months period. Nevertheless, the differences are solely caused by the different temporal resolution of the emissions.

In Figure 6.11, the difference in upper tropospheric ($\sim$8 km above ground) VMRs, averaged over the two months, is shown next to the absolute mean VMRs of the simulation with monthly emission data. The enhancement is stronger pronounced in

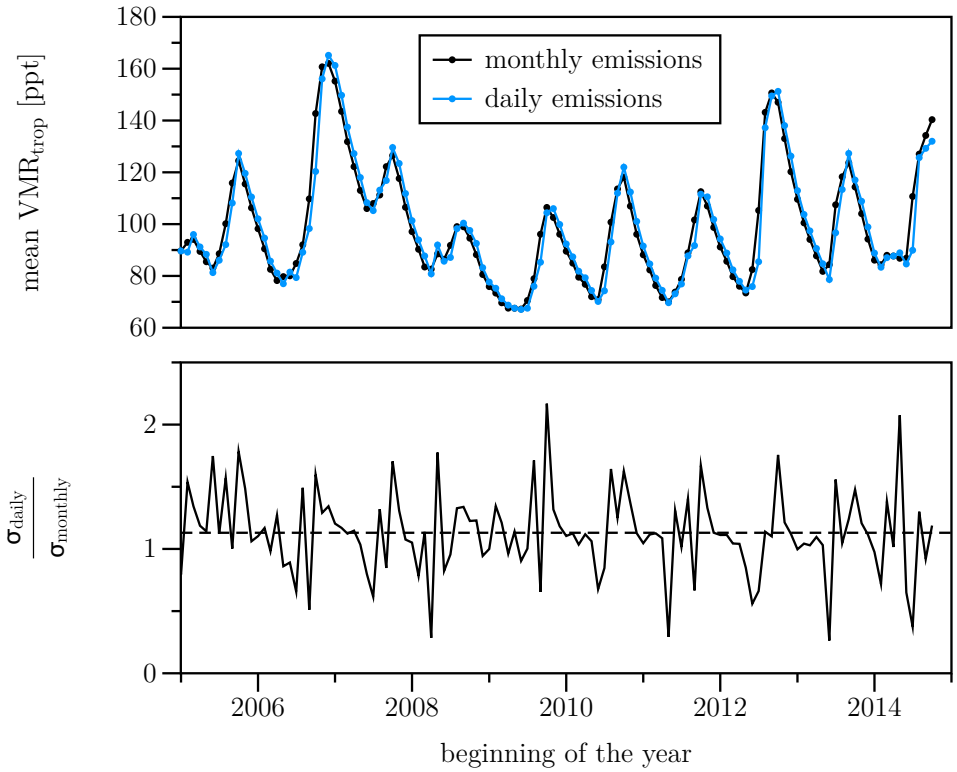

Figure 6.10.: Comparison of globally averaged tropospheric CH_3CN VMRs (upper panel) of the simulations with daily (blue circles) and monthly (black circles) resolved emissions. The differences in spatial variability of tropospheric CH_3CN between the two simulations are expressed by the ratio of the respective standard deviations (lower panel). The dashed line shows the mean ratio (1.13).

the simulation using daily resolved emissions (see right panel). This indicates that major amounts of the monthly released CH_3CN in these source regions were actually emitted over a time period considerably shorter than one month.

It also means that considerably larger quantities of trace gases emitted by biomass burning are rapidly transported into the UT than the simulation with monthly emissions suggests. This finding is of particular importance for the distribution of shorter-lived species, which account for a large proportion of total biomass burning emissions. Moreover, many short-lived trace gases emitted by biomass burning act as precursors of ozone and secondary organic aerosols (Keywood et al., 2013; Monks et al., 2015). As a greenhouse gas, ozone has a direct radiative forcing effect on climate. In addition, it indirectly influences the lifetimes of other greenhouse gases due to its role as primary source of OH radicals.

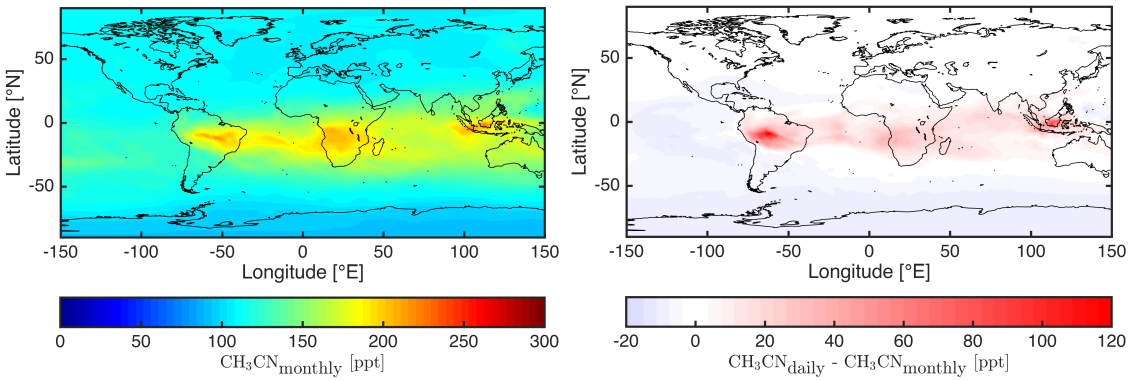

Figure 6.11.: Mean CH_3CN VMRs at model level 60 (∼8 km above ground) in the model simulation with monthly emission data (left panel) and differences in VMRs to the model simulation with daily emission data (right panel). In both panels, the VMRs of each grid cell have been averaged over the period from 31 August 2005 to 31 October 2005.

Also aerosols affect climate directly and indirectly (Ramanathan et al., 2001). The direct effect refers to the scattering and absorption of radiation (e.g. Atwater, 1970; Chýlek and Coakley, 1974). But they also interact with clouds in a way that they modify their radiative properties and lifetime resulting in an indirect radiative forcing (e.g. Twomey, 1974; Lohmann and Feichter, 2005).

The net effect of all these interactions strongly depends on the transport of precursors into regions where conditions are in favor of the processes. Long-range transport mainly occurs in the UT, where the colder and drier conditions reduce photochemical processing (e.g. Cain et al., 2012). To assess the impact of biomass burning on climate, it is therefore crucial to reproduce the actual distributions of these trace gases in the UT. However, in the simulation with monthly emissions the relevant precursor species would be largely removed chemically before being transported into the UT. Therefore, simulations with daily resolved biomass burning emissions are indispensable in this respect and CH_3CN measurements provided by IAGOS-CARIBIC could help to evaluate the transport of biomass burning emissions into the UT.

With regard to the simulations conducted here, the temporally coherent (daily resolved) emissions lead to enhanced VMRs in the outflow, whereas the uniformly distributed release of the same amount at least partially increases the hemispheric background. This can be observed in the VMRs over remote regions (e.g. the region southward of 40°S and large parts of the SH Pacific Ocean), where the mean VMRs of the simulation using monthly resolved emissions are higher.

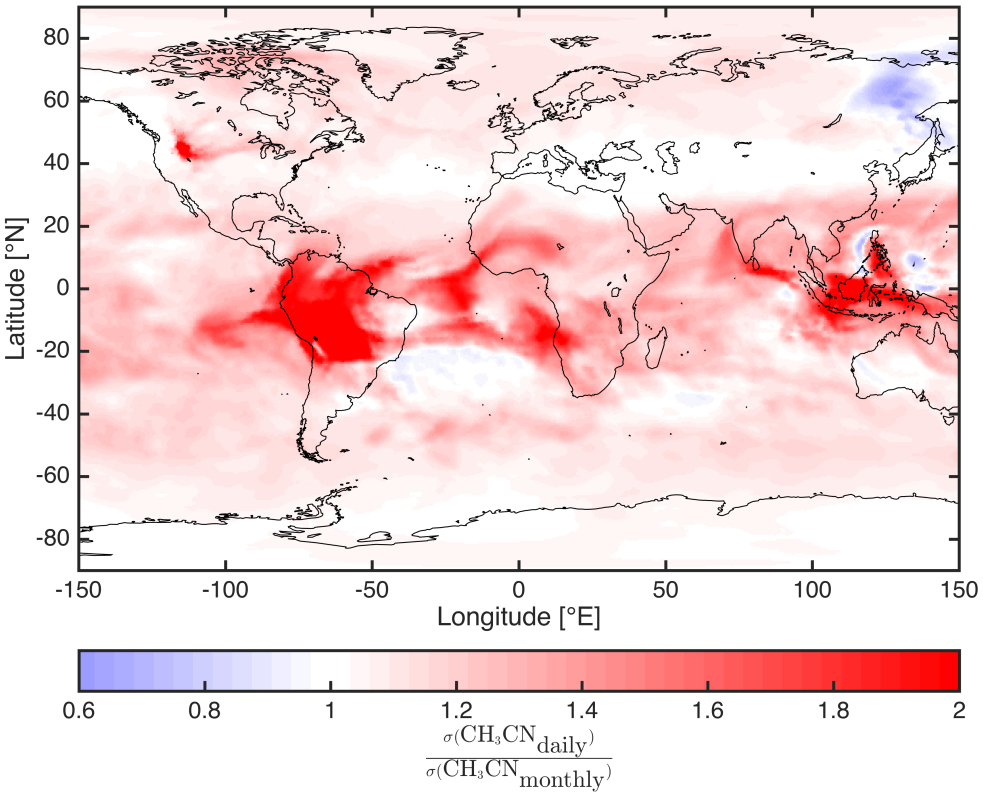

Figure 6.12.: Standard deviation ratio of daily CH_3CN VMRs at model level 60 (∼8 km above ground) in the model simulation with monthly and daily emission data in the period of 31 August 2005 to 31 October 2005. The colorbar is saturated at a factor of 2.

Also the temporal evolution of VMRs within the two month period shows a higher variation when using the daily resolved emission data. In Figure 6.12, the ratio of the standard deviations of daily VMRs in the two simulations is shown for the same model layer as in Figure 6.11. In 92 % of the grid cells in layer 60 (∼8 km above ground) the ratio is above unity. As expected, the temporal variation is highest over the source regions and in the outflow, where also the difference in mean VMRs is high between the two simulations. However, even in most of the regions, which did not show a deviation in mean VMRs (see Figure 6.11), the temporal variation in daily upper tropospheric VMRs is higher in the simulation with daily emissions.

On a global scale, the increase in the day-to-day variability, restricted to the considered model layer, is 14 %. In the tropics, the mean increase is 33 % and over the tropical rainforest of South America, the temporal variability is on average 88 % higher. At the surface (not shown), the relative difference in the standard deviations of both simulations is about twice as high.

Also the spatial variation increased in the considered two months (September and October 2005) when using the daily emissions. For each grid cell of model level 60, the standard deviation of the VMRs in neighboring grid cells and the grid cell itself was calculated. The global average ranges from 32 % on 23 September 2005 to 69 % on 16 September 2005.

All the above-mentioned findings indicate that the real-world variability in the distributions of trace gases emitted by biomass burning is far better reproduced when using daily instead of monthly resolved emissions data. Although the actual variability is probably still much higher than simulated, the integration of better resolved biomass burning emission fluxes into ICON-ART is an important step towards the intended point-to-point comparisons with CARIBIC observations and a more realistic simulation of the propagation of biomass burning emitted trace gases and aerosols into the highly climate sensitive tropopause region.

In addition, the improved reproducibility of the spatial variability has direct implications on the simulation of nonlinear atmospheric processes. In the presence of nonlinear chemical reactions, it does for instance matter whether adjacent air parcels mix with each other before or after chemical processes take place (Esler et al., 2001; Stohl et al., 2003). The merger of two reactants due to mixing can modify the abundance of other reactive species (e.g. the OH radical) and thus, accelerate or slow down chemical processing (e.g. Esler et al., 2001). Consequently, the temporal evolution of trace gas concentrations averaged over the volumes of both air parcels depends on the rate of mixing and the contrast in composition between the adjacent air parcels (Esler, 2003; Stohl et al., 2003). Although the dynamics, i.e. the rate of mixing, are the same in both model simulations, the homogenous distribution of monthly emissions can be equated to some form of premixing. This means that nonlinear atmospheric processes like stratospheric-tropospheric exchange or secondary aerosol formation are not correctly simulated quantitatively, when using the monthly resolved biomass burning emissions.

The sensitivity of simulated trace gas distributions to mixing processes becomes particular relevant with respect to process studies, which are intended in the near future to better understand the processes that lead to the observed chemical composition of biomass burning plumes encountered by CARIBIC.

6.7. Summary and conclusions

The integration of acetonitrile (CH_3CN) into the chemistry transport model ICON-ART allows for a systematic study of biomass burning and its influence on the chemical composition of the UTLS. Nevertheless, simulations rely on the provision of up-to-date and accurate emission data. At the beginning of this study, CH_3CN emissions were only available in the ACCMIP-MACCity inventory, restricted to the years before 2009 and a coarse temporal resolution.

In order to take full advantage of comparisons with CARIBIC observations, which constitute the longest time series of CH_3CN measurements in the UTLS and are ongoing, more recent emission fluxes of CH_3CN have been derived from the raw data of the latest GFED emission inventory (GFED4.1s).

For the years, in which both inventories and CARIBIC measurements are available (2006–2008), the emissions derived from GFED4.1s reproduce the CARIBIC observations within the uncertainties. However, the ACCMIP-MACCity inventory leads to considerably higher VMRs. In 2006, the enhanced VMRs cannot be explained by the CARIBIC observations and considered uncertainties. Strong deviations also occur in the annual cycle of CH_3CN VMRs in the extratropical UTLS. The strong discrepancy is mainly caused by the fact that the ACCMIP-MACCity includes considerably larger emissions of CH_3CN in the NH tropics compared to GFED. In contrast, the annual cycles of GFED and CARIBIC may deviate because of the missing pyroconvection in the model.

In the 2nd, more recent period (2012–2014), observations show a continuous increase in CH_3CN VMRs, whereas the remaining GFED simulation does not support such an increase. As the measurement instrument was strongly modified between 2008 and 2012 and the calibration procedure was changed from in-flight calibration to laboratory calibrations between two flight series, it must be assumed that the uncertainty associated with the measured VMRs is actually higher than estimated.

In the last part of the chapter, the effect of the temporal resolution of emissions on the distribution of CH_3CN VMRs in the UT was investigated. The spatial variability in the UT increased between 32 and 69 % when using daily instead of monthly resolved emissions. The homogeneous distribution of monthly emissions can be equated with stronger mixing. This has important impacts for future process studies, considering shorter-lived species emitted by biomass burning. As the simulated distributions of such gases are sensitive to mixing, model results and predictions can be subject to

substantial systematic errors when using monthly resolved emissions.

7. Summary and conclusions

This work reports on the completion of a new mass spectrometer developed for airborne VOC measurements, its first deployment in the UTLS onboard the research aircraft HALO and on two studies assessing the sources of atmospheric acetone and acetonitrile, respectively.

The instrument, named PTRMS-HALO in its final version, is the most compact and lightweight PTR-MS that has been deployed onboard aircraft so far. Moreover, it is the first PTR-MS worldwide that is completely controlled by a custom-made system including mass spectra acquisition. In contrast to the commercial controls, this new system has the great advantage that it can be easily modified and expanded by the user, e.g. with the latest instrumental developments. In addition, it is more lightweight and compact, which makes it well suited for deployment in environments with limited space such as aircraft.

Besides its unique control, this new instrument belongs to the very few PTR-MS devices worldwide fully customized to the conditions of atmospheric measurements onboard aircraft. As such, it is the result of 10 years of development and a total of 3 PhD projects. While the components development and assembly were accomplished in the previous projects, focus of this work was to finalize the control software (e.g. expanding it to autonomous operation onboard aircraft) and gas inlet system, to achieve the aeronautical certification necessary for operation onboard HALO, and to test and optimize the instrument in terms of reliability, sensitivity, usability and detection limits.

As a result, the instrument performed remarkably well during its first airborne deployment within the framework of the HALO campaign OMO. Main goal of the campaign was to examine the Atmosphere's self-cleaning capacity in the vicinity of the Asian summer monsoon. PTRMS-HALO fully contributed to this objective by measuring VOCs that are either known precursors of HO_x or tracers allowing conclusions about the origin or age of air mass. In this study, the high value of the

resulting data set is exemplarily shown based on a flight, on which outflow of the Asian summer monsoon has been presumably sampled, whereas the evaluation of the complete data set is objective of a separate manuscript (in preparation).

Following airborne deployment, the instrument was thoroughly characterized in the laboratory with the result that PTRMS-HALO is twice as sensitive as the average of instruments reported in the literature. This enhanced sensitivity is of great value for airborne measurements in the UTLS, as it enables the measurement of considerably more species of interest and data acquisition with a higher spatial resolution. As much of the knowledge about the atmosphere so far has been driven by what can be accurately measured and, if so, how fast it can be measured, the development of more sensitive devices such as PTRMS-HALO constitutes the foundations of future atmospheric research.

In this respect, the combination of the enhanced sensitivity achieved with PTRMS-HALO and the high spatial and temporal coverage achieved with the CARIBIC passenger aircraft appears particularly promising. As a result, the build-up of a largely identical instrument for deployment onboard the CARIBIC aircraft was started in this work. Although not being completed in this work, the new instrument considerably benefited from the experiences gained during testing and operating PTRMS-HALO. The data set generated with this new instrument among others will be of high relevance e.g. for top-down emission estimates and model validation.

Besides a description of the technical achievements, a major update on tropospheric enhancement ratios (EnRs) of acetone and CO is provided in this work. A new method to detect coherent correlations is applied to the CARIBIC data of acetone and CO and it is found that free tropospheric EnRs can be rather seen as chemical signatures of well-mixed boundary layer air and thus, of larger regional source patterns instead of distinct emissions from single point sources. Consequently, acetone-CO enhancement ratios are well suited to derive top-down estimates of regional emissions. In this study, the acetone emissions of two important source regions, North America and Southeast Asia, are assessed with this new approach. The top-down estimate for the North American sources (6 Tg a^{-1}) agrees well with bottom-up inventories (5.8 Tg a^{-1}), whereas the estimate for Southeast Asia (4.8 Tg a^{-1}) is $\sim$30 % higher than the one based on inventories (3.7 Tg a^{-1}), indicating that the latter might underestimate acetone emissions or overestimate CO emissions in this region.

With regard to the large uncertainties associated with bottom-up estimates of VOC emissions, an extension of this new approach to other source regions (e.g.

South America and Africa, which in sum account for about half of the global emissions of biogenically emitted VOCs and approximately two thirds of the global emissions from biomass burning) and species (e.g. methanol and acetonitrile) is highly recommended.

In the last part of this study, acetonitrile as a tracer for biomass burning is implemented into the chemistry transport model ICON-ART. Moreover, a tool for generating daily resolved emission data of acetonitrile and other species, subsequently used as model input, is developed. While previous biomass burning simulations in ICON-ART were generally restricted to the years before 2013, the new tool enlarges this time period until the end of 2016 at the time of writing.

Multi-annual simulations based on two different emission scenarios (ACCMIP-MACCity and GFED4.1s) are performed and compared among each other as well as with CARIBIC in-situ observations. One of the foremost results is that the two emissions scenarios lead to very different acetonitrile VMRs in the model simulations (190 ppt vs. 97 ppt in the upper troposphere).

For the years 2006–2008, the CARIBIC observations support the mean VMRs modeled based on the GFED4.1s emission scenario. In contrast, the high VMRs associated with the ACCMIP-MACCity emission scenario in 2006 cannot be explained by the observations within the respective uncertainties.

In the years following 2008, CARIBIC measurements apparently indicate an overall increase in tropospheric acetonitrile, which is not consistent with current biomass burning emission inventories. Modifications of the instrument and a change in the calibration procedure from in-flight calibration to laboratory calibrations might have led to an unconsidered increase in the uncertainties of measured VMRs. Further investigations, which are out of the scope of this study, are strongly recommended.

This situation also clearly exemplifies that there is an urgent need for new and more precise instruments such as PTRMS-HALO and PTRMS-CARIBIC to assess the overall emissions of VOCs and their impact on climate change and air quality.

Acknowledgments

Writing this thesis has been a period of learning, not only in the field of sciences, but also on a personal level. Therefore, I am grateful to those who gave me the chance to do this research and everybody, who has supported me in it.

First of all, I would like to express my sincere gratitude to my supervisor Prof. Johannes Orphal for the continuous support of my work, his personal guidance and motivation. I could not have imagined having a better doctoral supervisor.

Besides my supervisor, I am very thankful to Michael Höpfner for participating in this doctoral work as co-supervisor.

My sincere thanks also go to Andreas Zahn, who provided me the opportunity to join his team and to work on this very interesting topic in his laboratory. Without his support it would not have been possible to conduct this research.

With much appreciation I would like to express my gratitude to Marco Neumaier, Harald Bönisch and Roland Ruhnke for their personal guidance, expert advice and the many fruitful discussions.

Nobody has been more important to me in the pursuit of this project than my family. I would like to thank my parents Karin and Detmer Fischbeck for their encouragement and enduring support.

I thank Anna-Lena for her personal advice, patience and understanding during all periods of this work. It would have been impossible without your love and support.

I am deeply indebted to Frank Helleis and co-workers at the Max Planck Institute for Chemistry for developing the V25 system, their ever-lasting support in implementing it in our instruments and numerous hours of troubleshooting.

I am particularly grateful to Joel Brito, Felix Geiger and Simon Heger for their substantial contributions to the development and construction of the new instruments.

I would also like to take the opportunity to thank Alexander Streili, Benjamin Riexinger and co-workers at the workshop of IMK-ASF for manufacturing and constructing many parts of the new instruments with excellent precision on relatively short notice, which I appreciated very much.

I thank Michael Weimer for developing the emission module for ICON-ART and showing me how to implement new species in the model.

I would like to thank my former colleagues, in particular Julia Becker, Fabian Bartschke, Christoph Dyroff, Simon Heger and Helmut Widmann, for the good working atmosphere and mutual help.

I am very grateful to all the members of the CARIBIC project for the very warm welcome in this unique project, their interest in my work and support. In particular, I thank Carl Brenninkmeijer, Angela Baker, Ute Thorenz, Armin Rauthe-Schöch, Claus Koeppel, Dieter Scharffe, Florian Rubach, Markus Hermann, Denise Assmann, Greta Stratmann, Helmut Ziereis and Franz Slemr.

I acknowledge Astrud Wiesner, Sandra Leist and Derya Cayiroglu for their (not only administrative) support.

I thank Layal Safadi for the supervision of the instrument during OMO-ASIA. I am particularly grateful to the Fischer group at the Max Planck Institute for Chemistry for provision of the CO and CH_4 data and to all, who contributed to the campaign.

I thank Boris Schneider from Enviscope for the excellent cooperation during the aeronautical certification of the new instrument.

I am very grateful to James Randerson, Guido van der Werf and co-workers for providing the GFED fire emissions data and to Angelika Heil and Martin Schultz for provision of the ACCMIP-MACCity biomass burning emission dataset.

I thank the Centre National d'Etudes Spatiales (CNES) and the Centre National de la Recherche Scientifique (CNRS) – Institut National des Sciences de l'Univers (INSU) for distributing the data of several emission inventories in the ECCAD database. ECCAD is part of the ESPRI Data center (formerly Ether) and the emission database of the GEIA (Global Emissions InitiAtive) project. Moreover, I gratefully acknowledge NCAR Atmospheric Chemistry Division (ACD) for providing the TUV Radiation Model and the NOAA Air Resources Laboratory (ARL) for the provision of the HYSPLIT transport and dispersion model used in this thesis.

Last but not least, I thank Lufthansa, Lufthansa Technik and all CARIBIC partners for their ongoing support of the IAGOS–CARIBIC laboratory. Without it, this work would have been not possible.

Appendix

A. Sensitivity of EnR-based source estimates to the CO threshold

In Section 5.4, the choice to restrict the analysis to EnR with a CO enhancement greater than 10 times the measurement uncertainty of CO is motivated. Here, the analysis for North America (see Section 5.8) is repeated with thresholds for CO of exactly 10 ppb and 15 ppb.

In Table A.1, the results are compared with the previous analysis. The annual acetone source of (6.1 ± 3.1) Tg is in excellent agreement with the (6.0 ± 3.1) Tg derived when using 10 times the measurement uncertainty of CO as threshold.

Increasing the threshold to15 ppb reduces the dataset for North America by $\sim 75\,\%$, leading to the situation that there is not enough data for November and December, although North America is the region with the best coverage (see Table 5.7).

The mean of the monthly EnR decreases from 21.3 to 18.4 ppt ppb^{-1}, which can be explained as follows. The exclusion of events with CO enhancements of 10–15 ppb puts more emphasis on the events with high-CO enhancements, but the high-CO enhancements are not completely compensated by high-acetone enhancements; i.e. the EnRs of this subset are lower. Nevertheless, the means for all three requirements are still in the standard deviations of each other.

When changing the threshold to significantly lower CO enhancements, the monthly mean EnRs increase. However, in such a situation it apparently becomes impossible to distinguish between an increase caused by shifting the weight of certain EnRs and an increase related to the temporal evolution of EnRs, which we discussed in Section 5.4. Consequently, only the sensitivity of results to higher CO thresholds can be investigated. Thresholds higher than 15 ppb are not feasible with regard to the number of such events in our dataset.

	$\Delta CO > 10\sigma$			$\Delta CO > 10\,ppb$			$\Delta CO > 15\,ppb$		
Month	n	Mean + SD EnR	S_{Ac}	n	Mean + SD EnR	S_{Ac}	n	Mean + SD EnR	S_{Ac}
1	543	8.8 ± 4.6	0.1	465	9.0 ± 4.9	0.1	115	6.5 ± 6.2	0.1
2	339	8.5 ± 3.9	0.1	278	8.7 ± 4.1	0.1	154	9.0 ± 5.0	0.1
3	744	12.5 ± 4.9	0.2	688	12.6 ± 4.9	0.2	163	11.8 ± 5.3	0.2
4	1427	14.8 ± 10.2	0.3	1400	14.8 ± 10.3	0.3	362	12.4 ± 8.0	0.2
5	167	22.2 ± 9.1	0.5	167	22.2 ± 9.1	0.5	50	21.0 ± 5.8	0.5
6	568	40.2 ± 21.2	1.3	565	40.1 ± 21.2	1.3	51	29.8 ± 2.7	1.0
7	434	28.0 ± 14.0	1.1	434	28.0 ± 14.0	1.1	239	28.4 ± 13.8	1.1
8	1102	31.8 ± 16.7	1.0	1102	31.8 ± 16.7	1.0	361	24.9 ± 11.0	0.7
9	956	37.8 ± 16.7	0.7	722	40.2 ± 17.2	0.8	100	21.1 ± 10.1	0.4
10	397	25.2 ± 17.8	0.4	371	24.8 ± 17.9	0.4	53	34.2 ± 15.3	0.5
11	94	15.7 ± 7.7	0.2	77	16.0 ± 8.6	0.2	0	–	
12	99	9.5 ± 3.1	0.1	52	9.3 ± 3.2	0.1	4	3.7 ± 0.2	0.0
All	6870	21.3 ± 11.3	6.0 ± 3.1	6321	21.5 ± 11.6	6.1 ± 3.1	1652	18.4 ± 10.3	4.8 ± 1.9

Table A.1.: Results of three different cut-off requirements (top row) applied to the dataset for North America. For each month and cut-off requirement, the number of unique EnRs (n), the mean EnR and standard deviation in ppt ppb^{-1} and the resulting acetone source (S_{Ac}) in Tg are provided. The means and standard deviations for all months (last row) are based on the monthly values. Adopted from Fischbeck et al. (2017).

B. Matlab code used for HYSPLIT trajectory analysis

```
fid = fopen('trajectories.bat','wt'); % creates the file which will
% automatically execute HYSPLIT on a Windows PC
for i=1:17277 % loop through the matrix "flightroute" containing
    % the flight data. For each line a trajectory is calculated.
    % 1st column of flightroute: seconds since midnight (UTC)
    % 2nd column of flightroute: latitude of aircraft
    % 3rd column of flightroute: longitude of aircraft
    % 4th column of flightroute: altitude of aircraft in m
    hour = floor(flightroute(i,1)/3600);
    min = round((flightroute(i,1) -hour*60*60)/60);
    a = sprintf('%s%02d%s%02d%s', 'echo 15 08 06 ',hour,' ',min,...
        '     >CONTROL'); % string defining the trajectory start time.
    b = sprintf('%s%0.5f%s%0.5f%s%0.5f%s','echo ',...
        flightroute(i,2),'    ',flightroute(i,3),'    ',...
        flightroute(i,4),'   >>CONTROL'); % string defining the starting
    % position and altitude of the trajectory calculation
    c = sprintf('%s%d%s','echo ',flightroute(i,1),...
        '.txt%1          >>CONTROL'); % creates the string for each
    % HYSPLIT output file (one for each trajectory)
    fprintf(fid,'%s\n',a);
    fprintf(fid,'%s\n','echo 1                  >>CONTROL'); % defines
    % the number of starting positions
    fprintf(fid,'%s\n',b);
    fprintf(fid,'%s\n','echo -288               >>CONTROL'); % sets the
    % time period of the calculation to 288 hours (=12 days)
    fprintf(fid,'%s\n','echo 0                  >>CONTROL'); % sets the
    % vertical motion method to 0 (= use input model data)
    fprintf(fid,'%s\n','echo 20000.0            >>CONTROL'); % sets the
    % top of the model to 20000 m
    fprintf(fid,'%s\n','echo 12                  >>CONTROL'); % sets the
    % the number of input files. Filenames are given in the next lines
    fprintf(fid,'%s\n','echo C:/hysplit4/working/       >>CONTROL');
    fprintf(fid,'%s\n','echo 20150806_gdas0p5    >>CONTROL');
    fprintf(fid,'%s\n','echo C:/hysplit4/working/       >>CONTROL');
    fprintf(fid,'%s\n','echo 20150805_gdas0p5    >>CONTROL');
    fprintf(fid,'%s\n','echo C:/hysplit4/working/       >>CONTROL')
    fprintf(fid,'%s\n','echo 20150804_gdas0p5    >>CONTROL');
    fprintf(fid,'%s\n','echo C:/hysplit4/working/       >>CONTROL');
    fprintf(fid,'%s\n','echo 20150803_gdas0p5    >>CONTROL');
    fprintf(fid,'%s\n','echo C:/hysplit4/working/       >>CONTROL');
    fprintf(fid,'%s\n','echo 20150802_gdas0p5    >>CONTROL');
```

```
            fprintf(fid,'%s\n','echo C:/hysplit4/working/       >>CONTROL');
43          fprintf(fid,'%s\n','echo 20150801_gdas0p5    >>CONTROL');
            fprintf(fid,'%s\n','echo C:/hysplit4/working/       >>CONTROL');
45          fprintf(fid,'%s\n','echo 20150731_gdas0p5    >>CONTROL');
            fprintf(fid,'%s\n','echo C:/hysplit4/working/       >>CONTROL');
47          fprintf(fid,'%s\n','echo 20150730_gdas0p5    >>CONTROL');
            fprintf(fid,'%s\n','echo C:/hysplit4/working/       >>CONTROL');
49          fprintf(fid,'%s\n','echo 20150729_gdas0p5    >>CONTROL');
            fprintf(fid,'%s\n','echo C:/hysplit4/working/       >>CONTROL');
51          fprintf(fid,'%s\n','echo 20150728_gdas0p5    >>CONTROL');
            fprintf(fid,'%s\n','echo C:/hysplit4/working/       >>CONTROL');
53          fprintf(fid,'%s\n','echo 20150727_gdas0p5    >>CONTROL');
            fprintf(fid,'%s\n','echo C:/hysplit4/working/       >>CONTROL');
55          fprintf(fid,'%s\n','echo 20150726_gdas0p5    >>CONTROL');
            fprintf(fid,'%s\n','echo ./                 >>CONTROL');
57          fprintf(fid,'%s\n\n',c);
            fprintf(fid,'%s\n','\hysplit4\exec\hyts_std'); % executes the model
59          fprintf(fid,'%s\n\n','\hysplit4\exec\trajplot -itdump.%1 -oplot%1');
        end;
61      fclose(fid); % closes the "'trajectories.bat" file
```

Figure B.1.: Matlab code used for HYSPLIT trajectory analysis

```
1   IF (jsp == iTRCH3CN) then
      DO jb = i_startblk, i_endblk
3       CALL get_indices_c(p_patch, jb, i_startblk, i_endblk, &
          &                i_startidx, i_endidx, i_rlstart, i_rlend)
5       DO jc=i_startidx,i_endidx
          CALL WMO_tropopause( 1, 1, nlev, &
7           &  ncctop, nccbot, .FALSE., &
            &  p_diag%temp(jc,:,jb), p_diag%pres(jc,:,jb), &
9           &  ptropo(jc,jb), ktrpwmo(jc,jb), ktrpwmop1(jc,jb) )
          DO jk = 1,ktrpwmop1(jc,jb)
11          rate(jc,jk,jb,jsp) = 1._wp / 2207520000._wp
          ENDDO
13
          DO jk = ktrpwmo(jc,jb),nlev
15          rate(jc,jk,jb,jsp) = 1._wp / 58642214._wp
          ENDDO
17
          IF ((iforcing == inwp) .AND. (.NOT. ext_data%atm%llsm_atm_c(jc,jb)))
              THEN
19          DO jk = nlev-8,nlev
              rate(jc,jk,jb,jsp) = 1._wp / 1814400._wp
21          ENDDO
          END IF
23
          DO jk = 1,nlev
25          extra_3d(jc,jk,jb,1) = rate(jc,jk,jb,jsp)
          END DO
27      ENDDO
      ENDDO
29  ENDIF
```

Figure B.2.: Implemented Fortran code for the removal of CH_3CN in ICON-ART. The lines are part of the mo_art_chemtracer-module, which can be found in the directory "/src/art/chemistry/"

C. Acetonitrile simulations in ICON-ART

C.1. Changing the lifetime of CH_3CN

As it might be necessary to adapt the selected lifetimes for future studies, the implementation in the model code is shortly described in the following:

In ICON-ART, chemical tracer processes (production and removal) are programmed in the "mo_art_chemtracer" module, which can be found in the "/src/art/chemistry/" directory of the ICON-folder. Figure B.2 shows the Fortran code, which has been inserted for the removal of CH_3CN. In short, the displayed subroutine determines the removal rate of CH_3CN (in s^{-1}) for each grid cell. The position of the grid cell in the native ICON grid is defined by the variables jb, jc and jk.

To distinguish between the troposphere and stratosphere, the function WMO_tropopause is called in line 6ff. and writes for each model column (jc,jb) the lowest stratospheric model level into the variable ktrpwmop1(jc,jb) and the highest tropospheric model level into the variable ktrpwmo(jc,jb). Subsequently, the removal rate for all model levels above the tropopause (1/70 $years^{-1}$ = 1/2207520000 s^{-1}) is set in line 11. For the tropospheric model levels, the removal rate (1/22.3 $months^{-1}$ = 1/58642214 s^{-1}) is set in line 15. The removal rates for the grid cells in the marine boundary layer are (1/21 $days^{-1}$ = 1/1814400 s^{-1}) subsequently overwritten in line 20. The marine boundary layer is identified using the boolean land-sea-mask "ext_data%atm%llsm_atm_c(jc,jb)", which is true for columns over land and false for columns over the seas. The number of the lowest model levels, which are assigned to the marine boundary layer, is given in line 19 (nlev-**8**,nlev). Please note, that any modification of the parameters will only become effective after re-compiling the model.

C.2. Configuration of the emissions interface

Prior to a model simulation, the user has to specify the emission inventory to be used, the location of the respective preprocessed files and the number of lowest model layers into which the emissions shall be inserted. This is done in a TeX file, included in the subdirectory "/src/art/runctrl_examples/emiss_ctrl" of the ICON folder.

```
\begin{table}[h] \caption{Chemical Tracers and their emission folders.
        Type of emission: 10 = anthropogenic, 11 = biogenic,
        12 = biomass burning, 13 = biogenic online}\label{emiss_tracers}
    \begin{tabular}{l r c c l}\\
    \hline
    Name & number of types / type of emission
    & standard value (in kg m$^{-2}$ s$^{-1}$) / number of dimensions per
    timestep & vname & path \\
    \hline
TRCH3CN_chemtr  & 1  &  0.00E+01  &  &  \\
   & 12 & 2 & 1 & emiss & /pfs/imk/imk-asf/common/
      data_remapped_to_ICONgrid/emiss/CH3CN/BBE/GFED4.1s_Akagi_daily/R2B04 \\

%%EOMODES  <<<THIS LINE IS THE NECESSARY BREAKUP CONDITION FOR ICON READ>>>
    \hline
    \end{tabular}
\end{table}
```

Figure C.1.: TeX table of the ICON-ART emissions interface used to read in the daily GFED4.1s emissions files.

In Figure C.1, the contents of the file as used for the model simulation with daily GFED4.1s emissions is shown. All parameters related to the emissions of a specific species are included in a TeX table and separated by separated by ampersands. For a more general description of the structure, please refer to Weimer et al. (2017).

As only biomass burning emissions are considered, the number of emission types (2nd argument in line 10) is set to 1. The standard emission flux (3rd argument in line 10) is set to zero, as it is only of importance when no external emission data is read in. The number of lowest model layers into which the emissions are inserted (3rd argument in line 11) is set to 1 in this study.

The subsequent arguments in line 11 determine which emission inventory is used. In the preprocessed emission files of GFED4.1s, the data is included in the variable "emiss". The path refers to the directory, in which the respective files are stored. As files for different model resolutions are stored in different directories, a change of the model resolution requires adaption of these paths.

The ACCMIP-MACCity inventory has the peculiarity of distinguishing between forest fires and grassland/savanna fires. As the emissions of the two fuel types are

provided in separate variables ("emiss_for" and "emiss_gra"), the emissions interface needs to sum up both variables. This is achieved by replacing lines 10–12 in Figure C.1 by the following section:

```
   TRCH3CN_chemtr  & 2  &  0.00E+01  &  &  \\
2  & 12 & 2 & 1 & emiss_for & /pfs/imk/imk-asf/common/data_remapped_to_ICONgrid/
       emiss/CH3CN/BBE/MACCity/R2B04 \\
4  & 12 & 2 & 1 & emiss_gra & /pfs/imk/imk-asf/common/data_remapped_to_ICONgrid/
       emiss/CH3CN/BBE/MACCity/R2B04 \\
```

C.3. Changes of the file structure

Initial tests revealed that the DWD ICON tools expect a very specific format and file naming and that processing already fails in the case of small deviations. As the files of the ACCMIP-MACCity inventory were processed without errors, the file structure was taken as reference for the GFED file generation.

Therefore, after having calculated the gridded emissions, the script adapts the structure of the emissions and auxiliary information to the structure of the ACCMIP-MACCity files. The respective changes are summarized in Table C.1.

GFED4.1s	Raw data file		File generated for ICON input
Longitudinal grid	-180°E – 180°E	→	0°E – 360°E
Latitudinal grid	90°N – -90°N	→	-90°N – 90 °N
Absolute time	not specified	→	days since 1850-01-01 00:00
File format	HDF5	→	NetCDF
Exemplarily file name	GFED4.1s_*2015*.hdf5	→	GFED4.1s_emissions_all_biomassBurning _*2015*_*Akagi*_daily.nc

Table C.1.: Changes of the GFED4.1s raw data structure (left) to enable further processing by the DWD ICON tools.

C.4. Matlab code

```
1  %% options, please adjust
   first_year = 2003; % daily resolved data is available from 2003 onwards
3  last_year = 2016;

5  %%emission factors for acetonitrile in g kg-1. Taken from Agagi et al., 2011
   EF_SAVA = 0.11; % Savanna, grassland, and shrubland fires
7  EF_BORF = 0.61; % Boreal forest fires
   EF_TEMF = 0.61; % Temperate forest fires
```

```
EF_DEFO = 0.41; % Tropical forest fires [deforestation and degradation]
EF_PEAT = 3.70; % Peat fires
EF_AGRI = 0.21; % Agricultural waste burning

%% change the path to your current working folder
workpath='/Users/Garlich/Documents/MATLAB/Acetonitrile/GFED4';
dialog_title='Please specify the working directory of this project';
workpath = uigetdir(workpath, dialog_title);
cd(workpath);

%% save GFED4 HDF5-Rawdata files from website
choice = questdlg('(Re-)Download raw data from website?', ...
    'Download Options', ...
    'Yes please','No thank you','No thank you');

switch choice
    case 'Yes please'
        % url = 'http://www.falw.vu/~gwerf/GFED/GFED4/';
        url = 'http://www.geo.vu.nl/~gwerf/GFED/GFED4/'; % new address
        for i=first_year:last_year
            filename = sprintf('GFED4.1s_%d.hdf5',i); %creates the filename
                that will be searched on the directory
            fileurl = [url,filename];
            outfilename = websave(filename,fileurl);
        end;

    case 'No thank you'
end;

%% read GFED4-data into Matlab
counter = 0;
for y=first_year:last_year
    counter = counter + 1;
    clear EMISS MONTHEMISS DM DM_SAVA DM_BORF DM_TEMF DM_DEFO DM_PEAT DM_AGRI

    filename = sprintf('GFED%d.hdf5',y);
    doy = 0; % day of the year counter

    for m=1:12 % loop month
        month = sprintf('%02d',m);

        contentpath = ['/emissions/',month,'/DM'];
        DM = h5read(filename,contentpath);
        contentpath = ['/emissions/',month,'/partitioning/DM_SAVA'];
        DM_SAVA = h5read(filename,contentpath);
        contentpath = ['/emissions/',month,'/partitioning/DM_BORF'];
        DM_BORF = h5read(filename,contentpath);
        contentpath = ['/emissions/',month,'/partitioning/DM_TEMF'];
        DM_TEMF = h5read(filename,contentpath);
        contentpath = ['/emissions/',month,'/partitioning/DM_DEFO'];
        DM_DEFO = h5read(filename,contentpath);
        contentpath = ['/emissions/',month,'/partitioning/DM_PEAT'];
        DM_PEAT = h5read(filename,contentpath);
        contentpath = ['/emissions/',month,'/partitioning/DM_AGRI'];
        DM_AGRI = h5read(filename,contentpath);

```

```
        hdf5 = h5info(filename);
65      days_per_month = size(hdf5.Groups(4).Groups(m).Groups(1).Datasets,1);

67      if y<=2002
            days_per_month = 365.25/12; % should be improved
69      end;

71      for d=1:days_per_month % loop days
            doy = doy + 1;
73          day = sprintf('%d',d);
            contentpath = ['/emissions/',month,'/daily_fraction/day_',day];
75          Dayfraction = h5read(filename,contentpath);
            clear DAYEMISS
77          % DAYEMISS in kg m-2 s-1
            DAYEMISS = Dayfraction .* DM ./(24*60*60) .* 10^-3 .* (EF_SAVA .*
                DM_SAVA + EF_BORF .* DM_BORF + EF_TEMF .* DM_TEMF + EF_DEFO .*
                 DM_DEFO + EF_PEAT .* DM_PEAT + EF_AGRI .* DM_AGRI);
79          DAYEMISS = vertcat(DAYEMISS(721:1440,:),DAYEMISS(1:720,:));
            DAYEMISS = fliplr(DAYEMISS);
81          EMISS(:,:,doy) = DAYEMISS;
        end; % end of day-loop
83      MONTHEMISS(:,:,m) = DM ./(days_per_month*24*60*60) .* 10^-3 .* (
            EF_SAVA .* DM_SAVA + EF_BORF .* DM_BORF + EF_TEMF .* DM_TEMF +
            EF_DEFO .* DM_DEFO + EF_PEAT .* DM_PEAT + EF_AGRI .* DM_AGRI);
        MONTHEMISS(:,:,m) = vertcat(MONTHEMISS(721:1440,:,m),MONTHEMISS
            (1:720,:,m));
85      MONTHEMISS(:,:,m) = fliplr(MONTHEMISS(:,:,m));
    end; % end of month-loop
87
    %converts to single precision (as it is for ACCMIP_MACCITY)
89  EMISS = single(EMISS);
    MONTHEMISS = single(MONTHEMISS);
91
    %% Create output files in netcdf-format
93
    % name of output files for daily and monthly resolution
95  filename=sprintf('GFED4.1s_emissions_all_biomassBurning_%d_Akagi_daily.nc'
        ,y);
    filename_month=sprintf('GFED4.1s_emissions_all_biomassBurning_%
        d_Akagi_monthly.nc',y);
97
    % deletes previous output file
99  delete(filename);
    delete(filename_month);
101 % creates time variable; time is given in days since 1850-1-1 00:00:00
    ystring = sprintf('1/1/%d',y);
103 firstdayofyear = daysdif('1/1/1850',ystring);
    time = firstdayofyear:1:(firstdayofyear+doy-1);
105 time = time';
    time = single(time);
107 level = 2;

109 nccreate(filename,'date',...
        'Dimensions',{'date',doy},'Datatype','single');
111 %  'Format','netcdf4',...
    %  'DeflateLevel',level,...
```

```
113     %  'Shuffle',true,...
        ncwrite(filename,'date',time);
115     ncwriteatt(filename,'date','units','days since 1850-01-01');

117     month = [daysdif('1/1/2000',sprintf('1/1/%d',y)),...
            daysdif('1/1/2000',sprintf('2/1/%d',y)),...
119         daysdif('1/1/2000',sprintf('3/1/%d',y)),...
            daysdif('1/1/2000',sprintf('4/1/%d',y)),...
121         daysdif('1/1/2000',sprintf('5/1/%d',y)),...
            daysdif('1/1/2000',sprintf('6/1/%d',y)),...
123         daysdif('1/1/2000',sprintf('7/1/%d',y)),...
            daysdif('1/1/2000',sprintf('8/1/%d',y)),...
125         daysdif('1/1/2000',sprintf('9/1/%d',y)),...
            daysdif('1/1/2000',sprintf('10/1/%d',y)),...
127         daysdif('1/1/2000',sprintf('11/1/%d',y)),...
            daysdif('1/1/2000',sprintf('12/1/%d',y))];
129
        month = month';
131     month = single(month);
        nccreate(filename_month,'date',...
133         'Dimensions',{'date',12},'Datatype','single');
        %  'Format','netcdf4',...
135     %  'DeflateLevel',level,...
        %  'Shuffle',true,...
137     ncwrite(filename_month,'date',month);
        ncwriteatt(filename_month,'date','units','days since 1850-01-01');
139
        %creates longitude variable for 0.25 degree resolution
141     longitude = 0.125:0.25:359.875;
        longitude = longitude';
143     longitude = single(longitude);

145     nccreate(filename,'lon',...
            'Dimensions',{'lon',1440},'Datatype','single');
147     % 'DeflateLevel',level,...
        % 'Shuffle',true,...
149     ncwrite(filename,'lon',longitude);
        ncwriteatt(filename,'lon','units','degrees_east');
151
        nccreate(filename_month,'lon',...
153         'Dimensions',{'lon',1440},'Datatype','single');
        %  'DeflateLevel',level,...
155     %  'Shuffle',true,...
        ncwrite(filename_month,'lon',longitude);
157     ncwriteatt(filename_month,'lon','units','degrees_east');

159     %creates latitude variable for 0.25 degree resolution
        latitude = -89.875:0.25:89.875;
161     latitude = latitude';
        latitude = single(latitude);
163     nccreate(filename,'lat',...
            'Dimensions',{'lat',720},'Datatype','single');
165     % 'DeflateLevel',level,...
        % 'Shuffle',true,...
167     ncwrite(filename,'lat',latitude);
        ncwriteatt(filename,'lat','units','degrees_north');
```

```
169
        nccreate(filename_month,'lat',...
171         'Dimensions',{'lat',720},'Datatype','single');
        %  'DeflateLevel',level,...
173     %  'Shuffle',true,...
        %  'Datatype','single');
175     ncwrite(filename_month,'lat',latitude,1);
        ncwriteatt(filename_month,'lat','units','degrees_north');
177
        %creates daily emission data variable; emissions given in kg m-2 s-1
179     nccreate(filename,'emiss',...
            'Dimensions',{'lon',1440,'lat',720,'date',doy},'Datatype','single');
181     %  'DeflateLevel',level,...
        %  'Shuffle',true,...
183     ncwrite(filename,'emiss',EMISS);
        ncwriteatt(filename,'emiss','units','kg m-2 s-1');
185
        %creates monthly emission data variable; emissions given in kg m-2 s-1
187     nccreate(filename_month,'emiss',...
            'Dimensions',{'lon',1440,'lat',720,'date',12},'Datatype','single');
189     %  'DeflateLevel',level,...
        %  'Shuffle',true,...
191     ncwrite(filename_month,'emiss',MONTHEMISS);
        ncwriteatt(filename_month,'emiss','units','kg m-2 s-1');
193
    end; % end of year-loop
```

Figure C.2.: Matlab code used to generate the GFED-based acetonitrile emission files

Bibliography

ACCMIP: Emissions for Atmospheric Chemistry and Climate Model Intercomparison Project dataset - Data between year 1850 and 2000 from ACCMIP - distributed by ECCAD. Author: Jean-François Lamarque, 2010.

ACTRIS: WP4-NA4: Trace gases networking: Volatile organic carbon and nitrogen oxides Deliverable D4.9: Final SOPs for VOCs measurements, Technical report, `http://fp7.actris.eu/Portals/97/deliverables/PU/WP4_D4.9_M42_v2.pdf`, last access: 1 August 2017, 2014.

Akagi, S. K., Yokelson, R. J., Wiedinmyer, C., Alvarado, M. J., Reid, J. S., Karl, T., Crounse, J. D., and Wennberg, P. O.: Emission factors for open and domestic biomass burning for use in atmospheric models, Atmos. Chem. Phys., 11, 4039–4072, doi:10.5194/acp-11-4039-2011, 2011.

Akagi, S. K., Craven, J. S., Taylor, J. W., McMeeking, G. R., Yokelson, R. J., Burling, I. R., Urbanski, S. P., Wold, C. E., Seinfeld, J. H., Coe, H., Alvarado, M. J., and Weise, D. R.: Evolution of trace gases and particles emitted by a chaparral fire in California, Atmos. Chem. Phys., 12, 1397–1421, doi:10.5194/acp-12-1397-2012, 2012.

Allen, J. S.: The Detection of Single Positive Ions, Electrons and Photons by a Secondary Electron Multiplier, Phys. Rev., 55, 966, doi:10.1103/PhysRev.55.966, 1939.

Alvarado, M. J., Logan, J. A., Mao, J., Apel, E., Riemer, D., Blake, D., Cohen, R. C., Min, K.-E., Perring, A. E., Browne, E. C., Wooldridge, P. J., Diskin, G. S., Sachse, G. W., Fuelberg, H., Sessions, W. R., Harrigan, D. L., Huey, G., Liao, J., Case-Hanks, A., Jimenez, J. L., Cubison, M. J., Vay, S. A., Weinheimer, A. J., Knapp, D. J., Montzka, D. D., Flocke, F. M., Pollack, I. B., Wennberg, P. O., Kurten, A., Crounse, J., Clair, J. M. S., Wisthaler, A., Mikoviny, T., Yantosca, R. M., Carouge, C. C., and Le Sager, P.: Nitrogen oxides and PAN in plumes from boreal fires during ARCTAS-B and their impact on ozone: an integrated analysis of aircraft and satellite observations, Atmos. Chem. Phys., 10, 9739–9760, doi:10.5194/acp-10-9739-2010, 2010.

Alves, C. A., Vicente, A. M., Rocha, S., and Vasconcellos, P.: Hopanoid hydrocarbons in PM_{10} from road tunnels in São Paulo, Brazil, Air Qual. Atmos. Heal., 10, 799–807, doi:10.1007/s11869-017-0462-3, 2017.

Amann, A., Schwarz, K. E., Wimmer, G., and Witkovský, V.: Model based determination of detection limits for proton transfer reaction mass spectrometer, Meas. Sci. Rev., 10, 180–188, doi:10.2478/v10048-010-0031-5, 2010.

Ammann, C., Spirig, C., Neftel, A., Steinbacher, M., Komenda, M., and Schaub, A.: Application of PTR-MS for measurements of biogenic VOC in a deciduous forest, Int. J. Mass Spectrom., 239, 87–101, doi:10.1016/j.ijms.2004.08.012, 2004.

Ammann, C., Brunner, A., Spirig, C., and Neftel, A.: Technical note: Water vapour concentration and flux measurements with PTR-MS, Atmos. Chem. Phys., 6, 4643–4651, doi:10.5194/acp-6-4643-2006, 2006.

Andreae, M. O. and Merlet, P.: Emissions of trace gases and aerosols from biomass burning, Glob. Biogeochem. Cycles, 15, 955–966, doi:10.1029/2000GB001382, 2001.

Andreae, M. O., Artaxo, P., Fischer, H., Freitas, S. R., Grégoire, J.-M., Hansel, A., Hoor, P., Kormann, R., Krejci, R., Lange, L., Lelieveld, J., Lindinger, W., Longo, K., Peters, W., de Reus, M., Scheeren, B., Silva Dias, M. A. F., Ström, J., van Velthoven, P. F. J., and Williams, J.: Transport of biomass burning smoke to the upper troposphere by deep convection in the equatorial region, Geophys. Res. Lett., 28, 951–954, doi:10.1029/2000GL012391, 2001.

Apel, E. C., Hills, A. J., Lueb, R., Zindel, S., Eisele, S., and Riemer, D. D.: A fast-GC/MS system to measure C_2 to C_4 carbonyls and methanol aboard aircraft, J. Geophys. Res., 108, 8794, doi:10.1029/2002JD003199, 2003.

Apel, E. C., Brauers, T., Koppmann, R., Bandowe, B., Boßmeyer, J., Holzke, C., Tillmann, R., Wahner, A., Wegener, R., Brunner, A., Jocher, M., Ruuskanen, T., Spirig, C., Steigner, D., Steinbrecher, R., Gomez Alvarez, E., Müller, K., Burrows, J. P., Schade, G., Solomon, S. J., Ladstätter-Weißenmayer, A., Simmonds, P., Young, D., Hopkins, J. R., Lewis, A. C., Legreid, G., Reimann, S., Hansel, A., Wisthaler, A., Blake, R. S., Ellis, A. M., Monks, P. S., and Wyche, K. P.: Intercomparison of oxygenated volatile organic compound measurements at the SAPHIR atmosphere simulation chamber, J. Geophys. Res. Atmos., 113, 1–24, doi:10.1029/2008JD009865, 2008.

Arijs, E. and Brasseur, G.: Acetonitrile in the stratosphere and implications for positive ion composition, J. Geophys. Res. Atmos., 91, 4003–4016, doi:10.1029/JD091iD03p04003, 1986.

Armbruster, D. A. and Pry, T.: Limit of blank, limit of detection and limit of quantitation, Clin. Biochem. Rev., 29, 49–52, 2008.

Arnold, F. and Hauck, G.: Lower stratosphere trace gas detection using aircraft-borne active chemical ionization mass spectrometry, Nature, 315, 307–309, doi:10.1038/315307a0, 1985.

Arnold, F., Knop, G., and Ziereis, H.: Acetone measurements in the upper troposphere and lower stratosphere - implications for hydroxyl radical abundances, Nature, 321, 505–507, doi:10.1038/321505a0, 1986.

Arnold, F., Bürger, V., Droste-Fanke, B., Grimm, F., Krieger, A., Schneider, J., and Stilp, T.: Acetone in the upper troposphere and lower stratosphere: Impact on trace gases and aerosols, Geophys. Res. Lett., 24, 3017–3020, doi:10.1029/97GL02974, 1997.

Arnold, S. R., Chipperfield, M. P., and Blitz, M. A.: A three-dimensional model study of the effect of new temperature-dependent quantum yields for acetone photolysis, J. Geophys. Res., 110, D22 305, doi:10.1029/2005JD005998, 2005.

Arnold, S. R., Methven, J., Evans, M. J., Chipperfield, M. P., Lewis, A. C., Hopkins, J. R., McQuaid, J. B., Watson, N., Purvis, R. M., Lee, J. D., Atlas, E. L., Blake, D. R., and Rappenglück, B.: Statistical inference of OH concentrations and air mass dilution rates from successive observations of nonmethane hydrocarbons in single air masses, J. Geophys. Res., 112, D10S40, doi:10.1029/2006JD007594, 2007.

Atkinson, R.: Atmospheric chemistry of VOCs and NO_x, Atmos. Environ., 34, 2063–2101, doi:10.1016/S1352-2310(99)00460-4, 2000.

Atkinson, R. and Arey, J.: Atmospheric Degradation of Volatile Organic Compounds Atmospheric Degradation of Volatile Organic Compounds, Chem. Rev., 103, 4605–4638, doi:10.1021/cr0206420, 2003.

Atkinson, R., Baulch, D. L., Cox, R. A., Crowley, J. N., Hampson, R. F., Hynes, R. G., Jenkin, M. E., Rossi, M. J., and Troe, J.: IUPAC Task Group on Atmospheric Chemical Kinetic Data Evaluation, http://iupac.pole-ether.fr, Atmos. Chem. Phys., 4, 1461–1738, doi:10.5194/acp-4-1461-2004, 2004.

Atkinson, R., Baulch, D. L., Cox, R. A., Crowley, J. N., Hampson, R. F., Hynes, R. G., Jenkin, M. E., Rossi, M. J., and Troe, J.: Evaluated kinetic and photochemical data for atmospheric chemistry: Volume II – gas phase reactions of organic species, Atmos. Chem. Phys., 6, 3625–4055, doi:10.5194/acp-6-3625-2006, 2006.

Atwater, M. A.: Planetary Albedo Changes Due to Aerosols, Science, 170, 64–66, doi:10.1126/science.170.3953.64, 1970.

Baker, A. K., Beyersdorf, A. J., Doezema, L. A., Katzenstein, A., Meinardi, S., Simpson, I. J., Blake, D. R., and Sherwood Rowland, F.: Measurements of non-methane hydrocarbons in 28 United States cities, Atmos. Environ., 42, 170–182, doi:10.1016/j.atmosenv.2007.09.007, 2008.

Baker, A. K., Slemr, F., and Brenninkmeijer, C. A. M.: Analysis of non-methane hydrocarbons in air samples collected aboard the CARIBIC passenger aircraft, Atmos. Meas. Tech., 3, 311–321, doi:10.5194/amt-3-311-2010, 2010.

Baker, A. K., Traud, S., Brenninkmeijer, C. A., Hoor, P., Neumaier, M., Oram, D. E., Rauthe-Schöch, A., Sprung, D., Schloegl, S., Slemr, F., van Velthoven, P. F., Wernli, H., Zahn, A., and Ziereis, H.: Pollution patterns in the upper troposphere over Europe and Asia observed by CARIBIC, Atmos. Environ., 96, 245–256, doi:10.1016/j.atmosenv.2014.06.010, 2014.

Bange, H. W. and Williams, J.: New Directions: Acetonitrile in atmospheric and biogeochemical cycles, Atmos. Environ, 34, 4959–4960, 84, 5387–5391, doi:10.1016/S1352-2310(00)00364-2, 2000.

Barber, S., Blake, R. S., White, I. R., Monks, P. S., Reich, F., Mullock, S., and Ellis, A. M.: Increased Sensitivity in Proton Transfer Reaction Mass Spectrometry by Incorporation of a Radio Frequency Ion Funnel, Anal. Chem., 84, 5387–5391, doi:10.1021/ac300894t, 2012.

Beauchamp, J., Herbig, J., Dunkl, J., Singer, W., and Hansel, A.: On the performance of proton-transfer-reaction mass spectrometry for breath-relevant gas matrices, Meas. Sci. Technol., 24, 125 003, doi:10.1088/0957-0233/24/12/125003, 2013.

Beauchamp, J. and Zardin, E.: Odorant Detection by On-line Chemical Ionization Mass Spectrometry, in: Springer Handbook of Odor, edited by Buettner, A., pp. 49–50; Springer Handbooks, Springer, Cham, doi:10.1007/978-3-319-26932-0_18, 2017.

Bernath, P. F.: The Atmospheric Chemistry Experiment (ACE), J. Quant. Spectrosc. Radiat. Transf., 186, 3–16, doi:10.1016/j.jqsrt.2016.04.006, 2017.

Bernath, P. F., McElroy, C. T., Abrams, M. C., Boone, C. D., Butler, M., Camy-Peyret, C., Carleer, M., Clerbaux, C., Coheur, P.-F., Colin, R., DeCola, P., DeMazière, M., Drummond, J. R., Dufour, D., Evans, W. F. J., Fast, H., Fussen, D., Gilbert, K., Jennings, D. E., Llewellyn, E. J., Lowe, R. P., Mahieu, E., McConnell, J. C., McHugh, M., McLeod, S. D., Michaud, R., Midwinter, C., Nassar, R., Nichitiu, F., Nowlan, C., Rinsland, C. P., Rochon, Y. J., Rowlands, N., Semeniuk, K., Simon, P., Skelton, R., Sloan, J. J., Soucy, M.-A., Strong, K., Tremblay, P., Turnbull, D., Walker, K. A., Walkty, I., Wardle, D. A., Wehrle, V., Zander, R., and Zou, J.: Atmospheric Chemistry Experiment (ACE): Mission overview, Geophys. Res. Lett., 32, L15S01, doi:10.1029/2005GL022386, 2005.

Blake, R. S., Monks, P. S., and Ellis, A. M.: Proton-transfer reaction mass spectrometry, Chem. Rev., 109, 861–896, doi:10.1021/cr800364q, 2009.

Blitz, M. A., Heard, D. E., Pilling, M. J., Arnold, S. R., and Chipperfield, M. P.: Pressure and temperature-dependent quantum yields for the photodissociation of acetone between 279 and 327.5 nm, Geophys. Res. Lett., 31, L06 111, doi:10.1029/2003GL018793, 2004.

Bonaventura, L.: The ICON project: Development of a unified model using triangular geodesic grids, in: Seminar on Recent developments in numerical methods for atmospheric and ocean modelling, 6-10 September 2004, pp. 75–86, ECMWF, Shinfield Park, Reading, 2004.

Borbon, A., Gilman, J. B., Kuster, W. C., Grand, N., Chevaillier, S., Colomb, A., Dolgorouky, C., Gros, V., Lopez, M., Sarda-Esteve, R., Holloway, J., Stutz, J., Petetin, H., McKeen, S., Beekmann, M., Warneke, C., Parrish, D. D., and de Gouw, J. A.: Emission ratios of anthropogenic volatile organic compounds in northern mid-latitude megacities: Observations versus emission inventories in Los Angeles and Paris, J. Geophys. Res. Atmos., 118, 2041–2057, doi:10.1002/jgrd.50059, 2013.

Bourtsoukidis, E., Helleis, F., Tomsche, L., Fischer, H., Hofmann, R., Lelieveld, J., and Williams, J.: An aircraft gas chromatograph-mass spectrometer System for Organic Fast Identification Analysis (SOFIA): design, performance and a case study of Asian monsoon pollution outflow, Atmos. Meas. Tech. Discuss., 2017, 1–30, doi:10.5194/amt-2017-201, 2017.

Bowman, K. P.: Transport of carbon monoxide from the tropics to the extratropics, J. Geophys. Res. Atmos., 111, 1–12, doi:10.1029/2005JD006137, 2006.

Bravo, H., Sosa, R., Sánchez, P., Bueno, E., and González, L.: Concentrations of benzene and toluene in the atmosphere of the southwestern area at the Mexico City Metropolitan Zone, Atmos. Environ., 36, 3843–3849, doi:10.1016/S1352-2310(02)00292-3, 2002.

Breitenlechner, M., Fischer, L., Hainer, M., Heinritzi, M., Curtius, J., and Hansel, A.: PTR3: An Instrument for Studying the Lifecycle of Reactive Organic Carbon in the Atmosphere, Anal. Chem., 89, 5824–5831, doi:10.1021/acs.analchem.6b05110, 2017.

Brenninkmeijer, C. A. M., Crutzen, P. J., Fischer, H., Guesten, H., Hans, W., Heinrich, G., Heintzenberg, J., Hermann, M., Immelmann, T., Kersting, D., Maiss, M., Nolle, M., Pitscheider, A., Pohlkamp, H., Scharffe, D., Specht, K., and Wiedensohler, A.: CARIBIC – Civil Aircraft for Global Measurement of Trace Gases and Aerosols in the Tropopause Region, J. Atmos. Ocean. Technol., 16, 1373–1383, doi:10.1175/1520-0426(1999)016⟨1373:Ccafgm⟩2.0.Co;2, 1999.

Brenninkmeijer C. A. M., Slemr, F., Koeppel, C., Scharffe, D. S., Pupek, M., Lelieveld, J., Crutzen, P., Zahn, A., Sprung, D., Fischer, H., Hermann, M., Reichelt, M., Heintzenberg, J., Schlager, H., Ziereis, H., Schumann, U., Dix, B., Platt, U., Ebinghaus, R., Martinsson, B., Ciais, P., Filippi, D., Leuenberger, M., Oram, D., Penkett, S., van Velthoven, P., and Waibel, A.: Analyzing atmospheric trace gases and aerosols using passenger aircraft, Eos, Trans. Am. Geophys. Union, 86, 77–83, doi:10.1029/2005EO080001, 2005.

Brenninkmeijer, C. A. M., Crutzen, P., Boumard, F., Dauer, T., Dix, B., Ebinghaus, R., Filippi, D., Fischer, H., Franke, H., Frieβ, U., Heintzenberg, J., Helleis, F., Hermann, M., Kock, H. H., Koeppel, C., Lelieveld, J., Leuenberger, M., Martinsson, B. G., Miemczyk, S., Moret, H. P., Nguyen, H. N., Nyfeler, P., Oram, D., O'Sullivan, D., Penkett, S., Platt, U., Pupek, M., Ramonet, M., Randa, B., Reichelt, M., Rhee, T. S., Rohwer, J., Rosenfeld, K., Scharffe, D., Schlager, H., Schumann, U., Slemr, F., Sprung, D., Stock, P., Thaler, R., Valentino, F., van Velthoven, P., Waibel, A., Wandel, A., Waschitschek, K., Wiedensohler, A., Xueref-Remy, I., Zahn, A., Zech, U., and Ziereis, H.: Civil Aircraft for the regular investigation of the atmosphere based on an instrumented container: The new CARIBIC system, Atmos. Chem. Phys., 7, 4953–4976, doi:10.5194/acp-7-4953-2007, 2007.

Brilli, F., Gioli, B., Ciccioli, P., Zona, D., Loreto, F., Janssens, I. A., and Ceulemans, R.: Proton Transfer Reaction Time-of-Flight Mass Spectrometric (PTR-TOF-MS) determination of volatile organic compounds (VOCs) emitted from a biomass fire developed under stable nocturnal conditions, Atmos. Environ., 97, 54–67, doi:10.1016/j.atmosenv.2014.08.007, 2014.

Brioude, J., Kim, S.-W., Angevine, W. M., Frost, G. J., Lee, S.-H., McKeen, S. A., Trainer, M., Fehsenfeld, F. C., Holloway, J. S., Ryerson, T. B., Williams, E. J., Petron, G., and Fast, J. D.: Top-down estimate of anthropogenic emission inventories and their interannual variability in Houston using a mesoscale inverse modeling technique, J. Geophys. Res., 116, D20 305, doi:10.1029/2011JD016215, 2011.

Brioude, J., Angevine, W. M., Ahmadov, R., Kim, S.-W., Evan, S., McKeen, S. A., Hsie, E.-Y., Frost, G. J., Neuman, J. A., Pollack, I. B., Peischl, J., Ryerson, T. B., Holloway, J., Brown, S. S., Nowak, J. B., Roberts, J. M., Wofsy, S. C., Santoni, G. W., Oda, T., and Trainer, M.: Top-down estimate of surface flux in the Los Angeles Basin using a mesoscale inverse modeling technique: assessing anthropogenic emissions of CO, NO_x and CO_2 and their impacts, Atmos. Chem. Phys., 13, 3661–3677, doi:10.5194/acp-13-3661-2013, 2013.

Brito, J.: A Lightweight High-sensitivity Chemical Mass Spectrometer for Organic Compounds, Ph.D. thesis, Karlsruhe Institute of Technology (KIT), 2011.

Brito, J. and Zahn, A.: An unheated permeation device for calibrating atmospheric VOC measurements, Atmos. Meas. Tech., 4, 2143–2152, doi:10.5194/amt-4-2143-2011, 2011.

Brito, J., Sprung, D., and Zahn, A.: A lightweight, high-sensitivity PTR mass-spectrometer for measuring organic compounds on aircraft platforms, Verhandlungen der Deutschen Physikalischen Gesellschaft, 40, 2009.

Brito, J., Wurm, F., Yáñez-Serrano, A. M., de Assunção, J. V., Godoy, J. M., and Artaxo, P.: Vehicular Emission Ratios of VOCs in a Megacity Impacted by Extensive Ethanol Use: Results of Ambient Measurements in São Paulo, Brazil, Environ. Sci. Technol., 49, 11 381–11 387, doi:10.1021/acs.est.5b03281, 2015.

Brosseau, J. E. and Heitz, L. E.: Trace Gas Compound Emissions from Municipal Landfill Sanitary Sites, Atmos. Environ., 28, 285–293, 1994.

Brown, P. A.: Investigations of Proton Transfer Reaction Mass Spectrometry for applications in organophosphate detection and breath analysis, Ph.D. thesis, University of Birmingham, 2012.

Brunner, D., Staehelin, J., Jeker, D.: Large-Scale Nitrogen Oxide Plumes in the Tropopause Region and Implications for Ozone, Science, 282, 1305–1309, doi: 10.1126/science.282.5392.1305, 1998.

Brunner, D., Staehelin, J., Jeker, D., Wernli, H., and Schumann, U.: Nitrogen oxides and ozone in the tropopause region of the northern hemisphere: Measurements from commercial aircraft in 1995/1996 and 1997, J. Geophys. Res. Atmos., 106, 27 673–27 699, doi:10.1029/2001JD900239, 2001.

Budisulistiorini, S. H., Li, X., Bairai, S. T., Renfro, J., Liu, Y., Liu, Y. J., McKinney, K. A., Martin, S. T., McNeill, V. F., Pye, H. O. T., Nenes, A., Neff, M. E., Stone, E. A., Mueller, S., Knote, C., Shaw, S. L., Zhang, Z., Gold, A., and Surratt, J. D.: Examining the effects of anthropogenic emissions on isoprene-derived secondary organic aerosol formation during the 2013 Southern Oxidant and Aerosol Study (SOAS) at the Look Rock, Tennessee ground site, Atmos. Chem. Phys., 15, 8871–8888, doi:10.5194/acp-15-8871-2015, 2015.

Busch, K. L.: A Glossary for Mass Spectrometry, Mass Spectrom., 17, 26–34, 2002.

Cabada, J. C., Pandis, S. N., Subramanian, R., Robinson, A. L., Polidori, A., and Turpin, B.: Estimating the Secondary Organic Aerosol Contribution to $PM_{2.5}$ Using the EC Tracer Method Special Issue of Aerosol Science and Technology on Findings from the Fine Particulate Matter Supersites Program, Aerosol Sci. Technol., 38, 140–155, doi:10.1080/02786820390229084, 2004.

Cain, M., Methven, J., and Highwood, E. J.: Quantification of chemical and physical processes influencing ozone during long-range transport using a trajectory ensemble, Atmos. Chem. Phys., 12, 7015–7039, doi:10.5194/acp-12-7015-2012, 2012.

Calogirou, A., Larsen, B. R., and Kotzias, D.: Gas-phase terpene oxidation products: A review, Atmos. Environ., 33, 1423-1439, doi:10.1016/S1352-2310(98)00277-5, 1999.

Calvert, J., Derwent, R., Orlando, J., Tyndall, G., and Wallington, T.: Mechanisms of Atmospheric Oxidation of the Alkanes., Oxford University Press, Oxford, 1008 pp., 2008.

Campana, J. E.: Elementary theory of the quadrupole mass filter, Int. J. Mass Spectrom. Ion Phys., 33, 101–117, doi:10.1016/0020-7381(80)80042-8, 1980.

Cantrell, C. A.: Technical Note: Review of methods for linear least-squares fitting of data and application to atmospheric chemistry problems, Atmos. Chem. Phys., 8, 5477–5487, doi:10.5194/acp-8-5477-2008, 2008.

Cappellin, L., Loreto, F., Aprea, E., Romano, A., del Pulgar, J. S., Gasperi, F., and Biasioli, F.: PTR-MS in Italy: A Multipurpose Sensor with Applications in Environmental, Agri-Food and Health Science, Sensors, 13, 11 923–11 955, doi: 10.3390/s130911923, 2013.

Christner, E.: Messungen von Wasserisotopologen von der planetaren Grenzschicht bis zur oberen Troposphäre zur Untersuchung des hydrologischen Kreislaufs, Ph.D. thesis, Karlsruhe Institute of Technology (KIT), 2015.

Chýlek, P. and Coakley, J. A.: Aerosols and Climate, Science, 183, 75–77, doi: 10.1126/science.183.4120.75, 1974.

Clerbaux, C., Boynard, A., Clarisse, L., George, M., Hadji-Lazaro, J., Herbin, H., Hurtmans, D., Pommier, M., Razavi, A., Turquety, S., Wespes, C., and Coheur, P.-F.: Monitoring of atmospheric composition using the thermal infrared IASI/MetOp sounder, Atmos. Chem. Phys., 9, 6041–6054, doi:10.5194/acp-9-6041-2009, 2009.

Coheur, P.-F., Herbin, H., Clerbaux, C., Hurtmans, D., Wespes, C., Carleer, M., Turquety, S., Rinsland, C. P., Remedios, J., Hauglustaine, D., Boone, C. D., and Bernath, P. F.: ACE-FTS observation of a young biomass burning plume: first reported measurements of C_2H_4, C_3H_6O, H_2CO and PAN by infrared occultation from space, Atmos. Chem. Phys., 7, 5437–5446, doi:10.5194/acp-7-5437-2007, 2007.

Cooper, O., Stohl, A., Doherty, R., and Hess, P.: Conceptual Overview of Hemispheric or Intercontinental Transport Processes, in: Hemispheric Transport of Air Pollution 2007 – Air Pollution Studies No. 16, United Nations, New York and Geneva, 8–28, 2007.

Copeland, N., Cape, J. N., Nemitz, E., and Heal, M. R.: Volatile organic compound speciation above and within a Douglas fir forest, Atmos. Environ., 94, 86–95, doi:10.1016/j.atmosenv.2014.04.035, 2014.

Correa, S. M., Arbilla, G., Marques, M. R. C., and Oliveira, K. M. P. G.: The impact of BTEX emissions from gas stations into the atmosphere, Atmos. Pollut. Res., 3, 163–169, doi:10.5094/APR.2012.016, 2012.

Crippa, M., Janssens-Maenhout, G., Dentener, F., Guizzardi, D., Sindelarova, K., Muntean, M., Van Dingenen, R., and Granier, C.: Forty years of improvements in European air quality: Regional policy-industry interactions with global impacts, Atmos. Chem. Phys., 16, 3825–3841, doi:10.5194/acp-16-3825-2016, 2016.

Crutzen, P. J. and Andreae, M. O.: Biomass Burning in the Tropics: Impact on Atmospheric Chemistry and Biogeochemical Cycles, Science, 250, 1669–1678, 1990.

Crutzen, P. J., Williams, J., Pöschl, U., Hoor, P., Fischer, H., Warneke, C., Holzinger, R., Hansel, A., Lindinger, W., Scheeren, B., and Lelieveld, J.: High Spatial and Temporal Resolution Measurements of Primary Organics and their Oxidation Products over the Tropical Forests of Suriname, Atmos. Environ., 34, 1161, doi: doi:DOI:10.1016/S1352-2310(99)00482-3, 2000.

Currie, L. A.: Detection: International update, and some emerging di-lemmas involving calibration, the blank, and multiple detection decisions, Chemom. Intell. Lab. Syst., 37, 1, 151–181, doi:10.1016/S0169-7439(97)00009-9, 1997.

Custer, T. and Schade, G.: Methanol and acetaldehyde fluxes over ryegrass, Tellus B, 59, 673–684, doi:10.1111/j.1600-0889.2007.00294.x, 2007.

Daley, R.: The normal modes of the spherical non?hydrostatic equations with applications to the filtering of acoustic modes, Tellus A, 40, 96–106, doi: 110.1111/j.1600-0870.1988.tb00409.x, 1988.

Dawson, P. H.: Principles of Operation, Analytical Theory, Numerical Calculations, Fringing Fields and other Imperfections, in: Quadrupole Mass Spectrometry and its Applications, pp. 1–119, Elsevier, doi:10.1016/B978-0-444-41345-1.50010-1, 1976.

de Foy, B., Lei, W., Zavala, M., Volkamer, R., Samuelsson, J., Mellqvist, J., Galle, B., Martínez, A.-P., Grutter, M., Retama, A., and Molina, L. T.: Modelling constraints on the emission inventory and on vertical dispersion for CO and SO_2 in the Mexico City Metropolitan Area using Solar FTIR and zenith sky UV spectroscopy, Atmos. Chem. Phys. Atmos. Chem. Phys., 7, 781–801, doi:10.5194/acpd-6-6125-2006, 2007.

de Gouw, J. A., Warneke, C., Scheeren, H. A., van der Veen, C., Bolder, M., Scheele, M. P., Williams, J., Wong, S., Lange, L., Fischer, H., and Lelieveld, J.: Overview of the trace gas measurements on board the Citation aircraft during the intensive field phase of INDOEX, J. Geophys. Res. Atmos., 106, 28 453–28 467, doi:10.1029/2000JD900810, 2001.

de Gouw, J. A., Warneke, C., Karl, T., Eerdekens, G., van der Veen, C., and Fall, R.: Sensitivity and specificity of atmospheric trace gas detection by proton-transfer-reaction mass spectrometry, Int. J. Mass Spectrom., 223-224, 365–382, doi:10.1016/S1387-3806(02)00926-0, 2003a.

de Gouw, J. A., Goldan, P. D., Warneke, C., Kuster, W. C., Roberts, J. M., Marchewka, M., Bertman, S. B., Pszenny, A. A. P., and Keene, W. C.: Validation of proton transfer reaction-mass spectrometry (PTR-MS) measurements of gas-phase organic compounds in the atmosphere during the New England Air Quality Study (NEAQS) in 2002, J. Geophys. Res. Atmos., 108, doi:10.1029/2003JD003863, 2003b.

de Gouw, J. A., Warneke, C., Parrish, D. D., Holloway, J. S., Trainer, M., and Fehsenfeld, F. C.: Emission sources and ocean uptake of acetonitrile (CH_3CN) in the atmosphere, J. Geophys. Res. Atmos., 108, doi:10.1029/2002JD002897, 2003c.

de Gouw, J. A., Middlebrook, A. M., Warneke, C., Goldan, P. D., Kuster, W. C., Roberts, J. M., Fehsenfeld, F. C., Worsnop, D. R., Canagaratna, M. R., Pszenny, A. A. P., Keene, W. C., Marchewka, M., Bertman, S. B., and Bates, T. S.: Budget of organic carbon in a polluted atmosphere: Results from the New England Air Quality Study in 2002, J. Geophys. Res. D Atmos., 110, 1–22, doi:10.1029/2004JD005623, 2005.

de Gouw, J. A. and Warneke, C.: Measurements of volatile organic compounds in the earth's atmosphere using proton-transfer-reaction mass spectrometry, Mass Spectrom. Rev., 26, 223–257, doi:10.1002/mas.20119, 2007.

de Hoffmann, E. and Stroobant, V.: Mass Spectrometry Principles and Applications, 3rd edition, Wiley, 2007.

de Laat, A. T. J., de Gouw, J. A., Lelieveld, J., and Hansel, A.: Model analysis of trace gas measurements and pollution impact during INDOEX, J. Geophys. Res. Atmos., 106, 28 469–28 480, doi:10.1029/2000JD900821, 2001.

de Reus, M., Fischer, H., Arnold, F., de Gouw, J. A., Holzinger, R., Warneke, C., and Williams, J.: On the relationship between acetone and carbon monoxide in different air masses, Atmos. Chem. Phys., 3, 1709–1723, doi:10.5194/acp-3-1709-2003, 2003.

Diehl, T., Heil, A., Chin, M., Pan, X., Streets, D., Schultz, M., and Kinne, S.: Anthropogenic, biomass burning, and volcanic emissions of black carbon, organic carbon, and SO_2 from 1980 to 2010 for hindcast model experiments, Atmos. Chem. Phys. Discuss., 12, 24 895–24 954, doi:10.5194/acpd-12-24895-2012, 2012.

Dillon, M. B., Lamanna, M. S., Schade, G. W., Goldstein, A. H., and Cohen, R. C.: Chemical evolution of the Sacramento urban plume: Transport and oxidation, J. Geophys. Res. Atmos., 107, ACH 3–1–ACH 3–15, doi:10.1029/2001JD000969, 2002.

Dix, B., Brenninkmeijer, C. A. M., Friess, U., Wagner, T., and Platt, U.: Airborne multi-axis DOAS measurements of atmospheric trace gases on CARIBIC long-distance flights, Atmos. Meas. Tech., 2, 639–652, doi:10.5194/amt-2-639-2009, 2009.

Dixon, J. L., Beale, R., and Nightingale, P. D.: Production of methanol, acetaldehyde, and acetone in the Atlantic Ocean, Geophys. Res. Lett., 40, 4700–4705, doi:10.1002/grl.50922, 2013.

Dong, X. and Fu, J. S.: Understanding interannual variations of biomass burning from Peninsular Southeast Asia, part II: Variability and different influencesin lower and higher atmosphere levels, Atmos. Environ., 115, 9–18, doi:10.1016/j.atmosenv.2015.05.052, 2015.

Douglas, D. J.: Linear quadrupoles in mass spectrometry, Mass Spectrom. Rev., 28, 937–960, doi:10.1002/mas.20249, 2009.

Draxler, R. R.: HYSPLIT 4 User's Guide. NOAA Technical Memorandum ERL ARL-230, Technical report, 1999.

Draxler, R. R. and Hess, G. D.: Description of the HYSPLIT 4 Modeling System, Technical report NOAA Technical Memorandum ERL ARL-224, 1997.

Draxler, R. R. and Hess, G. D.: An Overview of the HYSPLIT_4 Modelling System for Trajectories, Dispersion, and Deposition, Aust. Meteorol. Mag., 47, 295–308, 1998.

Dufour, G., Szopa, S., Harrison, J., Boone, C., and Bernath, P.: Seasonal variations of acetone in the upper troposphere–lower stratosphere of the northern midlatitudes as observed by ACE-FTS, J. Mol. Spectrosc., 323, 67–77, doi:10.1016/j.jms.2016.02.006, 2016.

Duncan, B. N., Martin, R. V., Staudt, A. C., Yevich, R., and Logan, J. A.: Interannual and seasonal variability of biomass burning emissions constrained by satellite observations, J. Geophys. Res. Atmos., 108, 4100, doi:10.1029/2002JD002378, 2003.

Duncan, B. N., Logan, J. A., Bey, I., Megretskaia, I. A., Yantosca, R. M., Novelli, P. C., Jones, N. B., and Rinsland, C. P.: Global budget of CO, 1988–1997: Source estimates and validation with a global model, J. Geophys. Res. Atmos., 112, D22 301, doi:10.1029/2007JD008459, 2007.

Dyroff, C.: Tunable Diode-Laser Absorption Spectroscopy for Trace-Gas Measurements with High Sensitivity and Low Drift, Ph.D. thesis, Karlsruhe Institute of Technology (KIT), 2008.

Dyroff, C., Fütterer, D., and Zahn, A.: Compact diode-laser spectrometer ISOWAT for highly sensitive airborne measurements of water-isotope ratios, Appl. Phys. B, 98, 537–548, doi:10.1007/s00340-009-3775-6, 2010.

Dyroff, C., Sanati, S., Christner, E., Zahn, A., Balzer, M., Bouquet, H., McManus, J. B., González-Ramos, Y., and Schneider, M.: Airborne in situ vertical profiling of HDO / H216O in the subtropical troposphere during the MUSICA remote sensing validation campaign, Atmos. Meas. Tech., 8, 2037–2049, doi:10.5194/amt-8-2037-2015, 2015.

Ebi, K. L. and McGregor, G.: Climate change, tropospheric ozone and particulate matter, and health impacts, Environ. Health Perspect., 116, 1449–1455, doi:10.1289/ehp.11463, 2008.

ECCAD: Emissions of atmospheric Compounds and Compilation of Ancillary Data, available at: `http://eccad.sedoo.fr/eccad_extract_interface/JSF/page_contact.jsf`, doi:10.17616/R35324, 2013.

ECLIPSE GAINS 4a: Global emission data set developed with the GAINS model for the period 2005 to 2050 - Data between year 2005 and 2050 from ECLIPSE_GAINS_4a - distributed by ECCAD. Authors: Zbigniew Klimont, Chris Heyes, Peter Rafaj, 2013.

EDGARv3.2FT2000: Emission Database for Global Atmospheric Research - Data for year 2000 from EDGARv3.2FT2000 - distributed by ECCAD. Authors: Jos Olivier, John Van Aardenne, Frank Dentener, Laurens Ganzeveld, Jeroen Peters, 2005.

EDGARv4.2: Emission Database for Global Atmospheric Research - Data between year 1970 and 2008 from EDGARv4.2 - distributed by ECCAD. Author: Greet Maenhout, 2011.

Edwards, P. M., Brown, S. S., Roberts, J. M., Ahmadov, R., Banta, R. M., DeGouw, J. A., Dube, W. P., Field, R. A., Flynn, J. H., Gilman, J. B., Graus, M., Helmig, D., Koss, A., Langford, A. O., Lefer, B. L., Lerner, B. M., Li, R., Li, S.-M., McKeen, S. A., Murphy, S. M., Parrish, D. D., Senff, C. J., Soltis, J., Stutz, J., Sweeney, C., Thompson, C. R., Trainer, M. K., Tsai, C., Veres, P. R., Washenfelder, R. A., Warneke, C., Wild, R. J., Young, C. J., Yuan, B., and Zamora, R.: High winter ozone pollution from carbonyl photolysis in an oil and gas basin, Nature, 514, 351–354, doi:10.1038/nature13767, 2014.

Eerdekens, G., Ganzeveld, L., Vilà-Guerau de Arellano, J., Klüpfel, T., Sinha, V., Yassaa, N., Williams, J., Harder, H., Kubistin, D., Martinez, M., and Lelieveld, J.: Flux estimates of isoprene, methanol and acetone from airborne PTR-MS measurements over the tropical rainforest during the GABRIEL 2005 campaign, Atmos. Chem. Phys., 9, 4207–4227, doi:10.5194/acp-9-4207-2009, 2009.

Elias, T., Szopa, S., Zahn, A., Schuck, T., Brenninkmeijer, C., Sprung, D., and Slemr, F.: Acetone variability in the upper troposphere: analysis of CARIBIC observations and LMDz-INCA chemistry-climate model simulations, Atmos. Chem. Phys., 11, 8053–8074, doi:10.5194/acp-11-8053-2011, 2011.

Ellis, A. M. and Mayhew, C. A.: Proton Transfer Reaction Mass Spectrometry, John Wiley & Sons, Ltd, doi:10.1002/9781118682883.ch2, 2014.

Esler, J. G.: An integrated approach to mixing sensitivities in tropospheric chemistry: A basis for the parameterization of subgrid-scale emissions for chemistry transport models, J. Geophys. Res. Atmos., 108, D20, 4632, doi:10.1029/2003JD003627, 2003.

Esler, J. G., Tan, D. G. H., Haynes, P. H., Evans, M. J., Law, K. S., Plantevin, P.-H., and Pyle, J. A.: Stratosphere-troposphere exchange: Chemical sensitivity to mixing, J. Geophys. Res. Atmos., 106, 4717–4731, doi:10.1029/2000JD900405, 2001.

Everitt, B. S. and Hand, D. J.: Mixtures of normal distributions, in: Finite Mixture Distributions, pp. 25–57, Springer Netherlands, Dordrecht, doi:10.1007/978-94-009-5897-5_2, 1981.

Fabian, P., and Pruchniewicz, P. G.: Meridional distribution of ozone in the troposphere and its seasonal variations, J. Geophys. Res., 82, 2063–2073, doi:10.1029/JC082i015p02063, 1977.

Fares, S., Park, J.-H., Gentner, D. R., Weber, R., Ormeño, E., Karlik, J., and Goldstein, A. H.: Seasonal cycles of biogenic volatile organic compound fluxes and concentrations in a California citrus orchard, Atmos. Chem. Phys., 12, 9865–9880, doi:10.5194/acp-12-9865-2012, 2012.

Fiore, A. M.: Atmospheric chemistry: No equatorial divide for a cleansing radical, Nature, 513, 176–178, doi:10.1038/513176a, 2014.

Fischbeck, G., Bönisch, H., Neumaier, M., Brenninkmeijer, C. A. M., Orphal, J., Brito, J., Becker, J., Sprung, D., van Velthoven, P. F. J., and Zahn, A.: Acetone–CO enhancement ratios in the upper troposphere based on 7 years of CARIBIC data: new insights and estimates of regional acetone fluxes, Atmos. Chem. Phys., 17, 1985–2008, doi:10.5194/acp-17-1985-2017, 2017.

Fischer, E. V., Jacob, D. J., Millet, D. B., Yantosca, R. M., and Mao, J.: The role of the ocean in the global atmospheric budget of acetone, Geophys. Res. Lett., 39, L01 807, doi:10.1029/2011GL050086, 2012.

Fischer, E. V., Jacob, D. J., Yantosca, R. M., Sulprizio, M. P., Millet, D. B., Mao, J., Paulot, F., Singh, H. B., Roiger, A., Ries, L., Talbot, R. W., Dzepina, K., and Pandey Deolal, S.: Atmospheric peroxyacetyl nitrate (PAN): a global budget and source attribution, Atmos. Chem. Phys., 14, 2679–2698, doi:10.5194/acp-14-2679-2014, 2014.

Fischer, H., Birk, M., Blom, C., Carli, B., Carlotti, M., von Clarmann, T., Delbouille, L., Dudhia, A., Ehhalt, D., Endemann, M., Flaud, J. M., Gessner, R., Kleinert, A., Koopman, R., Langen, J., López-Puertas, M., Mosner, P., Nett, H., Oelhaf, H., Perron, G., Remedios, J., Ridolfi, M., Stiller, G., and Zander, R.: MIPAS: an instrument for atmospheric and climate research, Atmos. Chem. Phys., 8, 2151–2188, doi:10.5194/acp-8-2151-2008, 2008.

Folkins, I. and Chatfield, R.: Impact of acetone on ozone production and OH in the upper troposphere at high NO x, J. Geophys. Res. Atmos., 105, 11 585–11 599, doi:10.1029/2000JD900067, 2000.

Fortner, E. C., Zheng, J., Zhang, R., Berk Knighton, W., Volkamer, R. M., Sheehy, P., Molina, L., and André, M.: Measurements of Volatile Organic Compounds Using Proton Transfer Reaction – Mass Spectrometry during the MILAGRO 2006 Campaign, Atmos. Chem. Phys., 9, 467–481, doi:10.5194/acp-9-467-2009, 2009.

Frey, H. C.: Quantification of Uncertainty in Emissions Factors and Inventories, 16th Annual International Emission Inventory Conference Emission Inventories: "Integration, Analysis, and Communications", Raleigh, 14–18 May 2007, pp. 1–16, 2007.

Friedl-Vallon, F., Maucher, G., Seefeldner, M., Trieschmann, O., Kleinert, A., Lengel, A., Keim, C., Oelhaf, H., Fischer, H.: Design and characterization of the balloon-borne Michelson Interferometer for Passive Atmospheric Sounding (MIPAS-B2), Appl. Opt., 43, 3335–3355, doi:10.1364/AO.43.003335, 2004.

Friedl-Vallon, F., Gulde, T., Hase, F., Kleinert, A., Kulessa, T., Maucher, G., Neubert, T., Olschewski, F., Piesch, C., Preusse, P., Rongen, H., Sartorius, C., Schneider, H., Schönfeld, A., Tan, V., Bayer, N., Blank, J., Dapp, R., Ebersoldt, A., Fischer, H., Graf, F., Guggenmoser, T., Höpfner, M., Kaufmann, M., Kretschmer, E., Latzko, T., Nordmeyer, H., Oelhaf, H., Orphal, J., Riese, M., Schardt, G., Schillings, J., Sha, M. K., Suminska-Ebersoldt, O., and Ungermann, J.: Instrument concept of the imaging Fourier transform spectrometer GLORIA, Atmos. Meas. Tech., 7, 3565–3577, doi:10.5194/amt-7-3565-2014, 2014.

Friedli, H. R., Atlas, E., Stroud, V. R., Giovanni, L., Campos, T., and Radke, L. F.: Volatile organic trace gases emitted from North American wildfires, Glob. Biogeochem. Cycles, 15, 435–452, doi:10.1029/2000GB001328, 2001.

Galbally, I. E. and Kirstine, W.: The production of methanol by flowering plants and the global cycle of methanol, J. Atmos. Chem., 43, 195–229, doi:10.1023/A:1020684815474, 2002.

Garg, A., Bhattacharya, S., Shukla, P. R., and Dadhwal, V. K.: Regional and sectoral assessment of greenhouse gas emissions in India, Atmos. Environ., 35, 2679–2695, doi:10.1016/S1352-2310(00)00414-3, 2001.

Geiger, F.: Fast-response measurements of organic trace species in the Earth's atmosphere, Ph.D. thesis, Karlsruhe Institute of Technology (KIT), doi:10.5445/KSP/1000046297, 2015.

Geno, P. W.: Ion Detection in Mass Spectrometry, in: Mass Spectrom. Biol. Sci. A Tutor., edited by Gross, M. L., pp. 133–142, Springer Netherlands, Dordrecht, doi:10.1007/978-94-011-2618-2_7, 1992.

GFAS 1.0: Daily biomass burning inventory - Data between year 2000 and 2013 from GFASv1.0 - distributed by ECCAD. Author: Johannes Kaiser, 2012.

GFED 3: Global Fire Emissions Database, version 3 (GFED3) - Data between year 1997 and 2010 from GFED3 - distributed by ECCAD. Authors: Guido R. van der Werf, James T. Randerson, Louis Giglio, 2010.

GFED2: Global Fire Emissions Database, version 2 (GFED2) - Data between year 1997 and 2005 from GFED2 - distributed by ECCAD. Authors: Guido R. van der Werf, James T. Randerson, Louis Giglio, Jim Georges Collatz, Prasad Kasibhatla, 2005.

Giglio, L., van der Werf, G. R., Randerson, J. T., Collatz, G. J., and Kasibhatla, P.: Global estimation of burned area using MODIS active fire observations, Atmos. Chem. Phys., 6, 957–974, doi:10.5194/acp-6-957-2006, 2006.

Giglio, L., Randerson, J. T., and van der Werf, G. R.: Analysis of daily, monthly, and annual burned area using the fourth-generation global fire emissions database (GFED4), J. Geophys. Res. Biogeosciences, 118, 317–328, doi:10.1002/jgrg.20042, 2013.

Goebbert, D. J. and Wentold, P. G.: Water dimer proton affinity from the kinetic method: dissociation energy of the water dimer, Eur J Mass Spectrom, 10, 837–846, doi:10.1255/ejms.684, 2004.

Goldan, P. D., Kuster, W. C., Fehsenfeld, F. C., and Montzka, S. A.: The observation of a C5 alcohol emission in a North American pine forest, Geophys. Res. Lett., 20, 1039–1042, doi:10.1029/93GL00247, 1993.

Goldstein, A. H. and Galbally, I. E.: Known and Unexplored Organic Constituents in the Earth's Atmosphere, Environ. Sci. Technol., 41, 1514–1521, doi:10.1021/es072476p, 2007.

Goldstein, B. D., Brooks, B. W., Cohen, S. D., Gates, A. E., Honeycutt, M. E., Morris, J. B., Orme-Zavaleta, J., Penning, T. M., and Snawder, J.: The Role of Toxicological Science in Meeting the Challenges and Opportunities of Hydraulic Fracturing, Toxicol. Sci., 139, 271–283, 2014.

González, Y., Schneider, M., Dyroff, C., Rodríguez, S., Christner, E., García, O. E., Cuevas, E., Bustos, J. J., Ramos, R., Guirado-Fuentes, C., Barthlott, S., Wiegele, A., and Sepúlveda, E.: Detecting moisture transport pathways to the subtropical North Atlantic free troposphere using paired H2O-δD in situ measurements, Atmos. Chem. Phys., 16, 4251–4269, doi:10.5194/acp-16-4251-2016, 2016.

González Abad, G., Bernath, P. F., Boone, C. D., McLeod, S. D., Manney, G. L., Toon, G. C., Gonz, G., Abad, G. G., Bernath, P. F., Boone, C. D., McLeod, S. D., Manney, G. L., and Toon, G. C.: Global distribution of upper tropospheric formic acid from the ACE-FTS, Atmos. Chem. Phys., 9, 8039–8047, doi:10.5194/acp-9-8039-2009, 2009.

Gottschaldt, K.-D., Schlager, H., Baumann, R., Bozem, H., Eyring, V., Hoor, P., Jöckel, P., Jurkat, T., Voigt, C., Zahn, A., and Ziereis, H.: Trace gas composition in the Asian summer monsoon anticyclone: a case study based on aircraft observations and model simulations, Atmos. Chem. Phys., 17, 6091–6111, doi: 10.5194/acp-17-6091-2017, 2017.

Granier, C., Bessagnet, B., Bond, T., D'Angiola, A., van der Gon, H., Frost, G. J., Heil, A., Kaiser, J. W., Kinne, S., Klimont, Z., Kloster, S., Lamarque, J.-F., Liousse, C., Masui, T., Meleux, F., Mieville, A., Ohara, T., Raut, J.-C., Riahi, K., Schultz, M. G., Smith, S. J., Thompson, A., Aardenne, J., Werf, G. R., and Vuuren, D. P.: Evolution of anthropogenic and biomass burning emissions of air pollutants at global and regional scales during the 1980–2010 period, Clim. Change, 109, 163–190, doi:10.1007/s10584-011-0154-1, 2011.

Granier, C., Boulanger, D., D'Angiola, A., Darras, S., Liousse, C., Marlière, J.-F., Miéville, A., Paulin, M., Pignot, V., and Zemankova, K.: Access to Emissions Distributions and Related Ancillary Data through the ECCAD database, in: EGU Gen. Assem. Conf. Abstr., vol. 15, p. 10593, 2013.

Graus, M., Müller, M., and Hansel, A.: High resolution PTR-TOF: Quantification and formula confirmation of VOC in real time, J. Am. Soc. Mass Spectrom., 21, 1037–1044, doi:10.1016/j.jasms.2010.02.006, 2010.

Greenberg, J. P., Friedli, H., Guenther, A. B., Hanson, D., Harley, P., and Karl, T.: Volatile organic emissions from the distillation and pyrolysis of vegetation, Atmos. Chem. Phys., 6, 81–91, doi:10.5194/acp-6-81-2006, 2006.

Gross, J.: Massenspektrometrie - Ein Lehrbuch, Springer Berlin Heidelberg, 2013.

Grubler, A., Bai, X., Buettner, S., Dhakal, S., Fisk, D., Ichinose, T., Keirstead, J., Sammer, G., Satterthwaite, D., Schulz, N., Shah, N., Steinberger, J., and Weisz, H.: Urban Energy Systems, in: Global Energy Assessment – Toward a Sustainable Future, pp. 1307–1400, Cambridge University Press, Cambridge, 2012.

Grutter, M., Glatthor, N., Stiller, G. P., Fischer, H., Grabowski, U., Höpfner, M., Kellmann, S., Linden, A., and Von Clarmann, T.: Global distribution and variability of formic acid as observed by MIPAS-ENVISAT, J. Geophys. Res. Atmos., 115, 1–8, doi:10.1029/2009JD012980, 2010.

Guenther, A.: The contribution of reactive carbon emissions from vegetation to the carbon balance of terrestrial ecosystems, Chemosphere, 49, 837–844, doi: 10.1016/S0045-6535(02)00384-3, 2002.

Guenther, A., Hewitt, C., Erickson, D., Fall, R., Geron, C., Graedel, T., Harley, P., Klinger, L., Lerdau, M., Mckay, W. A., Pierce, T., Scholes B., Steinbrecher, R., Tallamraju, R., Taylor, J., and Zimmermann, P.: A global model of natural volatile organic compound emissions, J. Geophys. Res., 100, 8873–8892, doi:10. 1029/94JD02950, 1995.

Guenther, A., Archer, S., Greenberg, J., Harley, P., Helmig, D., Klinger, L., Vierling, L., Wildermuth, M., Zimmerman, P., and Zitzer, S.: Biogenic hydrocarbon emissions and landcover/climate change in a subtropical savanna, Phys. Chem. Earth, Part B Hydrol. Ocean. Atmos., 24, 659–667, doi:10.1016/S1464-1909(99)00062-3, 1999.

Guenther, A., Karl, T., Harley, P., Wiedinmyer, C., Palmer, P. I., and Geron, C.: Estimates of global terrestrial isoprene emissions using MEGAN (Model of Emissions of Gases and Aerosols from Nature), Atmos. Chem. Phys., 6, 3181–3210, doi:10.5194/acp-6-3181-2006, 2006.

Guenther, A. B., Jiang, X., Heald, C. L., Sakulyanontvittaya, T., Duhl, T., Emmons, L. K., and Wang, X.: The model of emissions of gases and aerosols from nature version 2.1 (MEGAN2.1): An extended and updated framework for modeling biogenic emissions, Geosci. Model Dev., 5, 1471–1492, doi:10.5194/gmd-5-1471-2012, 2012.

Guo, T., Chen, D. Y., and Lee, F. C.: Separation of the common-mode- and differential-mode-conducted EMI noise, IEEE Trans. Power Electron., 11, 480–488, doi:10.1109/63.491642, 1996.

Haagen-Smit, A. J.: Chemistry and Physiology of Los Angeles Smog, Ind. Eng. Chem., 44, 1342–1346, doi:10.1021/ie50510a045, 1952.

Haase, K. B., Keene, W. C., Pszenny, A. A. P., Mayne, H. R., Talbot, R. W., and Sive, B. C.: Calibration and intercomparison of acetic acid measurements using proton-transfer-reaction mass spectrometry (PTR-MS), Atmos. Meas. Tech., 5, 2739–2750, doi:10.5194/amt-5-2739-2012, 2012.

Halbritter, S.: Investigations on the use of breath gas analysis using Proton Transfer Reaction Mass Spectrometry for a non-invasive method of early Gestational Diabetes Mellitus diagnosis, Diploma Thesis, Technical University of Munich, 2011.

Hamm, S. and Warneck, P.: The interhemispheric distribution and the budget of acetonitrile in the troposphere, J. Geophys. Res. Atmos., 95, 20 593–20 606, doi:10.1029/JD095iD12p20593, 1990.

Hamm, S., Hahn, J., Helas, G., and Warneck, P.: Acetonitrile in the Troposphere: Residence Time due to Rainout and Uptake by the Ocean, Geophys. Res. Lett., 11, 1207–1210, doi:10.1029/GL011i012p01207,1984.

Hamm, S., Helas, G., and Warneck, P.: Acetonitrile in the air over Europe, Geophys. Res. Lett., 16, 483–486, doi:10.1029/GL016i006p00483, 1989.

Hansel, A., Jordan, A., Holzinger, R., Prazeller, P., Vogel, W., and Lindinger, W.: Proton transfer reaction mass spectrometry: on-line trace gas analysis at the ppb level, Int. J. Mass Spectrom. Ion Process., 149, 609–619, doi:10.1016/0168-1176(95)04294-U, 1995.

Hansel, A., Singer, W., Wisthaler, A., Schwarzmann, M., and Lindinger, W.: Energy dependencies of the proton transfer reactions $H_3O^+ + CH_2O \longrightarrow CH_2OH^+ + H_2O$, Int. J. Mass Spectrom. Ion Process., 167, 697–703, doi:10.1016/S0168-1176(97)00128-6, 1997.

Hansel, A. and Wisthaler, A.: A Method fro Real-Time Detection of PAN, PPN and MPAN in Ambient Air, Geophys. Res. Lett., 27, 895–898, doi:10.1029/1999GL010989, 2000.

Hanson, D. R., Koppes, M., Stoffers, A., Harsdorf, R., and Edelen, K.: Proton transfer mass spectrometry at 11 hPa with a circular glow discharge: Sensitivities and applications, Int. J. Mass Spectrom., 282, 28–37, doi:10.1016/j.ijms.2009.01.021, 2009.

Hao, W. M. and Liu, M.-H.: Spatial and Temporal Distribution of Tropical Biomass Burning, Glob. Biogeochem. Cycles, 8, 495–503, doi:10.1029/94GB02086, 1994.

Harden, J. W., Trumbore, S. E., Stocks, B. J., Hirsch, A., Gower, S. T., O'neill, K. P., and Kasischke, E. S.: The role of fire in the boreal carbon budget, Glob. Change Biol., 6, 174–184, doi:10.1046/j.1365-2486.2000.06019.x, 2000.

Harley, R. A. and Kean, A. J.: Chemical Composition of Vehicle-Related Volatile Organic Compound Emissions in Central California, Final Report, Contract 00-14CCOS, prepared for San Joaquin Valleywide Air Pollution Study Agency and California Air Resources Board, 43 pp., 2004.

Harley, P., Fridd-Stroud, V., Greenberg, J., Guenther, A., and Vasconcellos, P.: Emission of 2-methyl-3-buten-2-ol by pines: A potentially large natural source of reactive carbon to the atmosphere, J. Geophys. Res. Atmos., 103, 25 479–25 486, doi:10.1029/98JD00820, 1998.

Harley, P., Greenberg, J., Niinemets, Ü., and Guenther, A.: Environmental controls over methanol emission from leaves, Biogeosciences, 4, ,1083–1099, doi:10.5194/bg-4-1083-2007, 2007.

Harrison, J. J. and Bernath, P. F.: ACE-FTS observations of acetonitrile in the lower stratosphere, Atmos. Chem. Phys., 13, 7405–7413, doi:10.5194/acp-13-7405-2013, 2013.

Harrison, J. J., Humpage, N., Allen, N. D., Waterfall, A. M., Bernath, P. F., and Remedios, J. J.: Mid-infrared absorption cross sections for acetone (propanone), J. Quant. Spectrosc. Radiat. Transf., 112, 457–464, doi:10.1016/j.jqsrt.2010.09.002, 2011.

Harrison, J. J., Boone, C. D., and Bernath, P. F.: New organic molecules from ace satellite observations, in: 2013 Eumetsat Meteorological Satellite Conference 19th American Meteorological Society (AMS) Satellite Meteorology, Oceanography, and Climatology Conference, vol. 2013, pp. 3–5, 2013.

Hastie, D. R., Gray, J., Langford, V. S., Maclagan, R. G. A. R., Milligan, D. B., and McEwan, M. J.: Real-time measurement of peroxyacetyl nitrate using selected ion flow tube mass spectrometry, Rapid Commun. Mass Spectrom., 24, 343–348, doi:10.1002/rcm.4400, 2010.

Hauck, G. and Arnold, F.: Improved positive-ion composition measurements in the upper troposphere and lower stratosphere and the detection of acetone, Nature, 311, 547–550, doi:10.1038/311547a0, 1984.

Haynes, P. and Shuckburgh, E.: Effective diffusivity as a diagnostic of atmospheric transport: 1. Stratosphere, J. Geophys. Res. Atmos., 105, 22 777–22 794, doi:10.1029/2000JD900093, 2000.

Hayward, S., Hewitt, C. N., Sartin, J. H., and Owen, S. M.: Performance Characteristics and Applications of a Proton Transfer Reaction-Mass Spectrometer for Measuring Volatile Organic Compounds in Ambient Air, Environ. Sci. Technol., 36, 1554–1560, doi:10.1021/es0102181, 2002.

Haywood, J. and Boucher, O.: Estimates of the direct and indirect radiative forcing due to tropospheric aerosols: A review, Rev. Geophys., 38, 513–543, doi:10.1029/1999RG000078, 2000.

The HDF Group: Hierarchical Data Format, version 5, 1997–2017, `http://www.hdfgroup.org/HDF5/`, last access: 1 August 2017.

Heald, C. L., Jacob, D. J., Palmer, P. I., Evans, M. J., Sachse, G. W., Singh, H. B., and Blake, D. R.: Biomass burning emission inventory with daily resolution: Application to aircraft observations of Asian outflow, J. Geophys. Res., 108, 8811, doi:10.1029/2002JD003082, 2003.

Heard, D. E.: Field Measurements of Atmospheric Composition. In: Analytical Techniques for Atmospheric Measurement, edited by Heard, D. E., pp. 1–70, Blackwell Publishing, Oxford, 2006.

Heil, A. and Schulz, M.: ACCMIP-MACCity biomass burning emission dataset, available at: `http://accmip-emis.iek.fz-juelich.de/data/accmip/gridded_netcdf/accmip_maccity_biomassburning/`, 2014.

Heil, A., Schultz, M. G., Angiola, A., Mieville, A., and Granier, C.: MACCity (MACC/CityZEN EU projects) emissions dataset - Data between year 1960 and 2020 from MACCity - distributed by ECCAD, 2012.

Hein, R., Crutzen, P. J., and Heimann, M.: An inverse modeling approach to investigate the global atmospheric methane cycle, Glob. Biogeochem. Cycles, 11, 43–76, doi:10.1029/96GB03043, 1997.

Heinze, R., Dipankar, A., Henken, C. C., Moseley, C., Sourdeval, O., Trömel, S., Xie, X., Adamidis, P., Ament, F., Baars, H., Barthlott, C., Behrendt, A., Blahak, U., Bley, S., Brdar, S., Brueck, M., Crewell, S., Deneke, H., Di Girolamo, P., Evaristo, R., Fischer, J., Frank, C., Friederichs, P., Göcke, T., Gorges, K., Hande, L., Hanke, M., Hansen, A., Hege, H. C., Hoose, C., Jahns, T., Kalthoff, N., Klocke, D., Kneifel, S., Knippertz, P., Kuhn, A., van Laar, T., Macke, A., Maurer, V., Mayer, B., Meyer, C. I., Muppa, S. K., Neggers, R. A., Orlandi, E., Pantillon, F., Pospichal, B., Röber, N., Scheck, L., Seifert, A., Seifert, P., Senf, F., Siligam, P., Simmer, C., Steinke, S., Stevens, B., Wapler, K., Weniger, M., Wulfmeyer, V., Zängl, G., Zhang, D., and Quaas, J.: Large-eddy simulations over Germany using ICON: a comprehensive evaluation, Q. J. R. Meteorol. Soc., 143, 69–100, doi:10.1002/qj.2947, 2017.

Hellén, H., Schallhart, S., Praplan, A. P., Petäjä, T., and Hakola, H.: Using in situ GC-MS for analysis of C2-C7 volatile organic acids in ambient air of a boreal forest site, Atmos. Meas. Tech., 10, 281–289, doi:10.5194/amt-10-281-2017, 2017.

Herbin, H., Hurtmans, D., Clerbaux, C., Clarisse, L., and Coheur, P.-F.: $H_2{}^{16}O$ and HDO measurements with IASI/MetOp, Atmos. Chem. Phys., 9, 9433–9447, doi:10.5194/acp-9-9433-2009, 2009.

Hewitt, C. N., Hayward, S., and Tani, A.: The application of proton transfer reaction-mass spectrometry (PTR-MS) to the monitoring and analysis of volatile organic compounds in the atmosphere, J. Environ. Monit., 5, 1–7, doi:10.1039/b204712h, 2003.

Höglund-Isaksson, L.: Global anthropogenic methane emissions 2005-2030: Technical mitigation potentials and costs, Atmos. Chem. Phys., 12, 9079–9096, doi:10.5194/acp-12-9079-2012, 2012.

Holdeman, J., Humenik, F., and Lezberg, E.: NASA Global Atmospheric Sampling Program (GASP) data report for tape VL0004, Technical report, 1977.

Holton, J. R., Haynes, P. H., McIntyre, M. E., Douglass, A. R., Rood, R. B., and Pfister, L.: Stratosphere-troposphere exchange, Rev. Geophys., 33, 403–439, doi:10.1029/95RG02097, 1995.

Holzinger, R., Warneke, C., Hansel, A., Jordan, A., Lindinger, W., Scharffe, D. H., Schade, G., and Crutzen, P. J.: Biomass burning as a source of formaldehyde, acetaldehyde, methanol, acetone, acetonitrile, and hydrogen cyanide, Geophys. Res. Lett., 26, 1161–1164, doi:10.1029/1999GL900156, 1999.

Holzinger, R., Jordan, A., Hansel, A., and Lindinger, W.: Automobile Emissions of Acetonitrile: Assessment of its Contribution to the Global Source, J. Atmos. Chem., 38, 187–193, doi:10.1023/A:1006435723375, 2001.

Holzinger, R., Williams, J., Salisbury, G., Klüpfel, T., de Reus, M., Traub, M., Crutzen, P. J., and Lelieveld, J.: Oxygenated compounds in aged biomass burning plumes over the Eastern Mediterranean: evidence for strong secondary production of methanol and acetone, Atmos. Chem. Phys., 5, 39–46, doi:10.5194/acp-5-39-2005, 2005.

Holzinger, R., Millet, D. B., Williams, B., Lee, A., Kreisberg, N., Hering, S. V., Jimenez, J., Allan, J. D., Worsnop, D. R., and Goldstein, A. H.: Emission, oxidation, and secondary organic aerosol formation of volatile organic compounds as observed at Chebogue Point, Nova Scotia, J. Geophys. Res. Atmos., 112, 1–12, doi:10.1029/2006JD007599, 2007.

Hornbrook, R. S., Blake, D. R., Diskin, G. S., Fried, A., Fuelberg, H. E., Meinardi, S., Mikoviny, T., Richter, D., Sachse, G. W., Vay, S. A., Walega, J., Weibring, P., Weinheimer, A. J., Wiedinmyer, C., Wisthaler, A., Hills, A., Riemer, D. D., and Apel, E. C.: Observations of nonmethane organic compounds during ARCTAS – Part 1: Biomass burning emissions and plume enhancements, Atmos. Chem. Phys., 11, 11 103–11 130, doi:10.5194/acp-11-11103-2011, 2011.

Hoskins, B. J., McIntyre, M. E., and Robertson, A. W.: On the use and significance of isentropic potential vorticity maps, Q. J. R. Meteorol. Soc., 111, 877–946, doi:10.1002/qj.49711147002, 1985.

House, E.: Refinement of PTR-MS Methodology and Application to the Measurement of (O)VOCs from Cattle Slurry, Ph.D. thesis, University of Edinburgh, 2008.

Howarth, R. W., Ingraffea, A., and Engelder, T.: Natural gas: Should fracking stop?, Nature, 477, 271–275, doi:10.1038/477271a, 2011.

Hu, L.: Constraints on the sources and impacts of volatile organic compounds (VOCs) over North America from tall tower measurements, Ph.D. thesis, University of Minnesota, 2014.

Hu, L., Millet D. B., Mohr, M. J., Wells, K. C., Griffis, T. J., and Helmig, D.: Sources and seasonality of atmospheric methanol based on tall tower measurements in the US Upper Midwest, Atmos. Chem. Phys., 11, 11145–11156, doi:10.5194/acp-11-11145-2011, 2011.

Hu, L., Millet, D. B., Kim, S. Y., Wells, K. C., Griffis, T. J., Fischer, E. V., Helmig, D., Hueber, J., and Curtis, A. J.: North American acetone sources determined from tall tower measurements and inverse modeling, Atmos. Chem. Phys., 13, 3379–3392, doi:10.5194/acp-13-3379-2013, 2013.

Huang, G., Brook, R., Crippa, M., Janssens-Maenhout, G., Schieberle, C., Dore, C., Guizzardi, D., Muntean, M., Schaaf, E., and Friedrich, R.: Speciation of anthropogenic emissions of non-methane volatile organic compounds: A global gridded data set for 1970-2012, Atmos. Chem. Phys., 17, 7683–7701, doi:10.5194/acp-17-7683-2017, 2017.

Hudman, R. C., Murray, L. T., Jacob, D. J., Millet, D. B., Turquety, S., Wu, S., Blake, D. R., Goldstein, A. H., Holloway, J., and Sachse, G. W.: Biogenic versus anthropogenic sources of CO in the United States, Geophys. Res. Lett., 35, L04 801, doi:10.1029/2007GL032393, 2008.

Hunter, E. P. L. and Lias, G. S.: Evaluated Gas Phase Basicities and Proton Affinities of Molecules: An Update, J. Phys. Chem. Ref. Data, 27, 413–656, doi:10.1063/1.556018, 1998.

Hurvich, C. M. and Tsai, C.-L.: Regression and time series model selection in small samples, Biometrika, 76, 297–307, doi:10.1093/biomet/76.2.297, 1989.

HYDE 1.3: EDGAR-HYDE 1.3 Historical Inventory - Data between year 1890 and 1990 from HYDE1.3 - distributed by ECCAD. Authors: John Van Aardenne, 2001.

Igbafe, A. I., Jewell, L. L., Piketh, S. J., and Dlamini, T. S.: A Wintertime Impact of Dilution on Transformation Rate in the Planetary Boundary Layer, J. Environ. Informatics, 8, 34–48, 2006.

Innes, J. L.: Biomass Burning and Climate: An Introduction, in: Advances in Global Change Research: Biomass Burning and Its Inter-Relationships with the Climate System, edited by Innes, J. L., Beniston, M., and Verstraete, M. M., pp. 1–13, Springer Berlin Heidelberg, 2000.

Inomata, S., Tanimoto, H., Aoki, N., Hirokawa, J., and Sadanaga, Y.: A novel discharge source of hydronium ions for proton transfer reaction ionization: design, characterization, and performance, Rapid Commun. Mass Spectrom., 20, 1025–1029, doi:10.1002/rcm.2405, 2006.

Inomata, S., Tanimoto, H., Kato, S., Suthawaree, J., Kanaya, Y., Pochanart, P., Liu, Y., and Wang, Z.: PTR-MS measurements of non-methane volatile organic compounds during an intensive field campaign at the summit of Mount Tai, China, in June 2006, Atmos. Chem. Phys., 10, 7085–7099, doi:10.5194/acp-10-7085-2010, 2010.

Ionicon: `http://www.ionicon.com/sites/default/files/uploads/doc/flyer_2017_IONICON_ptr-tof_6000-X2.pdf`, last access: 1 August 2017.

Isodorov, V., Zenkevich, I., and Ioffe, B.: Volatile atmospheric compounds in the atmosphere of forests, Atmos. Environ., 19, 1–8, doi:10.1016/0004-6981(85)90131-3, 1985.

IUPAC: Compendium of Chemical Terminology, 2nd ed. (the "Gold Book"). Compiled by A. D. McNaught and A. Wilkinson. Blackwell Scientific Publications, Oxford (1997). XML on-line corrected version: http://goldbook.iupac.org (2006-) created by M. Nic, J. Jirat, B. Kosata; updates compiled by A. Jenkins., version 2.3.3., doi:10.1351/goldbook.L03540, 2014.

Jackson, L. S., Carslaw, N., Carslaw, D. C., and Emmerson, K. M.: Modelling trends in OH radical concentrations using generalized additive models, Atmos. Chem. Phys., 9, 2021–2033, doi:10.5194/acp-9-2021-2009, 2009.

Jackson, P. and Attalla, M. I.: N-Nitrosopiperazines form at high pH in post-combustion capture solutions containing piperazine: a low-energy collisional behaviour study., Rapid Commun. Mass Spectrom., 24, 3567–3577, doi:10.1002/rcm.4815, 2010.

Jackson, R. B., Vengosh, A., Carey, J. W., Davies, R. J., Darrah, T. H., O'Sullivan, F., and Petron, G.: The Environmental Costs and Benefits of Fracking, Annu. Rev. Environ. Resour., 39, 327–362, doi:10.1146/annurev-environ-031113-144051, 2014.

Jacob, D. J., Field, B. D., Jin, E. M., Bey, I., Li, Q., Logan, J. A., Yantosca, R. M., and Singh, H. B.: Atmospheric budget of acetone, J. Geophys. Res. Atmos., 107, 4100, doi:10.1029/2001JD000694, 2002.

Jacob, D. J., Field, B. D., Li, Q., Blake, D. R., de Gouw, J., Warneke, C., Hansel, A., Wisthaler, A., Singh, H. B., and Guenther, A.: Global budget of methanol: Constraints from atmospheric observations, J. Geophys. Res. D Atmos., 110, 1–17, doi:10.1029/2004JD005172, 2005.

Jaeglé, L., Jacob, D. J., Brune, W. H., Tan, D., Faloona, I. C., Weinheimer, A. J., Ridley, B. A., Campos, T. L., and Sachse, G. W.: Sources of HO_x and production of ozone in the upper troposphere over the United States, Geophys. Res. Lett., 25, 1709–1712, doi:10.1029/98GL00041, 1998.

Jaffe, D., Anderson, T., Covert, D., Kotchenruther, R., Trost, B., Danielson, J., Simpson, W., Berntsen, T., Karlsdottir, S., Blake, D., Harris, J., Carmichael, G., and Uno, I.: Transport of Asian air pollution to North America, Geophys. Res. Lett., 26, 711–714, doi:10.1029/1999GL900100, 1999.

Jäger, J. E.: Airborne VOC measurements on board the Zeppelin NT during the PEGASOS campaigns in 2012 deploying the improved Fast-GC-MSD System., Ph.D. thesis, University of Cologne, 2014.

Janssens-Maenhout, G., Petrescu, A. M. R., Muntean, M., and Blujdea, V.: Verifying Greenhouse Gas Emissions: Methods to Support International Climate Agreements, Greenh. Gas Meas. Manag., 1, 132–133, doi:10.1080/20430779.2011.579358, 2011.

Jardine, K., Yañez-Serrano, A. M., Williams, J., Kunert, N., Jardine, A., Taylor, T., Abrell, L., Artaxo, P., Guenther, A., Hewitt, C. N., House, E., Florentino, A. P., Manzi, A., Higuchi, N., Kesselmeier, J., Behrendt, T., Veres, P. R., Derstroff, B., Fuentes, J. D., Martin, S. T., and Andreae, M. O.: Dimethyl sulfide in the Amazon rain forest, Glob. Biogeochem. Cycles, 29, 19–32, doi:10.1002/2014GB004969, 2015.

Jenkin, M. E., Saunders, S. M., and Pilling, M. J.: The tropospheric degradation of volatile organic compounds: A protocol for mechanism development, Atmos. Environ., 31, 81–104, doi:10.1016/S1352-2310(96)00105-7, 1997.

Jobson, B. T., McKeen, S. A., Parrish, D. D., Fehsenfeld, F. C., Blake, D. R., Goldstein, A. H., Schauffler, S. M. and Elkins, J. W.: Trace gas mixing ratio variability versus lifetime in the troposphere and stratosphere: Observations, J. Geophys. Res., 104, 16091–16113, doi:10.1029/1999JD900126, 1999.

Jobson, B. T. and McCoskey, J. K.: Sample drying to improve HCHO measurements by PTR-MS instruments: laboratory and field measurements, Atmos. Chem. Phys., 10, 1821–1835, doi:10.5194/acp-10-1821-2010, 2010.

Johnson, K. A. and Johnson, D. E.: Methane emissions from cattle., J. Anim. Sci., 73, 2483–2492, doi:10.2527/1995.7382483x, 1995.

Jordan, A., Haidacher, S., Hanel, G., Hartungen, E., Märk, L., Seehauser, H., Schottkowsky, R., Sulzer, P., and Märk, T. D.: A high resolution and high sensitivity proton-transfer-reaction time-of-flight mass spectrometer (PTR-TOF-MS), Int. J. Mass Spectrom., 286, 122–128, doi:10.1016/j.ijms.2009.07.005, 2009a.

Jordan, A., Winkler, K., Lindinger, C., Feil, S., Mutschlechner, P., Hanel, G., Hartungen, E., Herbig, J., Märk, L., Sulzer, P., and Juerschik, S.: A Modular Ion Funnel For Improved Sensitivity in Proton-Transfer-Reaction-Time-Of-Flight Mass Spectrometry (PTR-TOFMS) Instruments, in: Contributions to AMSM 2017, 2nd International Conference on Applied Mathematics, Simulation and Modelling, 2017.

Jordan, C., Fitz, E., Hagan, T., Sive, B., Frinak, E., Haase, K., Cottrell, L., Buckley, S., and Talbot, R.: Long-term study of VOCs measured with PTR-MS at a rural site in New Hampshire with urban influences, Atmos. Chem. Phys., 9, 4677–4697, doi:10.5194/acp-9-4677-2009, 2009b.

Jost, C., Trentmann, J., Sprung, D., Andreae, M. O., and Dewey, K.: Deposition of acetonitrile to the Atlantic Ocean off Namibia and Angola and its implications for the atmospheric budget of acetonitrile, Geophys. Res. Lett., 30(60), 1837, doi:10.1029/2003GL017347, 2003a.

Jost, C., Trentmann, J., Sprung, D., Andreae, M. O., McQuaid, J. B., and Barjat, H.: Trace gas chemistry in a young biomass burning plume over Namibia: Observations and model simulations, J. Geophys. Res. Atmos., 108(D13), 8482, doi:10.1029/2002JD002431, 2003b.

Junhua, Y.: Isotope Pattern Calculator v4.0, available at: `http://yanjunhua.tripod.com/pattern.htm`, 2001.

Kaiser, J. W., Heil, A., Andreae, M. O., Benedetti, A., Chubarova, N., Jones, L., Morcrette, J.-J., Razinger, M., Schultz, M. G., Suttie, M., and van der Werf, G. R.: Biomass burning emissions estimated with a global fire assimilation system based on observed fire radiative power, Biogeosciences, 9, 527–554, doi:10.5194/bg-9-527-2012, 2012.

Kajos, M. K., Rantala, P., Hill, M., Hellen, H., Aalto, J., Patokoski, J., Taipale, R., Hoerger, C. C., Reimann, S., Ruuskanen, T. M., Rinne, J., and Petäjä, T.: Ambient measurements of aromatic and oxidized VOCs by PTR-MS and GC-MS: Intercomparison between four instruments in a boreal forest in Finland, Atmos. Meas. Tech., 8, 4453–4473, doi:10.5194/amt-8-4453-2015, 2015.

Kalogridis, C., Gros, V., Sarda-Esteve, R., Langford, B., Loubet, B., Bonsang, B., Bonnaire, N., Nemitz, E., Genard, A.-C., Boissard, C., Fernandez, C., Ormeño, E., Baisnée, D., Reiter, I., and Lathière, J.: Concentrations and fluxes of isoprene and oxygenated VOCs at a French Mediterranean oak forest, Atmos. Chem. Phys., 14, 10 085–10 102, doi:10.5194/acp-14-10085-2014, 2014.

Kaltsonoudis, C., Kostenidou, E., Florou, K., Psichoudaki, M., and Pandis, S. N.: Temporal variability and sources of VOCs in urban areas of the eastern Mediterranean, Atmos. Chem. Phys., 16, 14 825–14 842, doi:10.5194/acp-16-14825-2016, 2016.

Karl, T., Jobson, T., Kuster, W. C., Williams, E., Stutz, J., Shetter, R., Hall, S. R., Goldan, P., Fehsenfeld, F., and Lindinger, W.: Use of proton-transfer-reaction mass spectrometry to characterize volatile organic compound sources at the La Porte super site during the Texas Air Quality Study 2000, J. Geophys. Res., 108, 4508, doi:10.1029/2002JD003333, 2003.

Karl, T., Potosnak, M., Guenther, A., Clark, D., Walker, J., Herrick, J. D., and Geron, C.: Exchange processes of volatile organic compounds above a tropical rain forest: Implications for modeling tropospheric chemistry above dense vegetation, J. Geophys. Res., 109, D18 306, doi:10.1029/2004JD004738, 2004.

Karl, T., Apel, E., Hodzic, A., Riemer, D. D., Blake, D. R., and Wiedinmyer, C.: Emissions of volatile organic compounds inferred from airborne flux measurements over a megacity, Atmos. Chem. Phys., 9, 271–285, doi:10.5194/acp-9-271-2009, 2009.

Karl, T., Misztal, P. K., Jonsson, H. H., Shertz, S., Goldstein, A. H., and Guenther, A. B.: Airborne flux measurements of BVOCs above Californian oak forests: experimental investigation of surface and entrainment fluxes, OH densities, and Damköhler numbers, J. Atmos. Sci., 70, 3277–3287, doi:10.1175/jas-d-13-054.1, 2013.

Kaser, L., Karl, T., Schnitzhofer, R., Graus, M., Herdlinger-Blatt, I. S., DiGangi, J. P., Sive, B., Turnipseed, A., Hornbrook, R. S., Zheng, W., Flocke, F. M., Guenther, A., Keutsch, F. N., Apel, E., and Hansel, A.: Comparison of different real time VOC measurement techniques in a ponderosa pine forest, Atmos. Chem. Phys., 13, 2893–2906, doi:10.5194/acp-13-2893-2013, 2013.

Kegge, W. and Pierik, R.: Biogenic volatile organic compounds and plant competition, Trends Plant Sci., 15, 126–132, doi:10.1016/j.tplants.2009.11.007, 2010.

Kelly, R. T., Tolmachev, A. V., Page, J. S., Tang, K., and Smith, R. D.: The ion funnel: Theory, implementations, and applications, Mass Spectrom. Rev., 29, 294–312, doi:10.1002/mas.20232, 2010.

Kesselmeier, J. and Staudt, M.: Biogenic Volatile Organic Compounds (VOC): An Overview on Emission, Physiology and Ecology, J. Atmos. Chem., 33, 23–88, doi:10.1023/A:1006127516791, 1999.

Keywood, M., Kanakidou, M., Stohl, A., Dentener, F., Grassi, G., Meyer, C. P., Torseth, K., Edwards, D., Thompson, A. M., Lohmann, U., and Burrows, J.: Fire in the Air: Biomass Burning Impacts in a Changing Climate, Crit. Rev. Environ. Sci. Technol., 43, 40–83, doi:10.1080/10643389.2011.604248, 2013.

Khan, M., Cooke, M., Utembe, S., Archibald, A., Maxwell, P., Morris, W., Xiao, P., Derwent, R., Jenkin, M., Percival, C., Walsh, R., Young, T., Simmonds, P., Nickless, G., O'Doherty, S., and Shallcross, D.: A study of global atmospheric budget and distribution of acetone using global atmospheric model STOCHEM-CRI, Atmos. Environ., 112, 269–277, doi:10.1016/j.atmosenv.2015.04.056, 2015.

Kieber, R. J., Zhou, X., and Mopper, K.: Formation of carbonyl compounds from UV-induced photodegradation of humic substances in natural waters: Fate of riverine carbon in the sea, Limnol. Oceanogr., 35, 1503–1515, doi:10.4319/lo.1990.35.7.1503, 1990.

Kim, S., Karl, T., Helmig, D., Daly, R., Rasmussen, R., and Guenther, A.: Measurement of atmospheric sesquiterpenes by proton transfer reaction-mass spectrometry (PTR-MS), Atmos. Meas. Tech., 2, 99–112, doi:10.5194/amt-2-99-2009, 2009.

Kim, S., Karl, T., Guenther, A., Tyndall, G., Orlando, J., Harley, P., Rasmussen, R., and Apel, E.: Emissions and ambient distributions of Biogenic Volatile Organic Compounds (BVOC) in a ponderosa pine ecosystem: interpretation of PTR-MS mass spectra, Atmos. Chem. Phys., 10, 1759–1771, doi:10.5194/acp-10-1759-2010, 2010.

Kim, S. Y., Millet, D. B., Hu, L., Mohr, M. J., Griffis, T. J., Wen, D., Lin, J. C., Miller, S. M., and Longo, M.: Constraints on carbon monoxide emissions based on tall tower measurements in the US Upper Midwest., Environ. Sci. Technol., 47, 8316–24, doi:10.1021/es4009486, 2013.

Kirstine, W., Galbally, I., Ye, Y., and Hooper, M.: Emissions of volatile organic compounds (primarily oxygenated species) from pasture, J. Geophys. Res. Atmos., 103, 10 605–10 619, doi:10.1029/97JD03753, 1998.

Kirstine, W. V. and Galbally, I. E.: The global atmospheric budget of ethanol revisited, Atmos. Chem. Phys., 12, 545–555, doi:10.5194/acp-12-545-2012, 2012.

Kleinböhl, A., Toon, G. C., Sen, B., Blavier, J.-F. L., Weisenstein, D. K., and Wennberg, P. O.: Infrared measurements of atmospheric CH_3CN, Geophys. Res. Lett., 32, doi:10.1029/2005GL024283, 2005.

Klimont, Z., Smith, S. J., and Cofala, J.: The last decade of global anthropogenic sulfur dioxide: 2000–2011 emissions, Environ. Res. Lett., 8, 014 003, doi:10.1088/1748-9326/8/1/014003, 2013.

Knighton, W. B., Fortner, E. C., Herndon, S. C., Wood, E. C., and Miake-Lye, R. C.: Adaptation of a proton transfer reaction mass spectrometer instrument to employ NO^+ as reagent ion for the detection of 1,3-butadiene in the ambient atmosphere, Rapid Commun. Mass Spectrom., 23, 3301–3308, doi:10.1002/rcm.4249, 2009.

Knop, G. and Arnold, F.: Atmospheric acetonitrile measurements in the tropopause region using aircraft-borne active chemical ionization mass spectrometry, Planet. Space Sci., 35, 259–266, doi:10.1016/0032-0633(87)90094-8, 1987.

Kontkanen, J., Paasonen, P., Aalto, J., Bäck, J., Rantala, P., Petäjä, T., and Kulmala, M.: Simple proxies for estimating the concentrations of monoterpenes and their oxidation products at a boreal forest site, Atmos. Chem. Phys., 16, 13 291–13 307, doi:10.5194/acp-16-13291-2016, 2016.

Koppmann, R.: Chemistry of Volatile Organic Compounds in the Atmosphere, in: Handbook of Hydrocarbon and Lipid Microbiology, edited by Timmis, K. N., pp. 270–277, Springer Berlin Heidelberg, doi:10.1007/978-3-540-77587-4_18, 2010.

Koppmann, R. and Wildt, J.: Oxygenated Volatile Organic Compounds, in: Volatile Organic Compounds in the Atmosphere, edited by Koppmann, R., pp. 129–172, Blackwell Publishing, Oxford, 2007.

Kramp, F. and Volz-Thomas, A.: On the budget of OH radicals and ozone in an urban plume from the decay of C_5-C_8 hydrocarbons and NO_x, J. Atmos. Chem., 28, 263–282, 1997.

Krautstrunk, M. and Giez, A.: The Transition From FALCON to HALO Era Airborne Atmospheric Research, in: Atmospheric Physics - Background - Methods - Trends, edited by Schumann, U., pp. 609–624, Springer Berlin Heidelberg, 2012.

Kwasnik, M., Fuhrer, K., Gonin, M., Barbeau, K., and Fernández, F. M.: Performance, resolving power, and radial ion distributions of a prototype nanoelectrospray ionization resistive glass atmospheric pressure ion mobility spectrometer, Anal. Chem., 79, 7782–7791, doi:10.1021/ac071226o, 2007.

Lackner, B. C., Steiner, A. K., Ladstädter, F., and Kirchengast, G.: Trend Indicators of Atmospheric Climate Change Based on Global Climate Model Scenarios, in: New Horizons in Occultation Research: Studies in Atmosphere and Climate, p. 247ff., Springer Berlin Heidelberg, doi:10.1007/978-3-642-00321-9_20, 2009.

Lai, S. C., Baker, A. K., Schuck, T. J., Slemr, F., Brenninkmeijer, C. A. M., van Velthoven, P., Oram, D. E., Zahn, A., and Ziereis, H.: Characterization and source regions of 51 high-CO events observed during Civil Aircraft for the Regular Investigation of the Atmosphere Based on an Instrument Container (CARIBIC) flights between south China and the Philippines, 2005-2008, J. Geophys. Res., 116, D20 308, doi::10.1029/2011JD016375, 2011.

Lamarque, J.-F., Bond, T. C., Eyring, V., Granier, C., Heil, A., Klimont, Z., Lee, D., Liousse, C., Mieville, A., Owen, B., Schultz, M. G., Shindell, D., Smith, S. J., Stehfest, E., Van Aardenne, J., Cooper, O. R., Kainuma, M., Mahowald, N., McConnell, J. R., Naik, V., Riahi, K., and van Vuuren, D. P.: Historical (1850–2000) gridded anthropogenic and biomass burning emissions of reactive gases and aerosols: methodology and application, Atmos. Chem. Phys., 10, 7017–7039, doi:10.5194/acp-10-7017-2010, 2010.

Lamarque, J. F., Shindell, D. T., Josse, B., Young, P. J., Cionni, I., Eyring, V., Bergmann, D., Cameron-Smith, P., Collins, W. J., Doherty, R., Dalsoren, S., Faluvegi, G., Folberth, G., Ghan, S. J., Horowitz, L. W., Lee, Y. H., MacKenzie, I. A., Nagashima, T., Naik, V., Plummer, D., Righi, M., Rumbold, S. T., Schulz, M., Skeie, R. B., Stevenson, D. S., Strode, S., Sudo, K., Szopa, S., Voulgarakis, A., and Zeng, G.: The atmospheric chemistry and climate model intercomparison Project (ACCMIP): Overview and description of models, simulations and climate diagnostics, Geosci. Model Dev., 6, 179–206, doi:10.5194/gmd-6-179-2013, 2013.

Lamb, B., Guenther, A., Gay, D., and Westberg, H.: A national inventory of biogenic hydrocarbon emissions, Atmos. Environ., 21, 1695–1705, doi:10.1016/0004-6981(87)90108-9, 1987.

Langford, B., Davison, B., Nemitz, E., and Hewitt, C. N..: Mixing ratios and eddy covariance flux measurements of volatile organic compounds from an urban canopy (Manchester, UK), Atmos. Chem. Phys., 9, 1971–1987, doi:10.5194/acp-9-1971-2009, 2009.

Langford, B., Misztal, P. K., Nemitz, E., Davison, B., Helfter, C., Pugh, T. A. M., MacKenzie, A. R., Lim, S. F., and Hewitt, C. N.: Fluxes and concentrations of volatile organic compounds from a South-East Asian tropical rainforest, Atmos. Chem. Phys., 10, 8391–8412, doi:10.5194/acp-10-8391-2010, 2010.

Laothawornkitkul, J., Taylor, J. E., Paul, N. D., and Hewitt, C. N.: Biogenic volatile organic compounds in the Earth system: Tansley review, New Phytol., 183, 27–51, doi:10.1111/j.1469-8137.2009.02859.x, 2009.

Lathière, J., Hauglustaine, D. A., De Noblet-Ducoudré, N., Krinner, G., and Folberth, G. A.: Past and future changes in biogenic volatile organic compound emissions simulated with a global dynamic vegetation model, Geophys. Res. Lett., 32, L20 818, doi:10.1029/2005GL024164, 2005.

Lawrence, M. G., Jöckel, P., and von Kuhlmann, R.: What does the global mean OH concentration tell us?, Atmos. Chem. Phys., 1, 37–49, doi:10.5194/acp-1-37-2001, 2001.

Lee, M., Heikes, B. G., Jacob, D. J., Sachse, G., and Anderson, B.: Hydrogen peroxide, organic hydroperoxide, and formaldehyde as primary pollutants from biomass burning, J. Geophys. Res. Atmos., 102, 1301–1309, doi:10.1029/96JD01709, 1997.

Lee, A., Goldstein, A. H., Kroll, J. H., Ng, N. L., Varutbangkul, V., Flagan, R. C., and Seinfeld, J. H.: Gas-phase products and secondary aerosol yields from the photooxidation of 16 different terpenes, J. Geophys. Res. Atmos., 111, D17 305, doi:10.1029/2006JD007050, 2006.

Lefer, B. L., Talbot, R. W., Harriss, R. H., Bradshaw, J. D., Sandholm, S. T., Olson, J. O., Sachse, G. W., Collins, J., Shipham, M. A., Blake, D. R., Klemm, K. I., Klemm, O., Gorzelska, K., and Barrick, J.: Enhancement of acidic gases in biomass burning impacted air masses over Canada, J. Geophys. Res., 99, 1721–1737, doi:10.1029/93JD02091, 1994.

Lelieveld, J., Crutzen, P. J., Ramanathan, V., Andreae, M. O., Brenninkmeijer, C. A. M., Campos, T., Cass, G. R., Dickerson, R. R., Fischer, H., de Gouw, J. A., Hansel, A., Jefferson, A., Kley, D., de Laat, A. T. J., Lal, S., Lawrence, M. G., Lobert, J. M., Mayol-Bracero, O. L., Mitra, A. P., Novakov, T., Oltmans, S. J., Prather, K. A., Reiner, T., Rodhe, H., Scheeren, H. A., Sikka, D., and Williams, J.: The Indian Ocean Experiment: Widespread Air Pollution from South and Southeast Asia, Science, 291, 1031–1036, doi:10.1126/science.1057103, 2001.

Lelieveld, J., Butler, T. M., Crowley, J. N., Dillon, T. J., Fischer, H., Ganzeveld, L., Harder, H., Lawrence, M. G., Martinez, M., Taraborrelli, D., and Williams, J.: Atmospheric oxidation capacity sustained by a tropical forest, Nature, 452, 737–740, doi:10.1038/nature06870, 2008.

Lelieveld, J., Evans, J. S., Fnais, M., Giannadaki, D., and Pozzer, A.: The contribution of outdoor air pollution sources to premature mortality on a global scale, Nature, 525, 367–371, doi:10.1038/nature15371, 2015.

Lelieveld, J., Gromov, S., Pozzer, A., and Taraborrelli, D.: Global tropospheric hydroxyl distribution, budget and reactivity, Atmos. Chem. Phys., 16, 12 477–12 493, doi:10.5194/acp-16-12477-2016, 2016.

Lenschow, D. H.: Micrometeorological techniques for measuring biosphere-atmosphere trace gas exchange, in: Biog. Trace Gases Meas. Emiss. from Soil Water, edited by Matson, P. A., pp. 126–163, Blackwell Publishing Ltd, London, 1995.

Leuenberger, D., Koller, M., Fuhrer, O., and Schär, C.: A Generalization of the SLEVE Vertical Coordinate, Mon. Weather Rev., 138, 3683–3689, doi:10.1175/2010MWR3307.1, 2010.

Leung, F. Y. T., Logan, J. A., Park, R., Hyer, E., Kasischke, E., Streets, D., and Yurganov, L.: Impacts of enhanced biomass burning in the boreal forests in 1998 on tropospheric chemistry and the sensitivity of model results to the injection height of emissions, J. Geophys. Res. Atmos., 112, D10313, 1–15, doi:10.1029/2006JD008132, 2007.

Lewis, A. C., Evans, M. J., Hopkins, J. R., Punjabi, S., Read, K. A., Purvis, R. M., Andrews, S. J., Moller, S. J., Carpenter, L. J., Lee, J. D., Rickard, A. R., Palmer, P. I., and Parrington, M.: The influence of biomass burning on the global distribution of selected non-methane organic compounds, Atmos. Chem. Phys., 13, 851–867, doi:10.5194/acp-13-851-2013, 2013.

Li, Q., Jacob, D. J., Yantosca, R. M., Heald, C. L., Singh, H. B., Koike, M., Zhao, Y., Sachse, G. W., and Streets, D. G.: A global three-dimensional model analysis of the atmospheric budgets of HCN and CH_3CN: Constraints from aircraft and ground measurements, J. Geophys. Res. Atmos., 108, 8827, doi:10.1029/2002JD003075, 2003.

Li, Q., Jiang, J. H., Wu, D. L., Read, W. G., Livesey, N. J., Waters, J. W., Zhang, Y., Wang, B., Filipiak, M. J., Davis, C. P., Turquety, S., Wu, S., Park, R. J., Yantosca, R. M., and Jacob, D. J.: Convective outflow of South Asian pollution: A global CTM simulation compared with EOS MLS observations, Geophys. Res. Lett., 32, L14 826, doi:10.1029/2005GL022762, 2005.

Li, R., Kalenge, S., Hopke, P. K., Lebouf, R., Rossner, A., and Benedict, A.: Source apportionment of benzene downwind of a major point source, Atmos. Pollut. Res., 2, 138–143, doi:10.5094/APR.2011.018, 2011.

Li, R., Warneke, C., Graus, M., Field, R., Geiger, F., Veres, P. R., Soltis, J., Li, S.-M., Murphy, S. M., Sweeney, C., Pétron, G., Roberts, J. M., and de Gouw, J.: Measurements of hydrogen sulfide (H_2S) using PTR-MS: calibration, humidity dependence, inter-comparison and results from field studies in an oil and gas production region, Atmos. Meas. Tech., 7, 3597–3610, doi:10.5194/amt-7-3597-2014, 2014.

Li, J., Georgescu, M., Hyde, P., Mahalov, A., and Moustaoui, M.: Regional-scale transport of air pollutants: impacts of Southern California emissions on Phoenix ground-level ozone concentrations, Atmos. Chem. Phys., 15, 9345–9360, doi:10.5194/acp-15-9345-2015, 2015.

Li, S.-M., Leithead, A., Moussa, S. G., Liggio, J., Moran, M. D., Wang, D., Hayden, K., Darlington, A., Gordon, M., Staebler, R., Makar, P. A., Stroud, C. A., McLaren, R., Liu, P. S. K., O'Brien, J., Mittermeier, R. L., Zhang, J., Marson, G., Cober, S. G., Wolde, M., and Wentzell, J. J. B.: Differences between measured and reported volatile organic compound emissions from oil sands facilities in Alberta, Canada, Proc. Natl. Acad. Sci., 114, E3756–E3765, doi:10.1073/pnas.1617862114, 2017.

Lindinger, W. and Jordan, A.: Proton-transfer-reaction mass spectrometry (PTR-MS): on-line monitoring of volatile organic compounds at pptv levels, Chem. Soc. Rev., 27, 347–375, doi:10.1039/A827347Z, 1998.

Lindinger, W., Hansel, A., and Jordan, A.: On-line monitoring of volatile organic compounds at pptv levels by means of proton-transfer-reaction mass spectrometry (PTR-MS) medical applications, food control and environmental research, Int. J. Mass Spectrom. Ion Process., 173, 191–241, doi:10.1016/S0168-1176(97)00281-4, 1998.

Lobert, J. M., Scharffe, D. H., Hao, W. M., and Crutzen, P. J.: Importance of biomass burning in the atmospheric budgets of nitrogen-containing gases, Nature, 346, 552–554, doi:10.1038/346552a0, 1990.

Lohmann, U. and Feichter, J.: Global indirect aerosol effects: a review, Atmos. Chem. Phys., 5, 715–737, doi:10.5194/acp-5-715-2005, 2005.

Long, L. G. and Winefordner, J. D.: Limit of Detection A Closer Look at the IUPAC Definition, Anal. Chem., 55, 712–724, doi:10.1021/ac00258a724, 1983.

Loreto, F., Dicke, M., Schnitzler, J.-P., and Turlings, T. C. J.: Plant volatiles and the environment, Plant. Cell Environ., 37, 1905–1908, doi:10.1111/pce.12369, 2014.

MACCity: (MACC/CityZEN EU projects) emissions dataset - Data between year 1960 and 2020 from MACCity - distributed by ECCAD. Authors: 1- Anthropogenic: Ariela Angiola, Aude Mieville, Claire Granier; 2- Biomass burning: Angelika Heil, Martin G. Schultz, 2012.

Madronich, S. and Flocke, S.: The Role of Solar Radiation in Atmospheric Chemistry, pp. 1–26, Springer Berlin Heidelberg, Berlin, Heidelberg, doi:10.1007/978-3-540-69044-3_1, 1999.

Madronich, S., Chatfield, R. B., Calvert, J. G., Moortgat, G. K., Veyret, B., and Lesclaux, R.: A photochemical origin of acetic acid in the troposphere, Geophys. Res. Lett., 17, 2361–2364, doi:10.1029/GL017i013p02361, 1990.

Madronich, S., Flocke, F., Zeng, J., Petropavlovskikh, I., and Lee-Taylor, J.: Tropospheric Ultraviolet-Visible Model (TUV), Version 5.0, NCAR/ACD, 2010.

Marandino, C. A., De Bruyn, W. J., Miller, S. D., Prather, M. J., and Saltzman, E. S.: Oceanic uptake and the global atmospheric acetone budget, Geophys. Res. Lett., 32, L15 806, doi:10.1029/2005GL023285, 2005.

Mardiguian, M., Sweeney, D. L., and Swanberg, R.: Controlling Radiated Emisions by Design, Springer Berlin Heidelberg, 3rd edn., 2014.

Marenco, A., Thouret, V., Nédélec, P., Smit, H., Helten, M., Kley, D., Karcher, F., Simon, P., Law, K., Pyle, J., Poschmann, G., Von Wrede, R., Hume, C., and Cook, T.: Measurement of ozone and water vapor by Airbus in-service aircraft: The MOZAIC airborne program, an overview, J. Geophys. Res., 103, 25 631, doi:10.1029/98JD00977, 1998.

Martin, A.: AN-2162 Simple Success With Conducted EMI From DCDC Converters, Technical report, Texas Instruments Incorporated Application Report SNVA489C, 2013.

Martinsson, B. G., Friberg, J., Andersson, S. M., Weigelt, A., Hermann, M., Assmann, D., Voigtländer, J., Brenninkmeijer, C. A., Van Velthoven, P. J., and Zahn, A.: Comparison between CARIBIC aerosol samples analysed by accelerator-based methods and optical particle counter measurements, Atmos. Meas. Tech., 7, 2581–2596, doi:10.5194/amt-7-2581-2014, 2014.

Mauzerall, D. L., Logan, J. A., Jacob, D. J., Anderson, B. E., Blake, D. R., Bradshaw, J. D., Heikes, B., Sachse, G. W., Singh, H., and Talbot, B.: Photochemistry in biomass burning plumes and implications for tropospheric ozone over the tropical South Atlantic, J. Geophys. Res. Atmos., 103, 8401–8423, doi:10.1029/97JD02612, 1998.

McKeen, S. A. and Liu, S. C.: Hydrocarbon ratios and photochemical history of air masses, Geophys. Res. Lett., 20, 2363–2366, doi:10.1029/93GL02527, 1993.

McKeen, S. A., Liu, S. C., Hsie, E.-Y., Lin, X., Bradshaw, J. D., Smyth, S., Gregory, G. L., and Blake, D. R.: Hydrocarbon ratios during PEM-WEST A: A model perspective, J. Geophys. Res. Atmos., 101, 2087–2109, doi:10.1029/95JD02733, 1996.

McKeen, S. A., Gierczak, T., Burkholder, J. B., Wennberg, P. O., Hanisco, T. F., Keim, E. R., Gao, R.-S., Liu, S. C., Ravishankara, A. R., and Fahey, D. W.: The photochemistry of acetone in the upper troposphere: A source of odd-hydrogen radicals, Geophys. Res. Lett., 24, 3177–3180, doi:10.1029/97GL03349, 1997.

McLachlan, G. and Peel, D.: General Introduction, in: Finite Mix. Model., pp. 1–39, John Wiley & Sons, Inc., doi:10.1002/0471721182.ch1, 2000.

Mech, M., Orlandi, E., Crewell, S., Ament, F., Hirsch, L., Hagen, M., Peters, G., and Stevens, B.: HAMP-the microwave package on the high altitude and long range research aircraft (HALO), Atmos. Meas. Tech., 7, 4539–4553, doi:10.5194/amt-7-4539-2014, 2014.

Medina, S., Houze, R. A., Kumar, A., and Niyogi, D.: Summer monsoon convection in the Himalayan region: Terrain and land cover effects, Q. J. R. Meteorol. Soc., 136, 593–616, doi:10.1002/qj.601, 2010.

MEGAN-MACC: Biogenic emission inventory - Data between year 1980 and 2010 from MEGAN-MACC - distributed by ECCAD. Authors: Katerina Sindelarova, Alex Guenther, 2012.

Mellouki, A., Wallington, T. J., and Chen, J.: Atmospheric Chemistry of Oxygenated Volatile Organic Compounds: Impacts on Air Quality and Climate, Chem. Rev., 115, 3984–4014, doi:10.1021/cr500549n, 2015.

Messina, P., Lathière, J., Sindelarova, K., Vuichard, N., Granier, C., Ghattas, J., Cozic, A., and Hauglustaine, D. A.: Global biogenic volatile organic compound emissions in the ORCHIDEE and MEGAN models and sensitivity to key parameters, Atmos. Chem. Phys., 16, 14169–14202, doi:10.5194/acp-16-14169-2016, 2016.

Michel, C., Liousse, C., Grégoire, J. M., Tansey, K., Carmichael, G. R., and Woo, J. H.: Biomass burning emission inventory from burnt area data given by the SPOT-VEGETATION system in the frame of TRACE-P and ACE-Asia campaigns, J. Geophys. Res. D Atmos., 110, D09304, 1–15, doi:10.1029/2004JD005461, 2005.

Middleton, P.: Sources of air pollutants, in: Composition Chemistry, and Climate of the Atmosphere, edited by Singh, H. B., John Wiley & Sons, Inc., New York, 1995.

Mikoviny, T., Kaser, L., and Wisthaler, A.: Development and characterization of a High-Temperature Proton-Transfer-Reaction Mass Spectrometer (HT-PTR-MS), Atmos. Meas. Tech., 3, 537–544, doi:10.5194/amt-3-537-2010, 2010.

Millet, D. B., Jacob, D. J., Custer, T. G., de Gouw, J. A., Goldstein, A. H., Karl, T., Singh, H. B., Sive, B. C., Talbot, R. W., Warneke, C., and Williams, J.: New constraints on terrestrial and oceanic sources of atmospheric methanol, Atmos. Chem. Phys., 8, 7609–7655, doi:10.5194/acpd-8-7609-2008, 2008.

Misztal, P., Hewitt, C., Wildt, J., Blande, J., Eller, A., Fares, S., Gentner, D., Gilman, J., Graus, M., Greenberg, J., Guenther, A., Hansel, A., Harley, P., Huang, M., Jardine, K., Karl, T., Kaser, L., Keutsch, F., Kiendler-Scharr, A., Kleist, E., Lerner, B., Li, T., Mak, J., Nölscher, A., Schnitzhofer, R., Sinha, V., Thornton, B., Warneke, C., Wegener, F., Werner, C., Williams, J., Worton, D., Yassaa, N., and Goldstein, A.: Atmospheric benzenoid emissions from plants rival those from fossil fuels, Sci. Rep., 5, 12 064, 1–10, doi:10.1038/srep12064, 2015.

Misztal, P. K., Nemitz, E., Langford, B., Di Marco, C. F., Phillips, G. J., Hewitt, C. N., MacKenzie, A. R., Owen, S. M., Fowler, D., Heal, M. R., and Cape, J. N.: Direct ecosystem fluxes of volatile organic compounds from oil palms in South-East Asia, Atmos. Chem. Phys., 11, 8995–9017, doi:10.5194/acp-11-8995-2011, 2011.

Miyoshi, A., Hatakeyama, S., and Washida, N.: OH radical- initiated photooxidation of isoprene: An estimate of global CO production, J. Geophys. Res., 99, 18779–18787, doi:10.1029/94JD01334, 1994.

Möller, D.: Chemistry of the Climate System, De Gruyter, Berlin, Boston, 2014.

Monks, P. S.: Gas-phase radical chemistry in the troposphere, Chem. Soc. Rev., 34, 376–395, doi:10.1039/b307982c, 2005.

Monks, P. S., Archibald, A. T., Colette, A., Cooper, O., Coyle, M., Derwent, R., Fowler, D., Granier, C., Law, K. S., Mills, G. E., Stevenson, D. S., Tarasova, O., Thouret, V., Von Schneidemesser, E., Sommariva, R., Wild, O., and Williams, M. L.: Tropospheric ozone and its precursors from the urban to the global scale from air quality to short-lived climate forcer, Atmos. Chem. Phys., 15, 8889–8973, doi:10.5194/acp-15-8889-2015, 2015.

Moore, D. P. and Remedios, J. J.: Seasonality of Peroxyacetyl nitrate (PAN) in the upper troposphere and lower stratosphere using the MIPAS-E instrument, Atmos. Chem. Phys., 10, 6117–6128, doi:10.5194/acp-10-6117-2010, 2010.

Moore, D. P., Remedios, J. J., and Waterfall, A. M.: Global distributions of acetone in the upper troposphere from MIPAS spectra, Atmos. Chem. Phys., 12, 757–768, doi:10.5194/acp-12-757-2012, 2012.

Moussa, S. G., Leithead, A., Li, S. M., Chan, T. W., Wentzell, J. J. B., Stroud, C., Zhang, J., Lee, P., Lu, G., Brook, J. R., Hayden, K., Narayan, J., and Liggio, J.: Emissions of hydrogen cyanide from on-road gasoline and diesel vehicles, Atmos. Environ., 131, 185–195, doi:10.1016/j.atmosenv.2016.01.050, 2016.

Mu, M., Randerson, J. T., van der Werf, G. R., Giglio, L., Kasibhatla, P., Morton, D., Collatz, G. J., Defries, R. S., Hyer, E. J., Prins, E. M., Griffith, D. W., Wunch, D., Toon, G. C., Sherlock, V., and Wennberg, P. O.: Daily and 3-hourly variability in global fire emissions and consequences for atmospheric model predictions of carbon monoxide, J. Geophys. Res. Atmos., 116, 1–19, doi:10.1029/2011JD016245, 2011.

Mullaugh, K. M., Hamilton, J. M., Avery, G. B., Felix, J. D., Mead, R. N., Willey, J. D., and Kieber, R. J.: Temporal and spatial variability of trace volatile organic compounds in rainwater, Chemosphere, 134, 203–209, doi:10.1016/j.chemosphere.2015.04.027, 2015.

Müller, J.-F.: Geographical distribution and seasonal variation of surface emissions and deposition velocities of atmospheric trace gases, J. Geophys. Res. Atmos., 97, 3787–3804, doi:10.1029/91JD02757, 1992.

Müller, M., Mikoviny, T., Feil, S., Haidacher, S., Hanel, G., Hartungen, E., Jordan, A., Märk, L., Mutschlechner, P., Schottkowsky, R., Sulzer, P., Crawford, J. H., and Wisthaler, A.: A compact PTR-ToF-MS instrument for airborne measurements of volatile organic compounds at high spatiotemporal resolution, Atmos. Meas. Tech., 7, 3763–3772, doi:110.5194/amt-7-3763-2014, 2014.

Müller, M., Anderson, B. E., Beyersdorf, A. J., Crawford, J. H., Diskin, G. S., Eichler, P., Fried, A., Keutsch, F. N., Mikoviny, T., Thornhill, K. L., Walega, J. G., Weinheimer, A. J., Yang, M., Yokelson, R. J., and Wisthaler, A.: In situ measurements and modeling of reactive trace gases in a small biomass burning plume, Atmos. Chem. Phys., 16, 3813–3824, doi:10.5194/acp-16-3813-2016, 2016.

Muntean, F.: Transmission study for r.f.-only quadrupoles by computer simulation, Int. J. Mass Spectrom. Ion Processes, 151, 197–206, doi:10.1016/0168-1176(95)04319-5, 1995.

Myhre, G., Shindell, D., Breon, F.-M., Collins, W., Fuglestvedt, J., Huang, J., Koch, D., Lamarque, J.-F., Lee, D., Mendoza, B., Nakajima, T., Robock, A., Stephens, G., T., T., and Zhang, H.: Anthropogenic and Natural Radiative Forcing, in: Climate Change 2013: The Physical Science Basis. Contribution of Working Group I to the Fifth Assessment Report of the Intergovernmental Panel on Climate Change, Cambridge University Press, Cambridge, 2013.

National Research Council: Rethinking the Ozone Problem in Urban and Regional Air Pollution, The National Academies Press, Washington, D.C., doi:10.17226/1889, p. 194, 1991.

Nemecek-Marshall, M., Wojciechowski, C., Kuzma, J., Silver, G. M., and Fall, R.: Marine Vibrio Species Produce the Volatile Organic Compound Acetone, Appl. Environ. Microbiol., 61, 44–47, 1995.

NetCDF: Network Common Data Form by UCAR Unidata Data Services and Tools for Geoscience, `http://www.unidata.ucar.edu/software/netcdf/`, last access: 1 August 2017.

Neumaier, M., Ruhnke, R., Kirner, O., Ziereis, H., Stratmann, G., Brenninkmeijer, C. A. M., and Zahn, A.: Impact of acetone (photo)oxidation on HO_x production in the UT/LMS based on CARIBIC passenger aircraft observations and EMAC simulations, Geophys. Res. Lett., 41, 3289–3297, doi:10.1002/2014GL059480, 2014a.

Neuman, J. A., Huey, L. G., Ryerson, T. B., and Fahey, D. W.: Study of Inlet Materials for Sampling Atmospheric Nitric Acid, Environ. Sci. Technol., 33, 1133–1136, doi:10.1021/es980767f, 1999.

Novelli, P. C., Masarie, K. A., Lang, P. M., Hall, B. D., Myers, R. C., and Elkins, J. W.: Reanalysis of tropospheric CO trends: Effects of the 1997-1998 wildfires, J. Geophys. Res., 108, 4464, doi:10.1029/2002JD003031, 2003.

Nowak, J. B., Neuman, J. a., Kozai, K., Huey, L. G., Tanner, D. J., Holloway, J. S., Ryerson, T. B., Frost, G. J., McKeen, S. A., and Fehsenfeld, F. C.: A chemical ionization mass spectrometry technique for airborne measurements of ammonia, J. Geophys. Res., 112, D10S02, doi:10.1029/2006JD007589, 2007.

Nozière, B., Kalberer, M., Claeys, M., Allan, J., D'Anna, B., Decesari, S., Finessi, E., Glasius, M., Grgić, I., Hamilton, J. F., Hoffmann, T., Iinuma, Y., Jaoui, M., Kahnt, A., Kampf, C. J., Kourtchev, I., Maenhaut, W., Marsden, N., Saarikoski, S., Schnelle-Kreis, J., Surratt, J. D., Szidat, S., Szmigielski, R., and Wisthaler, A.: The Molecular Identification of Organic Compounds in the Atmosphere: State of the Art and Challenges, Chem. Rev., 115, 3919–3983, doi:10.1021/cr5003485, 2015.

Olivier, J. G. J., Peters, J., Granier, C., Petron, G., Muller, J.-F., and Wallens, S.: Present and future surface emissions of atmospheric compounds, POET Report No 2, EU project EVK2-1999-00011, available at: `http://tropo.aeronomie.be/pdf/POET_emissions_report.pdf`, 2003.

Olivier, J. G. J., Van Aardenne, J. A., Dentener, F. J., Pagliari, V., Ganzeveld, L. N., and Peters, J. A. H. W.: Recent trends in global greenhouse gas emissions:regional trends 1970–2000 and spatial distributionof key sources in 2000, Environ. Sci., 2, 81–99, doi:10.1080/15693430500400345, 2005.

Orlando, J. J., Nozière, B., Tyndall, G. S., Orzechowska, G. E., Paulson, S. E., and Rudich, Y.: Product studies of the OH- and ozone-initiated oxidation of some monoterpenes, J. Geophys. Res., 105, 11561–11572, doi:10.1029/2000JD900005, 2000.

Osman, M. K., Tarasick, D. W., Liu, J., Moeini, O., Thouret, V., Fioletov, V. E., Parrington, M., and Nédélec, P.: Carbon monoxide climatology derived from the trajectory mapping of global MOZAIC-IAGOS data, Atmos. Chem. Phys., 16, 10263-10282, doi:10.5194/acp-16-10263-2016, 2016

Ozenbaugh, R. L. and Pullen, T. M.: Common Mode and Differential Mode: Definition, Cause, and Elimination, in: EMI Filter Design, 3rd edn., CRC Press, Boca Raton, 272 pp., 2016.

Palmer, P. I., Jacob, D. J., Jones, D. B. A., Heald, C. L., Yantosca, R. M., Logan, J. A., Sachse, G. W., and Streets, D. G.: Inverting for emissions of carbon monoxide from Asia using aircraft observations over the western Pacific, J. Geophys. Res. Atmos., 108, 8828, doi:10.1029/2003JD003397, 2003.

Passant, N. R.: Speciation of UK emissions of non-methane volatile organic compounds, AEAT/ENV/R/0545, 1, AEA Technology, Oxon, Technical report, 2002.

Patokoski, J., Ruuskanen, T. M., Kajos, M. K., Taipale, R., Rantala, P., Aalto, J., Ryyppö, T., Nieminen, T., Hakola, H., and Rinne, J.: Sources of long-lived atmospheric VOCs at the rural boreal forest site, SMEAR II, Atmos. Chem. Phys., 15, 13 413–13 432, doi:10.5194/acp-15-13413-2015, 2015.

Paulot, F., Wunch, D., Crounse, J. D., Toon, G. C., Millet, D. B., Decarlo, P. F., Vigouroux, C., Deutscher, N. M., Abad, G. G., Notholt, J., Warneke, T., Hannigan, J. W., Warneke, C., De Gouw, J. A., Dunlea, E. J., De Mazière, M., Griffith, D. W., Bernath, P., Jimenez, J. L., and Wennberg, P. O.: Importance of secondary sources in the atmospheric budgets of formic and acetic acids, Atmos. Chem. Phys., 11, 1989–2013, doi:10.5194/acp-11-1989-2011, 2011.

Pechony, O. and Shindell, D. T.: Driving forces of global wildfires over the past millennium and the forthcoming century, Proc. Natl. Acad. Sci., 107, 19 167–19 170, doi:10.1073/pnas.1003669107, 2010.

Peeters, J. and Fantechi, G.: Gas-Phase (Photo) Chemical Processes in the Troposphere, in: Environ. Ecol. Chem. Vol. I, edited by Sabljic, A., p. 341, Eolss Publishers Co. Ltd., Oxford, 2009.

Peñuelas, J. and Llusià, J.: The Complexity of Factors Driving Volatile Organic Compound Emissions by Plants, Biol. Plant., 44, 481–487, doi:10.1023/A:1013797129428, 2001.

Petetin, H., Thouret, V., Fontaine, A., Sauvage, B., Athier, G., Blot, R., Boulanger, D., Cousin, J.-M., and Nédélec, P.: Characterising tropospheric O_3 and CO around Frankfurt over the period 1994-2012 based on MOZAIC-IAGOS aircraft measurements, Atmos. Chem. Phys., 16, 15 147–15 163, doi:10.5194/acp-16-15147-2016, 2016.

Pfeiffer Vacuum: Operating Instructions High Frequency Generators QMH 400–1, QMH 400–5, QMH 410–1, QMH 410–2, QMH 410–3, Internal number: BG 805 982 BE (0201), pp. 1-35, 2001.

Piccot, S. D., Watson, J. J., and Jones, J. W.: A global inventory of volatile organic compound emissions from anthropogenic sources, J. Geophys. Res., 97, 9897–9912, doi:10.1029/92JD00682,1992.

Pisso, I., Real, E., Law, K. S., Legras, B., Bousserez, N., Attié, J. L., and Schlager, H.: Estimation of mixing in the troposphere from Lagrangian trace gas reconstructions during long-range pollution plume transport, J. Geophys. Res. Atmos., 114, D19 301 1–11, doi:10.1029/2008JD011289, 2009.

Plumb, R. A.: Stratospheric Transport, J. Meteorol. Soc. Japan. Ser. II, 80, 793–809, doi:10.2151/jmsj.80.793, 2002.

Plumb, R. A., Stolarski, R., Hegglin, M. I., Prather, M. J., and Volk, C. M.: The Theory of Estimating Lifetimes Using Models and Observations, SPARC Lifetimes Report – SPARC Report No. 6, pp. 43–62, 2013.

Possell, M. and Loreto, F.: The Role of Volatile Organic Compounds in Plant Resistance to Abiotic Stresses: Responses and Mechanisms, in: Biology, Controls and Models of Tree Volatile Organic Compound Emissions, edited by Niinemets, U. and Monson, R. K., pp. 209–235, Springer, doi:10.1007/978-94-007-6606-8_8, 2013.

Pozzer, A., Pollmann, J., Taraborrelli, D., Jöckel, P., Helmig, D., Tans, P., Hueber, J., and Lelieveld, J.: Observed and simulated global distribution and budget of atmospheric C_2-C_5 alkanes, Atmos. Chem. Phys., 10, 4403–4422, doi:10.5194/acp-10-4403-2010, 2010.

Price, H. U., Jaffe, D. A., Cooper, O. R., and Doskey, P. V.: Photochemistry, ozone production, and dilution during long-range transport episodes from Eurasia to the northwest United States, J. Geophys. Res. Atmos., 109, D23S13, 1–10, doi:10.1029/2003JD004400, 2004.

Prinn, R. G.: The Cleansing Capacity of the Atmosphere, Annual Review of Environment and Resources, 28, 29–57, doi:10.1146/annurev.energy.28.011503.163425, 2003.

Ramanathan, V., Crutzen, P. J., Kiehl, J. T., and Rosenfeld, D.: Aerosols, Climate, and the Hydrological Cycle, Science, 294, 2119–2124, doi:10.1126/science.1064034, 2001.

Randel, W. J., Park, M., Emmons, L., Kinnison, D., Bernath, P., Walker, K. A., Boone, C., and Pumphrey, H.: Asian Monsoon Transport of Pollution to the Stratosphere, Science, 328, 611–613, doi:10.1126/science.1182274, 2010.

Randerson, J. T., van der Werf, G. R., Giglio, L., Collatz, G. J., and Kasibhatla, P. S.: Fire emissions from C_3 and C_4 vegetation and their influence on interannual variability of atmospheric CO_2 and $\delta^{13}CO_2$, Global Biogeochemical Cycles, 19, GB2019, doi:10.1029/2004GB002366, 2005.

Randerson, J. T., van der Werf, G. R., Collatz, G. J., Giglio, L., Still, C. J., Kasibhatla, P. S., Miller, J. B., White, J. W. C., DeFries, R. S., and Kasischke, E. S.: Global Fire Emissions Database, Version 2 (GFEDv2), Data set. Available on-line [http://daac.ornl.gov/] from Oak Ridge National Laboratory Distributed Active Archive Center, Oak Ridge, Tennessee, U.S.A., doi:10.3334/ORNLDAAC/834, 2006.

Randerson, J. T., Chen, Y., van der Werf, G. R., Rogers, B. M., and Morton, D. C.: Global burned area and biomass burning emissions from small fires, J. Geophys. Res. Biogeosciences, 117, G04 012, doi:10.1029/2012JG002128, 2012.

Rantala, P., Järvi, L., Taipale, R., Laurila, T. K., Patokoski, J., Kajos, M. K., Kurppa, M., Haapanala, S., Siivola, E., Petäjä, T., Ruuskanen, T. M., and Rinne, J.: Anthropogenic and biogenic influence on VOC fluxes at an urban background site in Helsinki, Finland, Atmos. Chem. Phys., 16, 7981–8007, doi:10.5194/acp-16-7981-2016, 2016.

Razavi, A., Karagulian, F., Clarisse, L., Hurtmans, D., Coheur, P. F., Clerbaux, C., Müller, J. F., and Stavrakou, T.: Global distributions of methanol and formic acid retrieved for the first time from the IASI/MetOp thermal infrared sounder, Atmos. Chem. Phys., 11, 857–872, doi:10.5194/acp-11-857-2011, 2011.

Real, E., Law, K. S., Weinzierl, B., Fiebig, M., Petzold, A., Wild, O., Methven, J., Arnold, S., Stohl, A., Huntrieser, H., Roiger, A., Schlager, H., Stewart, D., Avery, M., Sachse, G., Browell, E., Ferrare, R., and Blake, D.: Processes influencing ozone levels in Alaskan forest fire plumes during long-range transport over the North Atlantic, J. Geophys. Res. Atmos., 112, D10S41, doi:10.1029/2006JD007576, 2007.

Reeve, M. A.: Monsoon Onset in Bangladesh Reconciling Scientific and Societal Perspectives, Ph.D. thesis, University of Bergen, 2015.

Regelin, E., Harder, H., Martinez, M., Kubistin, D., Tatum Ernest, C., Bozem, H., Klippel, T., Hosaynali-Beygi, Z., Fischer, H., Sander, R., Jöckel, P., Königstedt, R., and Lelieveld, J.: HO_x measurements in the summertime upper troposphere over Europe: A comparison of observations to a box model and a 3-D model, Atmos. Chem. Phys., 13, 10 703–10 720, doi:10.5194/acp-13-10703-2013, 2013.

Reiner, T., Möhler, O., and Arnold, F.: Measurements of acetone, acetic acid, and formic acid in the northern midlatitude upper troposphere and lower stratosphere, J. Geophys. Res. Atmos., 104, 13 943–13 952, doi:10.1029/1999JD900030, 1999.

Reiner, T., Sprung, D., Jost, C., Gabriel, R., Mayol-Bracero, O. L., Andreae, M. O., Campos, T. L., and Shelter, R. E.: Chemical characterization of pollution layers over the tropical Indian Ocean: Signatures of emissions from biomass and fossil fuel burning, J. Geophys. Res. Atmos., 106, 28 497–28 510, doi:10.1029/2000JD900695, 2001.

Reinert, D., Prill, F., Frank, H., and Zängl, G.: ICON Database Reference Manual, Version 1.1.12, Deutscher Wetterdienst, doi:10.5676/DWD_pub/nwv/icon_1.1.12, 2017.

RETRO: emission inventory - Data between year 1960 and 2000 from RETRO - distributed by ECCAD. Authors: Øyvind Endresen, Stig B. Dalsøren, Martin G. Schultz, Angelika Heil, Judith Hoelzemann, Allan Spessa, Kirsten Thonicke, Johann Goldammer, José Miguel Pereira, 2005.

Revercomb, H. E. and Mason, E. A.: Theory of plasma chromatography/gaseous electrophoresis. Review, Anal. Chem., 47, 970–983, doi:10.1021/ac60357a043, 1975.

Rieger, D., Bangert, M., Bischoff-Gauss, I., Förstner, J., Lundgren, K., Reinert D., Schröter, J., Vogel, H., Zängl, G., Ruhnke, R., and Vogel, B.: ICON–ART 1.0 – a new online-coupled model system from the global to regional scale, JGeosci. Model Dev., 8, 1659-1676, doi:10.5194/gmd-8-1659-2015, 2015.

Riese, M., Ploeger, F., Rap, A., Vogel, B., Konopka, P., Dameris, M., and Forster, P.: Impact of uncertainties in atmospheric mixing on simulated UTLS composition and related radiative effects, J. Geophys. Res. Atmos., 117, 1–10, doi:10.1029/2012JD017751, 2012.

Ritzau, S. M., Laprade, B. N., Mrotek, S. R., and Leffingwell, R.: A Direct Comparison of a Resistive Glass and Stacked Ring Reflectron, Photonis, Technical report, available at: `https://www.photonis.com/uploads//literature/rgp/reflectron-learning.pdf`,2006.

Roberts, J. M., Fehsenfeld, F. C., Liu, S. C., Bollinger, M. J., Hahn, C., Albritton, D. L., and Sievers, R. E.: Measurements of aromatic hydrocarbon ratios and NO_x concentrations in the rural troposphere: Observation of air mass photochemical aging and NO_x removal, Atmos. Environ., 18, 2421–2432, doi:10.1016/0004-6981(84)90012-X, 1984.

Rogers, T. M., Grimsrud, E. P., Herndon, S. C., Jayne, J. T., Kolb, C. E., Allwine, E., Westberg, H., Lamb, B. K., Zavala, M., Molina, L. T., Molina, M. J., and Knighton, W. B.: On-road measurements of volatile organic compounds in the Mexico City metropolitan area using proton transfer reaction mass spectrometry, Int. J. Mass Spectrom., 252, 26–37, doi:10.1016/j.ijms.2006.01.027, 2006.

Roiger, A., Aufmhoff, H., Stock, P., Arnold, F., and Schlager, H.: An aircraft-borne chemical ionization – ion trap mass spectrometer (CI-ITMS) for fast PAN and PPN measurements, Atmos. Meas. Tech., 4, 173–188, doi:10.5194/amt-4-173-2011, 2011.

Roscoe, H. K. and Clemitshaw, K. C.: Measurement Techniques in Gas-Phase Tropospheric Chemistry: A Selective View of the Past, Present, and Future, Science, 276, 1065–1072, doi:10.1126/science.276.5315.1065, 1997.

Rothman, L. S., Gordon, I. E., Barbe, A., Benner, D., Bernath, P. F., Birk, M., Boudon, V., Brown, L. R., Campargue, A., Champion, J.-P., Chance, K., Coudert, L. H., Dana, V., Devi, V. M., Fally, S., Flaud, J.-M., Gamache, R. R., Goldman, A., Jacquemart, D., Kleiner, I., Lacome, N., Lafferty, W. J., Mandin, J.-Y., Massie, S. T., Mikhailenko, S. N., Miller, C. E., Moazzen-Ahmadi, N., Naumenko, O. V., Nikitin, A. V., Orphal, J., Perevalov, V. I., Perrin, A., Predoi-Cross, A., Rinsland, C. P., Rotger, M., Šimečková, M., Smith, M. A. H., Sung, K., Tashkun, S. A., Tennyson, J., Toth, R. A., Vandaele, A. C., and Vander Auwera, J.: The HITRAN 2008 molecular spectroscopic database, J. Quant. Spectrosc. Radiat. Transf., 110, 533–572, doi:10.1016/j.jqsrt.2009.02.013, 2009.

Russell, A. T.: Combustion Emissions, in: Air Pollution Cancer - IARC Scientific Publication, edited by Straif, K., Cohen, A., and Samet, J., vol. 161, pp. 37–47, International Agency for Research on Cancer of the World Health Organization, Geneva, 2013.

Ruuskanen, T. M.: Measurements of volatile organic compounds - from biogenic emissions to ambient concentrations, Ph.D. thesis, University of Helsinki, 2009.

Sadourny, R., Arakawa, A., and Mintz, Y.: Integration of the nondivergent barotropic vorticity equation with an icosahedral-hexagonal grid for the sphere, Mon. Weather Rev., 96, 351–356, doi:10.1175/1520-0493(1968)096⟨0351:IOTNBV⟩2.0.CO;2, 1968.

Safadi, L.: Volatile Organic Compounds (VOCs) measurements onboard the HALO research aircraft, PhD thesis, Karlsruhe Institute of Technology (KIT), in preparation.

Safadi, L. and Neumaier, M.: HKMS data of the OMO-Asia campaign, HALO Database, available at: `https://halo-db.pa.op.dlr.de/data_source/91`, 2016.

Sakamoto, K. M., Allan, J. D., Coe, H., Taylor, J. W., Duck, T. J., and Pierce, J. R.: Aged boreal biomass-burning aerosol size distributions from BORTAS 2011, Atmos. Chem. Phys., 15, 1633–1646, doi:10.5194/acp-15-1633-2015, 2015.

Sarkar, C., Sinha, V., Kumar, V., Rupakheti, M., Panday, A., S Mahata, K., Rupakheti, D., Kathayat, B., and G Lawrence, M.: Overview of VOC emissions and chemistry from PTR-TOF-MS measurements during the SusKat-ABC campaign: High acetaldehyde, isoprene and isocyanic acid in wintertime air of the Kathmandu Valley, Atmos. Chem. Phys., 16, 3979–4003, doi:10.5194/acp-16-3979-2016, 2016.

Schade, G. W. and Goldstein, A. H.: Seasonal measurements of acetone and methanol: Abundances and implications for atmospheric budgets, Global Biogeochem. Cycles, 20, GB1011, doi:10.1029/2005GB002566, 2006.

Schär, C., Leuenberger, D., Fuhrer, O., Lüthi, D., and Girard, C.: A New Terrain-Following Vertical Coordinate Formulation for Atmospheric Prediction Models, Mon. Weather Rev., 130, 2459–2480, doi:10.1175/1520-0493(2002)130⟨2459:ANTFVC⟩2.0.CO;2, 2002.

Scheeren, H. A., Fischer, H., Lelieveld, J., Hoor, P., Rudolph, J., Arnold, F., Bregman, B., Brühl, C., Engel, A., van der Veen, C., and Brunner, D.: Reactive organic species in the northern extratropical lowermost stratosphere: Seasonal variability and implications for OH, J. Geophys. Res. Atmos., 108, doi:10.1029/2003JD003650, 2003.

Schneider, J., Bürger, V., and Arnold, F.: Methyl cyanide and hydrogen cyanide measurements in the lower stratosphere: Implications for methyl cyanide sources and sinks, J. Geophys. Res., 102, 25 501–25 506, doi:10.1029/97jd02364, 1997.

Schneider, M.: MUSICA H_2O and δD (HDO/H_2O) data: in-situ, ground-based FTIR, and IASI, in: 7th GRUAN Implementation-Coordination Meet., 2015.

Schneider, M. and Hase, F.: Optimal estimation of tropospheric H_2O and δD with IASI/METOP, Atmos. Chem. Phys., 11, 11 207–11 220, doi:10.5194/acp-11-11207-2011, 2011.

Schneider, M., Blumenstock, T., Chipperfield, M. P., Hase, F., Kouker, W., Reddmann, T., Ruhnke, R., Cuevas, E., and Fischer, H.: Subtropical trace gas profiles determined by ground-based FTIR spectroscopy at Izana (28° N, 16° W): Five-year record, error analysis, and comparison with 3-D CTMs, Atmos. Chem. Phys., 5, 153–167, doi:10.5194/acp-5-153-2005, 2005.

Schneider, M., Yoshimura, K., Hase, F., and Blumenstock, T.: The ground-based FTIR network's potential for investigating the atmospheric water cycle, Atmos. Chem. Phys., 10, 3427–3442, doi:10.5194/acp-10-3427-2010, 2010.

Schneider, M., González, Y., Dyroff, C., Christner, E., Wiegele, A., Barthlott, S., García, O. E., Sepúlveda, E., Hase, F., Andrey, J., Blumenstock, T., Guirado, C., Ramos, R., and Rodríguez, S.: Empirical validation and proof of added value of MUSICA's tropospheric δD remote sensing products, Atmos. Meas. Tech., 8, 483–503, doi:10.5194/amt-8-483-2015, 2015.

Schneider, M., Wiegele, A., Barthlott, S., González, Y., Christner, E., Dyroff, C., García, O. E., Hase, F., Blumenstock, T., Sepúlveda, E., Mengistu Tsidu, G., Takele Kenea, S., Rodríguez, S., and Andrey, J.: Accomplishments of the MUSICA project to provide accurate, long-term, global and high-resolution observations of tropospheric {H2O,δD} pairs – a review, Atmos. Meas. Tech., 9, 2845–2875, doi:10.5194/amt-9-2845-2016, 2016.

Schnitzhofer, R., Wisthaler, A., and Hansel, A.: Real-time profiling of organic trace gases in the planetary boundary layer by PTR-MS using a tethered balloon, Atmos. Meas. Tech., 2, 773–777, doi:10.5194/amt-2-773-2009, 2009.

Schröter, J., Ruhnke, R., Rieger, D., Vogel, B., and Vogel, H.: Investigating atmospheric transport processes of trace gases with ICON-ART on different scales, in: Geophys. Res. Abstr., pp. EGU2016–11 606, European Geosciences Union, 2016.

Schuck, T. J., Brenninkmeijer, C. A. M., Slemr, F., Xueref-Remy, I., and Zahn, A.: Greenhouse gas analysis of air samples collected onboard the CARIBIC passenger aircraft, Atmos. Meas. Tech., 2, 449–464, doi:10.5194/amt-2-449-2009, 2009.

Schultz, M. G., Heil, A., Hoelzemann, J. J., Spessa, A., Thonicke, K., Goldammer, J. G., Held, A. C., Pereira, J. M. C., and van het Bolscher, M.: Global wildland fire emissions from 1960 to 2000, Glob. Biogeochem. Cycles, 22, GB2002, doi:10.1029/2007GB003031, 2008.

Schumann, U.: Probing the Atmosphere with Research Aircraft-European Aircraft Campaigns. In: Observing Systems for Atmospheric Composition: Satellite, Aircraft, Sensor Web and Ground-Based Observational Methods and Strategies, edited by Visconti, G., Di Carlo, P., Brune, W. Schoeberl, M., and Wahner, A., pp. 85–96, Springer, New York, doi:10.1007/978-0-387-35848-2_6, 2007.

Schumann, U., Fahey, D. W., Wendisch, M., and Brenguier, J.-L.: Introduction to airborne measurements of the Earth atmosphere and surface, in: Airborne Meas. Environ. Res. Methods Instruments, edited by Wendisch, M. and Brenuier, J.-L., pp. 1–5, Wiley, 2013.

Seiler, W. and Crutzen, P. J.: Estimates of gross and net fluxes of carbon between the biosphere and the atmosphere from biomass burning, Clim. Change, 2, 207–247, doi:10.1007/BF00137988, 1980.

Seiler, W. and Junge, C.: Decrease of carbon monoxide mixing ratio above the polar tropopause, Tellus, 21, 447–449, doi:10.1111/j.2153-3490.1969.tb00459.x, 1969.

Seinfeld, J. H.: Global Atmospheric Chemistry of Reactive Hydrocarbons, in: React. Hydrocarb. Atmos., edited by Hewitt, C. N., pp. 294–321, Academic Press, 1999.

Seinfeld, J. H. and Pandis, S. N.: Atmospheric Chemistry and Physics: from Air Pollution to Climate Change, John Wiley and Sons, Inc., New York, 1st edn., 1998.

Seinfeld, J. H. and Pandis, S. N.: Atmospheric Chemistry and Physics: From Air Pollution to Climate Change, John Wiley & Sons, Inc., New York, 3rd edn., 2016.

Shaffer, S. A., Tang, K. Q., Anderson, G. A., Prior, D. C., Udseth, H. R., and Smith, R. D.: A novel ion funnel for focusing ions at elevated pressure using electrospray ionization mass spectrometry, Rapid Commun. Mass Spectrom., 11, 1813–1817, 1997.

Shaw, M. D., Lee, J. D., Davison, B., Vaughan, A., Purvis, R. M., Harvey, A., Lewis, A. C., and Hewitt, C. N.: Airborne determination of the temporo-spatial distribution of benzene, toluene, nitrogen oxides and ozone in the boundary layer across Greater London, UK, Atmos. Chem. Phys., 15, 5083–5097, doi:10.5194/acp-15-5083-2015, 2015.

Shindell, D., Faluvegi, G., Lacis, A., Hansen, J., Ruedy, R., and Aguilar, E.: Role of tropospheric ozone increases in 20th-century climate change, J. Geophys. Res., 111, 1–11, doi:10.1029/2005JD006348, 2006.

Shrivastava, M., Zelenyuk, A., Imre, D., Beranek, J., Easter, R., Zaveri, R. A., and Fast, J.: Reformulating the atmospheric lifecycle of SOA based on new field and laboratory data, Atmos. Chem. Phys. Discuss., 2011, 20 107–20 139, doi:10.5194/acpd-11-20107-2011, 2011.

Simoneit, B. R.: Biomass burning - A review of organic tracers for smoke from incomplete combustion, Appl. Geochemistry, 17, 129–162, doi:10.1016/S0883-2927(01)00061-0, 2002.

Simpson, I. J., Akagi, S. K., Barletta, B., Blake, N. J., Choi, Y., Diskin, G. S., Fried, A., Fuelberg, H. E., Meinardi, S., Rowland, F. S., Vay, S. A., Weinheimer, A. J., Wennberg, P. O., Wiebring, P., Wisthaler, A., Yang, M., Yokelson, R. J., and Blake, D. R.: Boreal forest fire emissions in fresh Canadian smoke plumes: C_1-C_{10} volatile organic compounds (VOCs), CO_2, CO, NO_2, NO, HCN and CH_3CN, Atmos. Chem. Phys., 11, 6445–6463, doi:10.5194/acp-11-6445-2011, 2011.

Sindelarova, K., Granier, C., Bouarar, I., Guenther, A., Tilmes, S., Stavrakou, T., Müller, J.-F., Kuhn, U., Stefani, P., and Knorr, W.: Global data set of biogenic VOC emissions calculated by the MEGAN model over the last 30 years, Atmos. Chem. Phys., 14, 9317–9341, doi:10.5194/acp-14-9317-2014, 2014.

Singh, H. B., Salas, L. J., and Viezee, W.: Global distribution of peroxyacetyl nitrate, Nature, 321, 588–591, doi:10.1038/321588a0,1986.

Singh, H. B., Herlth, D, OHara, D., Zahnle, K., Bradshaw, J. D., Sandholm, S. T., Talbot, R., Crutzen, P. J., and Kanakidou, M.: Relationship of peroxyacetyl nitrate to active and total odd nitrogen at northern high latitudes: influence of reservoir species on NO_x and O_3, J. Geophys. Res., 97, 16523–16530, doi: 10.1029/91JD008901992.

Singh, H. B., Hara, D. O., Herlth, D., Sachse, W., Blake, D. R., Bradshaw, J. D., Kanakidou, M., and Crutzen, P. J.: Acetone in the atmosphere: Distribution, sources, and sinks, J. Geophys. Res., 99, 1805–1819, 1994.

Singh, H. B., Kanakidou, M., Crutzen, P. J., and Jacob, D. J.: High concentrations and photochemical fate of oxygenated hydrocarbons in the global troposphere, Nature, 378, 50–54, 1995.

Singh, H., Chen, Y., Tabazadeh, A., Fukui, Y., Bey, I., Yantosca, R., Jacob, D., Arnold, F., Wohlfrom, K., Atlas, E., Flocke, F., Blake, D., Blake, N., Heikes, B., Snow, J., Talbot, R., Gregory, G., Sachse, G., Vay, S., and Kondo, Y.: Distribution and fate of selected oxygenated organic species in the troposphere and lower stratosphere over the Atlantic, J. Geophys. Res. Atmos., 105, 3795–3805, doi:10.1029/1999JD900779, 2000.

Singh, H., Chen, Y., Staudt, A., Jacob, D., Blake, D., Heikes, B., and Snow, J.: Evidence from the Pacific troposphere for large global sources of oxygenated organic compounds., Nature, 410, 1078–1081, doi:10.1038/35074067, 2001.

Singh, H. B., Salas, L., Herlth, D., Kolyer, R., Czech, E., Viezee, W., Li, Q., Jacob, D. J., Blake, D., Sachse, G., Harward, C. N., Fuelberg, H., Kiley, C. M., Zhao, Y., and Kondo, Y.: In situ measurements of HCN and CH_3CN over the Pacific Ocean: Sources, sinks, and budgets, J. Geophys. Res., 108, 8795, doi:10.1029/2002jd003006, 2003.

Singh, H. B., Salas, Chatfield, Czech, Fried, Walega, Evans, Field, Jacob, Blake, Heikes, Talbot, Sachse, Crawford, Avery, Sandholm, and Fuelberg: Analysis of the atmospheric distribution, sources, and sinks of oxygenated volatile organic chemicals based on measurements over the Pacific during TRACE-P, J. Geophys. Res., 109, D15S07, doi:10.1029/2003JD003883, 2004.

Singh, H., Anderson, B., Brune, W., Cai, C., Cohen, R., Crawford, J., Cubison, M., Czech, E., Emmons, L., and Fuelberg, H.: Pollution influences on atmospheric composition and chemistry at high northern latitudes: Boreal and California forest fire emissions, Atmos. Environ., 44, 4553–4564, doi:10.1016/j.atmosenv.2010.08.026, 2010.

Sinha, V., Kumar, V., and Sarkar, C.: Chemical composition of pre-monsoon air in the Indo-Gangetic Plain measured using a new air quality facility and PTR-MS: High surface ozone and strong influence of biomass burning, Atmos. Chem. Phys., 14, 5921–5941, doi:10.5194/acp-14-5921-2014, 2014.

Sjostedt, S. J., Slowik, J. G., Brook, J. R., Chang, R. Y.-W., Mihele, C., Stroud, C. A., Vlasenko, A., and Abbatt, J. P. D.: Diurnally resolved particulate and VOC measurements at a rural site: indication of significant biogenic secondary organic aerosol formation, Atmos. Chem. Phys., 11, 5745–5760, doi:10.5194/acp-11-5745-2011, 2011.

Smith, D., Cheng, P., Spanel, P.: Analysis of petrol and diesel vapour and vehicle engine exhaust gases using selected ion flow tube mass spectrometry., Rapid Commun. Mass Spectrom., 16, 1124–1134, doi:10.1002/rcm.691, 2002.

Smith, D., Spanel, P., Dabill, D., Cocker, J., and Rajan, B.: On-line analysis of diesel engine exhaust gases by selected ion flow tube mass spectrometry., Rapid Commun. Mass Spectrom., 18, 2830–2838, doi:10.1002/rcm.1702, 2004.

Sonderfeld, H.: Charakterisierung und Einsatz eines PTR-ToF-MS zur Messung von flüchtigen organischen Verbindungen, Ph.D. thesis, University of Wuppertal, 2014.

Song, S., Selin, N. E., Soerensen, A. L., Angot, H., Artz, R., Brooks, S., Brunke, E. G., Conley, G., Dommergue, A., Ebinghaus, R., Holsen, T. M., Jaffe, D. A., Kang, S., Kelley, P., Luke, W. T., Magand, O., Marumoto, K., Pfaffhuber, K. A., Ren, X., Sheu, G. R., Slemr, F., Warneke, T., Weigelt, A., Weiss-Penzias, P., Wip, D. C., and Zhang, Q.: Top-down constraints on atmospheric mercury emissions and implications for global biogeochemical cycling, Atmos. Chem. Phys., 15, 7103–7125, doi:10.5194/acp-15-7103-2015, 2015.

Spanel, P. and Smith, D.: SIFT studies of the reactions of H3O+, NO+ and O2+ with a series of alcohols, Int. J. Mass Spectrom. Ion Process., 167, 375–388, doi:10.1016/S0168-1176(97)00085-2, 1997.

Spengler, J. D., Adgate, J. L., Buscalacchi Jr., A. J., Chew, G. L., Haines, A., Holland, S. M., Loftness, V. E., McCauley, L. A., Nazaroff, W. W., and Storey, E.: Climate Change, the Indoor Environment, and Health, The National Academies Press, Washington, D.C., 2011.

Spivakovsky, C. M., Logan, J. A., Montzka, S. A., Balkanski, Y. J., Foreman-Fowler, M., Jones, D. B. A., Horowitz, L. W., Fusco, A. C., Brenninkmeijer, C. A. M., Prather, M. J., Wofsy, S. C., and McElroy, M. B.: Three?dimensional climatological distribution of tropospheric OH: Update and evaluation, J. Geophys. Res., 105, 8931–8980, doi:10.1029/1999JD901006, 2000.

Sprung, D. and Zahn, A.: Deploying a PTR-MS onboard passenger aircraft (project CARIBIC) for on-line monitoring of volatile organic compounds in the UTLS, in: Contributions to 1st International Conference on Proton Transfer Reaction Mass Spectrometry and its Applications, edited by Hansel, A. and Märk, T. D., pp. 25–28, 2003.

Sprung, D. and Zahn, A.: Development of a fully automated PTR-MS for measurements onboard a passenger aircraft (CARIBIC-Project), in: Contributions to 2nd International Conference on Proton Transfer Reaction Mass Spectrometry and its Applications, edited by Hansel, A. and Märk, T. D., pp. 162–165, 2005.

Sprung, D. and Zahn, A.: Acetone in the upper troposphere/lowermost stratosphere measured by the CARIBIC passenger aircraft: Distribution, seasonal cycle, and variability, J. Geophys. Res., 115, D16 301, doi:10.1029/2009JD012099, 2010.

Sprung, D., Jost, C., Reiner, T., Hansel, A., and Wisthaler, A.: Acetone and acetonitrile in the tropical Indian Ocean boundary layer and free troposphere: Aircraft-based intercomparison of AP-CIMS and PTR-MS measurements, J. Geophys. Res. Atmos., 106, 28 511–28 527, doi:10.1029/2000JD900599, 2001.

Stavrakou, T., Müller, J.-F., De Smedt, I., Van Roozendael, M., van der Werf, G. R., Giglio, L., and Guenther, A.: Evaluating the performance of pyrogenic and biogenic emission inventories against one decade of space-based formaldehyde columns, Atmos. Chem. Phys., 9, 1037–1060, doi:10.5194/acp-9-1037-2009, 2009.

Steeghs, M., Bais, H. P., de Gouw, J., Goldan, P., Kuster, W., Northway, M., Fall, R., and Vivanco, J. M.: Proton-Transfer-Reaction Mass Spectrometry as a New Tool for Real Time Analysis of Root-Secreted Volatile Organic Compounds in Arabidopsis, Plant Physiol., 135, 47–58, doi:10.1104/pp.104.038703, 2004.

Stein, O., Schultz, M. G., Bouarar, I., Clark, H., Huijnen, V., Gaudel, A., George, M., and Clerbaux, C.: On the wintertime low bias of Northern Hemisphere carbon monoxide found in global model simulations, Atmos. Chem. Phys., 14, 9295–9316, doi:10.5194/acp-14-9295-2014, 2014.

Stein, A. F., Draxler, R. R., Rolph, G. D., Stunder, B. J. B., Cohen, M. D., and Ngan, F.: NOAA's HYSPLIT atmospheric transport and dispersion modeling system, Bull. Am. Meteorol. Soc., 96, 2059–2077, doi:10.1175/BAMS-D-14-00110.1, 2015.

Steinbacher, M., Dommen, J., Ammann, C., Spirig, C., Neftel, A., and Prevot, A. S. H.: Performance characteristics of a proton-transfer-reaction mass spectrometer (PTR-MS) derived from laboratory and field measurements, Int. J. Mass Spectrom., 239, 117–128, doi:10.1016/j.ijms.2004.07.015, 2004.

Stevens, B., Farrell, D., Hirsch, L., Jansen, F., Nuijens, L., Serikov, I., Brügmann, B., Forde, M., Linne, H., Lonitz, K., and Prospero, J. M.: The Barbados Cloud Observatory: Anchoring Investigations of Clouds and Circulation on the Edge of the ITCZ, Bull. Am. Meteorol. Soc., 97, 787–801, doi:10.1175/BAMS-D-14-00247.1, 2016.

Stiller, G. P., von Clarmann, T., Glatthor, N., Höpfner, M., Kellmann, S., Kimmich, E., Linden, A., Milz, M., Steck, T., and Fischer, H.: Retrievability of Upper Tropospheric Species and Parameters from MIPAS/ENVISAT Data, pp. 167–180, Springer Berlin Heidelberg, doi:10.1007/978-3-642-18875-6_20, 2004.

Stockwell, C. E., Veres, P. R., Williams, J., and Yokelson, R. J.: Characterization of biomass burning emissions from cooking fires, peat, crop residue, and other fuels with high-resolution proton-transfer-reaction time-of-flight mass spectrometry, Atmos. Chem. Phys., 15, 845–865, doi:10.5194/acp-15-845-2015, 2015.

Stockwell, C. E., Christian, T. J., Goetz, J. D., Jayarathne, T., Bhave, P. V., Praveen, P. S., Adhikari, S., Maharjan, R., DeCarlo, P. F., Stone, E. A., Saikawa, E., Blake, D. R., Simpson, I. J., Yokelson, R. J., and Panday, A. K.: Nepal Ambient Monitoring and Source Testing Experiment (NAMaSTE): emissions of trace gases and light-absorbing carbon from wood and dung cooking fires, garbage and crop residue burning, brick kilns, and other sources, Atmos. Chem. Phys., 16, 11 043–11 081, doi:10.5194/acp-16-11043-2016, 2016.

Stohl, A., James, P., Forster, C., Spichtinger, N., Marenco, A., Thouret, V., and Smit, H. G. J.: An extension of Measurement of Ozone and Water Vapour by Airbus In-service Aircraft (MOZAIC) ozone climatologies using trajectory statistics, J. Geophys. Res. Atmos., 106, 27 757–27 768, doi:10.1029/2001JD000749, 2001.

Stohl, A., Eckhardt, S., Forster, C., James, P., Spichtinger, N., and Seibert, P.: A replacement for simple back trajectory calculations in the interpretation of atmospheric trace substance measurements, Atmos. Environ., 36, 4635–4648, doi:10.1016/S1352-2310(02)00416-8, 2002.

Stohl, A., Bonasoni, P., Cristofanelli, P., Collins, W., Feichter, J., Frank, A., Forster, C., Gerasopoulos, E., Gäggeler, H., James, P., Kentarchos, T., Kromp-Kolb, H., Krüger, B., Land, C., Meloen, J., Papayannis, A., Priller, A., Seibert, P., Sprenger, M., Roelofs, G. J., Scheel, H. E., Schnabel, C., Siegmund, P., Tobler, L., Trickl, T., Wernli, H., Wirth, V., Zanis, P., and Zerefos, C.: Stratosphere-troposphere exchange: A review, and what we have learned from STACCATO, J. Geophys. Res. Atmos., 108, 8516, doi:10.1029/2002JD002490, 2003.

Stohl, A., Cooper, O. R., Damoah, R., Fehsenfeld, F. C., Forster, C., Hsie, E.-Y., Hübler, G., Parrish, D. D., and Trainer, M.: Forecasting for a Lagrangian aircraft campaign, Atmos. Chem. Phys., 4, 1113–1124, doi:10.5194/acp-4-1113-2004, 2004.

Stone, D., Whalley, L. K., and Heard, D. E.: Tropospheric OH and HO_2 radicals: field measurements and model comparisons, Chem. Soc. Rev., 41, 6348–6404, doi:10.1039/c2cs35140d, 2012.

Streets, D. G., Bond, T. C., Carmichael, G. R., Fernandes, S. D., Fu, Q., He, D., Klimont, Z., Nelson, S. M., Tsai, N. Y., Wang, M. Q., Woo, J.-H., and Yarber, K. F.: An inventory of gaseous and primary aerosol emissions in Asia in the year 2000, J. Geopghys. Res., 108, 8809, doi:10.1029/2002JD003093, 2003.

Sugiura, N.: Further analysts of the data by akaike' s information criterion and the finite corrections, Commun. Stat. - Theory Methods, 7, 13–26, doi:10.1080/03610927808827599, 1978.

Sulzer, P., Hartungen, E., Hanel, G., Feil, S., Winkler, K., Mutschlechner, P., Haidacher, S., Schottkowsky, R., Gunsch, D., Seehauser, H., Striednig, M., Jürschik, S., Breiev, K., Lanza, M., Herbig, J., Märk, L., Märk, T. D., and Jordan, A.: A Proton Transfer Reaction-Quadrupole interface Time-Of-Flight Mass Spectrometer (PTR-QiTOF): High speed due to extreme sensitivity, Int. J. Mass Spectrom., 368, 1–5, doi:10.1016/j.ijms.2014.05.004, 2014.

Taipale, R., Ruuskanen, T. M., Rinne, J., Kajos, M. K., Hakola, H., Pohja, T., and Kulmala, M.: Technical Note: Quantitative long-term measurements of VOC concentrations by PTR-MS – measurement, calibration, and volume mixing ratio calculation methods, Atmos. Chem. Phys., 8, 6681–6698, doi:10.5194/acp-8-6681-2008, 2008.

Talbot, R. W., Andreae, M. O., Berresheim, H., Jacob, D. J., and Beecher, K. M.: Sources and sinks of formic, acetic, and pyruvic acids over central Amazonia: 2. Wet season, J. Geophys. Res., 95, 16799–16811, doi:10.1029/JD095iD10p16799, 1990.

Tamaddoni, M., Sotudeh-Gharebagh, R., Nario, S., Hajihosseinzadeh, M., and Mostoufi, N.: Experimental study of the VOC emitted from crude oil tankers, Process Saf. Environ. Prot., 92, 929–937, doi:10.1016/j.psep.2013.10.005, 2014.

Tata, P., Withersppon, J., and Lue-Hing, C.: VOC Emissions from Wastewater Treatment Plants: Characterization, Control and Compliance, Lewis Publishers, Boca Raton, 432 pp., 2003.

Tereszchuk, K. A., González Abad, G., Clerbaux, C., Hadji-Lazaro, J., Hurtmans, D., Coheur, P.-F., and Bernath, P. F.: ACE-FTS observations of pyrogenic trace species in boreal biomass burning plumes during BORTAS, Atmos. Chem. Phys., 13, 4529–4541, doi:10.5194/acp-13-4529-2013, 2013a.

Tereszchuk, K. A., Moore, D. P., Harrison, J. J., Boone, C. D., Park, M., Remedios, J. J., Randel, W. J., and Bernath, P. F.: Observations of peroxyacetyl nitrate (PAN) in the upper troposphere by the Atmospheric Chemistry Experiment-Fourier Transform Spectrometer (ACE-FTS), Atmos. Chem. Phys., 13, 5601–5613, doi:10.5194/acp-13-5601-2013, 2013b.

Thornton, J. A., Wooldridge, P. J., Cohen, R. C., Martinez, M., Harder, H., Brune, W. H., Williams, E., Roberts, J., Fehsenfeld, F. C., Hall, S. R., Shetter, R., Wert, B. P., and Fried, A.: Ozone production rates as a function of NO_x abundances and HO_x production rates in the Nashville urban plume, J. Geophys. Res., 107, 1–17, doi:10.1029/2001jd000932, 2002.

Thouret, V., Cammas, J.-P., Suavage, B., Athier, G., Zbinden, R., Nédélec, P., Simon, P., and Karcher, F.: Tropopause referenced ozone climatology and inter-annual variability (1994–2003) from the MOZAIC programme, Atmos. Chem. Phys., 6, 1033-1051, doi:10.5194/acp-6-1033-2006, 2006.

Tie, X., Guenther, A., and Holland, E.: Biogenic methanol and its impacts on tropospheric oxidants, Geophys. Res. Lett., 30, 1881, doi:10.1029/2003GL017167, 2003.

TofWerk: `http://www.tofwerk.com/citof-ptr-release`, last access: 1 August 2017.

Tomita, H. and Satoh, M.: A new dynamical framework of nonhydrostatic global model using the icosahedral grid, Fluid Dyn. Res., 34, 357–400, doi:10.1016/j.fluiddyn.2004.03.003, 2004.

Tomsche, L., Parchatka, U., and Fischer, H.: TRIHOP TRISTAR data of the OMO-Asia campaign, HALO Database, available at: `https://halo-db.pa.op.dlr.de/data_source/38`, 2016a.

Tomsche, L., Pozzer, A., Zimmermann, P., Parchatka, U., and Fischer, H.: Trace gas transport out of the Indian Summer Monsoon, in: Geophys. Res. Abstr., vol. 18, p. 3828, European Geosciences Union, 2016b.

Tomsche, L., Pozzer, A., Zimmermann, P., Parchatka, U., Lelieveld, J., and Fischer, H.: Upper tropospheric CH_4 and CO affected by the Indian summer monsoon during OMO, in: Geophys. Res. Abstr., vol. 19, p. 2993, European Geosciences Union, 2017.

Traub, M., Fischer, H., de Reus, M., Kormann, R., Heland, H., Ziereis, H., Schlager, H., Holzinger, R., Williams, J., Warneke, C., de Gouw, J., and Lelieveld, J.: Chemical characteristics assigned to trajectory clusters during the MINOS campaign, Atmos. Chem. Phys., 3, 459–468, doi:10.5194/acp-3-459-2003, 2003.

Treadaway, V.: Measurement of Formic and Acetic Acid in Air by Chemical Ionization Mass Spectroscopy: Airborne Method Development, Ph.D. thesis, University of Rhode Island, 2015.

Trenberth, K. E. and Guillemot, C. J.: The total mass of the atmosphere, J. Geophys. Res. Atmos., 99, 23 079–23 088, doi:10.1029/94JD02043, 1994.

Turetsky, M. R., Kane, E. S., Harden, J. W., Ottmar, R. D., Manies, K. L., Hoy, E., and Kasischke, E. S.: Recent acceleration of biomass burning and carbon losses in Alaskan forests and peatlands, Nat. Geosci, 4, 27–31, doi:10.1038/ngeo1027, 2011.

Turquety, S., Logan, J. A., Jacob, D. J., Hudman, R. C., Leung, F. Y., Heald, C. L., Yantosca, R. M., Wu, S., Emmons, L. K., Edwards, D. P., and Sachse, G. W.: Inventory of boreal fire emissions for North America in 2004: Importance of peat burning and pyroconvective injection, J. Geophys. Res., 112, D12S03, doi:10.1029/2006JD007281, 2007.

Twomey, S.: Pollution and the planetary albedo, Atmos. Environ., 8, 1251–1256, doi:10.1016/0004-6981(74)90004-3, 1974.

Umweltbundesamt: Emission flüchtiger organischer Verbindungen ohne Methan (NMVOC): `http://www.umweltbundesamt.de/daten/luftbelastung/luftschadstoff-emissionen-in-deutschland/emission-fluechtiger-organischer-verbindungen`, lass access: 1 September 2017.

Valach, A. C., Langford, B., Nemitz, E., MacKenzie, A. R., and Hewitt, C. N.: Concentrations of selected volatile organic compounds at kerbside and background sites in central London, Atmos. Environ., 95, 456–467, doi:10.1016/j.atmosenv.2014.06.052, 2014.

van Aardenne, J. A., Dentener, F. J., Olivier, J. G. J., Goldewijk, C. G. M. K., and Lelieveld, J.: A $1^\circ \times 1^\circ$ resolution data set of historical anthropogenic trace gas emissions for the period 1890–1990, Global Biogeochem. Cycles, 15, 909–928, doi:10.1029/2000GB001265, 2001.

van der Werf, G. R., Randerson, J. T., and Giglio, L.: Global Fire Emissions Database, Version 4 (GFED4s) – Monthly and daily fire emissions 1997–2016: `http://www.geo.vu.nl/~gwerf/GFED/GFED4/Readme.pdf`, last access: 1 September 2017.

van der Werf, G. R., Randerson, J. T., Giglio, L., Collatz, G. J., Kasibhatla, P. S., and Arellano, A. F.: Interannual variability in global biomass burning emissions from 1997 to 2004, Atmos. Chem. Phys., 6, 3423–3441, doi:10.5194/acp-6-3423-2006, 2006.

van der Werf, G. R., Randerson, J. T., Giglio, L., Collatz, G. J., Mu, M., Kasibhatla, P. S., Morton, D. C., DeFries, R. S., Jin, Y., and van Leeuwen, T. T.: Global fire emissions and the contribution of deforestation, savanna, forest, agricultural, and peat fires (1997–2009), Atmos. Chem. Phys., 10, 11 707–11 735, doi:10.5194/acp-10-11707-2010, 2010.

van der Werf, G. R., Randerson, J. T., Giglio, L., van Leeuwen, T. T., Chen, Y., Rogers, B. M., Mu, M., van Marle, M. J. E., Morton, D. C., Collatz, G. J., Yokelson, R. J., and Kasibhatla, P. S.: Global fire emissions estimates during 1997–2016, Earth Syst. Sci. Data, 9, 697–720, doi:10.5194/essd-9-697-2017, 2017a.

van der Werf, G. R., Randerson, J. T., and Giglio, L.: Global Fire Emissions Database, Version 4 (GFED4s) – Monthly and daily fire emissions 1997–2016: `http://www.geo.vu.nl/~gwerf/GFED/GFED4/Readme.pdf`, last access: 1 September 2017, 2017b.

van Leeuwen., T. T., Peters, W., Krol, M. C., and van der Werf, G. R.: Dynamic biomass burning emission factors and their impact on atmospheric CO mixing ratios: J. Geophys. Res. Atmos., 118, 6797–6815, doi:10.1002/jgrd.50478, 2013.

van Velthoven, P. F.: Meteorological analysis of CARIBIC by KNMI: `http://projects.knmi.nl/campaign_support/CARIBIC/`, last access: 1 September 2017.

Vardavas, I. and Taylor, F.: Radiation and Climate: Atmospheric energy budget from satellite remote sensing, Oxford University Press, New York, 477 pp., 2007.

Vasilescu, G.: Electronic Noise and Interfering Signals Principles and Applications, Springer Berlin Heidelberg, 709 pp., 2005.

Vivaldo, G., Masi, E., Taiti, C., Caldarelli, G., and Mancuso, S.: The network of plants volatile organic compounds, Sci. Rep., 7, 11 050, doi:10.1038/s41598-017-10975-x, 2017.

Vlasenko, A., Slowik, J. G., Bottenheim, J. W., Brickell, P. C., Chang, R. Y.-W., Macdonald, A. M., Shantz, N. C., Sjostedt, S. J., Wiebe, H. A., Leaitch, W. R., and Abbatt, J. P. D.: Measurements of VOCs by proton transfer reaction mass spectrometry at a rural Ontario site: Sources and correlation to aerosol composition, J. Geophys. Res. Atmos., 114, D21305, doi:10.1029/2009JD012025, 2009.

Vlasenko, A., Macdonald, A. M., Sjostedt, S. J., and Abbatt, J. P. D.: Formaldehyde measurements by Proton transfer reaction – Mass Spectrometry (PTR-MS): correction for humidity effects, Atmos. Meas. Tech., 3, 1055–1062, doi: 10.5194/amt-3-1055-2010, 2010.

Voigt, C., Schumann, U., Minikin, A., Abdelmonem, A., Afchine, A., Borrmann, S., Boettcher, M., Buchholz, B., Bugliaro, L., Costa, A., Curtius, J., Dollner, M., Dörnbrack, A., Dreiling, V., Ebert, V., Ehrlich, A., Fix, A., Forster, L., Frank, F., Fütterer, D., Giez, A., Graf, K., Grooß, J.-U., Groß, S., Heimerl, K., Heinold, B., Hüneke, T., Järvinen, E., Jurkat, T., Kaufmann, S., Kenntner, M., Klingebiel, M., Klimach, T., Kohl, R., Krämer, M., Krisna, T. C., Luebke, A., Mayer, B., Mertes, S., Molleker, S., Petzold, A., Pfeilsticker, K., Port, M., Rapp, M., Reutter, P., Rolf, C., Rose, D., Sauer, D., Schäfler, A., Schlage, R., Schnaiter, M., Schneider, J., Spelten, N., Spichtinger, P., Stock, P., Walser, A., Weigel, R., Weinzierl, B., Wendisch, M., Werner, F., Wernli, H., Wirth, M., Zahn, A., Ziereis, H., and Zöger, M.: ML-CIRRUS: The Airborne Experiment on Natural Cirrus and Contrail Cirrus with the High-Altitude Long-Range Research Aircraft HALO, Bull. Am. Meteorol. Soc., 98, 271–288, doi:10.1175/BAMS-D-15-00213.1, 2017.

von Schneidemesser, E., Monks, P. S., Plass-Duelmer, C.: Global comparison of VOC and CO observations in urban areas, Atmos. Environ., 44, 5053–5064, doi: 10.1016/j.atmosenv.2010.09.010, 2010.

Voss, P. B., Zaveri, R. A., Flocke, F. M., Mao, H., Hartley, T. P., DeAmicis, P., Deonandan, I., Contreras-Jiménez, G., Martínez-Antonio, O., Figueroa Estrada, M., Greenberg, D., Campos, T. L., Weinheimer, A. J., Knapp, D. J., Montzka, D. D., Crounse, J. D., Wennberg, P. O., Apel, E., Madronich, S., and de Foy, B.: Long-range pollution transport during the MILAGRO-2006 campaign: a case study of a major Mexico City outflow event using free-floating altitude-controlled balloons, Atmos. Chem. Phys., 10, 7137–7159, doi:10.5194/acp-10-7137-2010, 2010.

Wagner, P. and Kuttler, W.: Biogenic and anthropogenic isoprene in the near-surface urban atmosphere – A case study in Essen, Germany, Sci. Total Environ., 475, 104–115, doi:10.1016/j.scitotenv.2013.12.026, 2014.

Wallington, T. J., Kaiser, E. W., and Farrell, J. T.: Automotive fuels and internal combustion engines: a chemical perspective., Chem. Soc. Rev., 35, 335–347, doi:10.1039/b410469m, 2006.

Wan, H., Giorgetta, M. A., Zängl, G., Restelli, M., Majewski, D., Bonaventura, L., Fröhlich, K., Reinert, D., Rípodas, P., Kornblueh, L., and Förstner, J.: The ICON-1.2 hydrostatic atmospheric dynamical core on triangular grids – Part 1: Formulation and performance of the baseline version, Geosci. Model Dev., 6, 735–763, doi:10.5194/gmd-6-735-2013, 2013.

Schwartz, S. E. and Warneck, P.: Units for use in atmospheric chemistry (IUPAC Recommendations 1995), Pure Appl. Chem., 67, 1377–1406, doi:10.1351/pac199567081377, 1995.

Warneke, C. and de Gouw, J.: Organic trace gas composition of the marine boundary layer over the northwest Indian Ocean in April 2000, Atmos. Environ., 35, 5923–5933, doi:10.1016/S1352-2310(01)00384-3, 2001.

Warneke, C., Karl, T., Judmaier, H., Hansel, A., Jordan, A., Lindinger, W., and Crutzen, P. J.: Acetone, methanol, and other partially oxidized volatile organic emissions from dead plant matter by abiological processes: Significance for atmospheric HO_x chemistry, Glob. Biogeochem. Cycles, 13, 9–17, doi:10.1029/98GB02428, 1999.

Warneke, C., Van Der Veen, C., Luxembourg, S., De Gouw, J. A., and Kok, A.: Measurements of benzene and toluene in ambient air using proton-transfer-reaction mass spectrometry: Calibration, humidity dependence, and field intercomparison, Int. J. Mass Spectrom., 207, 167–182, doi:10.1016/S1387-3806(01)00366-9, 2001.

Warneke, C., de Gouw, J. A., Stohl, A., Cooper, O. R., Goldan, P. D., Kuster, W. C., Holloway, J. S., Williams, E. J., Lerner, B. M., McKeen, S. A., Trainer, M., Fehsenfeld, F. C., Atlas, E. L., Donnelly, S. G., Stroud, V., Lueb, A., and Kato, S.: Biomass burning and anthropogenic sources of CO over New England in the summer 2004, J. Geophys. Res. Atmos., 111, D23S15, doi:10.1029/2005JD006878, 2006.

Warneke, C., McKeen, S. A., de Gouw, J. A., Goldan, P. D., Kuster, W. C., Holloway, J. S., Williams, E. J., Lerner, B. M., Parrish, D. D., Trainer, M., Fehsenfeld, F. C., Kato, S., Atlas, E. L., Baker, A., and Blake, D. R.: Determination of urban volatile organic compound emission ratios and comparison with an emissions database, J. Geophys. Res. Atmos., 112, doi:10.1029/2006JD007930, 2007.

Warneke, C., Bahreini, R., Brioude, J., Brock, C. A., De Gouw, J. A., Fahey, D. W., Froyd, K. D., Holloway, J. S., Middlebrook, A., Miller, L., Montzka, S., Murphy, D. M., Peischl, J., Ryerson, T. B., Schwarz, J. P., Spademan, J. R., and Veres, P.: Biomass burning in Siberia and Kazakhstan as an important source for haze over the Alaskan Arctic in April 2008, Geophys. Res. Lett., 36, 2–7, doi:10.1029/2008GL036194, 2009.

Warneke, C., Roberts, J. M., Veres, P., Gilman, J., Kuster, W. C., Burling, I., Yokelson, R., and De Gouw, J. A.: VOC identification and inter-comparison from laboratory biomass burning using PTR-MS and PIT-MS, Int. J. Mass Spectrom., 303, 6–14, doi:10.1016/j.ijms.2010.12.002, 2011.

Warneke, C., de Gouw, J. A., Holloway, J. S., Peischl, J., Ryerson, T. B., Atlas, E., Blake, D., Trainer, M., and Parrish, D. D.: Multiyear trends in volatile organic compounds in Los Angeles, California: Five decades of decreasing emissions, J. Geophys. Res. Atmos., 117, D00V17, doi:10.1029/2012JD017899, 2012.

Warneke, C., De Gouw, J. A., Edwards, P. M., Holloway, J. S., Gilman, J. B., Kuster, W. C., Graus, M., Atlas, E., Blake, D., Gentner, D. R., Goldstein, A. H., Harley, R. A., Alvarez, S., Rappenglueck, B., Trainer, M., and Parrish, D. D.: Photochemical aging of volatile organic compounds in the Los Angeles basin: Weekday-weekend effect, J. Geophys. Res. Atmos., 118, 5018–5028, doi:10.1002/jgrd.50423, 2013.

Warneke, C., Geiger, F., Edwards, P. M., Dube, W., Pétron, G., Kofler, J., Zahn, A., Brown, S. S., Graus, M., Gilman, J. B., Lerner, B. M., Peischl, J., Ryerson, T. B., de Gouw, J. A., and Roberts, J. M.: Volatile organic compound emissions from the oil and natural gas industry in the Uintah Basin, Utah: oil and gas well pad emissions compared to ambient air composition, Atmos. Chem. Phys., 14, 10 977–10 988, doi:10.5194/acp-14-10977-2014, 2014.

Warneke, C., Veres, P., Murphy, S. M., Soltis, J., Field, R. A., Graus, M. G., Koss, A., Li, S. M., Li, R., Yuan, B., Roberts, J. M., and De Gouw, J. A.: PTR-QMS versus PTR-TOF comparison in a region with oil and natural gas extraction industry in the Uintah Basin in 2013, Atmos. Meas. Tech., 8, 411–420, doi:10.5194/amt-8-411-2015, 2015.

Waterfall, A. M., Remedios, J. J., Allen G., and Sembhi, H.: Infrared remote sensing of organic compounds in the upper troposphere, Proceedings of the ENVISAT Symposium, Salzburg, September, 2004.

Weimer, M., Schröter, J., Eckstein, J., Deetz, K., Neumaier, M., Fischbeck, G., Hu, L., Millet, D. B., Rieger, D., Vogel, H., Vogel, B., Reddmann, T., Kirner, O., Ruhnke, R., and Braesicke, P.: An emission module for ICON-ART 2.0: implementation and simulations of acetone, Geosci. Model Dev., 10, 2471–2494, doi:10.5194/gmd-10-2471-2017, 2017.

Wendisch, M., Pöschl, U., Andreae, M. O., Machado, L. A. T., Albrecht, R., Schlager, H., Rosenfeld, D., Martin, S. T., Abdelmonem, A., Afchine, A., Araùjo, A. C., Artaxo, P., Aufmhoff, H., Barbosa, H. M. J., Borrmann, S., Braga, R., Buchholz, B., Cecchini, M. A., Costa, A., Curtius, J., Dollner, M., Dorf, M., Dreiling, V., Ebert, V., Ehrlich, A., Ewald, F., Fisch, G., Fix, A., Frank, F., Fütterer, D., Heckl, C., Heidelberg, F., Hüneke, T., Jäkel, E., Järvinen, E., Jurkat, T., Kanter, S., Kästner, U., Kenntner, M., Kesselmeier, J., Klimach, T., Knecht, M., Kohl, R., Kölling, T., Krämer, M., Krüger, M., Krisna, T. C., Lavric, J. V., Longo, K., Mahnke, C., Manzi, A. O., Mayer, B., Mertes, S., Minikin, A., Molleker, S., Münch, S., Nillius, B., Pfeilsticker, K., Pöhlker, C., Roiger, A., Rose, D., Rosenow, D., Sauer, D., Schnaiter, M., Schneider, J., Schulz, C., de Souza, R. A. F., Spanu, A., Stock, P., Vila, D., Voigt, C., Walser, A., Walter, D., Weigel, R., Weinzierl, B., Werner, F., Yamasoe, M. A., Ziereis, H., Zinner, T., and Zöger, M.: ACRIDICON–CHUVA Campaign: Studying Tropical Deep Convective Clouds and Precipitation over Amazonia Using the New German Research Aircraft HALO, Bull. Am. Meteorol. Soc., 97, 1885–1908, doi:10.1175/BAMS-D-14-00255.1, 2016.

Wenk, A.-K.: Optimierung und Anwendung eines schnellen GC-MS-Systems für mobile Messungen flüchtiger organischer Substanzen, Ph.D. thesis, University of Cologne, 2016.

Wenk, A.-K., Wegener, R., Hofzumahaus, A., and Wahner, A.: Development of a fast GC/MS-system for airborne measurements of Volatile Organic Compounds, Geophys. Res. Abstr., 12, 4254, 2010.

Wennberg, P. O., Hanisco, T. F., Jaeglé, L., Jacob, D. J., Hintsa, E. J., Lanzendorf, E. J., Anderson, J. G., Gao, R.-S., Keim, E. R., Donelly, S. G., Del Negro, L. A., Fahey, D. W., McKeen, S. A., Salawitch, R. J., Webster, C. R., May, R. D., Herman, R. L., Proffitt, M. H., Margitan, J. J., Atlas, E. L., Schauffler, S. M., Flocke, F., McElroy, C. T., and Bui, T. P.: Hydrogen Radicals, Nitrogen Radicals, and the Production of O_3 in the Upper Troposphere, Science, 279, 49–53, doi:10.1126/science.279.5347.49, 1998.

Wiegele, A., Schneider, M., Hase, F., Barthlott, S., García, O. E., Sepúlveda, E., González, Y., Blumenstock, T., Raffalski, U., Gisi, M., and Kohlhepp, R.: The MUSICA MetOp/IASI H_2O and δD products: characterisation and long-term comparison to NDACC/FTIR data, Atmos. Meas. Tech., 7, 2719–2732, doi:10.5194/amt-7-2719-2014, 2014.

Williams, J.: Organic trace gases in the atmosphere: An overview, Environ. Chem., 1, 125–136, doi:10.1071/EN04057, 2004.

Williams, J., and Koppmann, R.: Volatile Organic Compounds in the Atmosphere: An Overview, in: Volatile Organic Compounds in the Atmosphere, edited by Koppmann, R., pp. 1–32, Blackwell Publishing, Oxford, 2007.

Williamson, J. H.: Least-squares fitting of a straight line, Can. J. Phys., 46, 1845–1847, doi:10.1139/p68-523, 1968.

Wisthaler, A. and Weschler, C. J.: Reactions of ozone with human skin lipids: Sources of carbonyls, dicarbonyls, and hydroxycarbonyls in indoor air, Proc. Natl. Acad. Sci., 107, 6568–6575, doi:10.1073/pnas.0904498106, 2010.

Wisthaler, A., Hansel, A., Dickerson, R. R., and Crutzen, P. J.: Organic trace gas measurements by PTR-MS during INDOEX 1999, J. Geophys. Res., 107, 8024, doi:10.1029/2001JD000576, 2002.

Wisthaler, A., Tamás, G., Wyon, D. P., Strøm-Tejsen, P., Space, D., Beauchamp, J., Hansel, A., Märk, T. D., and Weschler, C. J.: Products of Ozone-Initiated Chemistry in a Simulated Aircraft Environment, Environ. Sci. Technol., 39, 4823–4832, doi:10.1021/es047992j, 2005.

Wisthaler, A., Apel, E. C., Bossmeyer, J., Hansel, A., Junkermann, W., Koppmann, R., Meier, R., Müller, K., Solomon, S. J., Steinbrecher, R., Tillmann, R., and Brauers, T.: Technical Note: Intercomparison of formaldehyde measurements at the atmosphere simulation chamber SAPHIR, Atmos. Chem. Phys., 8, 2189–2200, doi:10.5194/acp-8-2189-2008, 2008.

Wunch, D., Toon, G. C., Blavier, J. F., Washenfelder, R. A., Notholt, J., Connor, B. J., Griffith, D. W., Sherlock, V., Wennberg, P. O.: The total carbon column observing network, Philos Trans A Math Phys Eng Sci., 369, 2081–2112; doi: 10.1098/rsta.2010.0240, 2011.

Wyatt, S.: The generation of VOC's from stationary gas turbines and the impact on oxidation catalyst performance, MANE6960 AWPPCE Project Report, available at: `http://www.ewp.rpi.edu/hartford/~ernesto/F2013/AWPPCE/StudProj/Wyatt/Wyatt-PR-AP.pdf`, 2013.

Wyche, K. P., Monks, P. S., Ellis, A. M., Cordell, R. L., Parker, A. E., Whyte, C., Metzger, A., Dommen, J., Duplissy, J., Prevot, A. S. H., Baltensperger, U., Rickard, A. R., and Wulfert, F.: Gas phase precursors to anthropogenic secondary organic aerosol: detailed observations of 1,3,5-trimethylbenzene photooxidation, Atmos. Chem. Phys., 9, 635–665, doi:10.5194/acp-9-635-2009, 2009.

Yang, M., Beale, R., Smyth, T., and Blomquist, B.: Measurements of OVOC fluxes by eddy covariance using a proton-transfer-reaction mass spectrometer – method development at a coastal site, Atmos. Chem. Phys., 13, 6165–6184, doi:10.5194/acp-13-6165-2013, 2013.

Yokelson, R. J., Crounse, J. D., DeCarlo, P. F., Karl, T., Urbanski, S., Atlas, E., Campos, T., Shinozuka, Y., Kapustin, V., Clarke, A. D., Weinheimer, A., Knapp, D. J., Montzka, D. D., Holloway, J., Weibring, P., Flocke, F., Zheng, W., Toohey, D., Wennberg, P. O., Wiedinmyer, C., Mauldin, L., Fried, A., Richter, D., Walega, J., Jimenez, J. L., Adachi, K., Buseck, P. R., Hall, S. R., and Shetter, R.: Emissions from biomass burning in the Yucatan, Atmos. Chem. Phys., 9, 5785–5812, doi: 10.5194/acp-9-5785-2009, 2009.

Yokelson, R. J., Andreae, M. O., and Akagi, S. K.: Pitfalls with the use of enhancement ratios or normalized excess mixing ratios measured in plumes to characterize pollution sources and aging, Atmos. Meas. Tech., 6, 2155–2158, doi:10.5194/amt-6-2155-2013, 2013.

York, D.: Least-Squares Fitting of a Straight Line, Can. J. Phys., 44, 1079–1086, doi:10.1139/p66-090, 1966.

York, D., Evensen, N. M., Martinez, M. L., and De Basabe Delgado, J.: Unified equations for the slope, intercept, and standard errors of the best straight line, Am. J. Phys., 72, 367–375, doi:10.1119/1.1632486, 2004.

Yuan, B., Hu, W. W., Shao, M., Wang, M., Chen, W. T., Lu, S. H., Zeng, L. M., and Hu, M.: VOC emissions, evolutions and contributions to SOA formation at a receptor site in eastern China, Atmos. Chem. Phys., 13, 8815–8832, doi: 10.5194/acp-13-8815-2013, 2013.

Yuan, B., Koss, A., Warneke, C., Gilman, J. B., Lerner, B. M., Stark, H., and de Gouw, J. A.: A high-resolution time-of-flight chemical ionization mass spectrometer utilizing hydronium ions (H_3O^+ ToF-CIMS) for measurements of volatile organic compounds in the atmosphere, Atmos. Meas. Tech., 9, 2735–2752, doi:10.5194/amt-9-2735-2016, 2016.

Zahn, A. and Brenninkmeijer, C. A.: New Directions: A Chemical Tropopause Defined, Atmos. Environ., 37, 439–440, doi:10.1016/S1352-2310(02)00901-9, 2003.

Zahn, A., Brenninkmeijer, C. A. M., Asman, W. A. H., Crutzen, P. J., Heinrich, G., Fischer, H., Cuijpers, J. W. M., and van Velthoven, P. F. J.: Budgets of O_3 and CO in the upper troposphere: CARIBIC passenger aircraft results 1997-2001, J. Geophys. Res. Atmos., 107, 4337, doi:10.1029/2001JD001529, 2002.

Zahn, A., Brenninkmeijer, C. A. M., and van Velthoven, P. F. J.: Passenger aircraft project CARIBIC 1997–2002, Part I: the extratropical chemical tropopause, Atmos. Chem. Phys. Discuss., 4, 1091–1117, doi:10.5194/acpd-4-1091-2004, 2004.

Zahn, A., Brito, J., and Sprung, D.: A lightweight, high-sensitivity PTRMS for aircraft platforms, in: Contributions to 4th International Conference on Proton Transfer Reaction Mass Spectrometry and its Applications, edited by Hansel, A. and Dunkel, J., pp. 114–115, Innsbruck University Press, Innsbruck, 2009.

Zahn, A., Weppner, J., Widmann, H., Schlote-Holubek, K., Burger, B., Kühner, T., and Franke, H.: A fast and precise chemiluminescence ozone detector for eddy flux and airborne application, Atmos. Meas. Tech., 5, 363–375, doi:10.5194/amt-5-363-2012, 2012.

Zahn, A., Neumaier, M., Geiger, F., and Fischbeck, G.: PTRMS onboard passenger and research aircraft: technical realization, performance, and results, in: Contributions to 6th International Conference on Proton Transfer Reaction Mass Spectrometry and its Applications, edited by Hansel, A. and Dunkl, J., pp. 135–137, Innsbruck University Press, Innsbruck, 2013.

Zängl, G., Reinert, D., Rípodas, P., and Baldauf, M.: The ICON (ICOsahedral Non-hydrostatic) modelling framework of DWD and MPI-M: Description of the non-hydrostatic dynamical core, Q. J. R. Meteorol. Soc., 141, 563–579, doi:10.1002/qj.2378, 2015.

Zavala, M., Herndon, S. C., Slott, R. S., Dunlea, E. J., Marr, L. C., Shorter, J. H., Zahniser, M., Knighton, W. B., Rogers, T. M., Kolb, C. E., Molina, L. T., and Molina, M. J.: Characterization of on-road vehicle emissions in the Mexico City Metropolitan Area using a mobile laboratory in chase and fleet average measurement modes during the MCMA-2003 field campaign, Atmos. Chem. Phys. Discuss., 6, 4689–4725, doi:10.5194/acpd-6-4689-2006, 2006.

Zbinden, R. M., Thouret, V., Ricaud, P., Carminati, F., Cammas, J.-P., and Nédélec, P.: Climatology of pure tropospheric profiles and column contents of ozone and carbon monoxide using MOZAIC in the mid-northern latitudes (24° N to 50° N) from 1994 to 2009, Atmos. Chem. Phys., 13, 12 363–12 388, doi:10.5194/acp-13-12363-2013, 2013.

Zhao, J. and Zhang, R.: Proton transfer reaction rate constants between hydronium ion (H_3O^+) and volatile organic compounds, Atmos. Environ., 38, 2177–2185, doi:10.1016/j.atmosenv.2004.01.019, 2004.

Zhou, X. and Mopper, K.: Photochemical production of low-molecular-weight carbonyl compounds in seawater and surface microlayer and their air-sea exchange, Mar. Chem., 56, 201–213, doi:10.1016/S0304-4203(96)00076-X, 1997.

List of Figures

List of Tables